PROCEEDINGS

OF THE

HIGH-POWER MICROWAVE TUBE SYMPOSIUM

VOLUME 1

THE HEXAGON
FORT MONMOUTH, NEW JERSEY

SEPTEMBER 25 and 26, 1962

CO-SPONSORED BY
THE U. S. ARMY SIGNAL RESEARCH AND DEVELOPMENT LABORATORY
AND
THE ADVISORY GROUP ON ELECTRON DEVICES

PROCEEDINGS

of the

HIGH-POWER MICROWAVE TUBES SYMPOSIUM

Held at

The Hexagon, Fort Monmouth, New Jersey

on

25 and 26 September 1962

VOLUME 1

The services and materials required for the arrangement, handling and reporting of this Symposium have been furnished under Signal Corps Contract DA 36-039 SC-89076

By

ELECTRON DEVICES GROUP
ENGINEERING RESEARCH DIVISION
NEW YORK UNIVERSITY

HIGH-POWER MICROWAVE TUBES SYMPOSIUM

COMMITTEE

I. Reingold, Co-Chairman
U. S. Army Electronics Research and Development Laboratory, Fort Monmouth, New Jersey

H. J. Hersh, Co-Chairman
U. S. Army Electronics Research and Development Laboratory, Fort Monmouth, New Jersey

W. Kramer, Secretary
Working Group on Electron Devices
Advisory Group on Electron Devices
346 Broadway
New York 13, New York

The papers compiled herein are prepared in their entirety as submitted. Each paper reflects the viewpoint of its author, and the U. S. Army Electronics Research and Development Laboratory and the Advisory Group on Electron Devices do not necessarily subscribe to the ideas and opinions expressed therein.

VOLUME I

TABLE OF CONTENTS

*Now with Mictron, Inc., Albany, N. Y.

**Session III and three papers in Session IV are classified and are published in a Classified VOLUME 2, of this symposium.

A Broadband Megawatt Hollow Beam Multicavity Klystron

By

Lindsey B. Anderson, Raytheon Company

And

Abraham Bers, Massachusetts Institute of Technology
Department of Electrical Engineering and
Laboratory of Electronics

I. Introduction

In recent years there has been a great interest in incorporating a hollow beam in high power klystron devices. This interest is based on the fact that with the higher perveance achievable with a hollow beam, lower operating voltages would be necessary and a larger bandwidth could be achieved. It can be assumed that rf power output P_{rf} of a klystron is proportional to the total beam power, P_o, of the device,

$$P_{rf} = \eta P_o$$

where η is the efficiency of the klystron. Since,

$$P_o = I_o V_o = k V_o^{5/2}$$

where V_o is the beam voltage, I_o is the beam current and $k = I_o/V_o^{3/2}$ is the perveance, it can be concluded that,

$$P_{rf} = \eta k V_o^{5/2}$$

It can easily be seen from this expression that the rf power output is directly proportional to the perveance (assuming all other properties of the device remain constant). Therefore, an increase in the perveance of a klystron can result in an increase in the rf power output, without an increase in beam voltage, provided that the efficiency does not deteriorate.

The small-signal gain and bandwidth of a multicavity klystron are essentially determined by the characteristics of a single stage; namely, the bandwidth of each cavity and the gain between successive cavities.[1,2]

Electronic bandwidth Δf, of a klystron cavity can be defined as:

$$\Delta f = \frac{f_o}{Q_{el}}$$

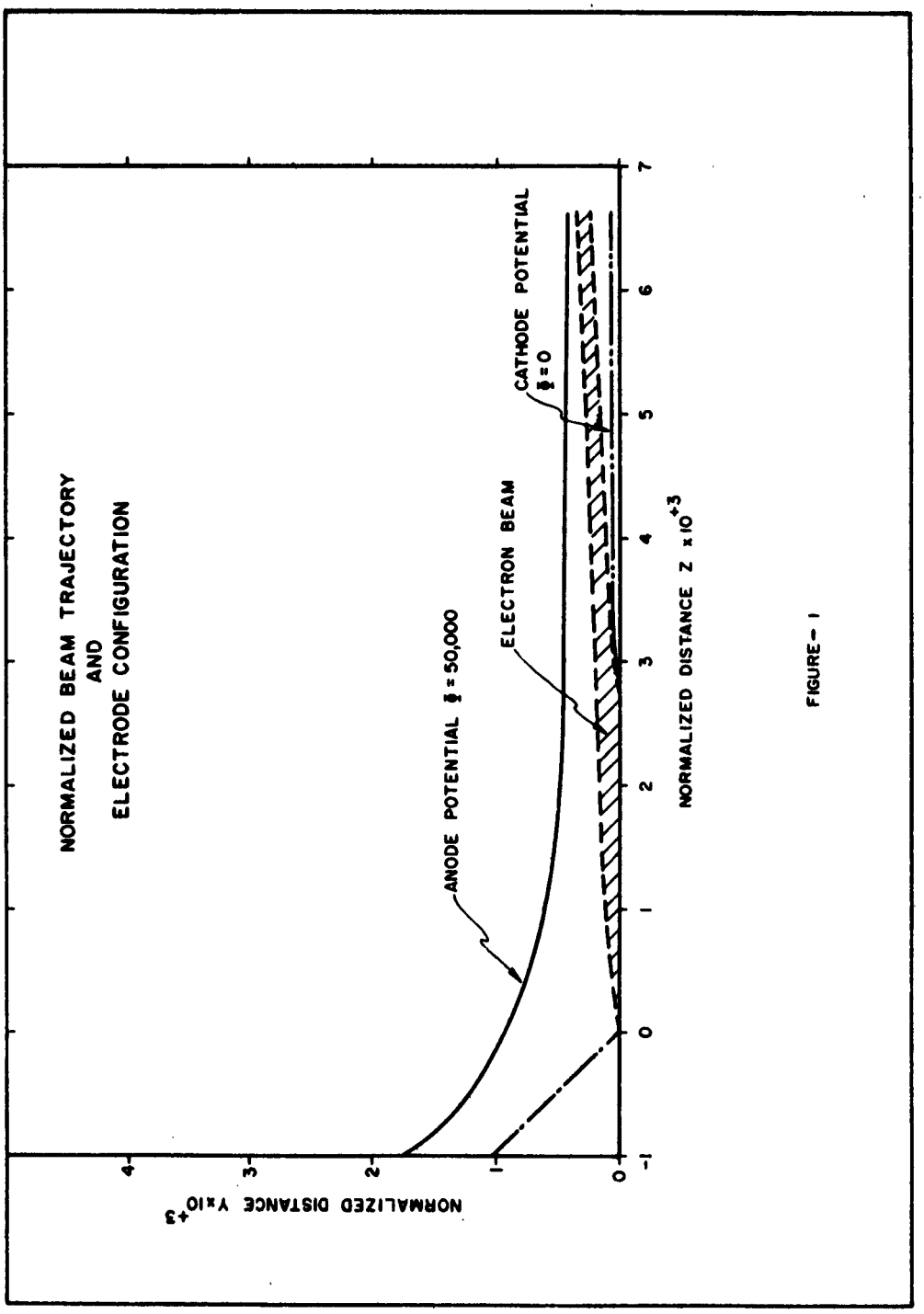
NORMALIZED BEAM TRAJECTORY
AND
ELECTRODE CONFIGURATION
ANODE POTENTIAL ϕ = 50,000
ELECTRON BEAM
CATHODE POTENTIAL
ϕ = 0
NORMALIZED DISTANCE Y x10+3
NORMALIZED DISTANCE Z x10+3
0
1
2
3
4
-1
0
1
2
3
4
5
6
7

FIGURE - 1

where Q_{el} is the electronic Q of the cavity and can be written in general terms as;

$$Q_{el} = \frac{1}{(R/Q)\, G_{el}}$$

where R/Q is the intrinsic impedance of the cavity and G_{el} is the electronic conductance of the cavity. The electronic conductance is proportional to the beam conductance, I_o/V_o,

$$G_{el} \sim G_o = \frac{I_o}{V_o} = P_o^{1/5}\, k^{4/5}$$

It is also a function of the beam-gap geometry and space charge. The per cent bandwidth of the klystron cavity can then be expressed as:

$$\frac{\Delta f}{f_o} \sim (R/Q)\; P_o^{1/5}\, k^{4/5}.$$

Thus, it can be seen that an increase in the perveance of a tube keeping all other factors constant will result in an increase in the electronic bandwidth.

It should be remembered, however, that an increase in perveance may cause a decrease in the gain of the device. In a very simplified manner, the power gain of a klystron stage[1] is proportional to,

$$g_{12}^2 \sim \frac{M^4}{\left(\frac{\omega_q}{\omega}\right)^2}$$

where M is a coupling coefficient, mostly a function of geometry, and ω_q is the reduced plasma radian frequency. For a fixed geometry and beam voltage, the expression can be approximately written as,

$$g_{12}^2 \sim \frac{1}{k}.$$

It can be seen from this expression that, if the dimensions and beam coupling of a klystron are held constant, the gain will vary inversely with the perveance.

It appears, therefore, that an increase in beam perveance of a klystron could result in lower voltage operation with greater bandwidth; however, these new features may have to be achieved at the expense of gain. With more care in the design of a hollow beam as well as the proper selection of gap lengths,

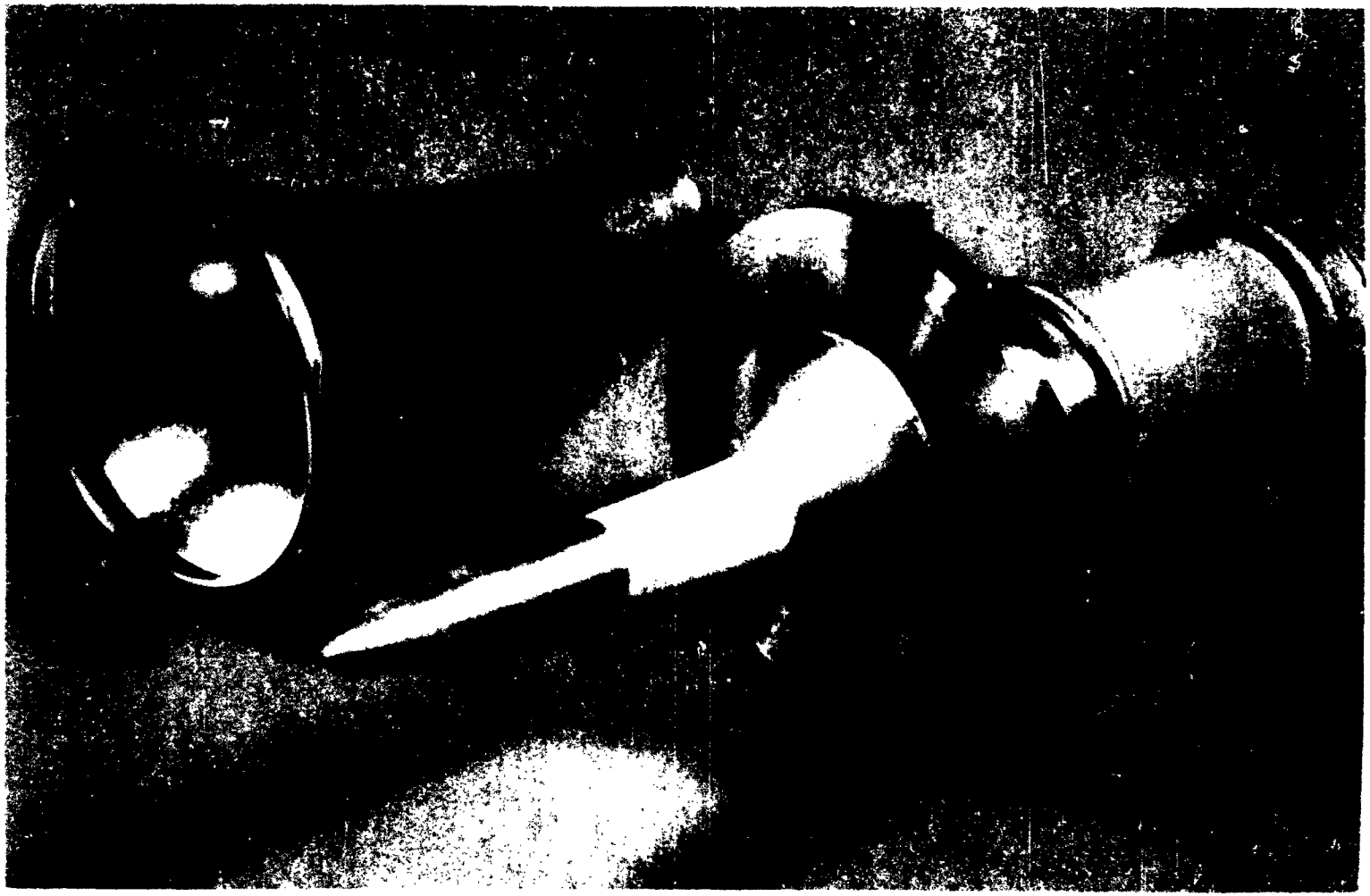

Figure 2 - Actual Conical Gun

an optimum condition may be reached in which acceptable tube design could be achieved. It should also be noted that an increase in tube efficiency may be expected because of the better rf coupling that can be achieved with a hollow beam. Because of these considerations, it was felt that the application of a hollow beam should be studied in a broadband klystron to determine the feasibility of such a combination. It is, therefore, the intention of this paper to report on the observations made on a broadband hollow beam klystron.

The major design problems which had to be overcome in order to study the effects of a hollow beam in a broadband klystron were the construction of the proper anode and cathode structure which would give a stable hollow beam. Also, proper design of the rf structure had to be considered so that reasonable gain and efficiency could be established. Since the consideration was for a broadband tube, a system of offering a constant impedance to the bunched current at the output gap over a reasonable frequency range had to be established. This led to the consideration of an output filter which would be incorporated in the output cavity of the klystron. Based on these design considerations, a seven-cavity hollow beam broadband klystron was constructed and the results obtained on this device are presented.

II. Anode and Cathode Design

The most suitable type of hollow beam gun that could be employed in the seven-cavity klystron was a form of magnetron injection gun. The basic design of this type of gun is to immerse a cylindrical cathode in a uniform magnetic field. There are, at present, no solutions known to provide a laminar hollow electron beam emanating from a cylindrical cathode in a uniform magnetic field; however, by employing conical cathode geometry, it is possible to obtain a solution and develop a technique for designing such a gun.

The design is further simplified if it is possible to find the equations of the trajectories in closed form. Techniques of analytic continuation of the potentials at the beam edge trajectories can then be used to determine the necessary gun electrodes. Such a procedure has been used successfully in the design of guns for cross-field beam tubes.[3,4] Work was carried out at Raytheon[5] in which an analogous procedure was developed for the design of a gun for longitudinal beam tubes. Electron trajectories were determined in closed form for a simplified two dimensional cathode geometry and equations determining the electrodes were solved. An appropriate set of trajectories and electrodes were then determined and corrected to apply approximately to a conical geometry. To reduce the amount of calculations which had to be done, the equations that determine the shape of the electrodes were solved by a digital computer. With the bulk of arithmetic done electronically, the complete design procedure for obtaining the desired hollow beam was carried out rapidly.

CHARACTERISTIC OF A BROADBAND HOLLOW BEAM KLYSTRON

CALCULATED VALUES

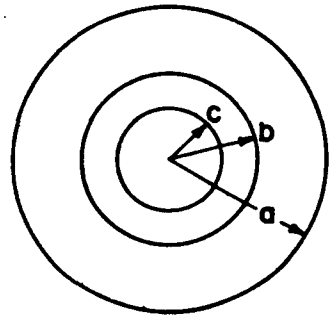

a = 1.608 cm.
b = 1.286 cm.
c = 1.093 cm.

$\beta_{ed} = 1.0$ rad.

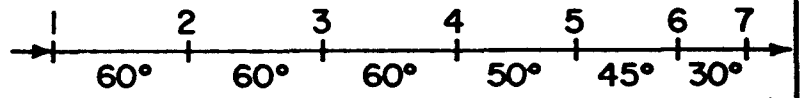

$\frac{\omega_p}{\omega} = .998$ $\frac{\omega_q}{\omega} = .115$

$V_0 = 50$ kv.
$I_0 = 78.4$ a.
$k = 7.0 \times 10^{-6}$
J_0 (cathode) $= 2.2$ a/cm^2
B = 1500 GAUSS (uniform)

$f_0 = 1300$ mc (BRANCH & MIHRAN)
$R_{el} = 3420\ \Omega$
$Q_{el} = 52$

MEASURED VALUES

$V_0 = 49.5$ kv.
$k = 7.26 \times 10^{-6}$
BEAM TRANSMISSION = 98.8%
B = APPROX. 1500 GAUSS (variable)

$Q_{el} = 45.5$
$g_{12} = 6.31$ db

FIGURE 3

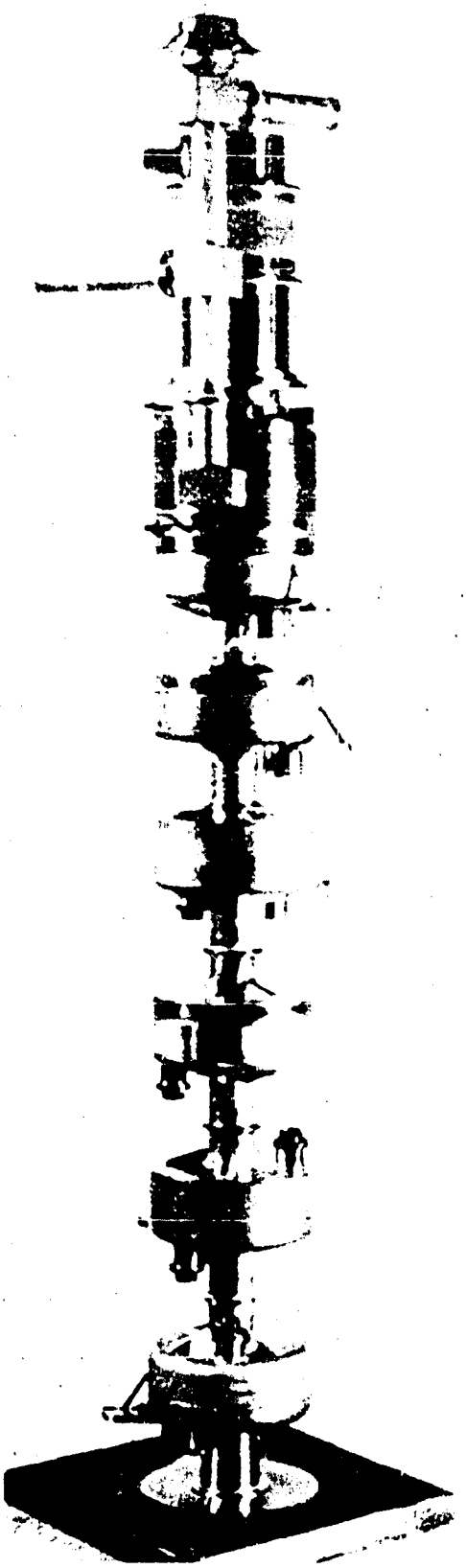

FIG. 4 - Seven Cavity Hollow-Beam Klystron

Figure 1 shows the result of the computer program utilized in determining the necessary electrode shapes that provide the proper beam formation.

The dimensions of the beam given by this program were the following:

$a = 1.608$ cm anode radius
$b = 1.286$ cm outer beam radius
$c = 1.093$ cm inner beam radius

These beam dimensions were based on a beam voltage of 50 kv which would produce a beam perveance of 7×10^{-6}. A cathode current density of 2.2 amps/cm^2 was selected corresponding to a uniform magnetic field of 1500 gauss and a cathode cone angle of two (2) degrees. Figure 2 depicts the actual conical gun that was constructed based on the computer design.

III. Design of the RF Structure

With the information on the beam shape, the electrical design of the broadband klystron was carried out using the available weak space charge theories of interaction. The reduced plasma wavelength λ_q was calculated based on the work of Branch and Mihran[6] resulting in a $\lambda_q = 81.4$ cm. This value was established for a 50 kv beam at a center frequency of 1300 Mc.

The electrical drift lengths were then chosen as follows:

$\theta_{12} = 60^\circ$
$\theta_{23} = 60^\circ$
$\theta_{34} = 60^\circ$
$\theta_{45} = 50^\circ$
$\theta_{56} = 45^\circ$
$\theta_{67} = 30^\circ$

where $\theta = (2\pi/\lambda_q)\ell$ and ℓ is the separation distance between center gaps of successive cavities.

This particular beam design yielded an $\frac{\omega_p}{\omega} = .998$ and $\frac{\omega_q}{\omega} = .151$. In previous experiments on hollow beam devices[7] with beams of the same dimensions and beam voltage, electronic Q's in the order of 50 to 90 were measured. Calculations of the electronic Q based on the work of Bers[8] were correlated with these measurements and reasonable agreement was noted. Employing the work of Bers, an electronic Q of 52 was calculated for the seven-cavity klystron. Actual measurements of the electronic Q in the seven-cavity device yielded an electronic Q of 45.5. The calculations of the Q_{el} were based on a beam with dimensions indicated interacting with gaps one radian in length.

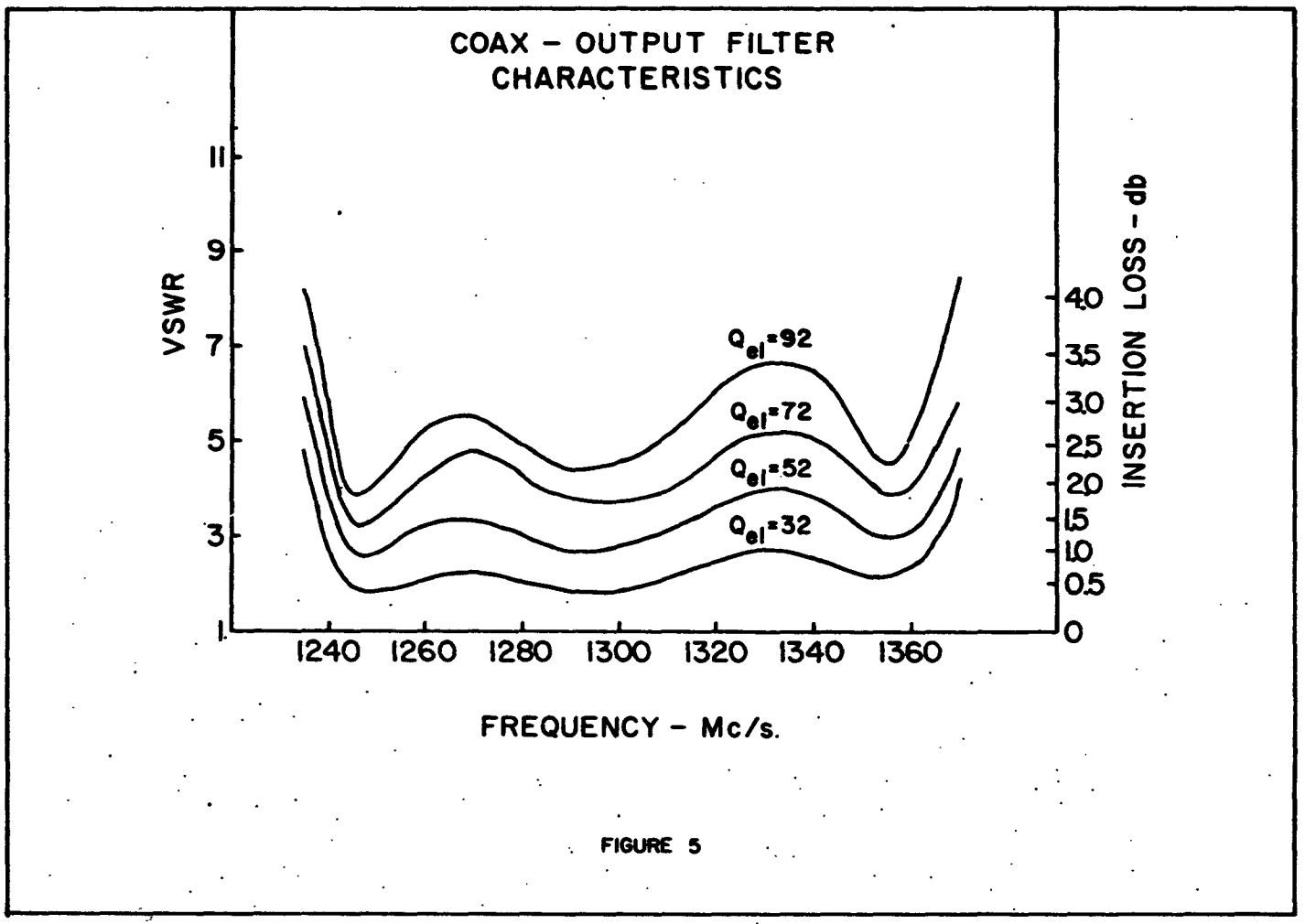
COAX – OUTPUT FILTER
CHARACTERISTICS
VSWR
11
9
7
5
3
1
INSERTION LOSS – db
40
35
30
25
20
15
10
0.5
0
Q_{el}=92
Q_{el}=72
Q_{el}=52
Q_{el}=32
1240
1260
1280
1300
1320
1340
1360
FREQUENCY – Mc/s.

FIGURE 5

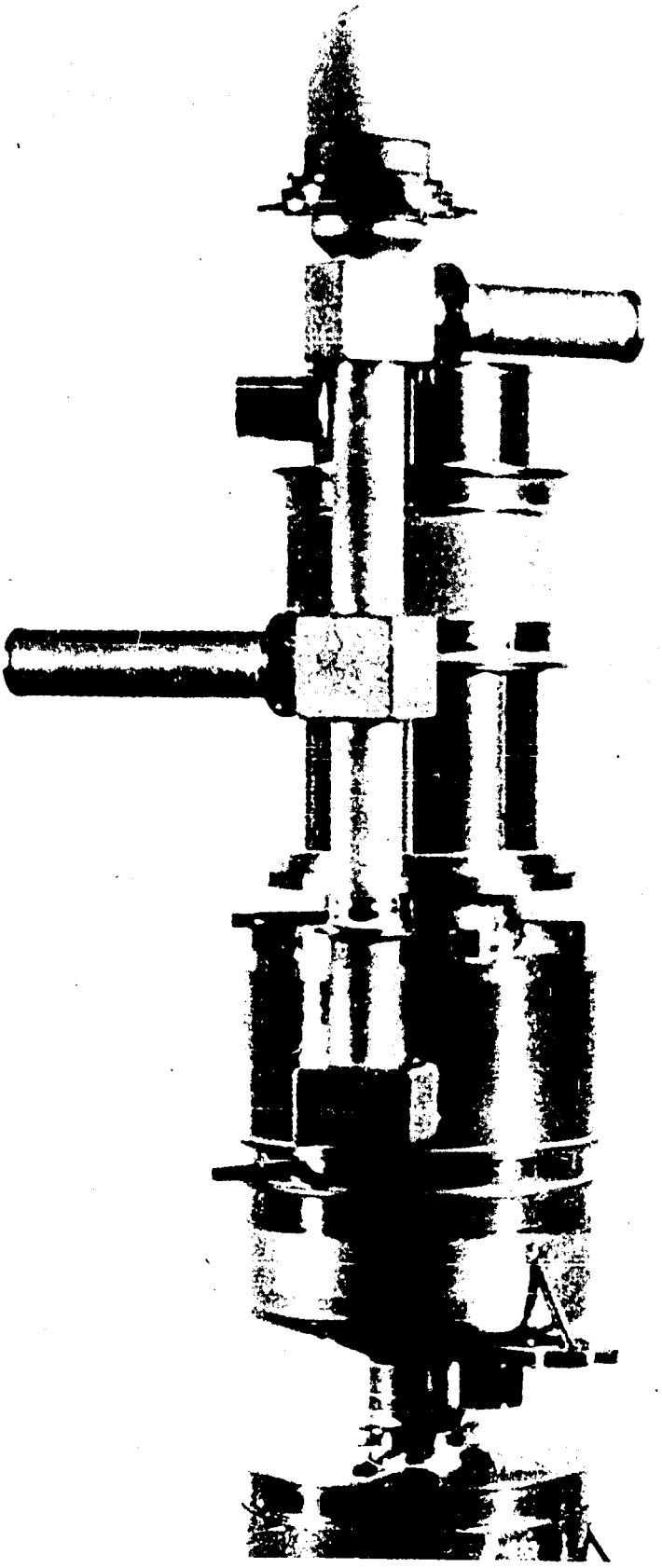

FIG. 6 - Output Filter on Seven-Cavity Hollow-Beam Klystron

Some preliminary work on the broadbanding techniques of a hollow beam klystron were carried out on a digital computer; but, because of the many variables that existed plus the lack of sound information on all the interactions of the electronic circuit with the hollow beam, it was felt that it would be more prudent to employ tuners in the first six cavities. Therefore, each cavity of the klystron was equipped with a ring tuner which permitted a tuning range of from 1200 Mc to 1400 Mc. With the use of such a tuner, the R/Q would be, of course, low (75). It was realized that the low R/Q of the cavities would have a great effect on the gain of the tube when broadbanded.

Figure 3 summarizes the important characteristics of the hollow beam klystron showing the variation in the calculated values to those actually measured. Figure 4 shows the seven-cavity hollow beam klystron that was constructed. This particular photograph does not include the gun structure. It can be noted from the photograph that each of the cavities has a tuner and rf loops to obtain measurements of gain per stage, electronic loading, and frequencies of the various cavities. It can also be noted from the figure that an isolated collector was employed. This was utilized to provide an electronic measurement of the beam transmission of the device. Since it was intended to operate the tube at a relatively low duty cycle (1.1×10^{-4}) calorimetric measurements of the beam transmission would not prove suitable.

IV. Output Filter Circuit

Since it was the intention of this study to build a broadband klystron, it was felt that a more constant impedance should be offered to the bunched current at the output gap. Because of this, an output filter circuit was considered. This output filter was patterned after a Tchebycheff network; however, in this case, one of the resonant circuits was active. This circuit was the seventh cavity of the klystron. Two external circuits were coupled to this active cavity forming a three-section Tchebycheff network. The external circuits consisted of coaxial stubs which offered the correct susceptance to the output coax of the tube. In this manner, a broadband filter arrangement was established. Figure 5 shows the output filter characteristics as a function of electronic loading of the gap. The filter was designed for an electronic Q of 52; however, since the possibility existed that the calculations on electronic loading could be in error, variations in the electronic Q from 32 to 92 were measured and are indicated in this figure. The electronic loading of the output cavity was simulated by teledeltos paper.

It can be seen from Figure 5 that a bandwidth of approximately 130 Mc was achieved with the proper electronic loading in the cavity. This output filter design was incorporated in the seven-cavity tube. A picture of the filter on the seven-cavity tube is shown in Figure 6.

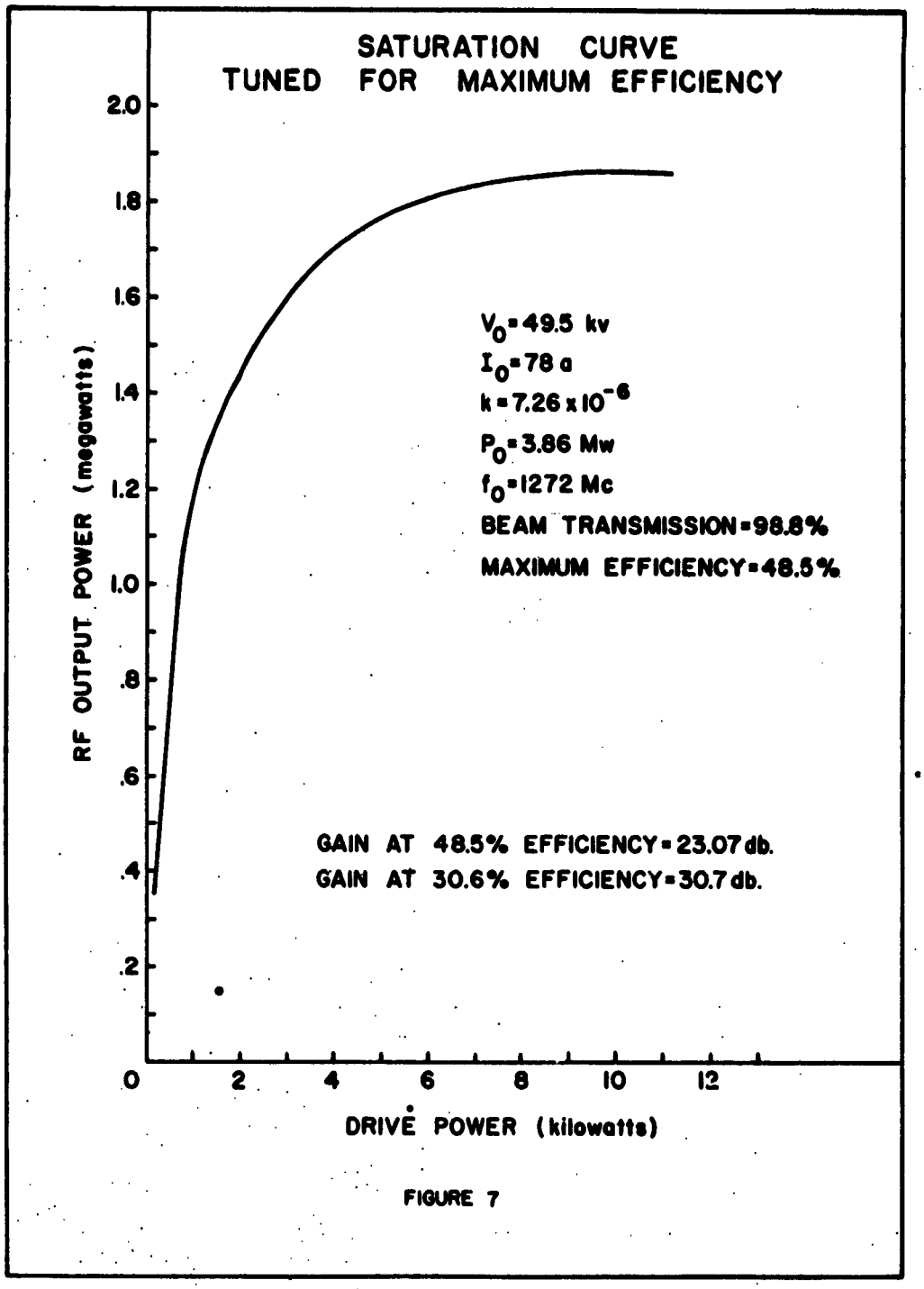
SATURATION CURVE
TUNED FOR MAXIMUM EFFICIENCY
RF OUTPUT POWER (megawatts)
2.0
1.8
1.6
1.4
1.2
1.0
.8
.6
.4
.2
0
2
4
6
8
10
12
DRIVE POWER (kilowatts)
V_0 = 49.5 kv
I_0 = 78 a
k = 7.26 x 10^{-6}
P_0 = 3.86 Mw
f_0 = 1272 Mc
BEAM TRANSMISSION = 98.8%
MAXIMUM EFFICIENCY = 48.5%
GAIN AT 48.5% EFFICIENCY = 23.07 db.
GAIN AT 30.6% EFFICIENCY = 30.7 db.

FIGURE 7

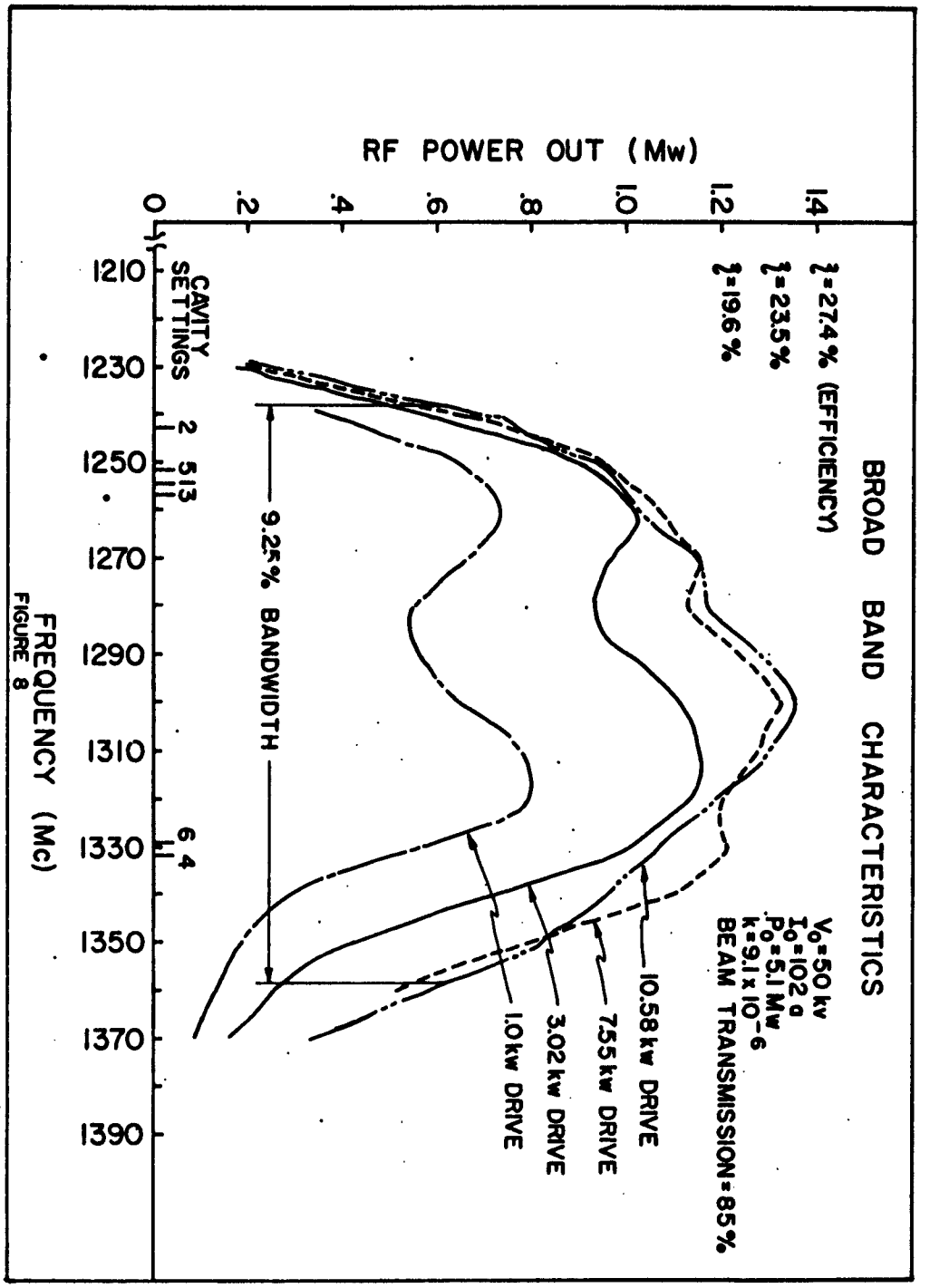
BROAD BAND CHARACTERISTICS
RF POWER OUT (Mw)
0
.2
.4
.6
.8
1.0
1.2
1.4
η=27.4% (EFFICIENCY)
η=23.5%
η=19.6%
V₀=50 kv
I₀=102 a
P₀=5.1 Mw
k=9.1 x 10⁻⁶
BEAM TRANSMISSION=85%
10.58 kw DRIVE
7.55 kw DRIVE
3.02 kw DRIVE
1.0 kw DRIVE
9.25% BANDWIDTH
CAVITY SETTINGS
2 5 3
6 4
1210
1230
1250
1270
1290
1310
1330
1350
1370
1390
FREQUENCY (Mc)
FIGURE 8

V. Test Results

Based on the design considerations previously outlined; a seven-cavity hollow beam broadband klystron was constructed; and the characteristics of the device were then studied. It should be pointed out that in the early operation of the tube, severe amounts of noise power and beam breakup were observed. This noise power was closely related to the adjustment of the magnetic field. It appeared that there were values of magnetic field which would cause exceedingly high amounts of noise power to be generated. At other values of the magnetic field, the beam behaved well and was reasonably quiet. One must realize that with the beam employed, changing the magnetic field greatly affects the perveance of the device. With proper control on the magnetic field, a perveance of 7.26×10^{-6} was established at a beam voltage in the region of 50 kv. At this perveance, a beam transmission of 98.8 per cent was measured.

The cavities were tuned for maximum power output from the tube. This data was taken at a frequency of 1272 Mc. By adjusting the cavities for maximum efficiency, 1.86 megawatts of power were achieved under saturated drive conditions. This results in efficiency of 48.5 per cent. The details of this measurement are shown in Figure 7.

The magnetic field configuration that attained this efficiency was reasonably close to the actual design value of 1500 gauss. Even with the relatively high efficiency of this device, the gain of the tube was low--23 db at saturation, and 31 db at the beginning of the small signal region. The cavities were not all synchronously tuned to achieve this efficiency. The frequencies of the cavities were the following:

Cavity No. 1	1289 Mc
Cavity No. 2	1283 Mc
Cavity No. 3	1371 Mc
Cavity No. 4	1233 Mc
Cavity No. 5	1264 Mc
Cavity No. 6	1277 Mc

It is interesting to note that the third cavity is quite removed from the drive frequency of 1272 Mc.

In order to study the broadband characteristics of this tube, measurements were taken at various gun perveances. By adjusting the magnetic field, a beam perveance of 9.1×10^{-6} was established. The cavities of the klystron were adjusted to give maximum bandwidth and the broadband characteristics were then studied.

Figure 8 shows the bandwidth characteristics of the tube as a function of

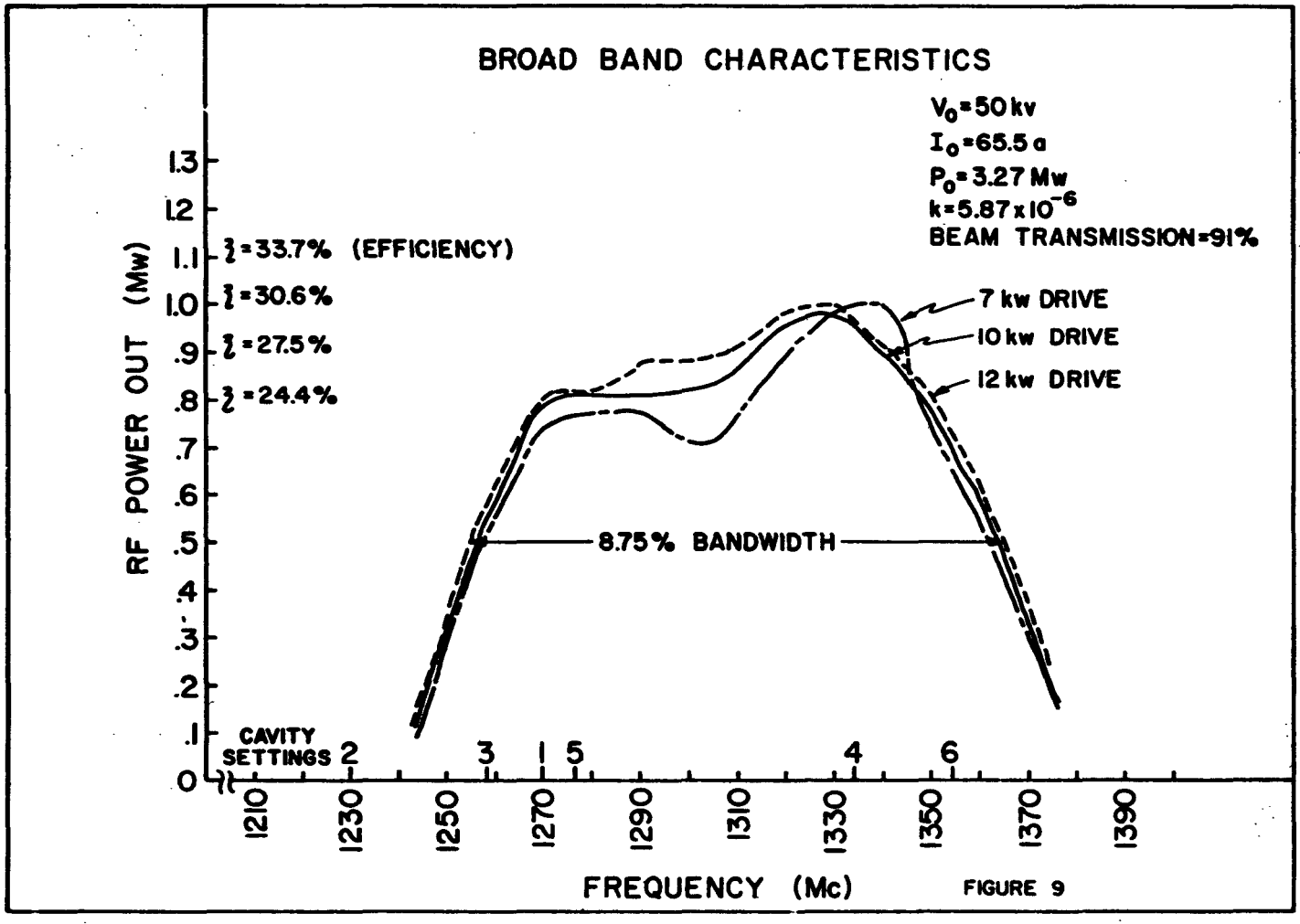
BROAD BAND CHARACTERISTICS
V_0=50 kv
I_0=65.5 a
P_0=3.27 Mw
k=5.87x10^{-6}
BEAM TRANSMISSION=91%
η=33.7% (EFFICIENCY)
η=30.6%
η=27.5%
η=24.4%
7 kw DRIVE
10 kw DRIVE
12 kw DRIVE
8.75% BANDWIDTH
RF POWER OUT (Mw)
0
.1
.2
.3
.4
.5
.6
.7
.8
.9
1.0
1.1
1.2
1.3
CAVITY SETTINGS 2 3 1 5 4 6
1210
1230
1250
1270
1290
1310
1330
1350
1370
1390
FREQUENCY (Mc)

FIGURE 9

various drive powers. It is clearly seen that the efficiency as well as the gain of the device operating under these conditions is low. However, a bandwidth of 9.25 per cent is established. It is also interesting to note that the sixth cavity was in the pass band. Attempts to move the cavity out of the pass band into the high frequency level resulted in very poor performance from the klystron.

Readjusting the magnetic field such that the perveance was 5.87×10^{-6}, other broadband characteristics of the klystron were studied. Figure 9 shows the results obtained with operation at this perveance. It can be observed that the efficiency was in the order of 30 per cent and that the bandwidth for the particular cavity settings was 8.75 per cent. Again, the sixth cavity of the klystron was within the pass band of the tube; and any attempts to raise the sixth cavity frequency resulted in poor operation of the device.

The magnetic field was readjusted such that a perveance of 7.26×10^{-6} was re-established. Since the output filter that was employed in the klystron was designed for an electronic Q of 52 in the output cavity and since the electronic Q of the cavity was different from this designed value(45.5), a matching section was placed between the tube and the waterload. The cavities were adjusted for broadband operation and Figure 10 shows the results of these measurements. It can be seen from this figure that an electronic bandwidth of 6.3 per cent was achieved, at a maximum efficiency of 35 per cent. Again, it should be noted that the sixth cavity was in the pass band of the tube.

VI. Conclusion

As a result of this study, it has been shown that a high perveance hollow beam will interact with a microwave circuit such as a klystron. Relatively good efficiency can be attained by proper matching between the beam and the output circuit. There appears to be a serious problem associated with the gain that can be achieved with a hollow beam device. The noise characteristic of a cross-field beam must be seriously considered. Data has been presented to support the theory that a hollow beam tube can be easily broadbanded; however, more consideration should be given to the method of broadbanding.

One of the primary factors that must be considered in the design of a klystron employing a hollow beam is the beam design and stability. More study is necessary to understand the beam stability problems and the proper coupling of a microwave circuit with a hollow beam. With improved beam designs and more information regarding the interaction of a hollow beam with a microwave circuit, it appears that a high efficiency device can be achieved. However, the amount of gain that can be attained with such a tube must be further studied.

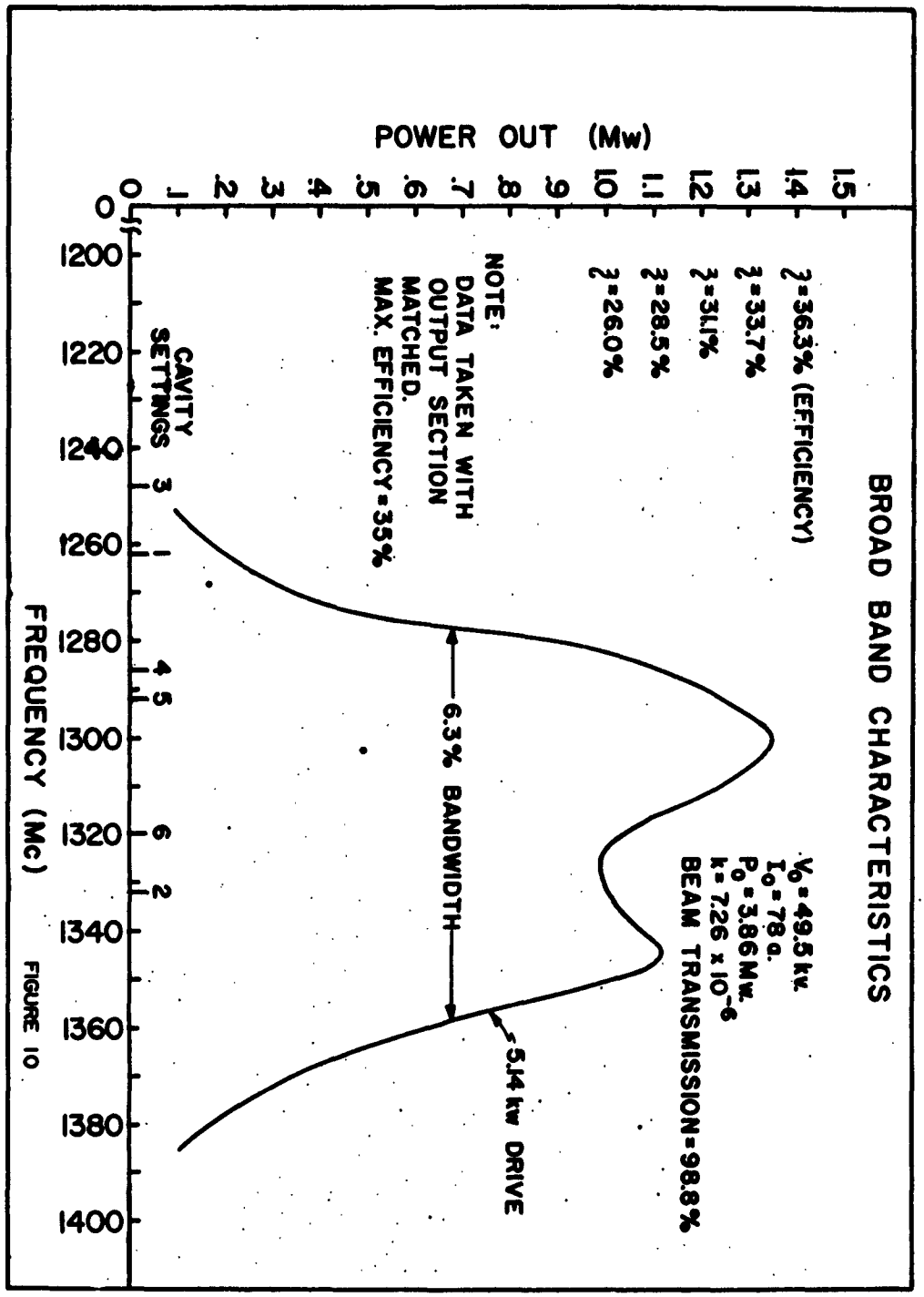
BROAD BAND CHARACTERISTICS
POWER OUT (Mw)
FREQUENCY (Mc)
η=36.3% (EFFICIENCY)
η=33.7%
η=31.1%
η=28.5%
η=26.0%
NOTE:
DATA TAKEN WITH
OUTPUT SECTION
MATCHED.
MAX. EFFICIENCY=35%
V_0=49.5 kv.
I_0=78 a.
P_0=3.86 Mw.
k=7.26 x 10^{-6}
BEAM TRANSMISSION=98.8%
6.3% BANDWIDTH
5.14 kw DRIVE
CAVITY
SETTINGS
3 1 4 5 6 2

FIGURE 10

VI. Acknowledgements

The authors of this paper would like to extend their gratitude to Mr. Kenneth Keller for his efforts in testing the device, to Mr. Arthur Parris for his contributions in the microwave circuit design, and to Mr. Walter Burger for his efforts in the construction of the tube. Finally, appreciation is extended to Mr. James N. Lind for his encouragement throughout the progress of the program.

References

1. Bers, A., "Linear Space-Charge Theory of Gap Interaction between an Electron Beam and Electromagnetic Fields," MIKROWELLENRÖHREN, Friedr Vieweg and Sohn, Braunschweig , Germany, June, 1960, Pages 53-60.

2. Bers, A. "Multicavity Klystrons", Quarterly Progress Report, Research Laboratory of Electronics, Massachusetts Institute of Technology, January, 1957, Pages 40-49.

3. Kino, G.S., "A Design Method for Crossed-Field Electron Guns," IRE Trans., PGED, July 1960, Pages. 179-186.

4. Kino, G. S. and Taylor, N.J.,"The Design and Performance of a Magnetron Injection Gun," IRE Trans., PGED, Vol. ED-9, Pages 1-11,January, 1962.

5. Bers, A., Anderson, L., and Keller, K., "Theory and Design of a Conical Electron Gun for Producing a Hollow Beam," Raytheon Company, Report No. PT-277, July, 1961.

6. Branch, G.M., and Mihran, T.G., "Plasma Frequency Reduction Factors in Electron Beams," IRE Trans., 1955, Page 3.

7. Anderson, L.B., "A Review of the Hollow Beam Development Work Accomplished at Raytheon's Spencer Laboratory from April 1, 1960, to June 1, 1961." Raytheon Report, June, 1961.

8. Bers, A., "Linear Space-Charge Theory of Gap Interaction between an Electron Beam and Electromagnetic Fields," <u>Op. Cit.</u>.

THE MULTIPLE-BEAM TRAVELLING WAVE KLYSTRON

By

M. R. Boyd* R. A. Dehn T. G. Mihran

General Electric Co., Schenectady, N. Y.

In addition to the need for very high power levels in present-day microwave systems, there is a growing requirement for wide dynamic bandwidth. Bandwidths of 100 to 300 Mc only satisfy present specifications and values up to 1000 Mc or 30% at S-band may be required in a few years.

The technique for utilizing a multiplicity of electron beams in a single rf interaction circuit has led to the multiple beam klystron as a means for generating very high power levels. The MBK can also be broadbanded by conventional stagger tuning and loading techniques. These approaches may lead to 10 or even 15% bandwidth, but greater values do not seem probable. However, a modification of the MBK circuit results in a traveling wave klystron with a very large bandwidth capability.

This approach stems from the traveling-wave klystron (TWK) which Ginzton proposed in 1948. This tube was analyzed and a model was built by Mihran in 1949. The basic TWK is illustrated in Fig. 1. Here an elongated ribbon beam of electrons traverse the gaps of two ridge-loaded waveguides which constitute the input and output circuits. These guides are terminated in their characteristic impedance, hence the bandwidth will be as large as the guide bandwidth itself.

The operation of the elementary TWK can be seen in Fig. 2. The top part of the figure shows the cross section again and the lower section shows the rf voltage $\propto V_0$ which propagates on the input guide due to the rf drive power. This voltage will velocity-modulate the beam in a progressive phase as the input signal propagates from left to right. In the drift distance between the two guides, bunching takes place and a density modulated current will induce waves in the upper or output waveguide.

The build-up of signal in the output waveguide can be seen by considering small current elements, Δx, in width. If we assign a magnitude ΔI to the ac component of the first current element, this

*Now at Mictron, Inc., Albany, N. Y.

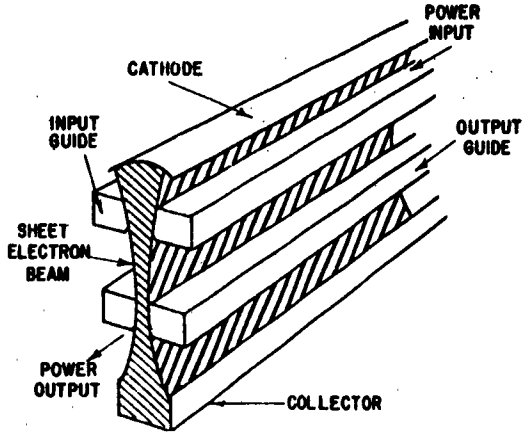

Fig. 1 - Original Travelling-Wave Klystron

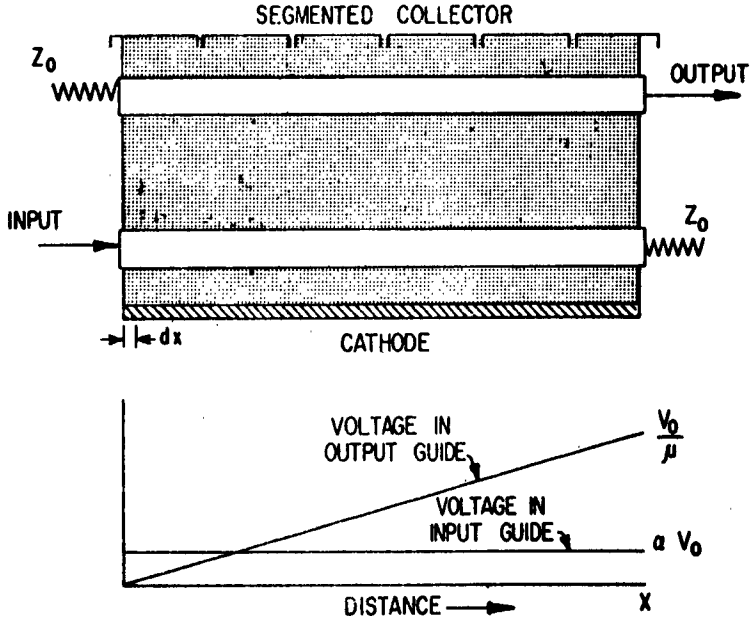

Fig. 2 - Buildup in a TWK

current will set up a voltage in the output guide equal to $\Delta I Z_o/2$ at the start of the transient build-up of output signal. This wave will propagate in both the positive and negative X directions. In the positive direction, the next element will be in phase with the wave arriving from the left and its contribution to the output will add to produce a wave of increased amplitude propagating to the right. Waves propagating to the left in this output guide become increasingly out of phase with the driving current and effectively cancel. When steady state is reached, the output guide voltage will build up to the right in a linear manner as shown in Fig. 2 and very little energy will propagate to the left.

If the X dimension of the structure is made long enough, the output guide voltage will eventually reach the level required for optimum energy extraction from the electron beam, shown by a value V_o / μ where V_o is dc beam voltage and μ is a gap coefficient. This length of structure is called the build-up distance. Since the efficiency at the high voltage end will be the usual two-cavity klystron efficiency and vary linearly to zero at the left end, the efficiency of a buildup unit of TWK will be half of a two-cavity klystron. Additional tube structure could be added and operated at full efficiency, provided the waveguide characteristic impedance is tapered downward with distance to hold the voltage at the optimum value as power builds up. The overall efficiency will then asymptotically approach the full two-gap klystron value.

Ridged waveguides have low impedance, hence a long build-up distance is required. Also, the techniques for producing stable sheet beams have not been developed. It was these problems which prevented Mihran from achieving a practical TWK amplifier in 1949. The gain of this first model never exceeded unity, although the basic principles of traveling-wave bunching and directed output were demonstrated.

An operational TWK can be made by optimizing the waveguide characteristic impedance by periodic loading and then utilizing conventional cylindrical electron beams instead of sheet beams. The ω-β diagram of Fig. 3 shows the characteristic of a ridge-loaded waveguide as the solid curve. The horizontal axis is in βD units where D is a chosen periodic distance. The bandwidth of the unmodified ridge guide is excessive - usually more than 2 octaves and the impedance is low. Impedance is inversely proportional to the group velocity, $d\omega/d\beta$

The impedance can be increased by reduction of the bandwidth. This can be accomplished by either periodic capacitive or inductive loading, or a combination of both. Since the use of cylindrical beams is contemplated, the capacitive loading will take the form of conventional drift tube gaps. Then the bandwidth and impedance are determined by appropriate inductive loading. In addition, some form of taper is required to match the resulting TWK structure to appropriate external transmission systems over the desired bandwidth. Here the techniques of cavity filter design can be used.

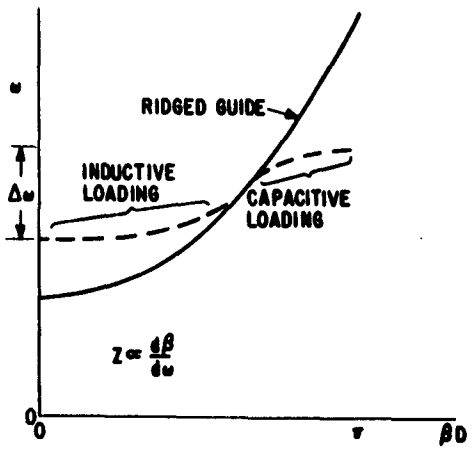

Fig. 3 - Loaded-Waveguide Phase Characteristic

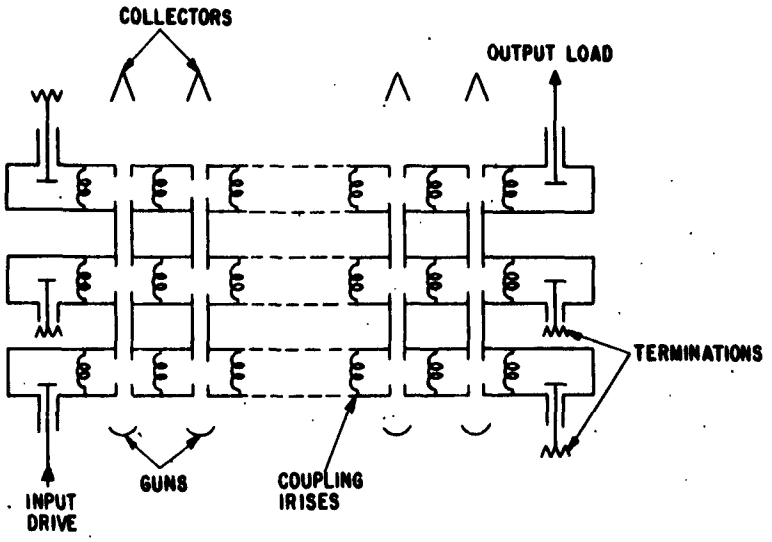

Fig. 4 - Schematic of TWK Circuit

When the periodic loading is optimized for given bandwidth and unit beam, the number of beams required to achieve optimum rf voltage in the output guide is easily determined.

If the impedance characteristic is essentially flat over a given bandwidth, the impedance-bandwidth product is a constant. The consequence of this relationship is that the number of beams required for build-up is directly equal to the ratio of the TWK bandwidth to the bandwidth capability of one of the beam units. This means that factors of 5, 10 or more in bandwidth can be achieved by, in effect, investing some beam power in the build-up section.

In order to experimentally verify some of the predicted characteristics of the TWK, an 8 beam L-band amplifier was constructed utilizing external-circuit klystrons. These were relatively low-power, low perveance beams with only moderate bandwidth capability but with good efficiency and excellent adaptability for circuit modification. At a 0.5 microperveance, the bandwidth of the unit klystron is 3.4 Mc at 725 Mc. Gain is 24 db and efficiency averages 44% for a ten-tube sample. The TWK was designed to utilize four of these beams in the build-up and four more at high efficiency. Thus the expected bandwidth would be 13.6 Mc.

Physically, the circuit was a modification of a multiple beam klystron which had been built earlier. The sketch in Fig. 4 shows three filter waveguide circuits in which the capacitive interaction gaps periodically load a waveguide with appropriate inductive loading provided by iris apertures midway between capacitors. Transition sections at the ends couple from the filter waveguide to coaxial line terminations. Each circuit had twelve sections and standard maximally - flat filter design techniques were used to determine the sizes of the inductive irises required to achieve a 14 Mc bandwidth centered around 750 Mc.

In the conventional filter design, impedance tapering takes place from the center outward toward each end, so that it is not practical to drive each filter section with a beam. The L-band amplifier had ten electron beams which could be operated in various combinations, but eight beams resulted in the closest to optimum performance.

The penultimate circuit in Fig. 4 is shown as a terminated filter, although it was not always operated in that fashion. For optimum bunching efficiency the penultimate gaps should present an inductive impedance to the beams as is the case when a resonator is tuned to a frequency higher than the operating frequency. The problem of how to achieve this condition over the broad bandwidth of a TWK was bypassed in early tests by either reducing penultimate gap impedance essentially to zero or by closing off the inductive irises completely to create individual tuned resonators for each gap.

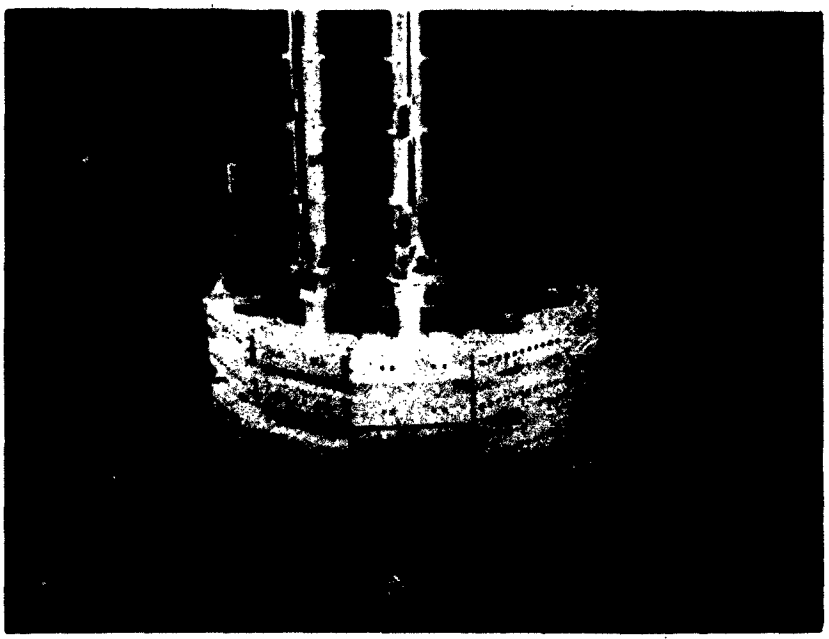

Fig. 5 - L-Band TWK Amplifier

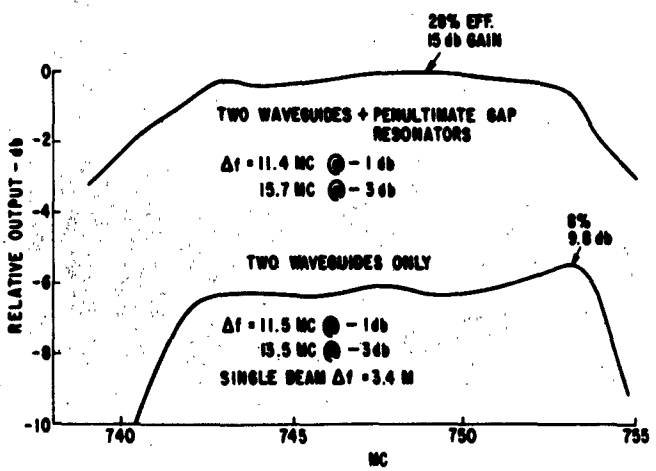

Fig. 6 - Eight-Beam TWK Output

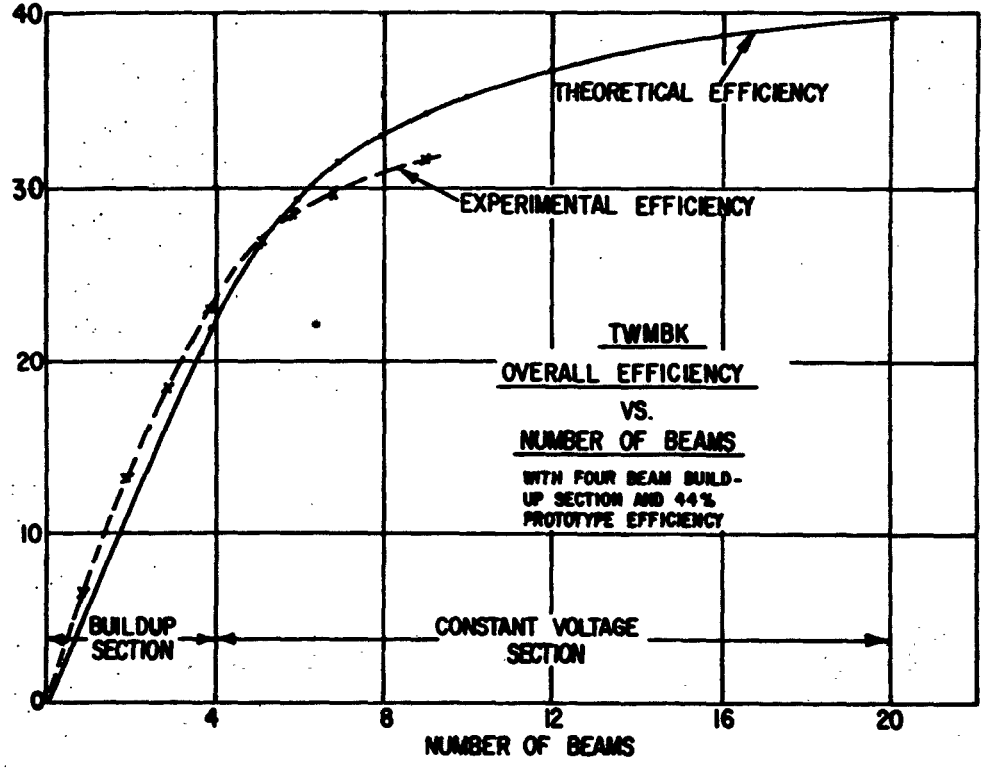

Fig. 7 - Efficiency of TWK

The far end of this input filter is terminated to absorb the drive power which was not dissipated in the beam loading and a similar termination at the reverse terminal of the output filter absorbs the backward energy due either to imperfect cancellation of the waves induced by the beams, or energy reflected from an imperfect load.

A photograph of the TWK amplifier is shown in Fig. 5. The twelve sections of the filter are arranged in a circle with the collectors of the individual beams shown as the dark cylinders at the top and the three filter decks shown below. The output filter terminations connect to the top ends of the coaxial lines rising vertically from the top deck. The remaining terminations are not visible in this view.

The guns are located below the iron base plate which serves as the lower pole piece for the focussing magnet. One large solenoid surrounds the entire system to simultaneously focus all beams and a top pole piece, shown in partial section below the collectors, completes the magnetic circuit.

Typical performance of this amplifier is shown in Fig. 6 with the two-gap case in the lower curve and a three-gap result in the upper curve. The two-gap curve was taken by radically detuning the penultimate gap circuits. While this corresponds to an overly long drift length, the experiment verified the expected hot bandwidth of the tube circuits and did result in positive gain. The upper curve shows the output obtained when optimum impedance is developed at each penultimate gap. This was done by retuning individual resonators at each of these gaps for every frequency of measurement. The optimized bunching results in an increase in efficiency from 8% to 28%. In both cases the bandwidth is essentially four times that of the prototype klystron. In the light of further filter circuit work which has been done, the bandpass flatness and skirt attenuation can be improved over the characteristics shown here - flatness within 0.5 db over the bandwidth appears possible.

The gain of this amplifier was around 9 db for the two-waveguide case and 15 db for the case of tuned penultimate gaps. Comparison of these figures with the 24 db of the prototype klystron reflects the lower impedance of the input filter circuit. The development of a higher gain TWK will require the incorporation of more interaction gaps along the beam with associated filter circuits.

The efficiency of a TWK can be made to asymptotically approach that of the unit beam by utilizing a number of beams following the build up. This is illustrated in Fig. 7 for the case of 44% efficiency of the prototype beam. Also shown are experimental points taken by operating various numbers of beams, up to nine, in the L-band amplifier. The departure of the 7, 8, and 9 beam cases from the theoretical curve is largely due to the low impedance we were forced to use at the ends of the filter network

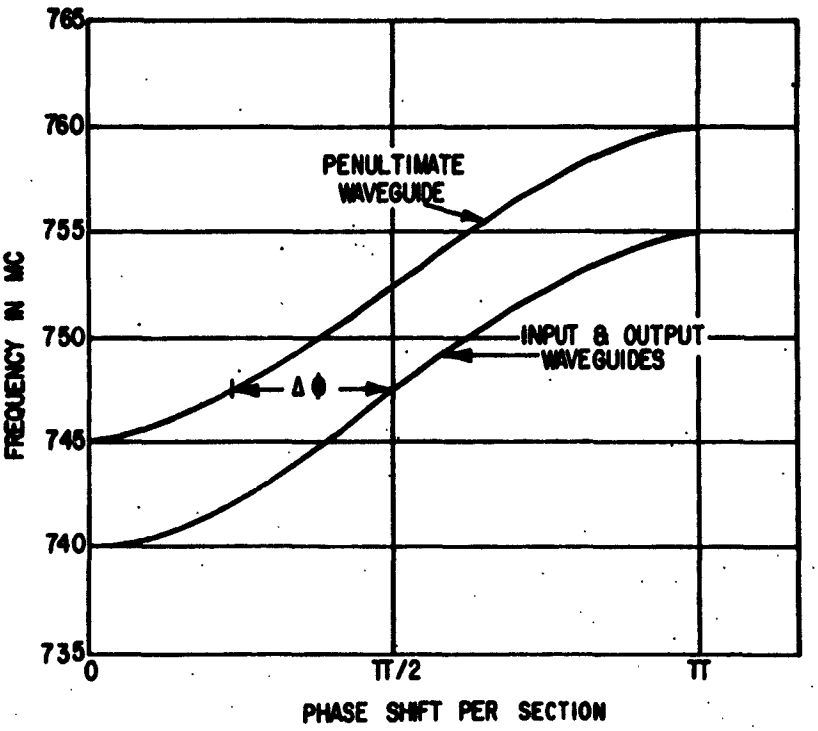

Fig. 8 - Phase-Slip
in Penultimate Filter

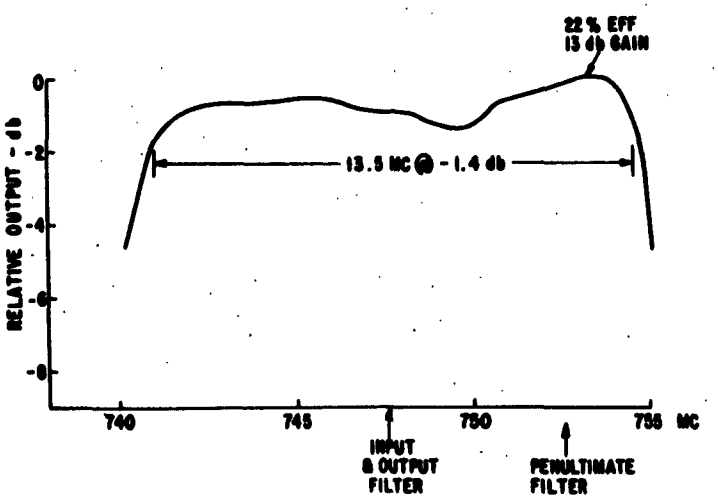

Fig. 9 - Six Beam TWK Output

as it was designed. Filter designs with impedance taper optimized for good efficiency are possible and should permit attainment of the higher values. For the case illustrated here a total of 12 to 20 beams, four of which are build-up, would yield efficiencies in the high thirties.

Of course, the operation of a TWK with tuned penultimate gaps negates the otherwise broadband capabilities of the amplifier. Various methods for achieving proper penultimate impedance over a bandwidth were considered. The most promising at the time this work was done was to utilize a filter circuit for the penultimate gaps, but to offset the bandpass of this filter with respect to the other two. This is shown in Fig. 8. By raising the bandpass of the penultimate circuit, the phase shift in it is less than that in the other circuits by an amount $\Delta\phi$ which is essentially fixed over the bandpass of the tube. This offset was chosen to be roughly 30° per section, so that the phase of the penultimate gap voltage would progressively lead the driving current. The system is a compromise in that the phase continues to slip beyond the desired 90° value and eventually becomes too large.

With the given amount of phase slip, optimum performance was achieved with six rather than eight beams. This is illustrated in Fig. 9. Now the efficiency is 20-22% as compared with 8% two-waveguide and 28% tuned penultimate cases. There is now a 1.4 db variation over the design bandwidth. While this is a workable system, another approach to be discussed in a companion paper promises to give superior performance.

As far as is known, this was the first successful TWK amplifier to be constructed. The performance, while not superpower or super bandwidth, verifies the principles. Now by the use of several beams to build up the rf level, the bandwidth of linear beam tubes can be extended well beyond 10%; values in excess of 25% appear realizable. After the build-up stage, power level can be increased by using additional beams without degradation in bandwidth. In addition, the bandpass characteristic can be made very flat in amplitude and linear in phase by using many filter sections.

This study was initiated under the sponsorship of the Army Redstone Guided Missile Agency.

THE DESIGN OF WIDE BAND TRAVELING WAVE KLYSTRONS

By

M. R. Boyd* and W. J. Pohl

General Electric Company, Schenectady, N. Y.

INTRODUCTION

In this paper we discuss the salient design problems of the TWK and describe how these have been tackled during the course of the preliminary work on an experimental 15% bandwidth, 1.5 MW, 3 guide, S-band tube having the specification shown in Fig. 1. Notice particularly the low operating voltage which can be obtained by the use of multiple beams. Fig. 2 shows the general schematic of the tube. We shall discuss the general design of the periodically-loaded guide; the impedance taper in the output guide; the transition from loaded guide to standard S-band guide; broadband windows, and the penultimate guide. Finally we shall briefly review the calculated overall performance capabilities of this type of tube.

(a) The Uniform Periodically-Loaded Waveguide

The interaction gaps in the three waveguides of the structure produce periodic capacitative loading and we shall discuss first the properties of such periodically-loaded structures. This configuration can be accurately represented by an equivalent circuit in which the capacitative loading is considered to be lumped, and the connecting transmission line to be uniform since the gap dimensions are small compared to a wavelength. Fig. 3 shows the $\omega/\beta D$ curve calculated from the circuit analogue of a transmission line loaded with lumped susceptances and also the experimentally measured points obtained for the same loaded waveguide. The basic equations relating phase shift per section and impedance to the circuit parameters are shown in Fig. 4.

From these we may calculate the constants for given bandwidth requirements and physical dimensions. From equation (1) and (3) it can be shown that, for moderate bandwidths, the impedance bandwidth product

*Now with Mictron, Inc., Albany, N. Y.

TARGET OUTPUT POWER	1.5 MW
TARGET BANDWIDTH	15% TO 3 db
	14% TO 1 db
CENTER FREQUENCY	3000 MC
BEAM VOLTAGE	35 KV
BEAM CURRENT	13 AMPS x 10 = 130 AMPS
MAX DUTY	.003
GAIN	20 db

Fig. 1 - Specification for
S-Band TWK

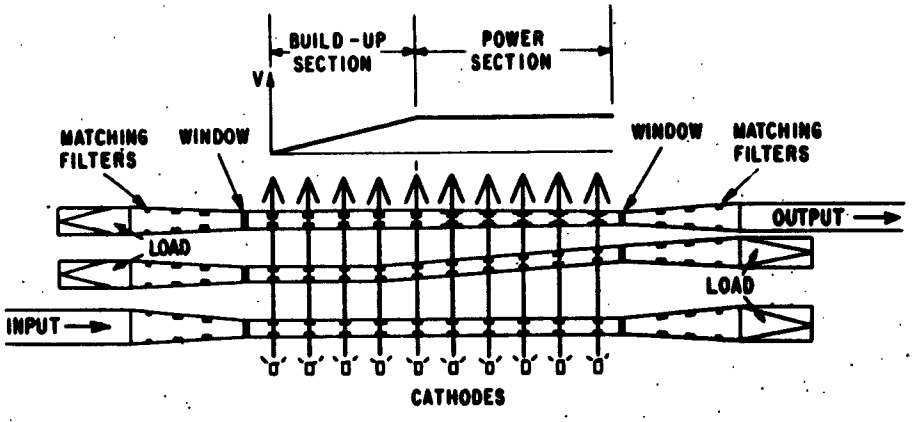

Fig. 2 - TWK Schematic

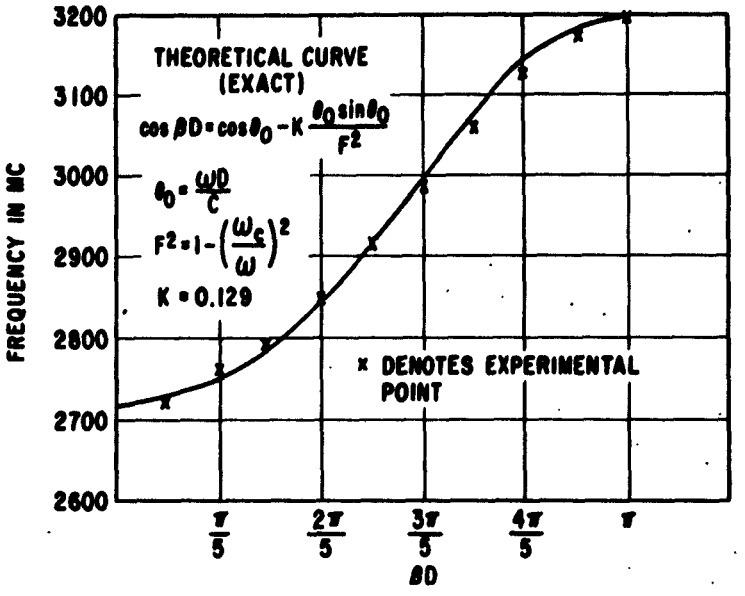

Fig. 3 - Frequency/Phase Characteristic of Loaded Guide

$$\cos\beta D = \cos\beta_0 D - \frac{BZ_0}{2}\sin\beta_0 D \qquad (1)$$

$$Z = Z_{opv}\frac{\beta_0 D}{\sin\beta D} \qquad (2)$$

$$Z_{pv} = \frac{\bar{\omega}}{\left(\frac{d\omega}{d[\beta D]}\right)}\left(\bar{R/Q}\right) \qquad (3)$$

WHERE $\beta D = \frac{\omega F D}{c}$

B = LOADING SUSCEPTANCE

$Z_{opv} = \frac{754\pi b}{aF}$

$\left(\frac{\bar{R}}{Q}\right)$ IS VALUE OF $\frac{R}{Q}$ AS MEASURED AT $\pi/2$ MODE i.e AT $\omega = \bar{\omega}$, BAND CENTER

ω = ANGULAR FREQUENCY

D = PERIODIC DISTANCE

$F = \sqrt{1-\left(\frac{fc}{f}\right)^2}$

WHERE fc = CUT OFF FREQUENCY

$f = \frac{2\pi}{\omega}$

a = WAVEGUIDE WIDTH

b = WAVEGUIDE HEIGHT

Fig. 4 - Basic Loaded Wave-Guide Equations

is given by the expression:

$$Z_{pv}\left(\frac{\Delta\omega}{2\omega_c}\right) = \frac{R}{Q}$$

We see therefore that for a given gap configuration the impedance-bandwidth product is constant.

(b) The Efficiency-Bandwidth Relation

The build up of rf voltage takes place linearly in the periodically loaded guide whose impedance is dictated by its bandwidth. The greater the bandwidth, the lower will be the impedance, and hence the greater the number of beams required to build up the r. f. voltage to its optimum value. The overall efficiency for a fixed output power will be reduced as the bandwidth is increased since more beams will be required in the build-up section and these contribute power at only 1/2 their normal efficiency. The number of build up beams required is approximately equal to the required bandwidth ratio. For example, to attain a flat bandwidth 3 times that obtainable from a single beam requires 3 beams for build up. In a ten beam tube the overall efficiency would be (10-3/2)/10 = 8. 5, i. e. about 85% of that of the prototype single beam tube. Thus a bandwidth improvement of three times is obtained with only a small decrease in efficiency. It is also evident that as the number of output beams is increased the loss in efficiency becomes smaller.

(c) The Impedance Taper in the Output Guide

The efficiency of each beam in the power section may be kept a maximum if the r-f voltage remains constant everywhere along the section. V_{rf}^2/Z_{pv} is the power in the circuit at any point. Therefore, as power is progressively added the impedance of the circuit must be progressively reduced. From equation (2) we see that this may be done by progressively reducing the R/Q of successive sections of the guide. In addition the same $\omega/\beta D$ characteristic must be maintained at the successive sections in order to maintain the passband, to insure phase linearity, and to maintain synchronism with the input signal.

Fig. 5 shows how the above was accomplished in practice. Perturbation methods were used to determine the R/Q values and it should be emphasized that it is the power-voltage impedance as seen by the wave which is being successively reduced. The beams see a constant impedance insofar as the circuit r-f voltage and the beam injected current are kept constant. Examination of equations (1), (2) and(3) reveals that since Z_{pv} and R/Q are proportional to the height of the guide they may be progressively reduced by reducing the guide height. To maintain the same $\omega/\beta D$ curve at all points additional lumped capacitance and

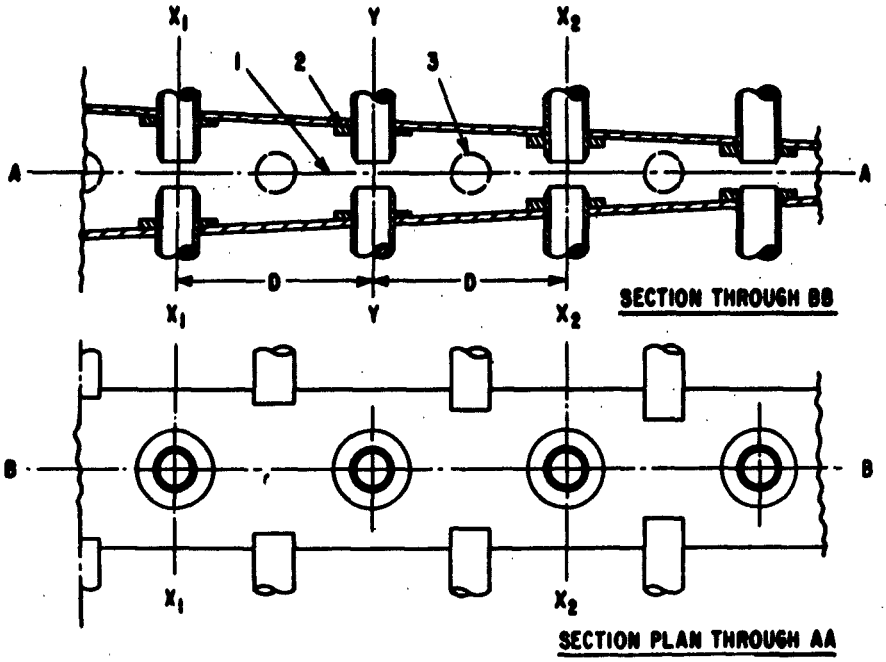

Fig. 5 - Impedance Taper

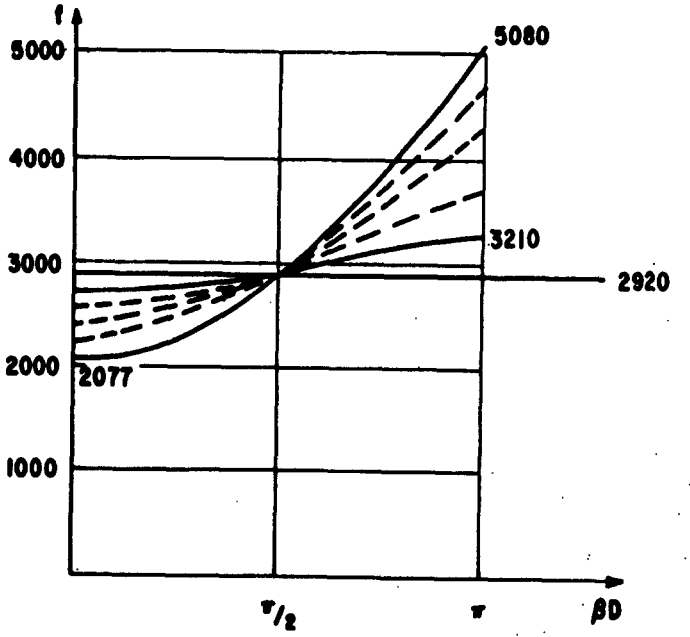

Fig. 6 - Curves of Filter Taper

inductance must be added. This is accomplished by the addition of the larger cylindrical protrusions and the tuning slugs. These are adjusted to the correct values experimentally during cold test.

(d) The Transition From the Loaded Guide to Standard S-Band Guide

The loaded structure with its relatively narrow passband must be matched to an unloaded S-band waveguide. The ω / β D curves for the two structures are shown in Fig. 6. The change in slope of the curves, which represents the group velocity, must take place in the macthing filter. This can be accomplished by building a number of filter sections which have ω / β D progressively changing from that of the loaded structure to that of the S-band guide, at the same time maintaining the $\pi / 2$ phase shift per section at band center. Such a matching filter section was built and consisted of a linearly tapered waveguide successively loaded with progressively smaller lumped capacitances, which disappear when the taper assumes the S-band guide dimensions. At this point the periodicity D is $\lambda_g / 4$ for unloaded waveguide. Fig. 7 shows such a tapered filter and the cold test equipment which was used to demonstrate it. Experimentally, it was found that a taper having 10 loading points provides adequate squareness of the transmitted frequency response curve.

(e) Wideband Windows

The first solution to the wide band window problem consisted simply of replacing one of the lumped capacitative susceptances in the filter by a window having an equal susceptance. Such a window, being in a guide with very small height, does not have a high-power carrying capability because of high electric field gradients. Also, the capacitative protrusions in the transition outside the window present another arc-over hazard. A solution to this difficulty was found by making an abrupt change from capacitative loading to inductive loading inside the tube, and then integrating the window into the inductively-loaded structure. This permits the use of a sizable window in S-band guide having a reasonable thickness (130 mils) and adequately low-voltage gradients. The transition filters were built with irises in S-band guide. Transmission and reflection curves for the output taper and window structure are shown in Fig. 8.

(f) The Design of the Penultimate Guide

In conventional klystrons the maximum efficiency is usually obtained by detuning the penultimate cavity to a frequency above that of the operating frequency; i. e., working at a point on the inductive skirt of the resonance curve. Under this condition the circuit voltage reverses as the bunch center traverses the gap, and as a consequence the bunch is further compressed. To achieve a similar enhancement of efficiency in a wideband TWK requires a circuit which presents a high inductive reactance that is constant over the band of interest; i. e., the traveling-wave voltage should

Fig. 7 - Cold Test Equipment

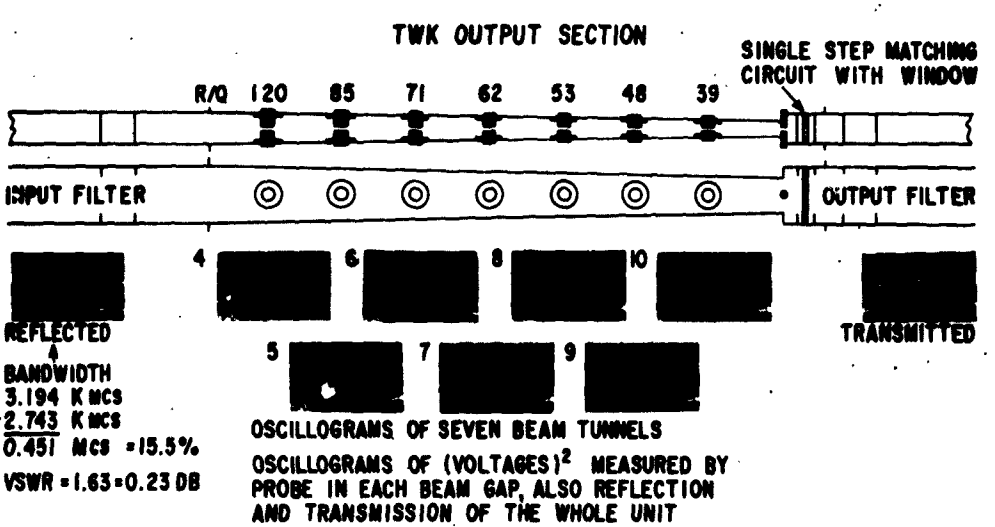

EACH POINT ON THIS CURVE REPRESENTS THE SUM OF THE RF VOLTAGES AT SEVEN GAPS, (NO. 4-10 INCLUSIVE)

THIS REPRESENTS THE OUTPUT POWER VS FREQUENCY CHARACTERISTICS IF EACH BEAM MADE AN EQUAL RF CURRENT CONTRIBUTION

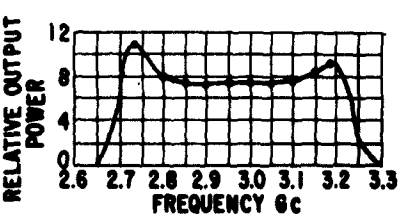

Fig. 8

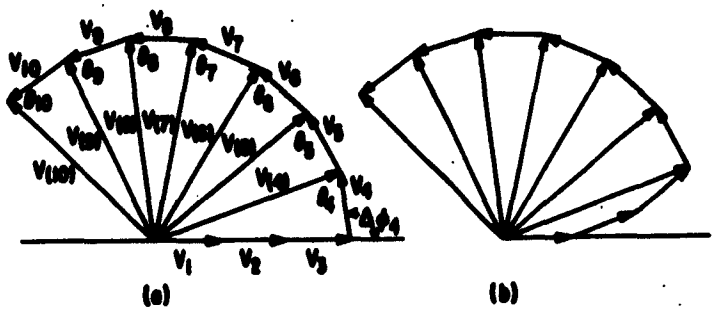

Fig. 9 - Vector Addition of Beam Voltage Contributions in the Penultimate Waveguide

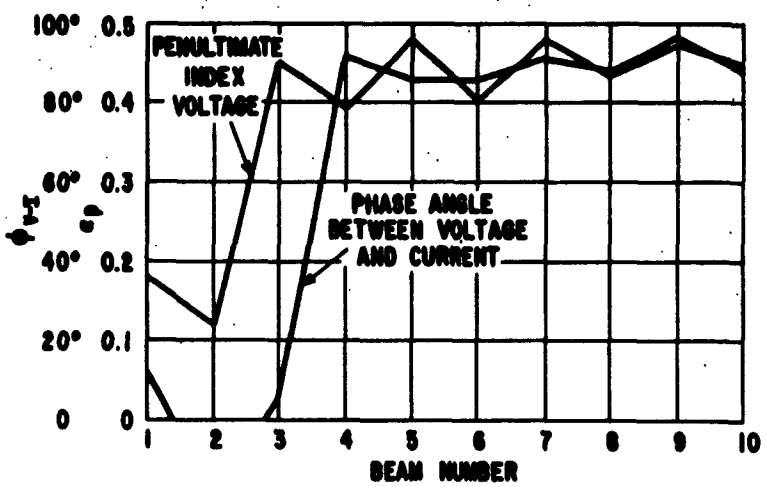

Fig. 10 - Penultimate Guide Phase Angle and Amplitude

always lead the current bunch by 90°. It is possible, by introducing a phase difference either in the circuit or in the beam drift, to have the current bunch arrive at approximately the required phase. There is also a second requirement, that the voltage swing in the penultimate gap should have the correct magnitude, which in normal klystrons is in the region of 0.2 to 0.4 times the beam voltage.

The adjustemnt of circuit phase velocity as described in the preceding paper has serious limitations since it is accompanied by a restriction in bandwidth capability. The more promising method for this phase control is in the variation of drift distance between gaps. This technique avoids bandwidth limitation almost completely. Fig. 9 shows the vector addition of successive voltage contributions. Here only the forward-wave combinations are considered, and the constant phase shift in the circuit is ignored since it is the same in both waveguides. The lengths of the individual vectors are the same, indicating equal driving currents at various gaps. V_1, V_2, and V_3 are the in-phase contribution of the first three beams. These must be in phase in order to effect a voltage buildup, to the required value of voltage swing in the output gap, so for these the drift lengths are equal. If the drift angle of the fourth beam is increased by an angle ϕ_4 relative to the first, the resultant voltage will differ in phase from V_4 by the angle θ_4. θ_4 is the angle between resultant voltage and the driving current in the fourth gap and should be approximately 90°. The resultant angle θ_5 between V_5 and the fifth driving current can also be made to be 90°. This condition can be maintained for any number of beams by progressively slipping the phase of the subsequent driving beams. The resultant voltages should be of constant amplitude (i.e., about 0.4 V_o) to insure optimum efficiency, as was mentioned previously. We see from the configuration of the vector diagram that to achieve a constant magnitude the phase angles have to be somewhat less than 90°.

This method was simulated on a computer and Fig. 10 illustrates the result, showing the magnitudes and phase angles relative to the incoming beam current bunch. This result was achieved after several trial adjustments of the drift lengths, and indicates that consistently good bunching conditions may be obtained. The effect of frequency variation across the band was also investigated and it is readily shown that the deviation in phase slip is proportional to the fractional deviation in frequency. Thus, for example, a 100° band center phase slip between two beams would become 107.5° and 92.5° at the band edges for a 15% bandwidth tube.

(g) The TWK Performance Equations

The computer program permits the accurate calculation of the voltages and currents and phase angles in a periodically-loaded transmission line for given induced currents. It therefore gives an accurate picture of performance at all frequencies taking both forward and backward waves into account. However, the design data supplied to the

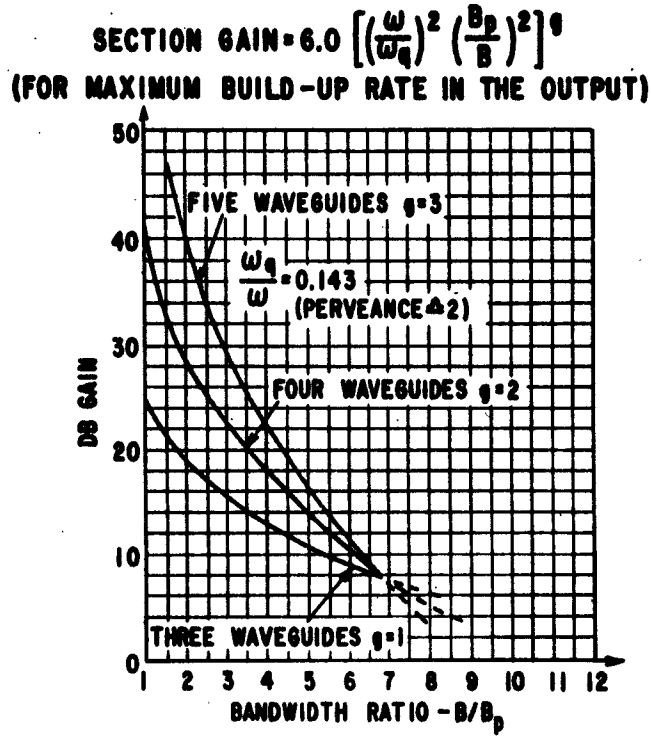

Fig. 11 - Effect of Adding Waveguides to TWK Build-Up

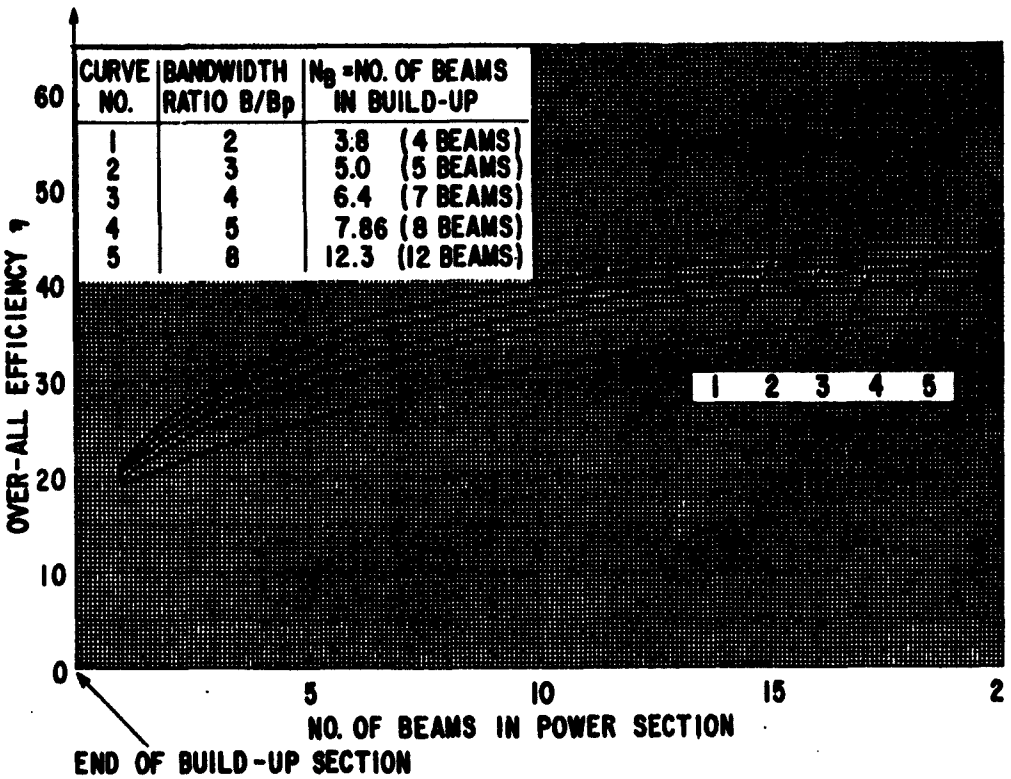

Fig. 12 - TWK Overall Efficiency

computer must be derived from approximate performance calculations. Such a set of approximate performance equations has been derived for the TWK and serves to make a good preliminary estimate of the tube's capability, and also indicates the limitations accompanying given output power and bandwidth capabilities.

Starting with given power output and bandwidth requirements and a suitable prototype beam current and voltage, we assume that the currents and voltages in the penultimate guide correspond to maximum efficiency of operation in the power section of the tube. From this, from from conventional small-signal klystron theory, and from a knowledge of impedance levels at the gaps for given bandwidth requirements, we can calculate:

(a) The R/Q required at the gaps, and the waveguide dimensions.
(b) The number of buildup beams required.
(c) The number of power beams required.
(d) The average lengths of the drift tunnels.
(e) The number of buildup beams in the penultimate guide and the buildup rate in the output guide.
(f) The power gain of each waveguide and hence the overall gain and drive power requirements.
(g) The efficiency.

Fig. 11 shows the effect of additional intermediate guides on the gain of the build-up section and demonstrates the cost of bandwidth at the expense of gain.

Fig. 12 shows the overall efficiency of a three-guide TWK. Again we see that increasing the bandwidth requires the number of build-up beams to be increased and hence reduces the overall efficiency.

The mechanical and electrical design for the experimental S-band tube is now nearly complete and the tube will soon be constructed in order to demonstrate the principles outlined above with practical results.

Acknowledgement

The travelling wave klystron work was initiated under ARGMA Contract No. DA 30-069-ORD-2793, and the subsequent work reported here was funded by the General Electric Company. Work is now being continued under Signal Corps sponsorship.

MODULATOR DESIGN CONSIDERATIONS

By

G. W. Taylor and S. Schneider

U. S. Army Electronics Research and Development Laboratory

INTRODUCTION

The superpower amplifier development programs have presented and continue to present a tremendous challenge to the tube designer. Simultaneously, a challenge is presented to select and design the most effective modulator for pulsing these superpower tubes. A variety of factors must be considered in determining the modulator design.

MODULATOR TYPES

Modulators fall into the following two basic classes: 1) the cathode- (or plate-) pulsed type; and 2) the auxiliary-electrode-pulsed type. The cathode-pulsed type can be accomplished in either of two ways (Fig. 1). Fig. 1a is the line-type modulator where the required single-pulse energy is stored during the interpulse period and then delivered at the required time. The only available line-type modulator switch tubes for high powers are the hydrogen thyratron and mercury-pool tubes. Fig. 1b shows a storage-condenser-type modulator with a series-connected switch tube. In this type modulator the pulse energy is drawn from a large energy-storage reservoir. The pulse energy is controlled by the switch tube, which is a high-vacuum type.

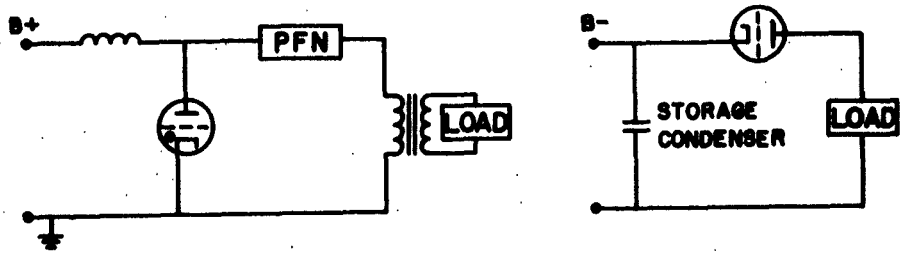

A. LINE-TYPE MODULATOR

B. STORAGE-CONDENSER MODULATOR (SERIES TYPE)

FIG. 1 CATHODE-PULSED

The second class of modulator, the auxiliary-electrode pulsed, can also be accomplished in two ways (Fig. 2). Fig. 2a is a floating-deck modulator, which uses two high-vacuum switch tubes. One tube is used to turn on the beam of the rf tube. This tube charges up the capacitance of the auxiliary-electrode circuit to the desired voltage and supplies the small loss associated with leakage and intercepted beam current. The second tube turns the beam off by discharging the capacitance and then clamps the auxiliary electrode to the cathode with suitable bias. Fig. 2b shows an auxiliary-electrode-pulsed modulator with the pulse-voltage transformer coupled to the auxiliary electrode. The switch tube may be either a gas type or a high-vacuum type.

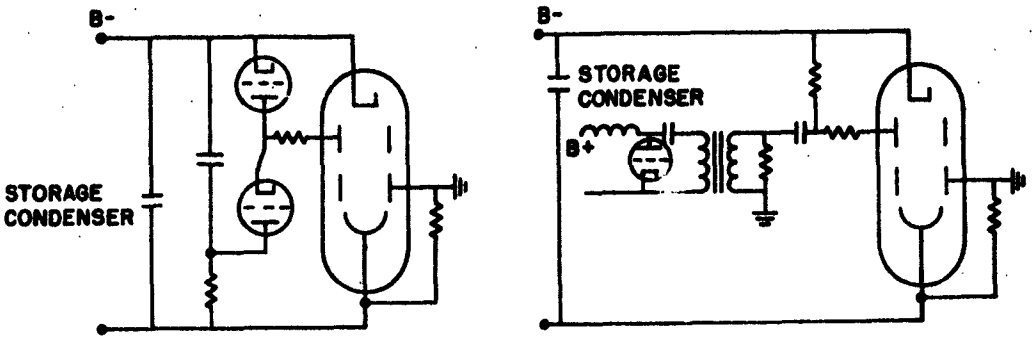

A. FLOATING DECK B. TRANSFORMER COUPLED

FIG. 2 AUXILIARY-ELECTRODE-PULSED

MODULATOR CHARACTERISTICS

In selecting which of these modulators is best for a particular system, many factors must be considered. The more important factors that should be considered are shown in Table I. It can be seen that, relatively speaking, the stored energy is low for only the line-type modulator, which stores only enough energy for a single pulse. In all the other modulators the total stored energy must be much greater than that required by a single pulse. For example, if a minimum pulse droop of 1% is required, a maximum of 2% of the stored energy can be used for each pulse. The stored energy can be reduced somewhat in the storage-condenser cathode-pulsed modulator by using the modulator tube as a regulator; however, the stored energy will still remain considerably greater than in the line-type case. The amount of stored energy also effects the need for protective circuitry. The use of protective devices, such as crowbars, is considered essential in superpower work if the modulator is an auxiliary-electrode-pulsed type or a storage-condenser cathode-pulsed type. Protective circuitry such as inverse and backswing clippers are strongly recommended for the line-type modulator.

TABLE I COMPARISON CHART

	Cathode-Pulsed		Auxiliary-Electrode-Pulsed	
	Line-Type	Storage Condenser	Floating Deck	Transformer-Coupled
Stored Energy	Low	High	High	High
Protective Devices for RF Tube and Other Components	Clippers	Crowbar	Crowbar	Crowbar and Clippers
Protective Device for Modulator Tube	None	Crowbar	Crowbar (Optional)	Crowbar (If High-Vacuum Tube)
Flexibility (Variable Pulse Width and Pulse Coding)	Limited	Good to Excellent	Good to Excellent	Limited
Droop	None	Can Be Very Low	Function of Storage Capacitor	Function of Storage Capacitor
Ripple	1%	Low	Low	Low

Another very important factor that the modulator designer must consider is modulator flexibility. By the term flexibility we mean the ability to vary pulse width and pulse repetition rate and to operate with close-spaced coded pulses. The cathode-pulsed storage-condenser and auxiliary-electrode floating-deck modulators have the greatest flexibility. Although the other two types could be built with flexibility they would generally be more complex.

Two additional factors that must be considered are pulse droop and ripple. There will be no pulse droop for a line-type modulator if network and pulse transformer are correctly designed. It is difficult, however, to reduce pulse ripple much below 1% without the use of clamping circuits. Pulse ripple on the other type modulators can be made very low. The auxiliary-electrode-pulsed modulators present a problem of pulse droop on the main supply voltage if the stored energy is to be kept within reasonable limits. In the case of the cathode-pulsed storage-condenser modulator, good pulse droop characteristics can be obtained using the switch tube as a regulator.

MODULATOR SELECTION

Although the comparison chart (Table I) gives many important factors that should be considered when selecting the type modulator, it is impossible to recommend any one of the modulator types as being preferred to all others. Each particular system requirement, if intelligently examined from the standpoint of equipment performance characteristics against such items as weight, size, and initial and maintenance cost, will provide the answer for that particular system. In general, however, it can be stated that, if only one or two fixed pulse widths are required, and at a limited range of repetition rate, the cathode-pulsed line-type modulator is smaller and more economical. This has been shown for a particular case by C. J. Eichenauer, Jr. and R. D. Smith in a paper entitled "Superpower Klystron Pulsing Considerations".[1] They compared a line-type cathode pulser to a modulating-anode pulser for the case where the peak power requirement is 150 megawatts at 3000 kilowatts of average power and the pulse duration is either 10 or 500 microseconds. For the 10-microsecond case, the volume, the weight, and the cost of the line-type pulser are 28%, 54%, and 72%, respectively, of the condenser-bank pulser. For the 500-microsecond pulse length, the volume, the weight, and the cost of the line-type pulser are 12%, 53%, and 67%, respectively, of the equivalent equipment utilizing a condenser-bank pulser.

If continually-variable pulse widths or close-spaced coded pulses are a necessity, the situation reverses and either the storage-condenser cathode-pulsed or the floating-deck auxiliary-electrode-pulsed modulator is preferred. The cathode-pulsed type has the advantage of simplifying the design of the rf tube but obviously requires the use of a modulator tube capable of passing the peak pulse current. If, however, phase stability is important, a series regulator capable of passing peak pulse current will possibly be required anyway. Because existing modulator tubes are voltage-limited, it is often necessary to use an auxiliary-electrode-pulsed modulator with transformer coupling. This type of modulator, even with a high-vacuum switch tube, has somewhat limited flexibility.

These remarks on modulator selection have considered two extreme cases where the choice is relatively clear cut. For intermediate cases the choice is not as clear and all factors must be critically examined.

MODULATOR TUBES

Since the choice of modulator tubes is an important factor, let us look at some of the available high-power switches. Table II shows the important ratings on three commercially-available hydrogen thyratrons and the highest-power developmental thyratron:

TABLE II HIGH-POWER HYDROGEN THYRATRONS

	Commercialised			Under Development
Characteristic	1257	7390	7890	Z-5212
Peak Forward Voltage (kv)	33	30	40	50
Peak Pulse Current (A)	1980	1000	2400	2000
Average Current (A)	2.6	4.0	4.0	8*
RMS Current (A)	60	75	75	126
Prr (pps)	360	1300	360	4000
Pb Factor x 10^9	20	39	55	400
Average Power (KW	33	60	80	200
Peak Power (MW)	33	15	48	50

*At reduced Pb has potential of 16 amperes average (cathode area 4 times area of 7890)

The commercially-available tubes are characterised by average power capabilities of tens of kilowatts and peak powers of tens of megawatts. The developmental tube has a rating of 200 kilowatts average at 50 megawatts peak. Development of this tube is near completion and all ratings shown have been demonstrated simultaneously on a limited number of samples.

The next type of device to be considered is the mercury-pool switch, as typified by the Ignitron. Ratings on three of the higher-power devices of this type are shown in Table III:

TABLE III IGNITRONS			
Characteristic	GL-6228	Z-5233	Z-5234
Peak Forward Voltage (kv)	25	30	30
Peak Inverse Voltage (kv)	1	1	1
Peak Anode Current (A)	1600	1600	3200
Average Current (A)	160	160	320
RMS Anode Current (A)	500	500	1000
Prr (pps)	60	60	60
Tp (μs)	1000	1000	1000

Tubes of this type are only partially evaluated for modulator service. Inherently, this type of modulator tube is capable of handling very-high average power.

Table IV shows a few of the available high-vacuum switch tubes together with their characteristic ratings.

TABLE IV HIGH-VACUUM MODULATOR TUBES						
a. For Storage Condenser						
Type Number	Eb (kvdc)	Peak Ib (A)	Tp (μs)	Duty	Peak Output (MW)	PP (KW)
7560	50	550	1000	.01	20	175
6398	65	350	15	.002	-	100
WX-445	80	600	-	.01	37	-
8038	125	175	1000	.01	20	5
*A-15034	40	275	3000	.05	10	41
*D-1037	65	650	-	-	30	-
b. For Floating Deck						
7668	150	15	1000	.01	2	0.75
L-3408	200	30	10	.006	-	12.
*L-3620	320	30	10	-	9	30.
*Development Types						

The tubes in Table IV have peak output powers of tens of megawatts and average output power capability of from tens to hundreds of kilowatts. Although these power-handling capabilities are impressive, they fall far short of the power required. For the modulator designer to meet the challenge presented by the superpower program and build the modulator required for the job, it is felt that higher-power modulator tubes are required. Specific recommendations for the required modulator tubes are shown in Table V:

TABLE V FUTURE MODULATOR-TUBE OBJECTIVES

Gas Line-Type Modulator	Phase A	Phase B
Peak Forward Voltage (kv)	100	100
Peak Power (MW)	200	400
Peak Current (A)	4000	8000
Average Power (KW)	400	4000
High-Vacuum Modulator		
Plate Voltage (kvdc)	350	
Peak Current (A)	1200	
Peak Output Power (MW)	400	
Average Output Power (MW)	4	

This table shows both a hydrogen thyratron and a high-vacuum switch tube capable of giving a peak output power of 400 megawatts at an average output of 4 megawatts.

MODULATOR CIRCUITRY

All modulators require protective circuitry of one form or another to avoid the damaging effects of an arc occurring any place in the system. The discussion will be limited to high-speed protection. The damaging effects of an arc in a line-type modulator are not as severe as in the other types since the stored energy in the capacitors is limited. It is still necessary, however, to provide adequate protection. The simplest and most effective method of protection is to install a matched far-end-of-line clipper on the pulse network. The circuit is shown in Fig. 3:

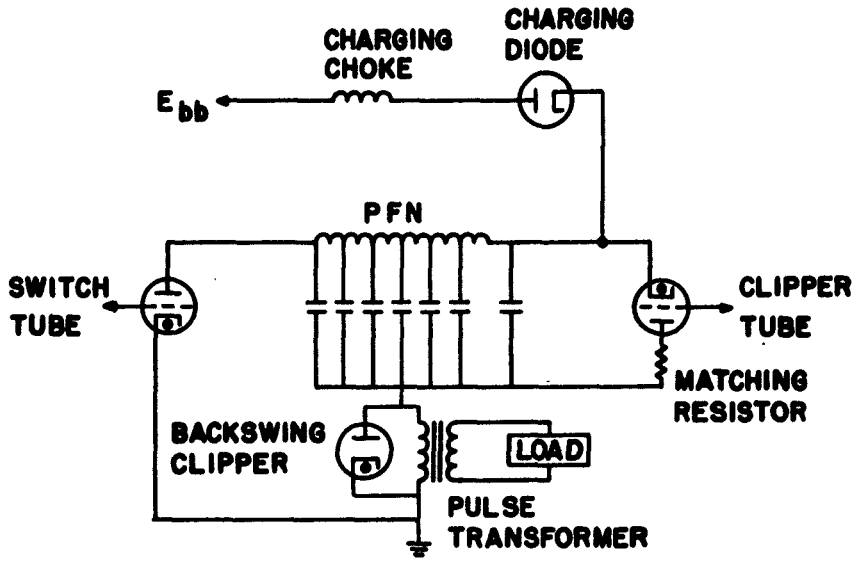

FIG. 3 INVERSE & BACKSWING CLIPPER CIRCUIT

The resistor in series with the clipper tube is matched to the network and dissipates the inverse energy. This protects the circuit components against the effect of load faulting. When a load fault occurs, the negative mismatch of the circuit increases and the inverse voltage rises. This, in turn, increases the voltage to which the line charges. Successive faults can produce extremely-high voltages across all the circuit components. Since the clipper tube removes the inverse voltage after each pulse, this type of runaway condition is avoided. Other advantages of this circuit are improved regulation of the output pulse and improved performance of the gas tube switch by the removal of inverse voltage and energy after each pulse. Tubes designed for this operation are available for use with hydrogen thyratrons up to the 1257. Above that level conventional thyratrons must be used. It is also desirable to use a backswing clipper across the primary of the pulse transformer as an aid in protecting the microwave generator. Normally, the use of clippers is sufficient protection in a line-type modulator. The one exception may be the case where long pulses in the order of hundreds of microseconds are generated. In this case, if the microwave generator has a tendency to arc early in the pulse, a simple shorting circuit across the primary pulse transformer may have to be employed. This decision must be dictated by experience with each tube type.

In the other types of modulators, the primary protection required is to divert the stored energy in the condenser bank in the event of a fault. We have established the following specific requirements for a crowbar and its associated circuit:

1. Fast Firing	The crowbar device itself should be capable of firing in 0.1 microsecond.
2. Logic-Driver Delays	The total delays, including the sensing circuit and the logic-driver circuit should not exceed 0.5 microsecond. This requirement should be rigidly adhered to since the quicker the energy diversion the greater the odds are of extinguishing the fault arc.
3. Infinite Voltage Range	The device should have an infinite voltage range that is Vmax/Vmin equal to infinity. This provides the ability to check the crowbar with zero voltage applied. More important, it permits the next requirement to be met.
4. Repetitive Firing	Repetitive firing should be at a spacing of one to ten milliseconds for a period of time longer than necessary to permit the circuit breakers to act. This provides continuous protection against the effects of storage-condenser recharge and the reignition of the arc in the event the microwave generator has become gassy.
5. Low Trigger Energy	The energy required to trigger the crowbar should be less than a few joules. This simplifies the trigger design and also prevents the possibility of large amounts of trigger energy being dumped into the rf tube.
6. Low Voltage Drop	A low arc drop, in the order of a few hundred volts, is desirable. This aids in quenching the rf tube arc or reducing the residual current flow thru the tube.

7.	Self Firing	The crowbar should be self-firing in the event of a fault at high voltages should the logic circuit fail, thus providing a minimum protection at all times.
8.	100% Overvoltage Gap Setting	A 100% overvoltage setting on the gaps helps prevent spurious firing due to environmental conditions.
9.	Quiet Operation	Quiet operation permits placement at the most convenient point in the circuit, even if in a working area.
10.	Low Inductance Configuration	A low inductance configuration permits rapid reduction of voltage across the rf tube.

The crowbar should be placed in the circuit as shown in Fig. 4. The sensor should detect any fault in the tube circuit. The resistance between the condenser bank and the crowbar should be the maximum necessary to protect the condensers. It should be capable of withstanding the full operating voltage of the equipment, since this voltage will be impressed across the resistor when the crowbar fires. Inductance in crowbar-capacitance bank loop, to slow the rate of rise of current during a fault, is desirable. This permits the crowbar to act before excessive current and a well-established arc appear in the rf tube, and it improves the probability of the arc being extinguished. At the same time, inductance must be avoided in the crowbar-tube loop. The inductor prevents immediate reduction of voltage across the rf tube and may dissipate its energy in the tube. This inhibits the quenching processes and reduces the probability of arc extinction. Since there is finite possibility that arc extinction may not occur in the rf tube, it is necessary to provide as large a series resistance as is compatible with system operation to limit the residual current in the crowbar-tube loop.

A system[2,3] that has met these requirements has been developed at this Laboratory and has demonstrated successful operation in the VA-852 and the SAL-155 equipments. It is a sequentially-fired multiple-gap system. It is flexible and can be designed with relative ease for most applications. Fig. 5 shows the effect of the crowbar on the fault current through an 852 klystron at full voltage. In this case the current was limited to 300 amperes peak rather than several thousand amperes and decayed to zero within two microseconds. The gas change noted in the tube was negligible and permitted immediate reapplication of voltage.

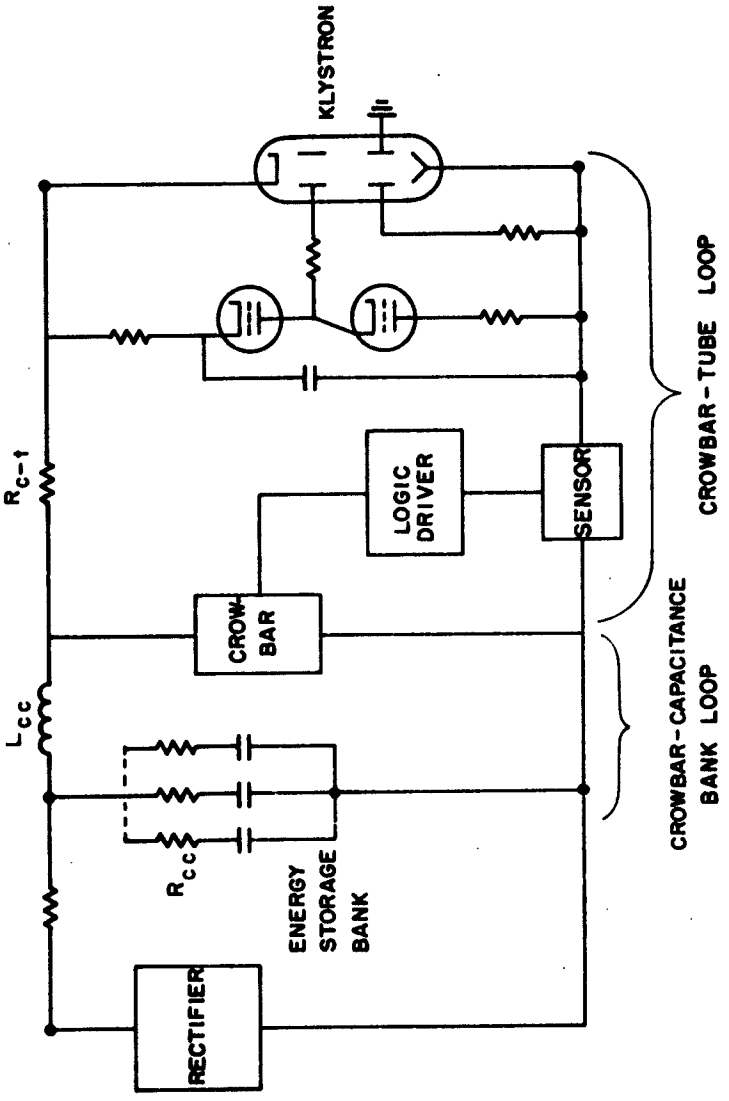

FIG. 4 CROWBAR PLACEMENT

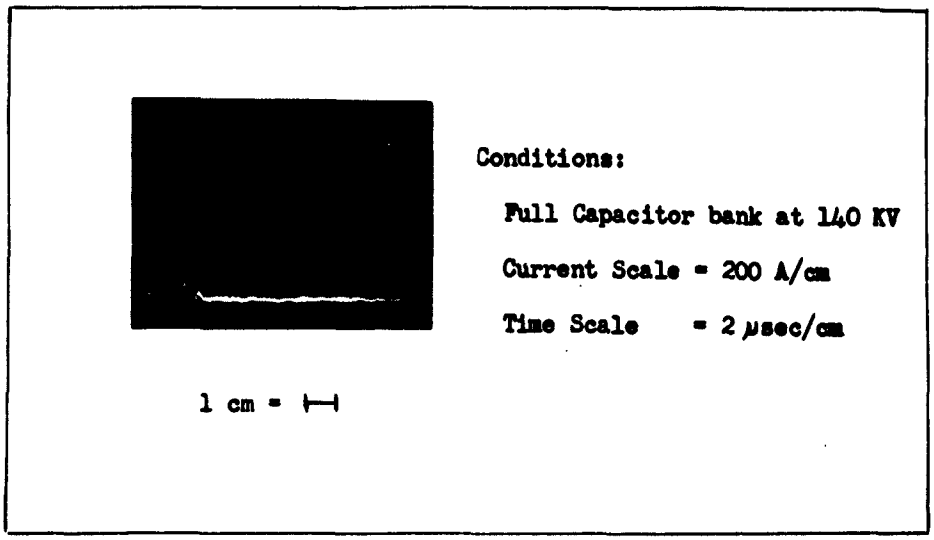

Fig. 5 Tube Fault Current with Crowbar Operating

To date, the crowbar developed by this Laboratory is the only proven type that meets the discussed requirements. Other techniques are being worked on or have been proposed that may also meet these requirements.

REFERENCES

1. Eichenauer, C. J., Jr., Smith, R. D., "Superpower Klystron Pulsing Considerations", Proceedings of the Sixth Symposium on Hydrogen Thyratrons and Modulators, May 1960.

2. Schneider, Sol, Zinn, M. H., Buffa, Anthony J., "The USASRDL Electronic Crowbar", Proceedings of the Seventh Symposium on Hydrogen Thyratrons and Modulators, May 1962.

3. Grotz, G., "A 300-KV Multigap Crowbar", Proceedings of the Seventh Symposium on Hydrogen Thyratrons and Modulators, May 1962

SUPER POWER GENERATION BY LINEAR BEAM TUBES

By

Thomas Sege

Sperry Electronic Tube Division

Sperry Rand Corporation

Great Neck, New York

This paper deals with present day high-power linear beam tube technology and status.

Before presenting some power frequency curves, a review of the basis on which they were prepared is described. The plots of peak power, average power, and energy per pulse as a function of frequency are based upon tubes that are available today. Power performance of specific tubes is shown on these figures. The curves were prepared by drawing a line of constant beam power density through that existing tube which represents the highest figure for this parameter. The plots thus represent the power that may be achieved by extending to other frequencies the techniques used in existing tubes.

These techniques incidentally are far from being the most advanced known laboratory technology. They represent, rather, today's commercial manufacturing feasibility; namely,

(a) Collector and interaction structure power dissipation densities of under 500 wattsper square centimeter, less than one-tenth the figure attained with advanced vortex cooling schemes.

(b) Electron gun area convergence ratios of typically between 30 to 1 and 70 to 1. This contrasts with convergence ratios, ten times as great as this, which have already been demonstrated in various laboratories.

(c) Conservative cathode current densities as shown in figure 1.

For constant perveance, it can be shown that power output varies as $1/F^{3.3}$ up to the relativistic voltage region. In the plots shown, a more conservative 2.2 to 2.4 power of frequency is used.

Figure 2 shows peak power available as a function of frequency. The numbers 1 through 6 as shown on figures 2, 3 and 4 correspond to the listed companies and university which have existing tubes which operate in the designated areas.

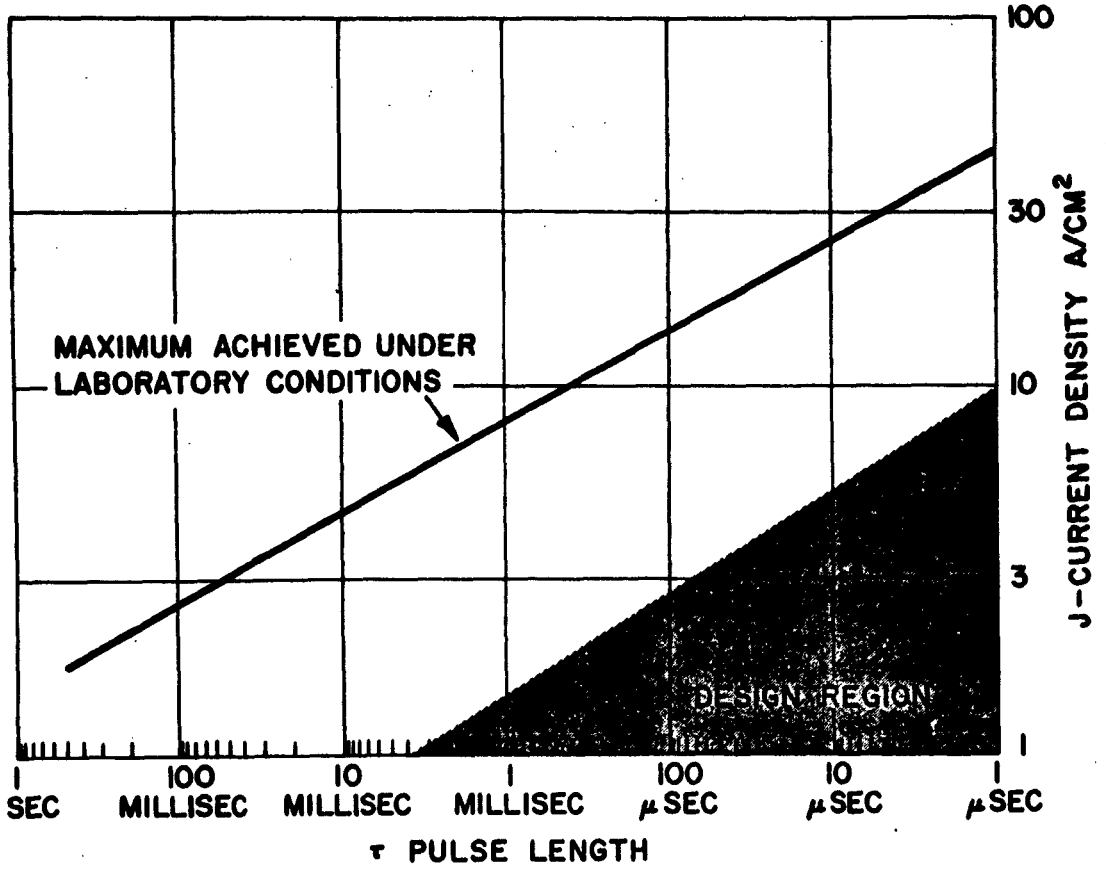

CATHODE CURRENT DENSITY VS. PULSE LENGTH

FIGURE 1

THE NUMBERS 1 THROUGH 6 ARE APPLICABLE TO THE COMPANIES AND UNIVERSITY SPECIFIED IN THE TEXT.

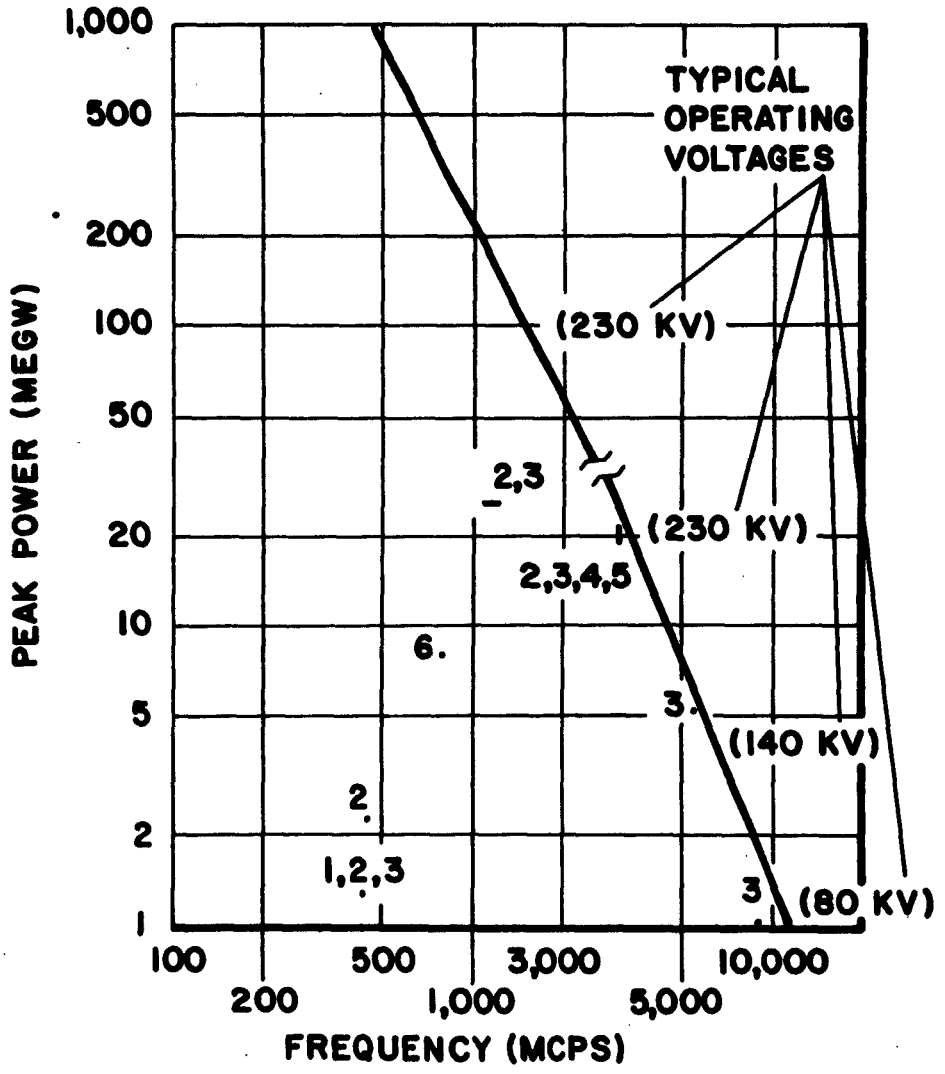

PEAK POWER VS FREQUENCY FOR MEGAWATT KLYSTRONS

FIGURE 2

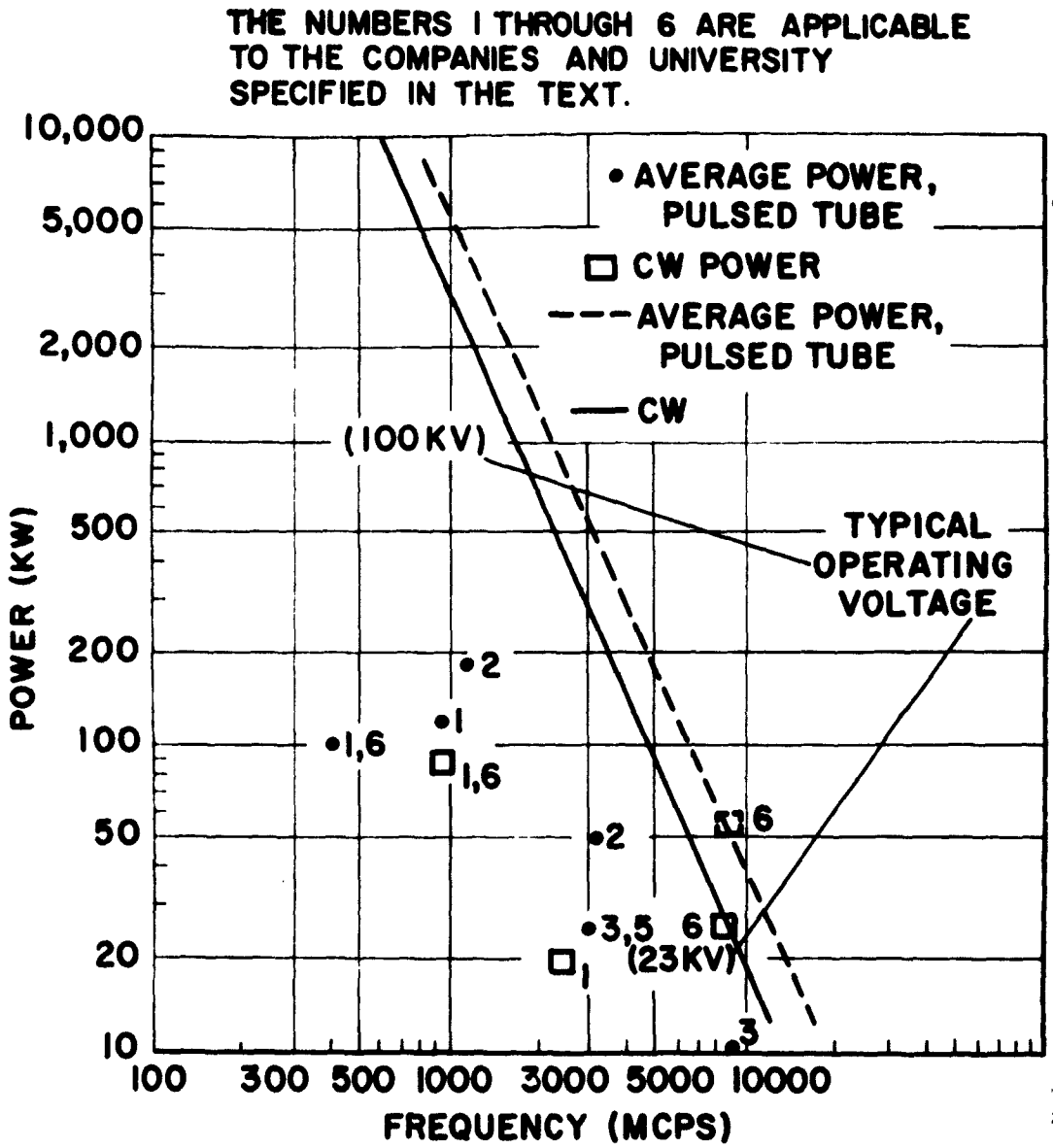

AVERAGE POWER VS. FREQUENCY FOR HIGH POWER KLYSTRONS

FIGURE 3

1. Eitel-McCullough
2. Litton Industries
3. Sperry Electronic Tube Division
4. Stanford University
5. Thomson Houston (France)
6. Varian Associates

The perveance is allowed to vary with power level, with low perveance at the lower powers, and higher and higher perveance at the higher power levels. Finally, above a certain power level, it is assumed that a high-perveance hollow beam would be used in order to keep the voltage from becoming excessively high. A hollow beam is used since it does not appear practical to operate a high-power klystron with a solid beam of micro perveance much higher than 3 to 4. With a hollow beam, this limitation is removed to some extent. Magnetron injection guns are typically considered for use in these designs with perveances of 8, 10 or higher. In addition to the lower operating voltage due to high-perveance hollow beams, there are some bandwidth advantages accruing as well.

It can be seen in figure 2 that if present day C- and X-band megawatt tubes are scaled to lower frequencies, extremely high peak powers become available.

Figure 3 is a plot of average power capability as a function of frequency. Two lines are shown, one for cw tubes and a higher one for the average power of pulse tubes, the latter being higher due to the larger size beam that can be used in these tubes. Again, based on achieved X-band power, it can be seen that the average power capability of the klystron is extremely high.

Figure 4 illustrates the energy per pulse capability of klystrons. These curves are based on consideration of instantaneous heating occurring during the pulse; heating affecting the surface of the metal only, which cannot be helped by improved cooling.

Figure 5 shows some typical combined operating characteristics for possible klystron designs based on established technology. The efficiencies shown are very much on the conservative side. Higher efficiencies have been achieved, in tunable klystrons: 40 to 45 percent in S-, C- and X-band; 50 to 55 percent in UHF and L-band and up to 60 percent by SERL in 10 megawatt, 400 megacycle klystrons.

So these are the power levels attained or attainable in the field (as opposed to the laboratory) today. Before pole vaulting into superpower - not defined at the present time - two figures representing limiting beam powers as a function of frequency based on achievable cathode current densities are presented.

THE NUMBERS I THROUGH 6 ARE APPLICABLE TO THE COMPANIES AND UNIVERSITY SPECIFIED IN THE TEXT.

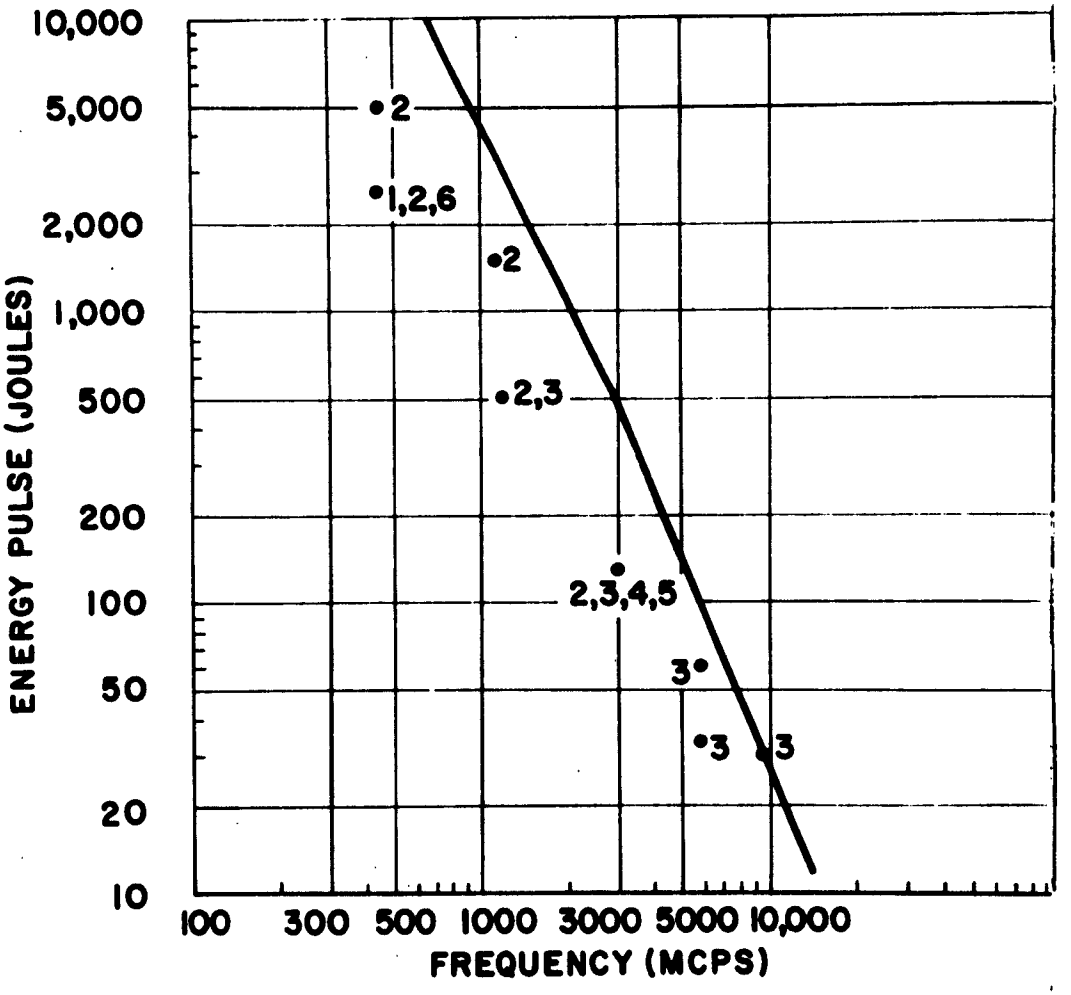

JOULES/ JOLT VS. FREQUENCY FOR MEGAWATT KLYSTRONS

FIGURE 4

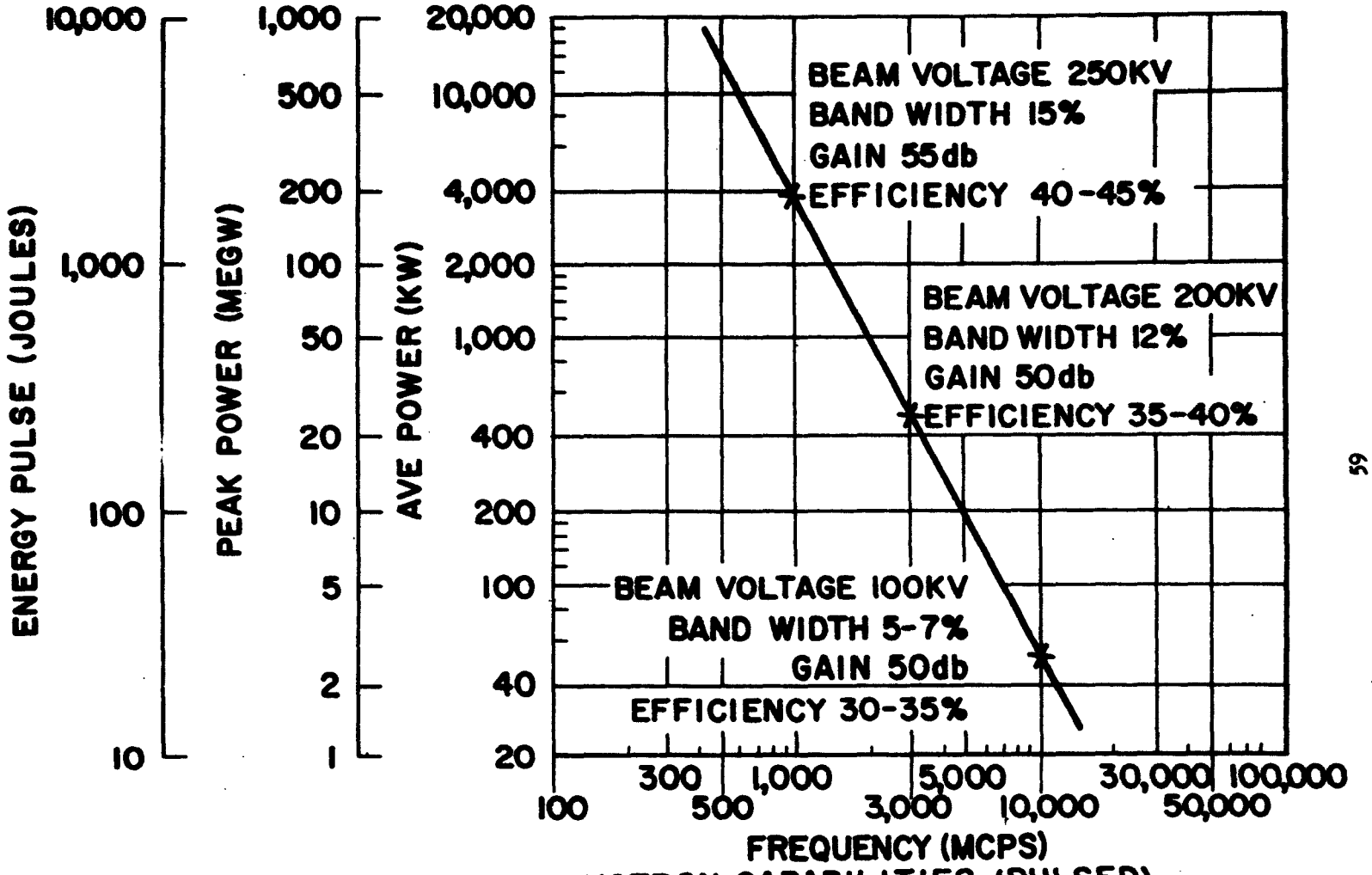

PRESENT MEGAWATT KLYSTRON CAPABILITIES (PULSED)
FIGURE 5

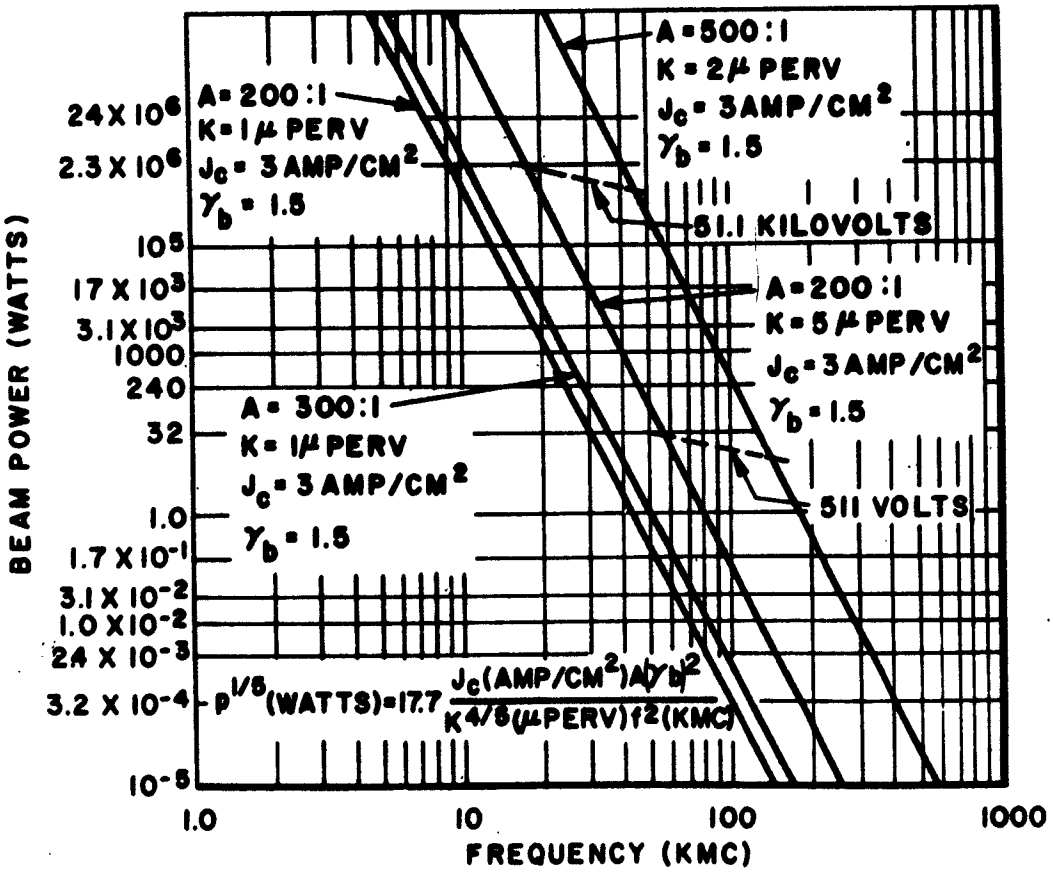

CURRENT LIMITED POWER VERSUS FREQUENCY FOR NEW SOLID BEAM GUNS

FIGURE 6

Figure 6 shows attainable beam powers as a function of frequency for solid beams, for various perveances, and area convergence ratios as limited by cathode current density. It is noted that beam-power input in excess of 3 megawatts is possible at X-band.

Figure 7 shows similar curves for hollow beams. The variation with frequency for this is slower since hollow beams can be used at larger diameters due to their finite thickness as compared to solid beams. However, this is compensated for by the relatively lower area convergence ratios realized to date in magnetron injection hollow-beam guns. The power limitation for hollow-beam tube is less than for solid beam.

A review of some other implications of a large jump in power from today's reality is considered. First, consider a 20 to 40 fold increase in power level to one megawatt cw at X-band.

It has been shown in earlier curves that cathode current density need not be a limiting factor - thus examination of some of the other parameters of such a design, is considered.

Collectors are the least of the problems in designing linear beam tubes. They can be made as large as needed to dissipate the residual beam power at a conservative density, for example, a 6 to 8 inch in diameter, 3 foot long collector could dissipate 2-1/2 megawatts of beam power and keep the power density below 1/2 kw/cm^2.

In order to assess interaction structure limitations on superpower highlights of a hypothetical one megawatt X-band klystron design are utilized.

Figure 8-A shows some of the design parameters; the design efficiency is very conservative; the small beam diameter selected means the beam power density is fairly high. However, it is only a little over twice what has already been achieved under experimental conditions.

Confined flow magnetic focusing drift tube interception of 1 percent or less as already achieved would be used. The conservative assumption that all of the drift tube interception will occur in a single drift tube even though this tube would probably have 4 drift tubes is made. Under these conditions, the dissipation power density is 2-1/2 to 5 kw/cm^2. It must be considered here that 1 percent drift tube interception is not inherent in such a device; consequently, there is reasonable expectation of doing better.

Figure 8-B shows calculations for r-f losses in a single gap output cavity. From this calculation it can be seen that assuming a Qo of 5,000 for the output cavity, and a R/Q of 100 optimum, Q loaded is 100, and the power loss in the output cavity is 5 kilowatts. If the very conservative assumption that 1/2 of the r-f losses are in the gapface, then the dissipation density is 6 kilowatts/cm^2. A more realistic assumption of uniform power loss on a cavity surface makes the dissipation density 1 to 2 kilowatts/cm^2. High turbulent liquid cooling would be required to dissipate these powers. Much can be gained on this through the use of extended interaction output structures - as a multiple gap cavity. For instance, for a 3 gap arrangement the overall R/Q of the interaction structure is 3 times as

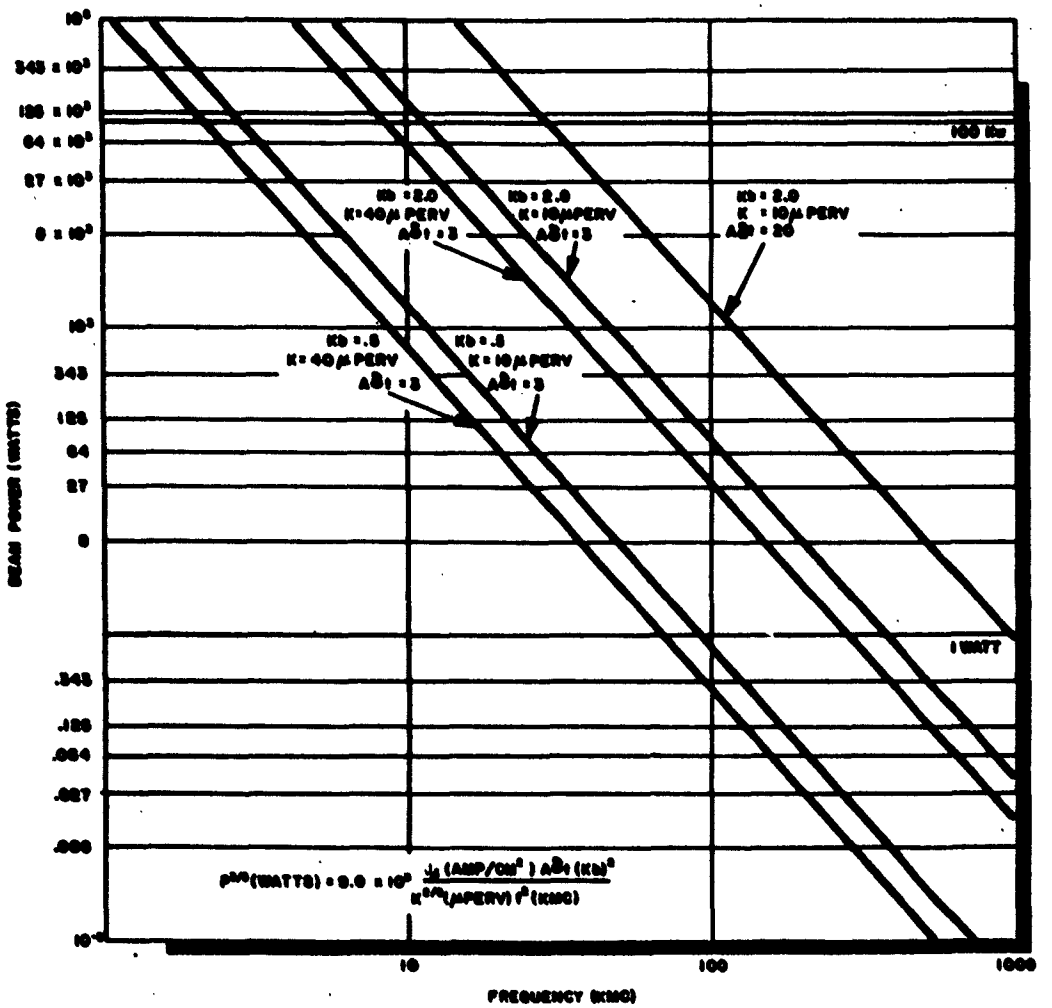

CURRENT LIMITED POWER VERSUS FREQUENCY FOR HOLLOW BEAM GUNS

FIGURE 7

Beam

Choose	K	= 1	0.5	μ perv
Then, for 40% assumed efficiency	Pb	= 2.5	2.5	Megw
and	Eb	= 90	120	Kv
	Ib	= 27	21	amps

Electrical Dimensions

To get good efficiency, choose	γ b	= .5	.5	
then	b	= .16	.185	cm
and	πb^2	= .08	.11	cm^2
and beam power density		= 31	23	$megw/cm^2$
for	a/b	= 1.4	1.4	
	a	= .22	.26	cm

Drift Tube Dissipation

For 1% beam interception, the last drift tube	Pd.t.	25	25	KW
For drift distance	L	3.5	6.0	cm
Intercepting area	Ad.t.	5	10	cm^2
Power Dissipation	Pd.t./Ad.t.	5	2.5	KW/cm^2

A

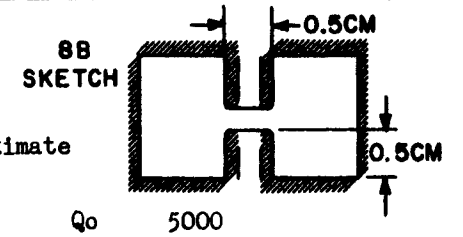

8B SKETCH

Cavity RF Dissipation

For single gap output cavity, approximate gap dimensions would be

	Cavity	Qo	5000	
For R/Q 100,	Load	QL	100	
Ratio of cavity loss to output power		Qo/QL	50	
Cavity Loss			20	KW
Assume 1/2 RF loss in nibs, then per nib			5	KW
Dissipating surface area per nib			0.8	cm^2
RF loss power density			6	KW/cm^2

Cathode Loading

Area convergence ratio	200:1	300:1	
Cathode area	16	33	cm^2
Cathode loading	1.7	0.65	$amps/cm^2$

B

DESIGN PARAMETERS FOR ONE MEGAWATT C-W X-BAND KLYSTRON

FIGURE 8

great as for a single cavity, and results in an optimum loaded Q that is 1/3 that for a single output cavity. Consequently, the total loss in the 3 coupled cavities is 1/3 what it would be for a single cavity; on a per cavity basis it becomes 1/9. This brings the dissipation density down to less than 1/2 kw/cm^2.

In this paper some very difficult problems have been glossed over - the last of which is the problem of transmitting very high power through waveguide windows, but this is a subject of other papers. There are other problems, for instance, the problem of even a momentary loss of beam control due to magnetic field failure or misadjustment. It is clear that in dealing with these kind of power densities that a tube could be destroyed in a very few microseconds in the event of such a failure. Much work will need to be done to resolve the problems to improve interlocking and the development of improved waveguide components. These types of problems are common to all superpower electron devices.

It may be seen from this presentation that considerably higher powers may be generated at the lower waveguide frequencies than have already been accomplished. This appears possible by the application of those techniques now used in the more advanced high frequency tubes to these lower frequencies. In addition, a great stride forward in excess of an order of magnitude, may be made through the careful application of the most advanced present laboratory techniques to superpower linear beam tubes.

THE BIASED-GAP KLYSTRON

By

Ibrahim Hefni

Lincoln Laboratory,* Massachusetts Institute of Technology

Abstract

When an accelerating DC potential is applied across the output gap of a conventional multicavity klystron, the available RF output power increases as the applied bias voltage increases. It was found experimentally that the available output power is related to the bias voltage by the simple linear equation $P_{av} = I_1 (V_o + V_b)$, where P_{av} is the available output power, I_1 is a constant representing the fundamental component of the RF beam current, V_o is the beam voltage and V_b is the bias voltage.

With the output gap biased and the collector depressed to ground potential, it was possible to increase the tube efficiency, sometimes by as much as 10 percent, in spite of the fact that the collector was not designed for proper depressed operation. The highest efficiency achieved was about 65 percent; however, it should be possible to attain higher efficiencies after modifying the collector.

Besides increasing klystron efficiency, the biased-gap method offers other advantages, such as reducing both the beam interception and the possibility of multipactor at the output gap. Also, the technique can be used for automatic phase and gain control and for the quantitative evaluation of the various parameters of the klystron.

*Operated with support from the U. S. Advanced Research Projects Agency

I. Introduction

Linear beam amplifiers, such as the klystron, are known to be less efficient than cross-field amplifiers. Our aim is to investigate quantitatively the various factors affecting klystron efficiency, and devise methods to increase the efficiency without sacrificing the stability or high gain of the klystron.

Theoretically, the efficiency of the multicavity klystron is known only through approximate analysis based on many simplifying assumptions. The theories can be summarized very briefly as follows (Fig. 1):

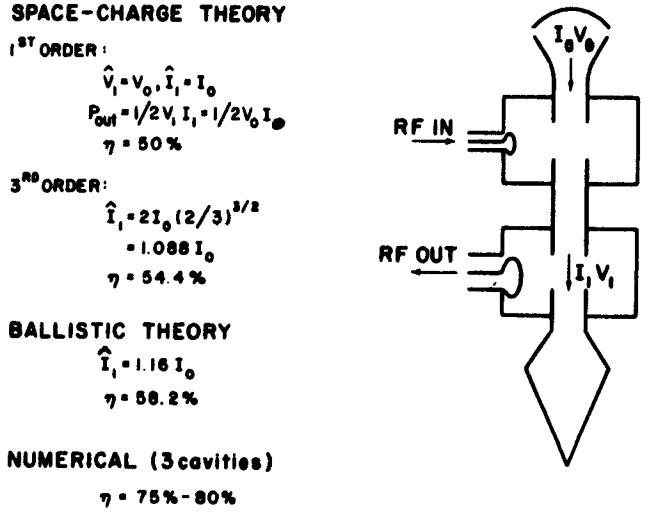

Fig. 1. Theoretical efficiency of multicavity klystron.

For a beam with input DC power given by I_0V_0, the RF output power is given by I_1V_1 . . . , where I_1 is the fundamental component of the RF current in the bunched beam and V_1 is the corresponding RF voltage developed across the output gap. The peak value of the RF voltage $\hat{V}_1$ cannot exceed the beam voltage V_0 very much; otherwise electrons will turn back towards the cathode. The peak value of the RF current $\hat{I}_1$, on the other hand, is determined by the bunching mechanism. Various theories predict different values for I_1. For instance, in the first-order space-charge theory all the quantities are assumed to be sinusoidal. Thus $\hat{I}_1$ will be equal to I_0, and the maximum efficiency is only 50 percent. Using third-order approximation in the space-charge theory,[1] we find that the maximum efficiency is about 54.4 percent. On the other hand, if we use the simple ballistic theory, where all the space-charge forces are neglected, we find that the maximum efficiency is about 58.2 percent.[2]

These values were derived for klystrons having two cavities with

infinitesimal gaps. For three-cavity klystrons the previous values will still apply if the three cavities are synchronously tuned and have high gain. But if the second cavity is tuned to a higher frequency, the current modulation from the first and second cavities will be more in phase-addition rather than in phase-quadrature, and higher efficiencies can be expected. Numerical calculations show that under ideal conditions the theoretical efficiency of multicavity klystrons can be as high as 75 to 80 percent.[3]

In practice, efficiencies as high as 60 percent have been achieved with conventional design, but the majority of commercial klystrons still have much lower efficiencies of 30 to 40 percent.

From this brief review of klystron efficiency we come to the following conclusions:

(1). There is a large gap between the experimental efficiencies and the efficiencies predicted by the approximate theories, and it is desirable to narrow this gap.

(2). The maximum theoretical efficiency of multicavity klystrons under ideal conditions is less than 80 percent. Therefore, if we are aiming at a practical efficiency of 80 percent or more, a nonconventional design should be sought.

The various attempts to improve klystron efficiency follow two main lines of research. In the first, the efforts are toward improving the bunching mechanism, for instance by devising RF structures other than the simple resonant gaps. In the second, it is assumed that the klystron bunching mechanism is fundamentally inefficient and the aim is to recover the energy from the spent beam before it is dissipated as heat in the collector.

At Lincoln Laboratory we are taking both approaches because we feel that, even with very good bunching, it would be necessary to recover the energy from the spent beam in order to achieve very high efficiency over a wide frequency band. However the techniques we are using in both cases are somewhat different from those used previously. In this paper we describe some of our efforts to recover energy from the spent beam.

The method used previously for recovering energy from the spent beam is known as "depressed collector." In this method, the energy is recovered in DC form and fed back to the DC input. Unfortunately, the success of this method at present is rather limited and does not seem to justify the complications added to the collector and modulator. In the method we are using, the energy from the spent beam is recovered directly in the form of RF energy, and the isolation between the DC input and DC output is maintained. This is achieved by applying accelerating DC potential across the output gap.

II. Biased Output-Gap

As mentioned before, the maximum RF power available from the klystron is limited by the maximum RF voltage, which can be developed across the output gap without turning back too many electrons. Therefore, if we apply an accelerating DC potential across the output gap we should expect an increase in the available RF power. Consequently our first task

was to find experimentally the relation between the gap voltage and the available output power.

The vehicle we used for this experiment is a commercial 2-kw CW klystron amplifier.* It has a floating collector and four external cavities. The efficiency of this tube is relatively high (40 to 55 percent). We redesigned the output cavity so that we could apply a DC potential across the output gap. Figure 2 shows the output power P_{rf} vs the bias voltage V_b plotted for different beam voltages V_o.

The output power was optimized at zero bias voltage each time the beam voltage was changed. The bias voltage was then increased, and without changing any of the other tube variables the output power increased as shown by the points on the solid lines. Naturally, as we increased the bias voltage we expected the beam impedance to increase also. Therefore, for maximum output power, we had to increase the load impedance to match the new beam impedance. This we achieved by reducing the output coupling. The output power after the impedance matching was always found to be the available RF power. In other words, except for the tuning of the output cavity, which had to be adjusted very slightly, all the other tube variables were still optimum. The available power is shown in Fig. 2 by the circular points which lie approximately on the dotted straight lines, giving the simple experimental relation between the available power and bias voltage as

$$P_{av} = I_1 (V_o + V_b)$$

where P_{av} = the available RF power, I_1 = a constant proportional to the fundamental component of the RF beam current, V_o = beam voltage, and V_b = bias voltage.

Actually, this simple relation might have been expected from this type of klystron because the gap transit angle was relatively small. (The maximum change in the coupling coefficient was less than 3 percent.) The difference between the solid and dotted lines represents the mismatch due to the change in the beam impedance.

An important point worthy of mention concerning this experiment has to do with the beam transmission. At full drive power, the beam transmission at zero bias voltage was about 94.5 percent. As the bias voltage was increased, we noticed that the beam transmission also increased; and at full bias voltage, the beam transmission was over 99 percent. This shows that most of the beam body interception at full drive power takes place near the edges of the output gap. Such a result also might have been expected because of the strong retarding RF field at the output gap.

Returning to the efficiency, we found that the RF output power increased directly in proportion to the ratio of the bias voltage divided by the beam voltage -- V_b / V_o; and since the beam transmission was almost 100 percent, the DC power input increased correspondingly in proportion to V_b / V_o. Therefore, the total tube efficiency remained unchanged. In order to recover the energy from the spent beam and thus increase the

*Eimac 4 KM3000LR

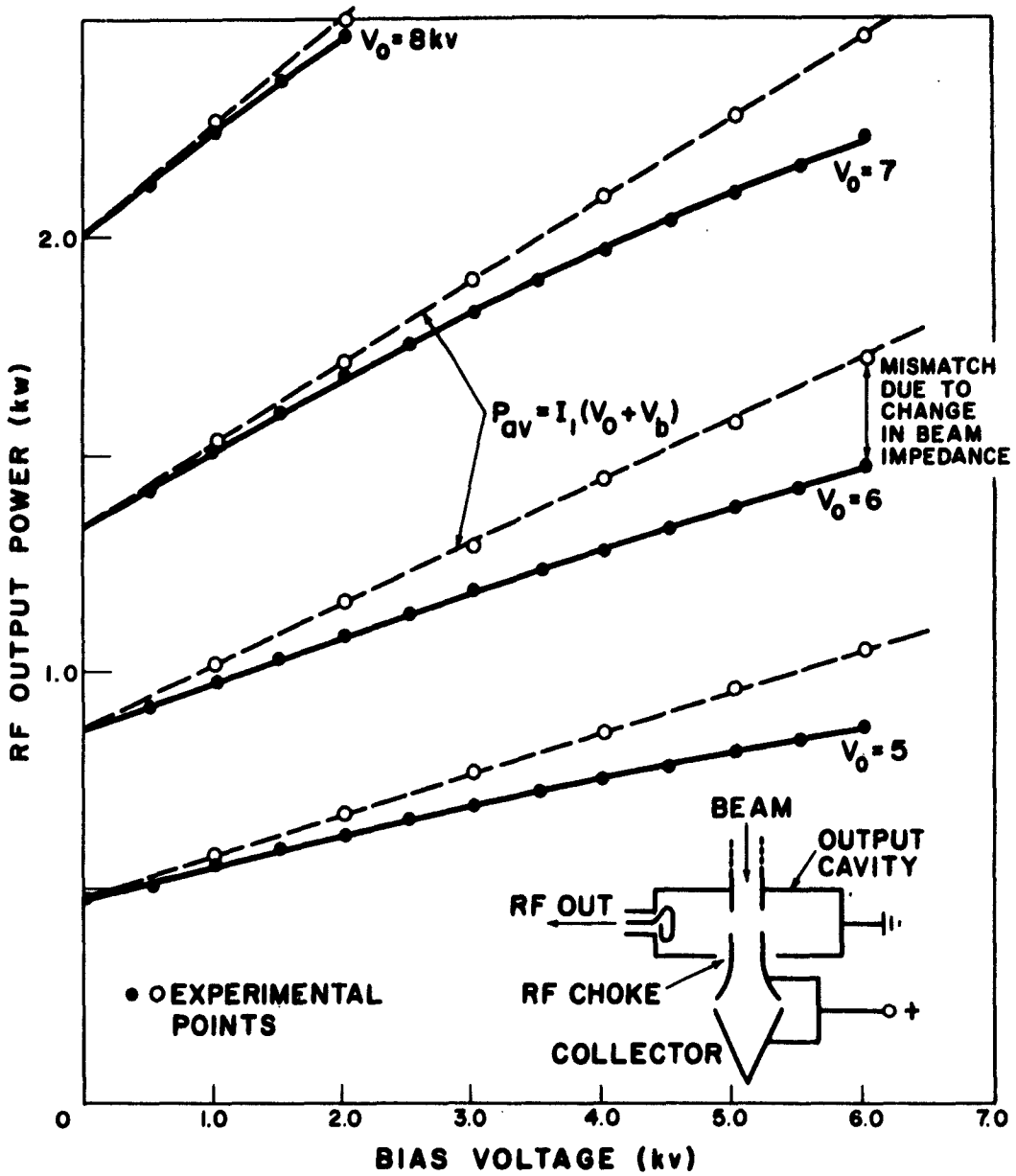

Fig. 2. Output power of biased-gap klystron

tube efficiency, we could simply depress the collector to a ground potential as shown in Fig. 3. The beam current would then divide between the

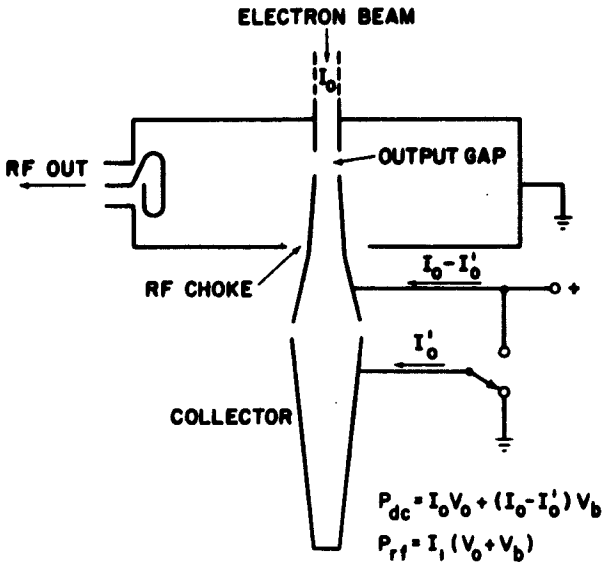

Fig. 3. Biased-gap depressed-collector klystron.

collector and the accelerating electrode. However, should we operate a collector at a depressed potential, we would have to satisfy two requirements for proper operation. First, the retarded electrons should have no adverse effect upon the RF characteristics. Second, the electrons should be collected with minimum kinetic energy.

Judging from previous work on the depressed collector, particularly at Varian,[4] the first requirement seems to be easily satisfied by using a flycatcher design and by properly shielding the collection region from the magnetic focusing field. The second requirement depends on the velocity distribution in the spent beam and is a matter of compromise between the complexity in collector design and the desired increase in efficiency. Experience has shown, moreover, that a collector with at least two segments is necessary for efficient operation. The collector of the tube we used in the first experiment was not designed for depressed operation and, as Fig. 4 indicates, the two requirements were far from being satisfied. In fact, the axial component of the magnetic field extends right through the collection region. This axial magnetic field tends to focus the returned electrons back to the RF interaction region, and can bring about spurious oscillations.

However, before trying to modify the collector, we ran some tests on the tube with the collector grounded, and it was rather surprising to

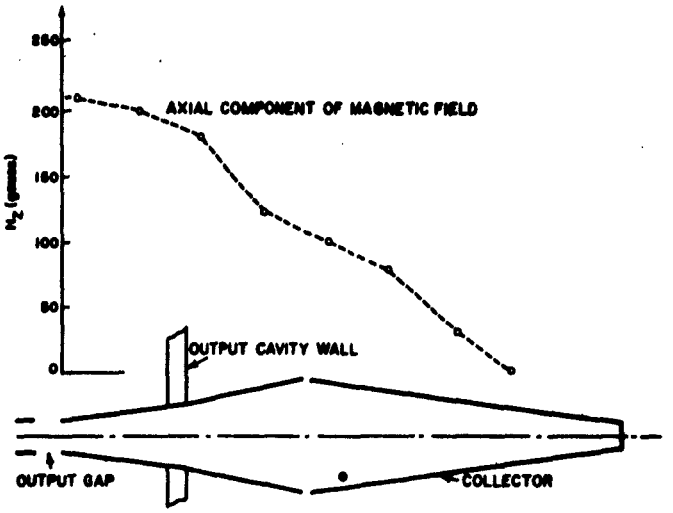

Fig. 4. Axial magnetic field in the collector region.

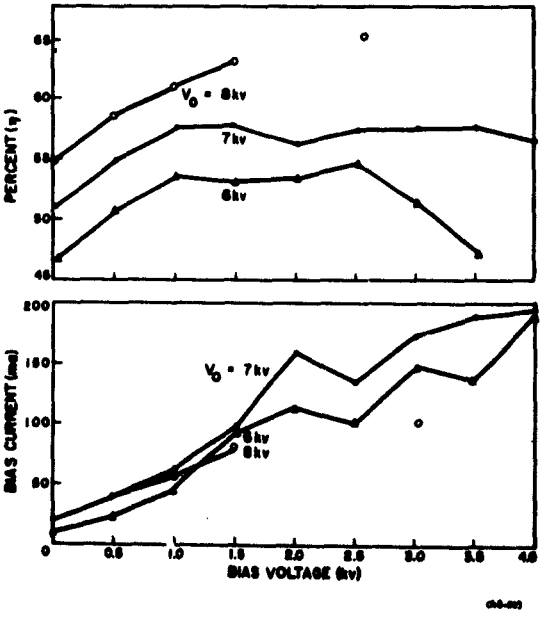

Fig. 5. Efficiency of biased-gap depressed-collector klystron.

find that it was possible to increase the efficiency of the tube sometimes by as much as 10 percent. Figure 5 shows the results of some of these tests. It shows at the top a plot of efficiency vs bias voltage for different values of beam voltage, and at the bottom, a plot of bias current vs bias voltage. For bias voltages up to 15 percent of the beam voltage, the output power increases in almost the same way as in the case of the nondepressed collector. But when the bias voltage is further increased, it becomes somewhat difficult to optimize the output power and the magnetic field adjustments become critical. The highest efficiency achieved was by 65 percent. However, the results shown are by no means optimum, and after modifying the collector we hope to increase the efficiency to 70 or 75 percent.

III. Conclusion

Besides the increase in klystron efficiency, the biased-gap method offers other advantages. (1) The focusing action of the DC field reduces the beam interception where it is most serious -- at the output gap. (2) The electric force acting on the electrons at the output gap has different values in each direction, reducing the possibility of multipactor at the output gap. (3) The accelerating DC potential in the gaps increases the directivity of the beam, and thus improves stability. (4) The biased-gap method promises to be useful in the evaluation and studies of various klystron parameters. (5) Finally, the technique may be used for automatic phase and gain control.

The main limitation on the biased-gap technique seems to be the voltage hold-off capability of the RF choke for very high power. However, we do not believe this to be a serious obstacle.

BIBLIOGRAPHY

1. Paschke, F., "Nonlinear Theory of a Velocity-Modulated Electron Beam with Finite Diameter," RCA Rev. 21, 53 (March 1960).

2. Hamilton, Knipp and Kuper, "Klystrons and Microwave Triodes," Radiation Lab. Series, McGraw-Hill Co. (1948) 7, 209.

3. Webber, S. E., "Large Signal Analysis of Multicavity Klystron" Trans. IRE PGED ED-5, 306 (October 1958).

4. McCune, E., "Depressed Collector Klystron (VA-843) Development Program," Final Report, Varian Associates (March 1961).

THE ELECTROMAGNETIC AMPLIFYING LENS; PROGRESS AND POTENTIALITIES

By

W. C. Brown

Raytheon Company

Significant advances in obtaining greater amounts of power output from conventional approaches to microwave tube design have been made by taking advantage of higher beam perveance, better beam containment, higher efficiency, better cooling techniques, and the like. In the case of the Amplitron, for example, it has been possible to increase the power-handling capability of the continuous-cathode, crossed-field device by one to two orders of magnitude by taking advantage of the inherently high efficiency of the device and greatly improved cooling techniques.

However, as the desired power levels are further increased, two limitations of conventional tube approaches become apparent. One of these is the difficulty of handling high average and peak power levels in conventional waveguide feeds and in conventional vacuum windows. The second limitation in the conventional tube approach is in the small electronic interaction area which presents an upper limit to the amount of power that can be handled in the interaction region. It is likely that if super tube development is to be carried further, we will have to look for new approaches which will adequately handle the high rf power levels at the terminals of the tube and provide greatly enlarged interaction areas.

Consider the problem of handling the power at the input and output of the device. If we avoid the influence of contemporary tube design and think in more basic terms, we note that the ideal situation would be to amplify the free space wave directly as shown in Figure 1, without channeling it first into a conventional waveguide.

A passive device analogous to the active device shown in Figure 1, is the microwave lens. In one form of microwave lens, shown in Figure 2, the free space wave impinging upon the input face of the structure is split and channeled between a number of parallel plates and processed in such a manner as to change the shape of the wave front. The microwave lens concept in which the input wave is fed into a multiplicity of waveguides suggests a similar device for processing a free space wave in such a manner as to provide gain. In this form, such a device could be accurately described as an "Electromagnetic Amplifying Lens".

The symmetry of the situation shown in Figure 1 suggests that the phase front of the wave being amplified be everywhere normal to the axis of the tube. However,

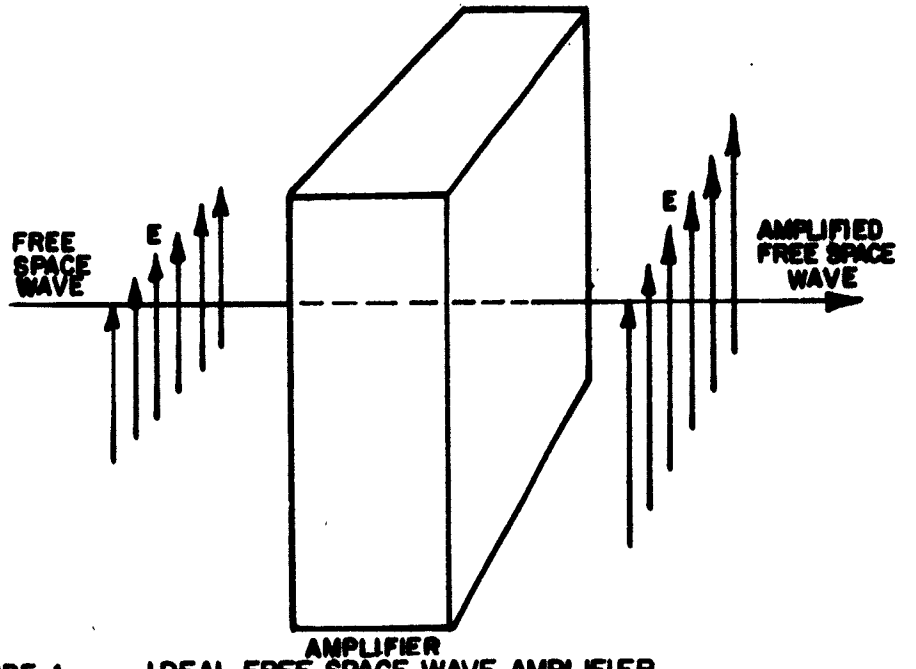

FIGURE 1 IDEAL FREE SPACE WAVE AMPLIFIER

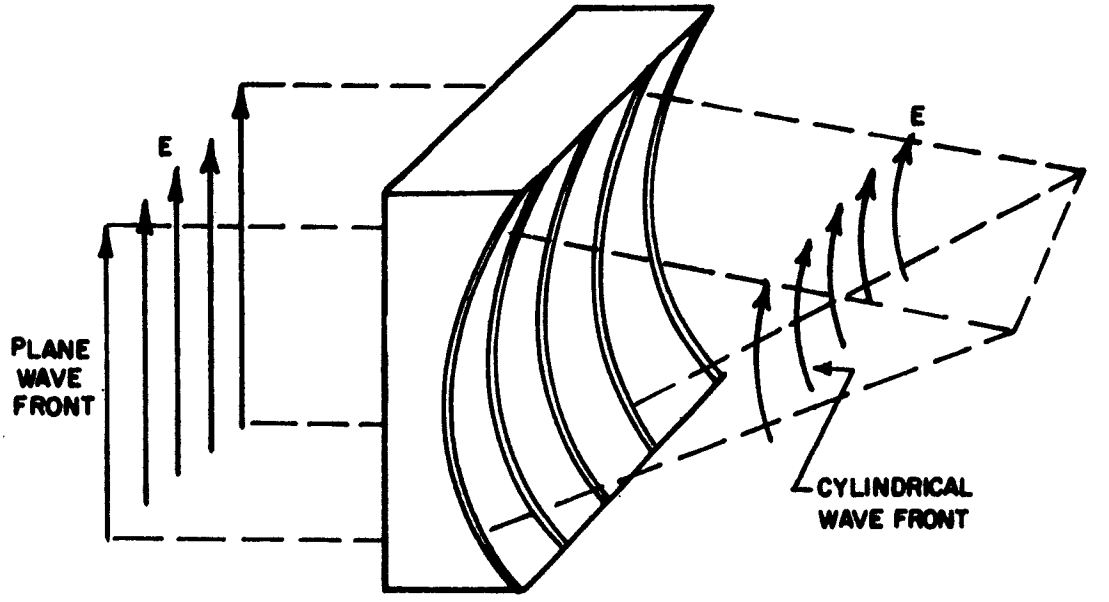

MICROWAVE LENS PROCESSING
OF FREE SPACE WAVES

FIGURE 2

an efficient electronic interaction mechanism and a low operating potential are desired. These requirements suggest the equivalent of a slow-wave structure in the interaction area. On the other hand, we would like an interaction structure of sufficient generality to be suitable for handling very high frequencies, if necessary, and this suggests a clean waveguide-like structure unencumbered with straps or interdigital fingers. Such clean structures usually propagate fast waves only.

This seeming contradiction in requirements can be resolved by employing fast wave propagation of the signal through the lens while arranging for the signal to interact with an electron stream whose transverse movement with respect to the direction of propagation is established by crossed dc electric and dc magnetic fields. It then becomes necessary that the input wave be processed in such a manner as to make possible the transverse slow-wave interaction between the electron stream and the rf wave.

In the EAL concept, this processing is accomplished, as shown in Figure 3, by the use of a large number of waveguides which are symmetrically arranged with respect to the free space wave excitation and so are excited with equal amplitude and phase; however, in the transition region between the input face of the tube and the electronic interaction region, adjacent waveguides are dimensioned to have different phase velocities so that the energy in adjacent waveguides arrives at the input to the interaction region 180^{o} out of phase.

In the interaction region, the use of half-width waveguides establishes electric fields at the edges of the waveguides which face the cathode. A rotating space charge interacts with these fields. The half-width waveguides serve the same function as vanes in a conventional magnetron and the analogy is further strengthened in that the potentials on adjacent vane tips in a plane normal to the axis of the tube are 180^{o} out of phase as they are in the conventional pi-mode magnetron.

Some explanation of the interaction between the fast moving waves in the axial direction with the slow moving electrons in the transverse direction is necessary to complete a qualitative introduction to the EAL concept. The shape of the space charge in the interaction area is much like that of a large revolving helical gear. The rf energy, which is introduced at the input, phase focuses the electronic space charge into spokes which interact with the rf wave in such a manner as to convert the potential energy of the electrons directly into rf energy--in exactly the same manner in which the magnetron or Amplitron operates. Because of the helical nature of the space charge spoke configuration, the traveling rf wave and rotating space charge spokes keep in synchronism as the wave travels along the structure. The interaction between the space charge and the rf circuit is shown in Figure 4. It is interesting to note that the interaction mechanism works equally well whether the tube is initially excited at the input or output by an rf signal. However, once the space charge spokes and the proper direction of spiral of the space charge cloud is established by the introduction of rf, the induced currents tend to add in phase in the output direction, and tend to cancel towards the input direction, providing directional gain. A quantitative analysis of the interaction and gain mechanism has been made.[1]

1 Analysis of a New Crossed-Field Amplifier, The "EAL", or Electromagnetic Amplifying Lens - by W. C. Brown and G. E. Dombrowski - IRE Transactions - Vol. ED-9, No. 2, March 1962

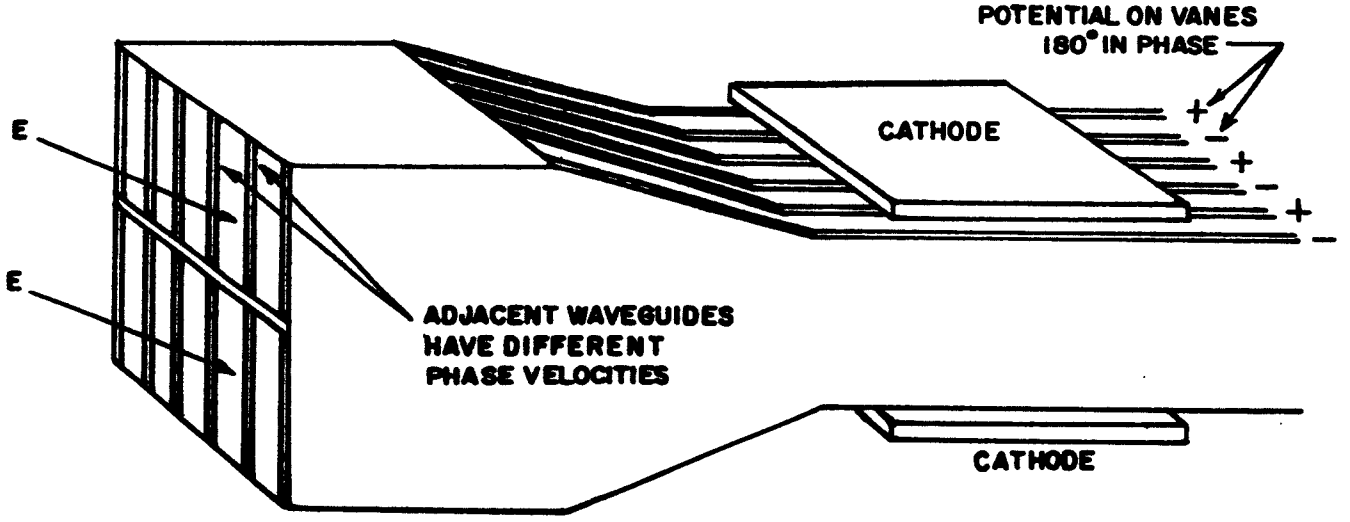

PROCESSING OF FREE SPACE WAVE FOR
SLOWWAVE ELECTRONIC INTERACTION

FIGURE 3

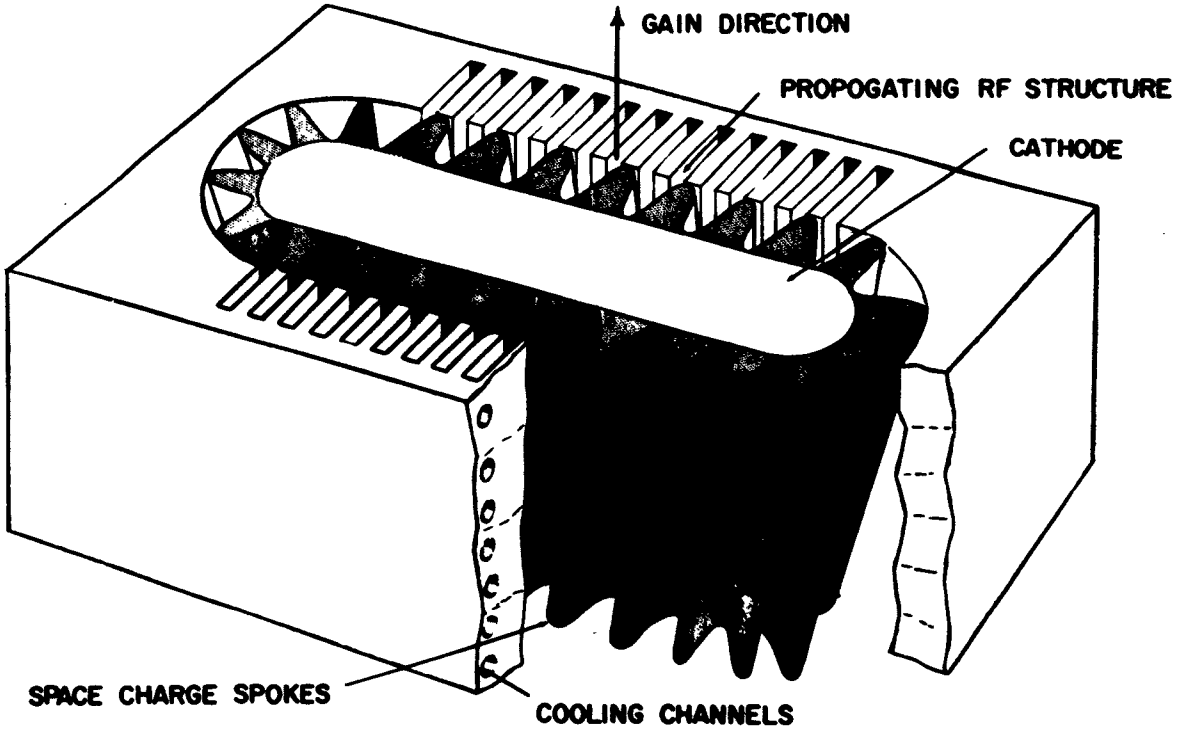

CROSS SECTION OF EAL INTERACTION AREA

FIGURE 4

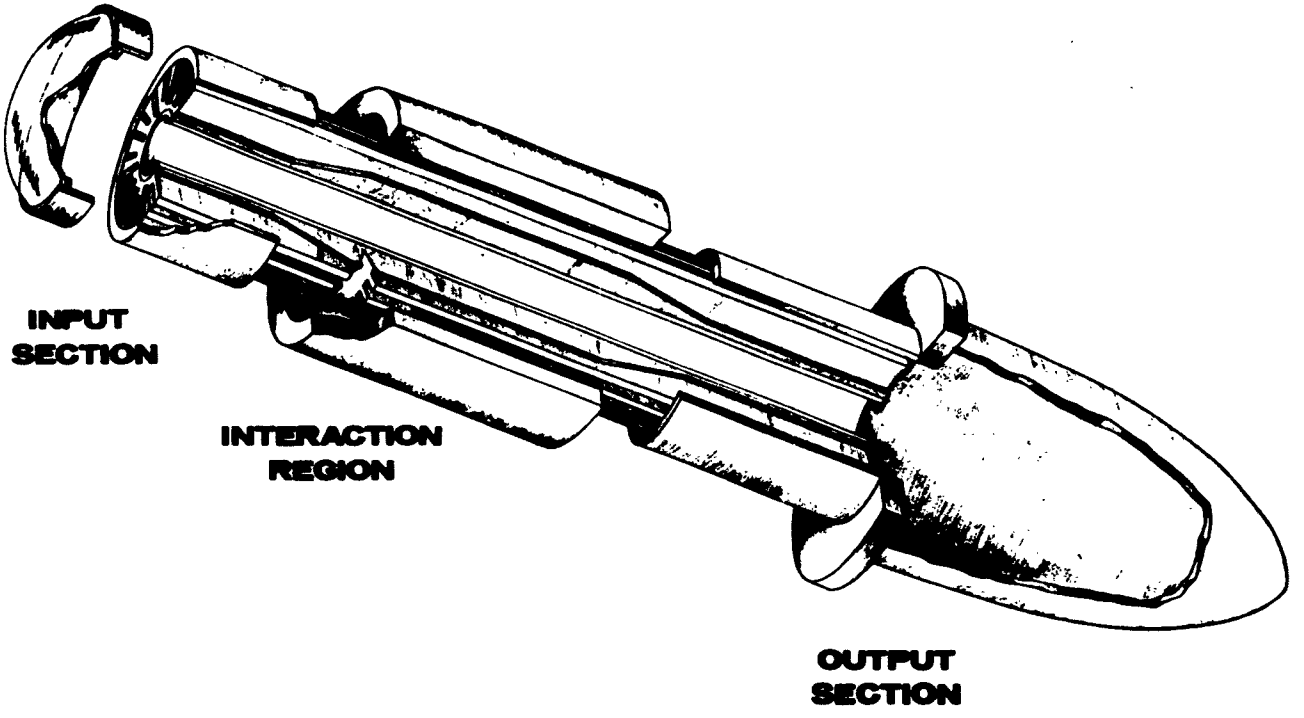

SCHEMATIC OF EAL WITH CYLINDRICAL GEOMETRY

FIGURE 5

At this point, we would like to report on the progress that has been made toward reducing the EAL concept to hardware and experimental evaluation. Because of the importance of evaluating the quasi-optical method of handling the power at the input and the output feeds, it was found desirable to build a tube of substantial size relative to one free space wavelength. Since such structures are physically very large in the L- and S-band regions, it seemed advisable to do the initial evaluation work in the X-band region. It also seemed desirable for construction reasons to use a geometry possessing cylindrical symmetry. The resulting schematic for such a device is shown in Figure 5; the actual device in cold-test status is shown in Figure 6. A flat window will be used on the input of the device and an ogival shaped radome on the output of the device. Otherwise, the input and the output structures are identical. There are 220 separate waveguides which are symmetrically excited by means of a TE_{01} coaxial line mode, which is simply obtained from a TE_{01} mode in a hollow waveguide. A triangular wedge is inserted in alternate waveguides which decreases the phase shift relative to that in the adjacent guides. As waves in adjacent waveguides emerge from the full-width guide, they are 180° out of phase. There is a broadband matching section between the full-width and half-width guides.

Although this is the first cold test model of an EAL tube, the cold test results approximate closely those characteristics which are desired. Figure 7 shows a cross-section of the field pattern of the energy radiated at the output end. As expected, it is doughnut-shaped and well defined demonstrating that the integrity of the phase front of the wave at the input is maintained as it emerges from the output.

The attenuation through the device has been measured at 9,000 mcs/sec. which is near the center of the intended operating frequency range. The measured attenuation was 1.01 db. The calculated attenuation assuming only I^2R losses was .48 db. The circuit losses in an amplifier having appreciable gain would be important only in the output half of the interaction area section and in the output transition section. Circuit efficiencies based on this assumption are 89% and 94% for the measured and calculated attenuations of 1.01 and .48 db respectively for the complete tube.

Figure 8 shows the field patterns in the interaction area obtained by a balanced dipole probe. Although there are some irregularities, it should be noted that the field pattern compares very favorably with field patterns that have been taken in efficient and well behaved magnetrons.

The three-dimensional ω-β diagram for the interaction region of this tube is shown in Figure 9. In the circumferential propagating direction designated as plane β_θ of Figure 9, the situation is identical to that of an unstrapped magnetron with the cathode surface behaving as one side of a transmission line. This configuration results in characteristics which are those of a low pass filter with an upper cutoff frequency of approximately 5600 megacycles. 5600 megacycles is also the low cutoff frequency of the purely axial mode system. The operating frequency is much above this at 9000 megacycles, providing an opportunity to selectively load the system near the cutoff region, thereby discouraging unwanted oscillation in this region. It should be pointed out that the most likely defect in the EAL device will be its tendency to oscillate in unwanted modes, and the success or failure of the device may well rest

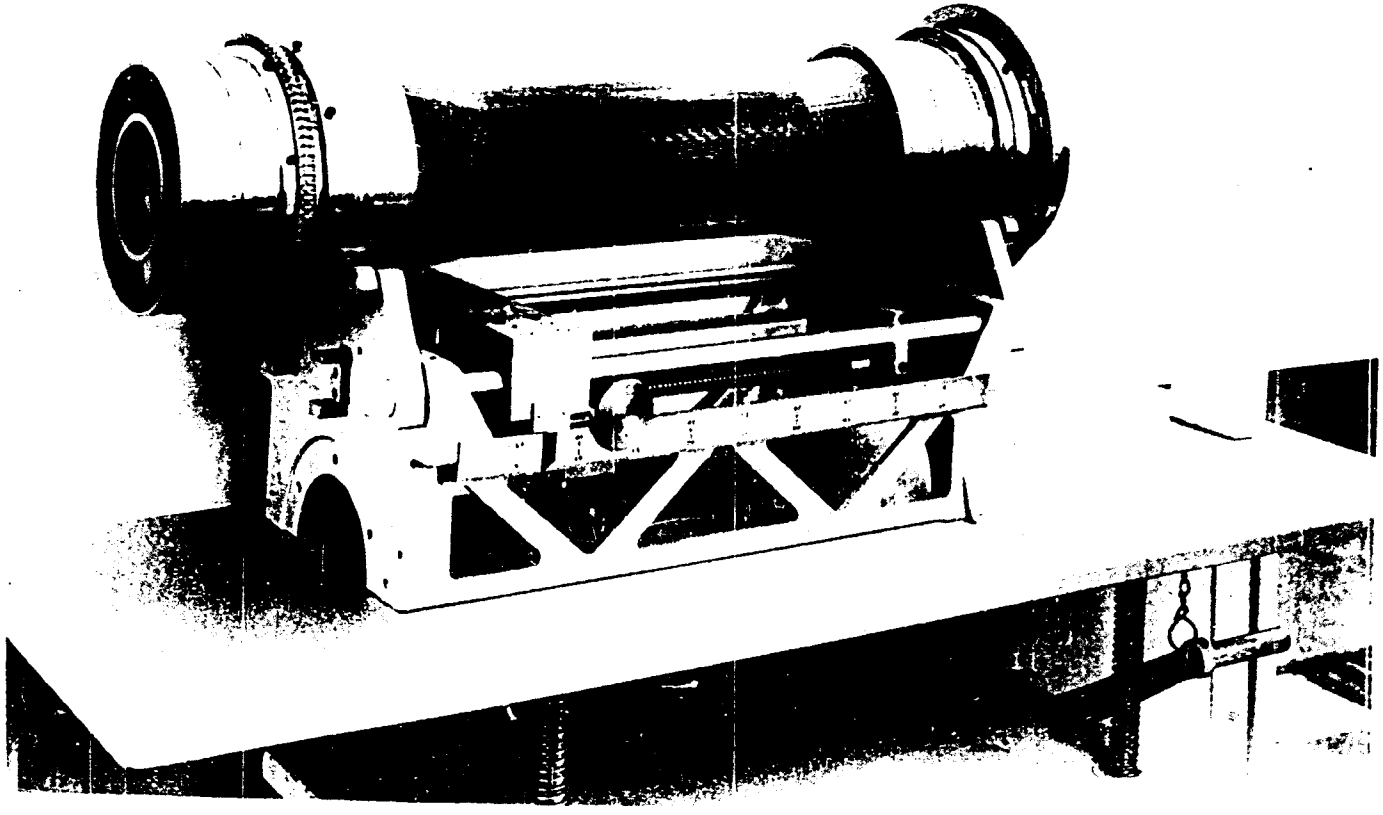

CYLINDRICAL X BAND "E A L" MODEL
IN COLD TEST

FIGURE 6

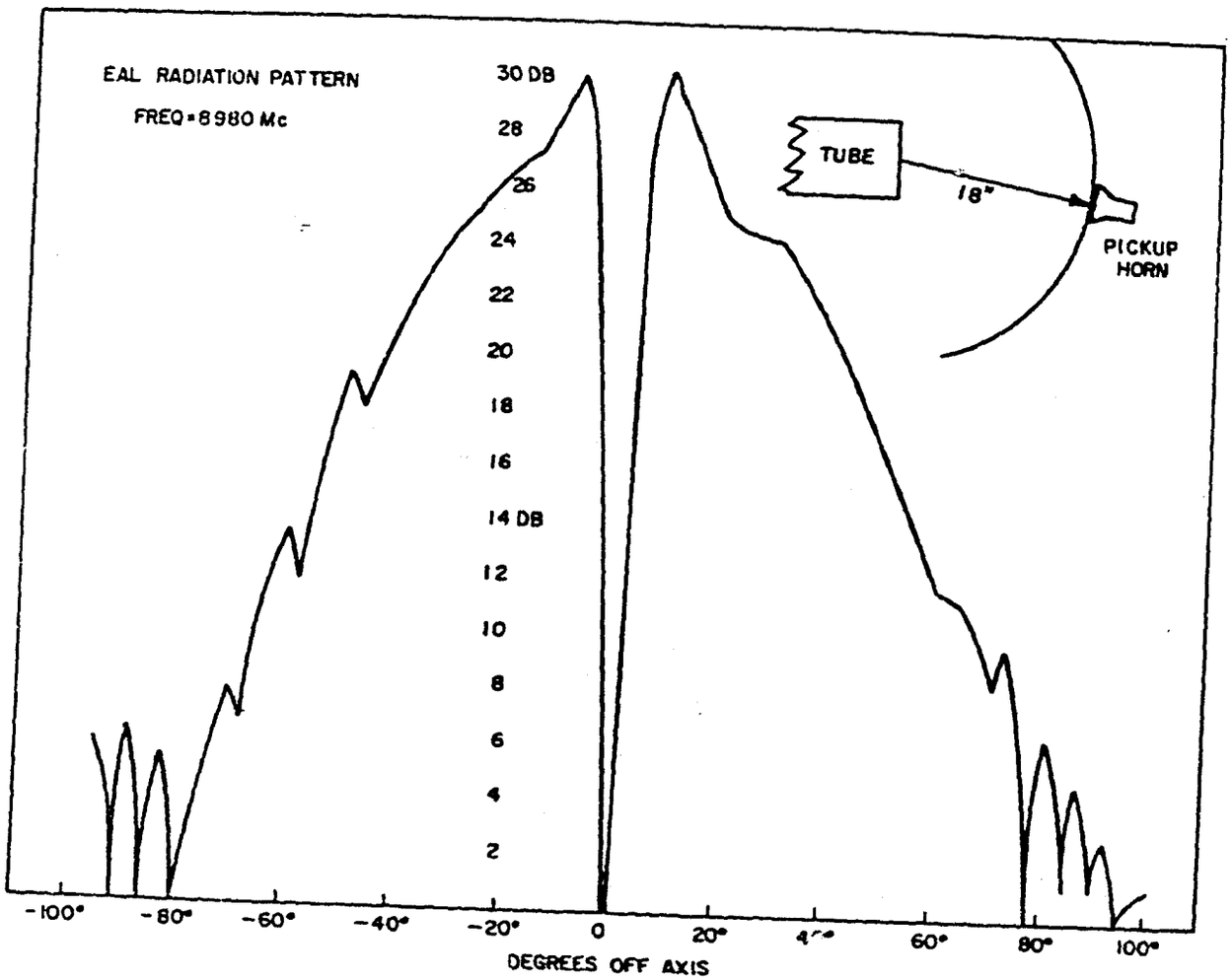

FIELD PATTERN OF RADIATED ENERGY
AT OUTPUT OF EAL TUBE SHOWN IN FIG. 6

FIGURE 7

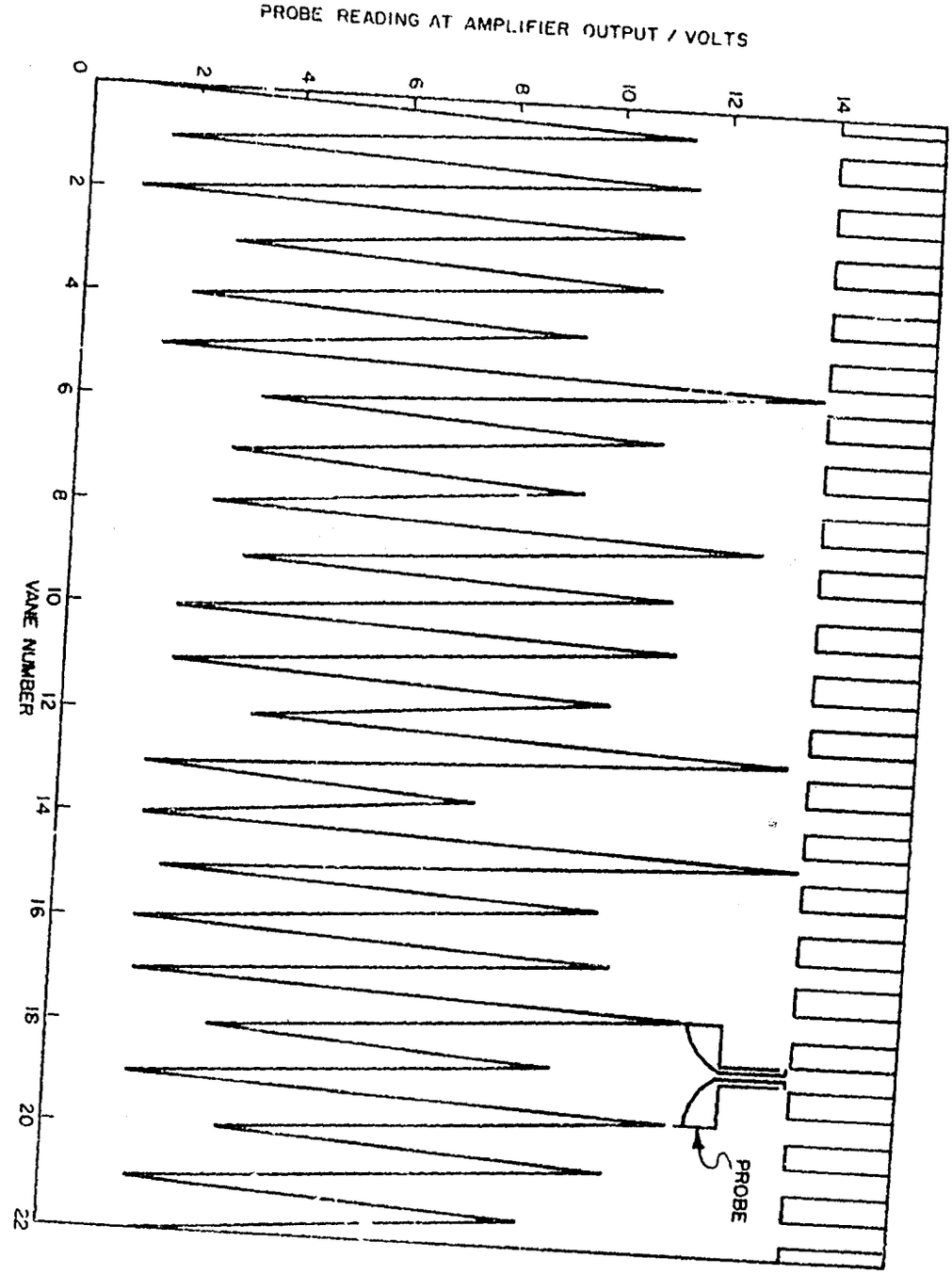

TYPICAL FIELD PATTERN IN INTERACTION AREA OBTAINED BY A BALANCED DIPOLE PROBE

FIGURE 8

upon the ability to control these modes. In this respect, it is noted that the use of a multiplicity of symmetrically excited waveguides provides an opportunity for novel methods of mode control.

The expected electrical performance characteristics of the particular EAL design shown in Figure 6 are shown in Figure 10. It will be noted that this device operates at low voltages but very high current levels. The I_0 for this particular design is 7,900 amperes. If it is assumed that the tube will operate at I_0, an operating value consistent with analogous magnetron and Amplitron operation, we find a total input power at 25 kilovolts of 197 megawatts. The corresponding input impedance is 3.2 ohms. The corresponding microperveance is 2000. At 60% efficiency, the peak power output would be 117 megawatts. There is sufficient anode dissipation represented by the 450 square centimeters of vane tip area to allow a pulse duration of 28 microseconds at this rf output level--assuming a ratio of peak dissipation to average dissipation density of two, and a maximum vane tip temperature rise of 500°C.

The average power-handling capability of such a device, when outfitted with advanced cooling techniques is very large. Five kilowatts per square centimeter is a conservative dissipation density. With a ratio of peak to average dissipation density of two, there would be a total anode dissipation of 1.12 megawatts for the 450 sq. cm anode. A corresponding average rf output, assuming 60% efficiency would be 1.7 megawatts. If the average dissipation density is raised to five kilowatts/sq. cm., an apparently feasible value based upon data reported on by Mr. Zettler, elsewhere in these proceedings, and an efficiency of 67% is assumed, the average rf output would be 4.5 megawatts.

Figure 11 gives the predicted gain[1] for a tube with $\alpha = 0.02$ as a function of interaction area length. The radian distance traversed, θ, is measured in terms of the interference wave number, 2β, of the cold waveguide. $\theta = 4\pi \ell / \lambda_g$ where λ_g is the cold wavelength in the guide, and ℓ is the interaction-area length. A stable gain of 20 db is predicted.

It is intended to operate the first hot test model of this tube with a cold platinum cathode. Mr. Zettler, elsewhere in these proceedings, describes an experiment in which a water-cooled platinum cathode was used with success in a high power CW Amplitron. It was found that the tube would draw no current with the application of proper anode potential and magnetic field, but that current would immediately flow upon the application of rf drive power. In the EAL device, the use of a cold platinum cathode will greatly simplify the construction of the device. Platinum was chosen as a material because it has the highest secondary emission ratio of any of the pure metals. The use of platinum should also give indefinitely long cathode life.

The electrical and mechanical design features of the EAL device are of special interest for high power millimeter wave tubes. In the millimeter region, a large interaction area and high emission current density from the cathode are mandatory. A cathode in a crossed-field device has an almost unlimited emission density because of the secondary emission phenomena which is the dominant emission mechanism. The anode dissipation capability of an EAL tube in the 4 MM region is about 3

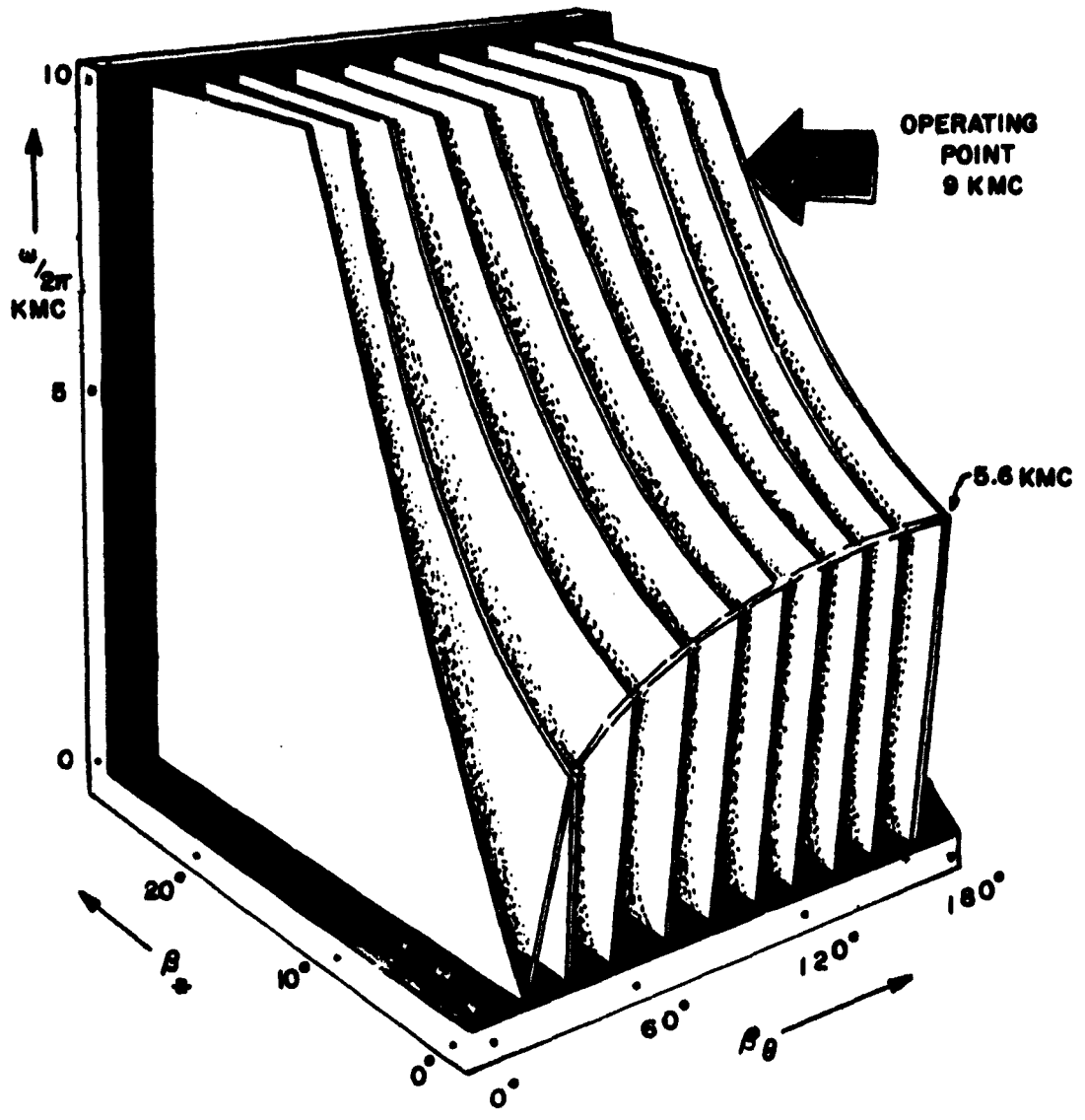

THREE DIMENSIONAL $\omega\beta$ DIAGRAM FOR THE INTERACTION AREA OF THE "E A L" DIVICE

FIGURE 9

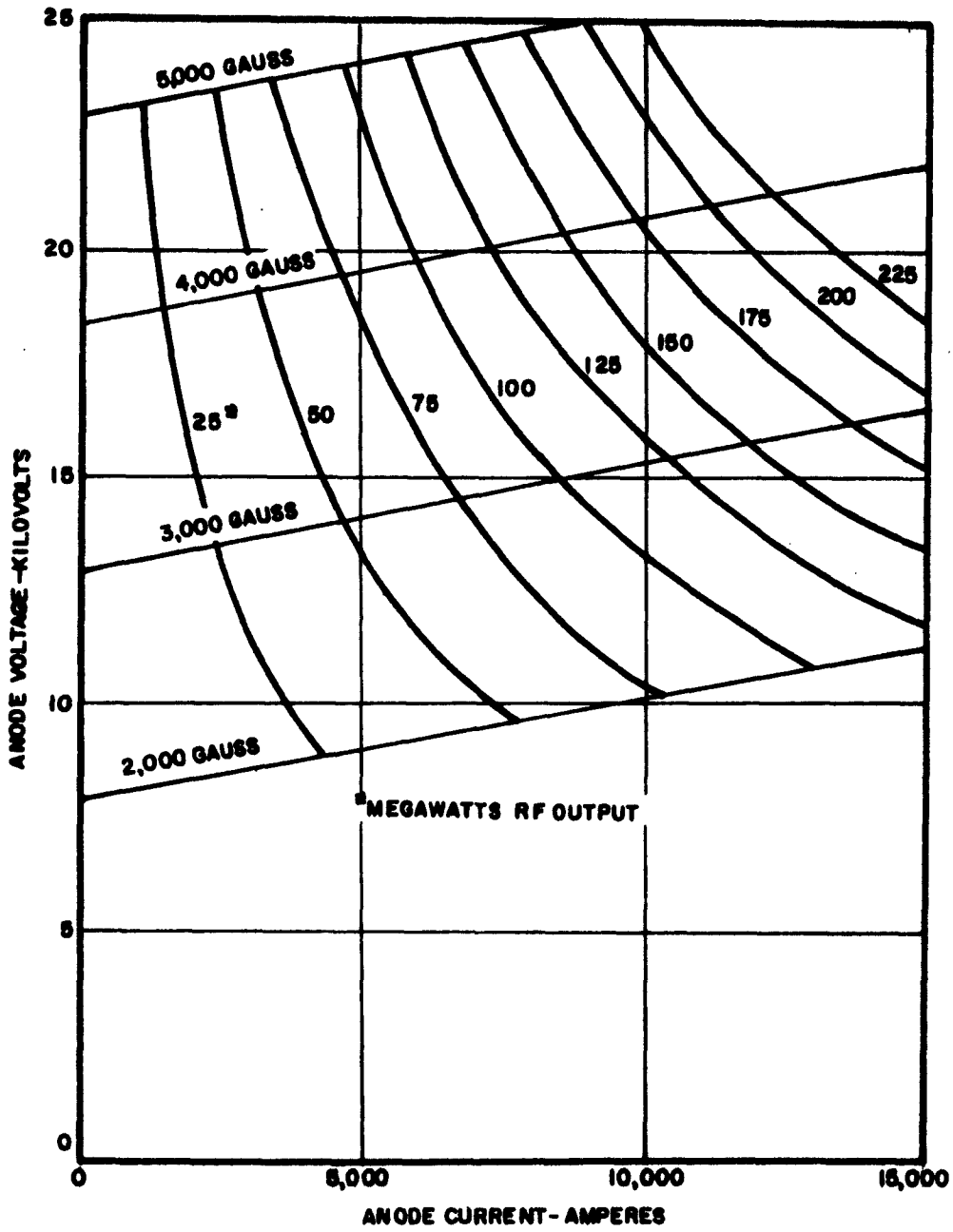

THEORETICAL PULSED PERFORMANCE CHARACTERISTICS
OF "EAL" DEVICE SHOWN IN FIGURE 6

FIGURE 10

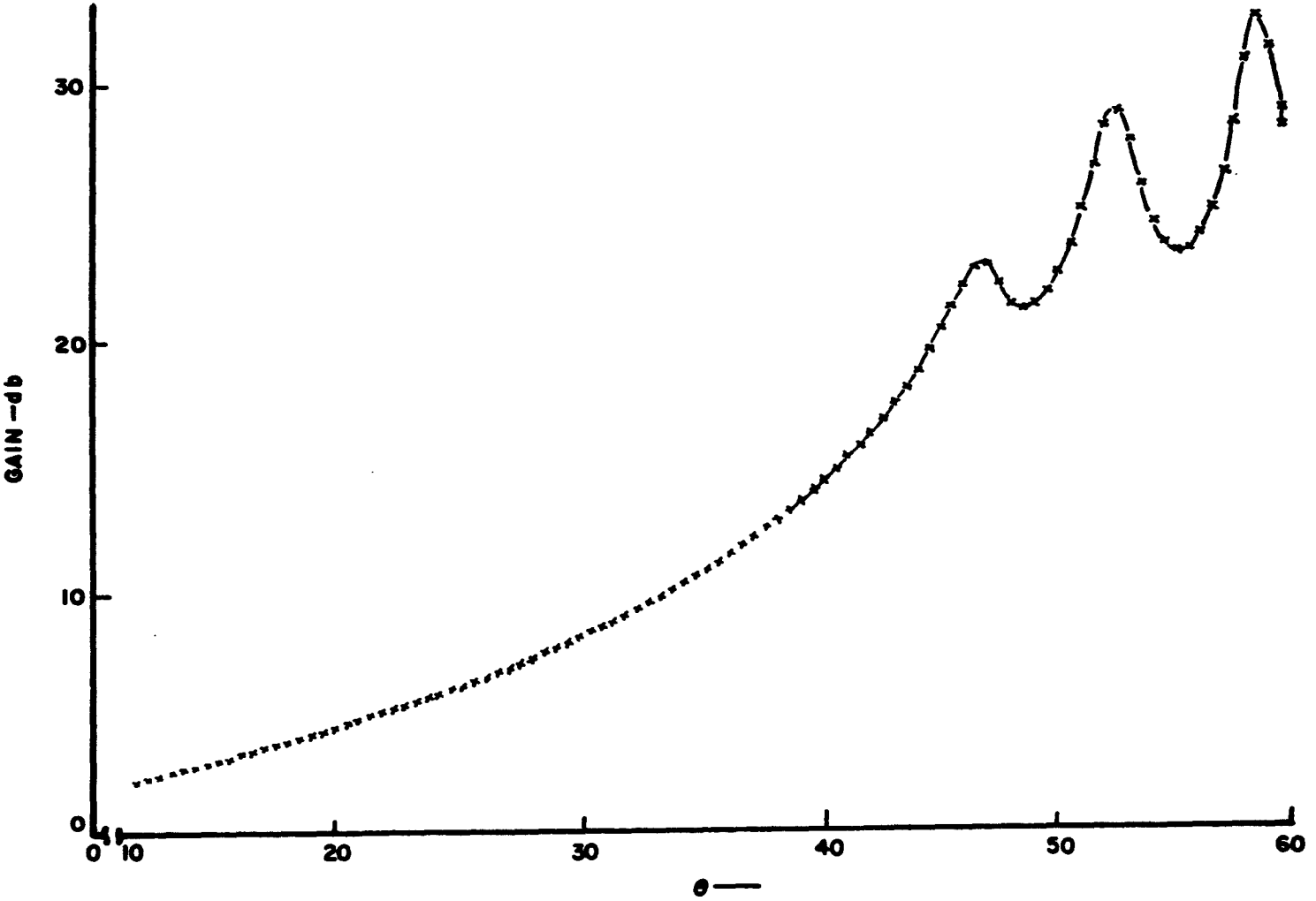

FIGURE 11 "EAL" FORWARD POWER GAIN $\lambda = 0.02$

kilowatts per square centimeter. This results from the fact that as shown in Figure 12, the transmission path from the tips of the vanes to the water cooling channels at the base of the vanes is comparatively short.

A proposed 4 MM tube is shown in Figure 13. This tube can be made to the necessary mechanical tolerances by means of available machining and assembly techniques. The total anode area of this tube is approximately 49 square centimeters. If a temperature drop of 300°C between the vane tips and the water cooling channels is permitted, then 3.9 kilowatts of heat would be removed for each square centimeter of anode area. After making allowances for the ratio of peak to average dissipation density of two to one, the total effective dissipation is 96 kilowatts. If an electronic efficiency of 60% is assumed, a value consistent with the high magnetic field that will be used, a total of 144 kilowatts would be generated.

Circuit losses cannot be neglected in this type of structure and they compute to be 7% in the interaction region plus another 8% in the 2 cm long phase conversion section at the output. It is estimated that the circuit efficiency of the amplifier would be approximately 85% bringing the total power output down to 120 kilowatts. The EAL design approach to high average power in the millimeter region is most effective because there is adequate room at the base of the vanes to employ water cooling channels to take care of the dissipated heat. The advantage of this feature is shown in Figure 14 where the EAL construction principle utilizing a multiplicity of waveguides is compared with a tube design with a single cylindrical waveguide operating in the TE_{01} mode at the core of the tube.

In conclusion, it may be stated that the desirable features of the EAL device as an approach to very large amounts of power in the microwave and millimeter regions, are (1) the handling of the energy at the input and the output of the device in a quasi-optical fashion, (2) the very large interaction areas which are made available, (3) the clean mechanical construction which makes it possible to extend the design into the millimeter region, (4) the use of a water cooled metallic cathode, and (5) the high efficiency of crossed-field interaction. The control of modes in the device is likely to constitute a major problem. The development of the EAL device has been successfully carried through the cold test stage.

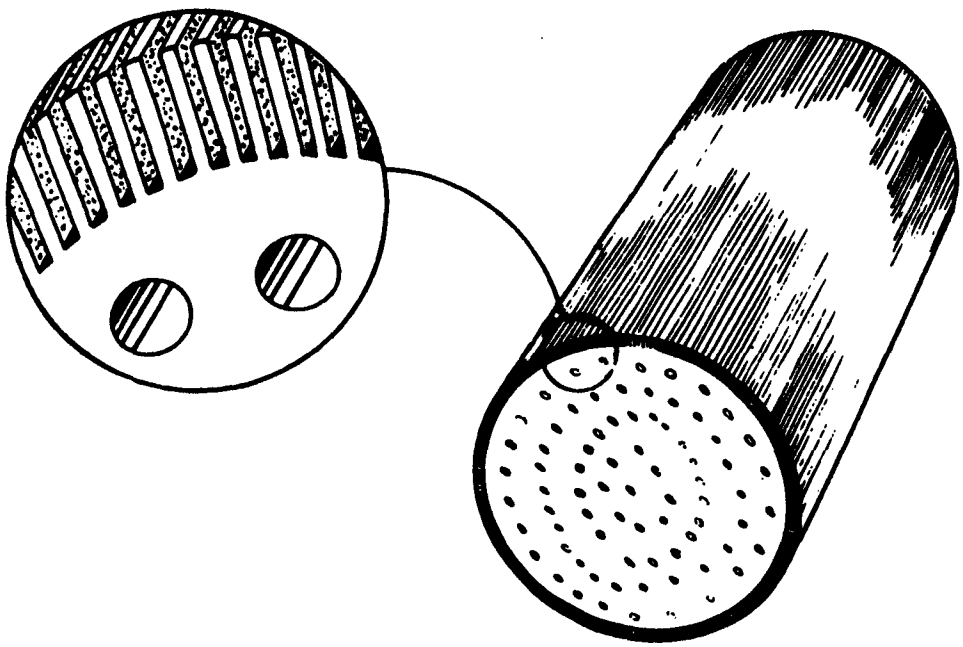

CROSS-SECTION OF ANODE AND RF
STRUCTURE SHOWING COOLING

FIGURE 12

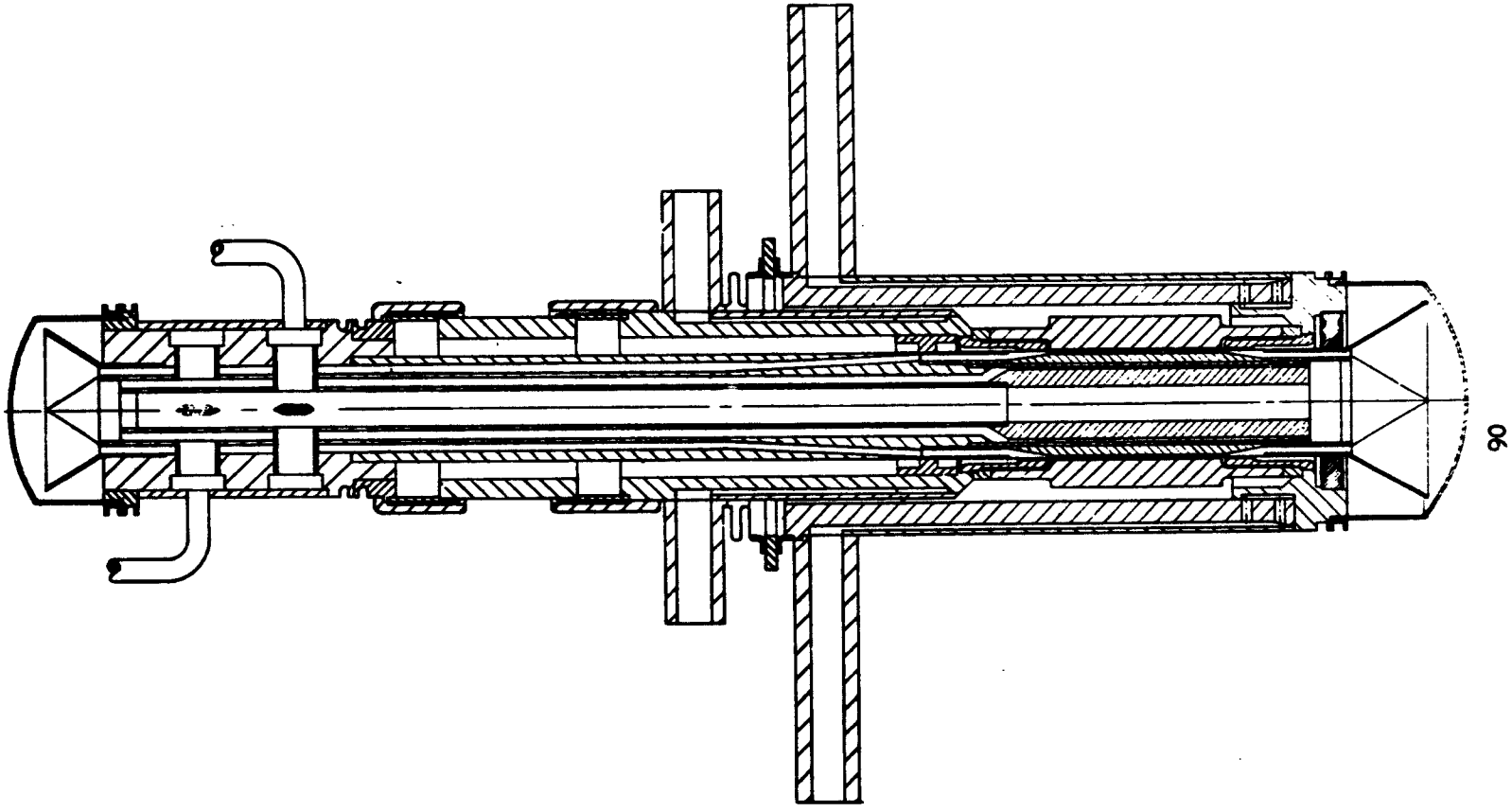

100 KW - 4mm EAL AMPLIFIER

FIGURE 13

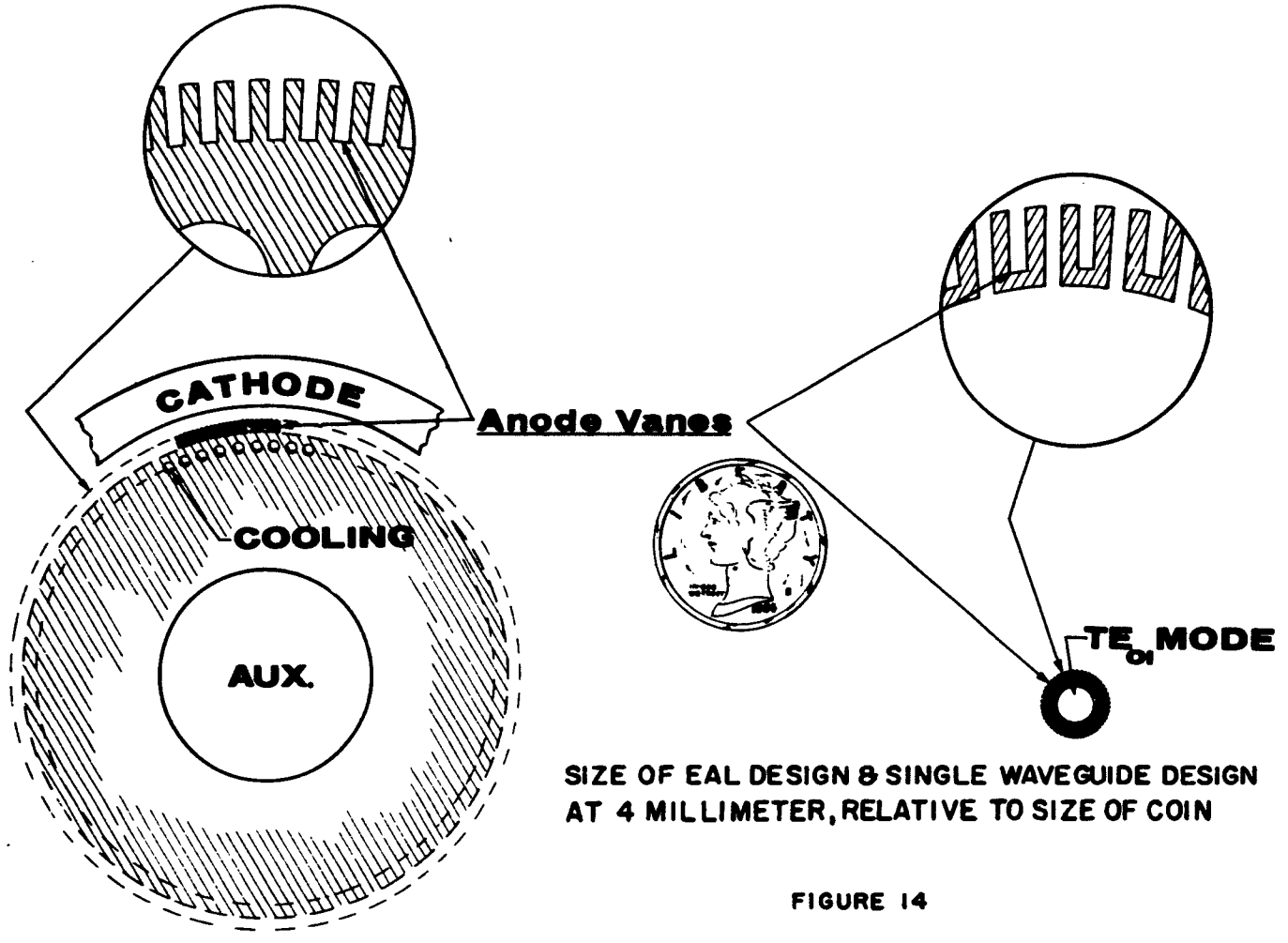

SIZE OF EAL DESIGN & SINGLE WAVEGUIDE DESIGN
AT 4 MILLIMETER, RELATIVE TO SIZE OF COIN

FIGURE 14

IMPROVED PERFORMANCE CHARACTERISTICS OF MEGAWATT TWT'S

By

M. Chodorow, R. A. Craig and D. K. Winslow

Microwave Laboratory
W. W. Hansen Laboratories of Physics
Stanford University
Stanford, California

A number of related structures[1] are used at Stanford to evaluate and improve the performance characteristics of megawatt traveling-wave tubes. The cloverleaf, centipede and the long-slot interaction circuits have been evaluated with respect to peak power output, efficiency, and bandwidth in the S-band frequency range. The centipede tube has to date given the largest saturated 3 db bandwidth (18 per cent) at a peak power of 3 megawatts and 30 per cent efficiency with relatively high small-signal gain (30 db). An amplifier comprising the long-slot coupled circuit has exhibited the possibility of bandwidths of about 25 per cent, but lower gain and efficiency prevented definitive measurements. A tapered cloverleaf circuit has been tested as a multimegawatt amplifier, and the results and analysis indicate that both oscillation suppression and efficiency improvement should be obtained in an amplifier with a properly designed circuit taper. A cloverleaf circuit was designed for high peak power operation and delivered eight megawatts at 200 kv. The operation of this tube at higher power levels was not possible because of upper passband oscillations. Improved attenuators and electron gun optics should improve these results. The selective attenuation of undesired modes has been accomplished in both cloverleaf and centipede tubes by using lossy ceramic attenuators properly located in the rf fields of the structures. Recent calculations and cold test measurements show that the higher order modes (as well as the band-edge frequencies which are responsible for the pulse-edge oscillations) can be sufficiently loaded to obtain the required stability by using resonant slots to couple the undesired frequencies from the structure to an external guide.

THE LONG-SLOT TWT

The long-slot coupled circuit[2] TWT uses the interaction between the electron beam and the electromagnetic wave of the second passband of the circuit. The long slots cut into the magnetic field region of the coupling plates are resonant at a frequency below the desired operating band. This gives a "slot" passband which may be either backward- or forward-wave depending upon how the coupling is perturbed by the "fins" inserted in the cavity over each slot to properly shape the operating passband. Figure 1 shows a sample slot, a fin, and the sever termination used in the tube. In

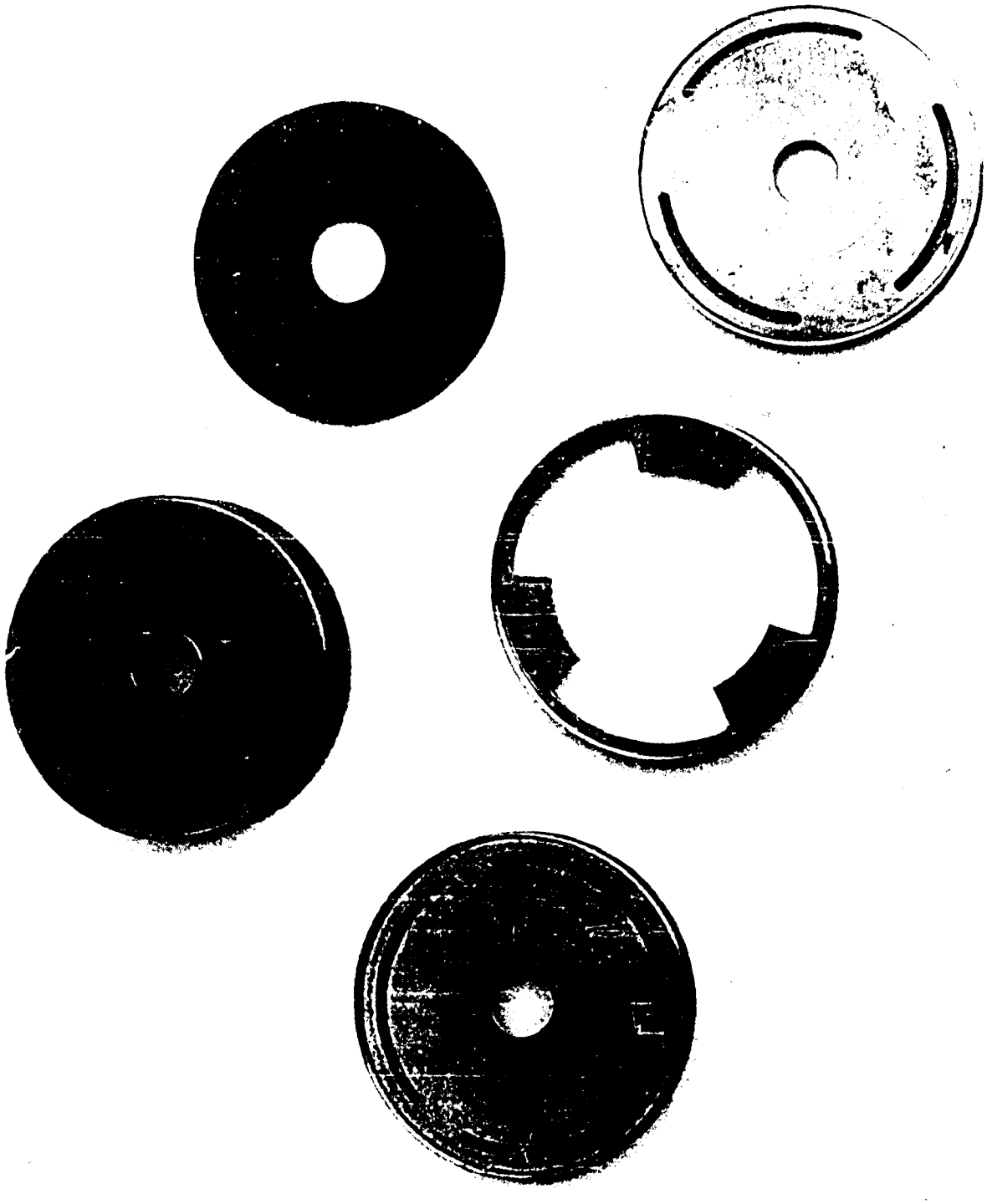

Fig. 1. Photograph of section components and a sever for the long-slot TWT.

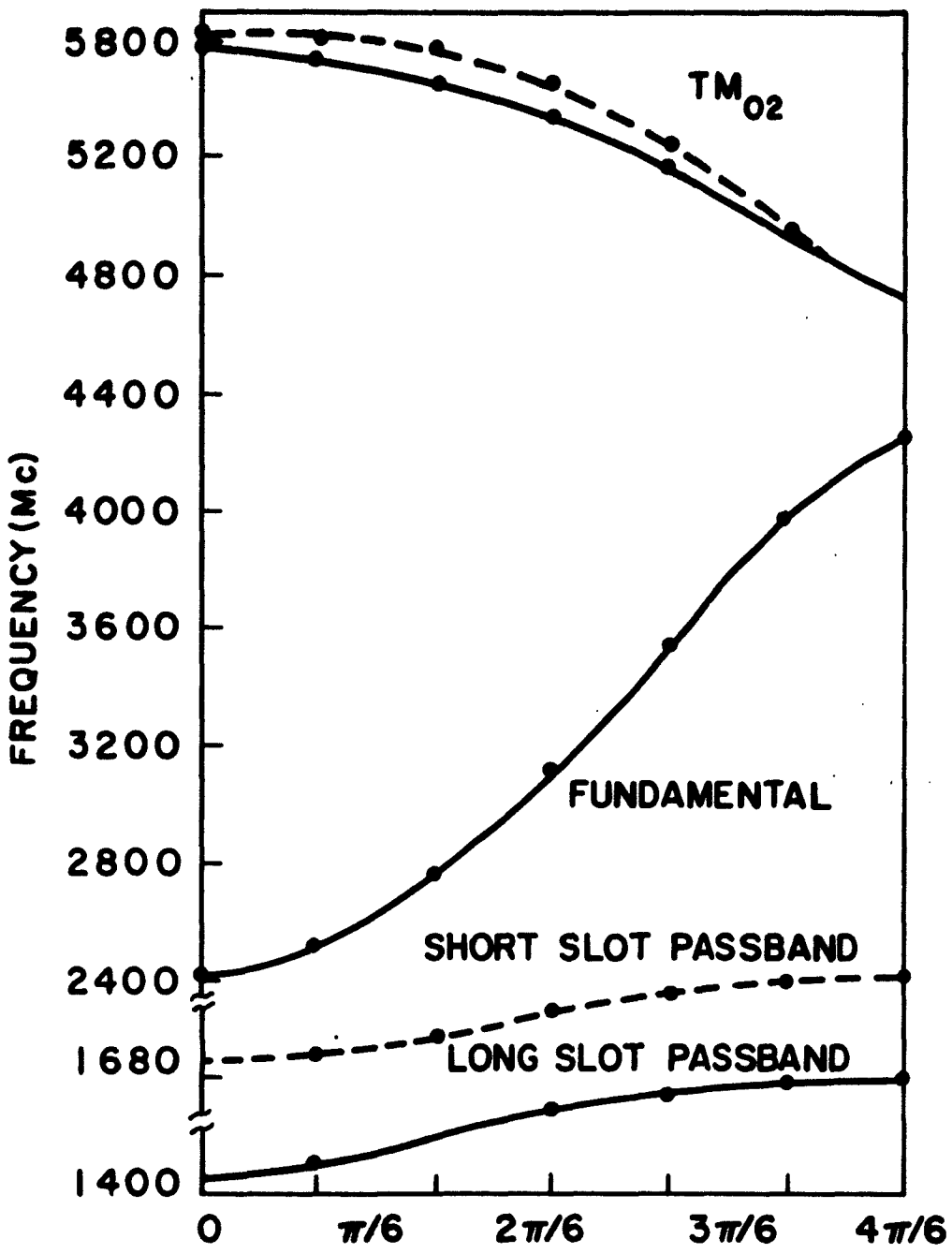

Fig. 2. Dispersion diagram of the long-slot TWT

the tube described here, the "slot" passband is a forward-wave and is quite narrow (approximately 1%). Figure 2 shows the measured ω-β characteristics for several passbands. Notice that there are two slot passbands. These arise because there are two different length slots used in the circuit. In order to prevent the slot passband from oscillating it is necessary to break it up in some manner, and this is accomplished by providing two disks with slots slightly longer than the next two and so on. Thus, the structure consists of two "long" slots and two "short" slots which give rise to the two passbands shown. Each of these two cavity sections is too short to give sufficient gain as a TWT to cause oscillations, and the tube should be stable in this region. The difference in slot lengths does not cause an appreciable difference in the fundamental passband, but does cause a slight shift in the TM_{02} passband as can be seen from Fig. 2.

Tests on the first amplifier were quite encouraging.[3] Small signal gain in excess of 20 db for voltages over 110 kv was obtained from 3100 - 3900 Mc/s. Efficiency as high as 30% was measured at 125 kv. The low gain of the amplifier, 25 to 30 db, made it difficult to saturate the amplifier, but a combination of magnetron and high power TWT's gave some data which indicates that saturation bandwidths of 20 to 30% at megawatt power levels might be obtained. Relatively poor impedance matches at the couplers cause the extreme variations in the small signal gain and detract from the reliability of the saturation gain measurements.

Oscillations were observed at about 5400 Mc/s, corresponding to interaction in the TM_{02} passband and at 1490 Mc/s, which is related to the slot passband. The latter appear to be monotron oscillations and, unlike those in the upper passband, were not suppressed by the application of sufficient rf drive. Monotron oscillations can occur because the alternate cavities formed by the "long" and "short" slot disks can be resonant with fairly high values of Q. It has since been found that the application of Kanthal, a lossy metal, in the vicinity of the slots will lower this Q by a factor of 20 or more and thus eliminate these oscillations.[4] The upper passband oscillations, it has been found, may be the result of a slight misalignment of the slots and/or fins which cause high reflections at discrete frequencies in this passband. However, it is difficult to obtain a good impedance match to the coupler and sever termination in this region so a selective loading scheme has been developed to suppress these oscillations.

Adding a series of resonant slots which radiate into a lossy waveguide to the outer periphery of the slow-wave circuit has given a net attenuation of about 1.8 db per cavity at frequencies near the low frequency cut-off of the TM_{02} passband.[6] Since the lossy waveguide is below cut-off in the fundamental passband and the slots are not resonant at these frequencies, little power is lost at the normal operating frequencies. The attenuation in the upper passband is more than the nominal gain so oscillations should not now build up in the structure. Note that the observed oscillations were not backward-wave since they were not voltage tunable.

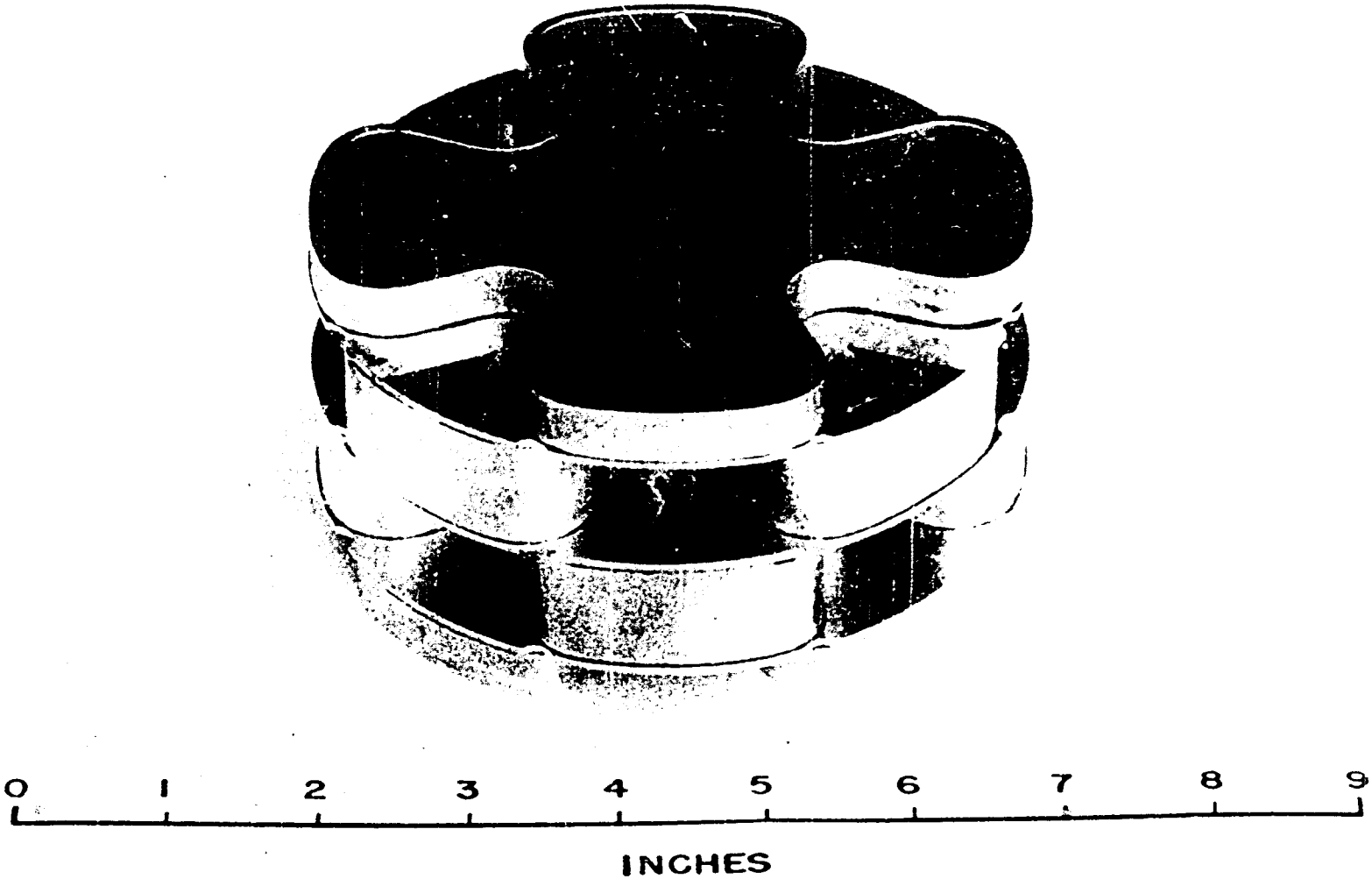

Fig. 3. A photograph of cloverleaf TWT sections

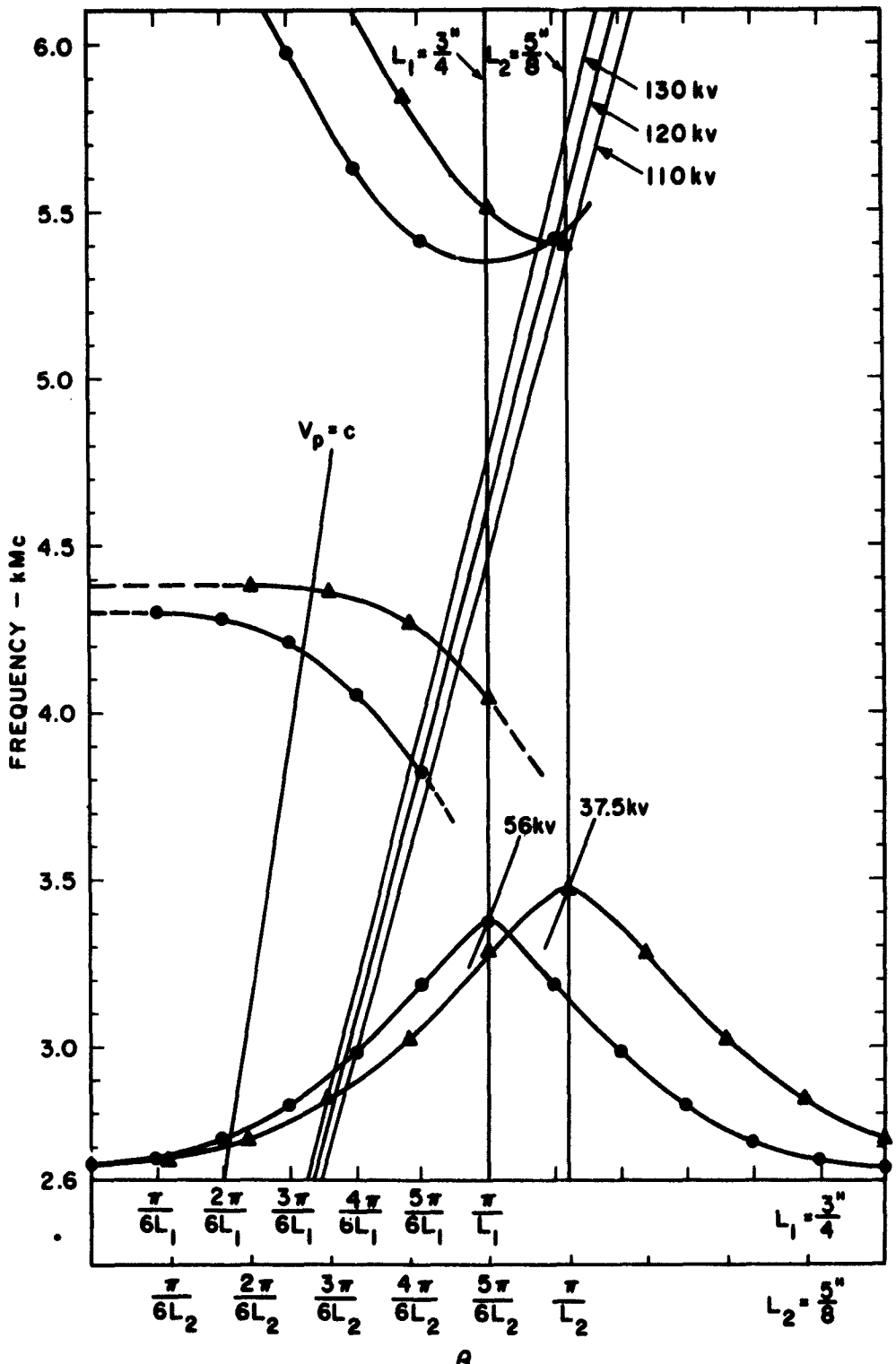

Fig. 4. The dispersion diagram of the tapered cloverleaf TWT

Now that the oscillation problem is solved, in principal, a new tube is being constructed which should have at least 20% bandwidth at multi-megawatt power levels with efficiencies of 30% at midband. Circuit tapering, easily applied to this simply constructed tube, should further enhance its performance.

THE TAPERED CLOVERLEAF TWT

A cloverleaf tube was designed and constructed[3] in which the circuit taper was linear in velocity insofar as cavity height is concerned. Typical cloverleaf sections are shown in Fig. 3. However, the slot length and central hole diameter were changed in such a way that the low frequency cut-off ("0" mode) was unchanged while the upper frequency cut-off ("π" mode) was gradually increased in frequency. Thus, while the cavity height varied from 0.750 in. to 0.625 in. in a linear manner, the phase velocity at midband (2950 Mc/s) varied from 0.588 c to 0.516 c (V_0 to 0.7 V_0) . This is considerably less than the velocity variation between the two upper cut-off frequencies of the first and last cavities of the tapered sections as can be seen directly from Fig. 4. The last six cavities of an eleven-cavity output section were tapered. The entire tube consists of ten uniform cavities at the input, eight uniform cavities in the center section and the eleven cavities in the output. The small-signal gain varied from 35 to 38 db near midband when the beam voltage was 120 kv with a perveance 2×10^{-6} electron gun.

The particular design was used to prevent pulse-edge oscillations which are the result of the beam at some voltage below operating voltage being in synchronism with rf wave at the upper cut-off where the interaction impedance is high. The combination of the frequency "taper" at the upper cut-off and the velocity taper should decrease the effective length of the output section to both backward-wave and pulse edge oscillations, but not affect the forward-wave gain and efficiency. If this is truly the case, attenuation in this section of the amplifier can be reduced to a value sufficient only to suppress forward-wave regeneration and thus provide the possibility of optimum efficiency.

The first model[3,4] constructed as described above had attenuation sufficient to stabilize a nontapered tube, so no increase in efficiency was observed. An efficiency of 28% based on collector current was obtained. This is probably quite realistic because a misalignment of the electron gun[3] caused most of the interceptions to occur on the input section. The bandwidth to the 3 db points at saturation was about 12% and the output was symmetrical about the center frequency.

Figure 5 shows normalized curves at output power vs input power with frequency as a parameter. It is easily seen that the power characteristic is more linear than a corresponding tube made with exactly the same circuit dimensions but with no tapering. At frequencies below the synchronous frequency the tube behaves as a linear amplifier until about 1 db below

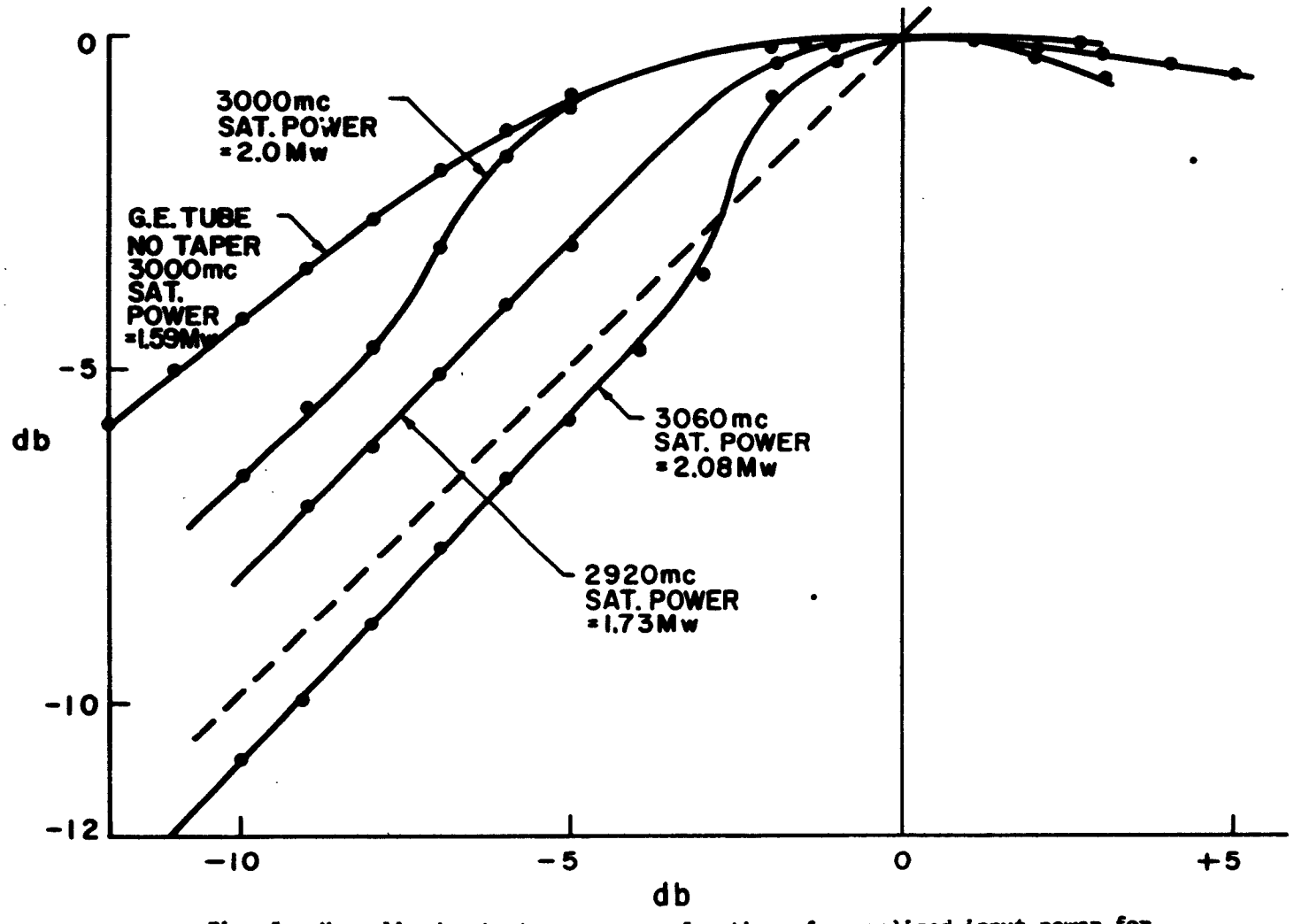

Fig. 5. Normalized output power as a function of normalized input power for both tapered and uniform cloverleaf circuits, V_0 = 120 kv.

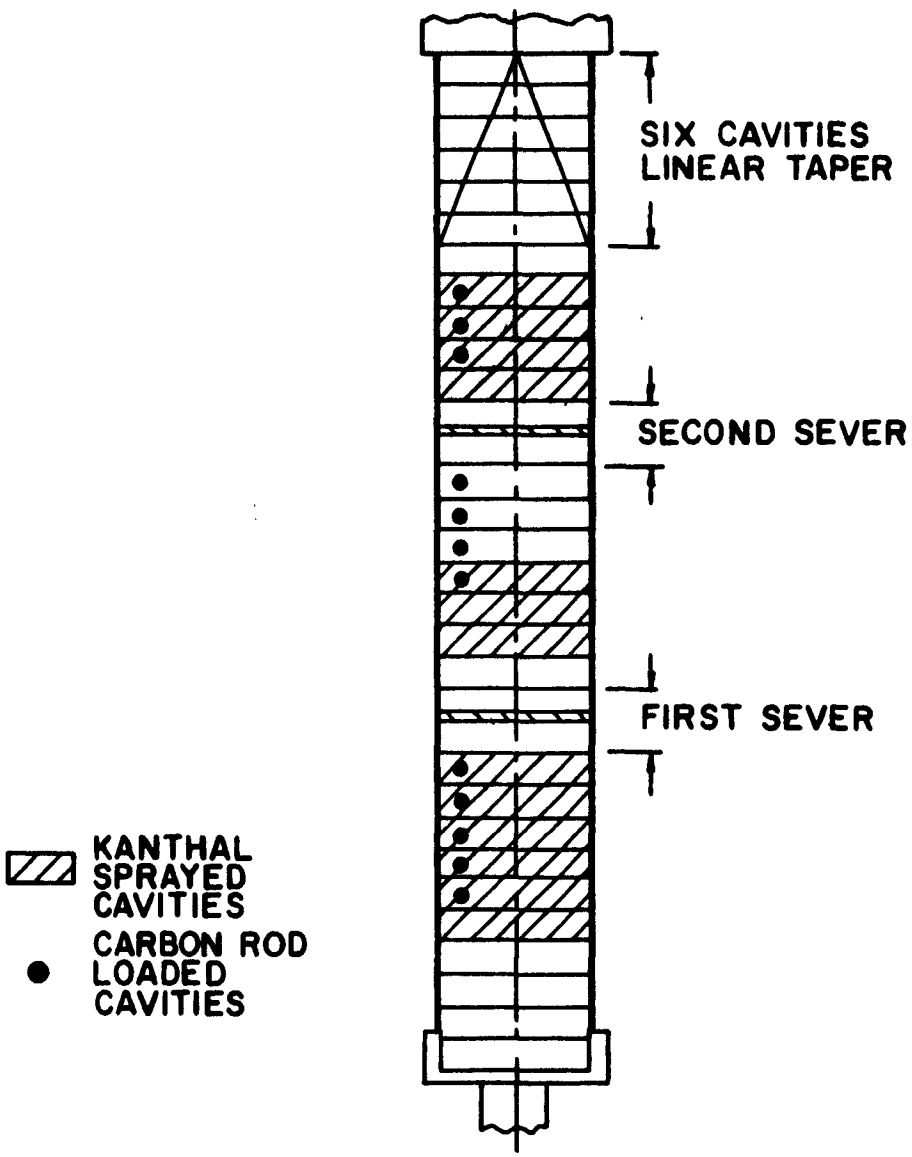

Fig. 6. Distribution of loss in the modified linear tapered cloverleaf TWT

saturation. Beyond this point it saturates abruptly as the drive power is further increased. It can be seen that at frequencies near midband the gain increases slightly as the drive is increased. This effect begins at about 4 db below maximum power output and becomes more noticeable as the frequency is raised. At a typical frequency of 3060 Mc/s, this increase in gain has a maximum value of 2.3 db above the small signal value of 33 db. At still higher frequencies the gain is too low to observe this gain increase with the limited drive power available, although the performance is expected to be approximately the same. At the lower frequencies the small signal gain is so high (38 db at 2920 Mc/s) that a small increment in the gain could not be easily detected. At higher operating voltages the results are essentially the same, but with a higher power output. It is important to note that the tapered tube requires a much smaller variation in drive power to bring the tube from the linear region to saturation than did the nontapered tube.

Pulse-edge oscillations did not occur in the output sections of the amplifier even though it was one cavity longer than the input. This type of oscillation was generated in the input section, however, and was amplified in the output. The input was more heavily loaded than the output as can be seen from Fig. 6, so the misalignment of the gun must have enhanced oscillation generation in the input section. It was impossible to suppress them in the input by adjusting the magnetic field without seriously affecting the power output of the amplifier. The identity of frequencies measured at both the input and output ends proved that the output was not oscillating independently.

The taper of the slow-wave circuit was not designed to improve efficiency. Analyses made by Hess of the University of California and Meeker and Rowe of the University of Michigan indicate that when one tapers the circuit velocity to remain in phase with the electron bunch, theoretical efficiencies of 50% should be attained. The limit appears to be caused by the fact that if one maintains the proper phase, the velocity spread is excessive or, conversely, if one attempts to hold the velocity spread at a minimum, the phase spread of the electrons will be excessive. Each of these problems is compounded as space-charge is increased. In the tapered cloverleaf tube the space-charge is small enough to allow efficiencies of 45% or so when the taper is proper and loss in the output section is not excessive.

THE TEN MEGAWATT CLOVERLEAF TWT

The objectives of this program were to construct a TWT amplifier capable of delivering 10 mw of peak power with good bandwidth and efficiency. It was decided to modify the cloverleaf circuit shown in Fig. 3 for this purpose. The cold passband ranged from 2.7 to 3.5 kMc/s and the one-inch beam aperture provided good beam coupling at all frequencies. The wider-than-normal bandwidth for this circuit results in a somewhat lower interaction impedance and, consequently, a somewhat lower electronic efficiency.

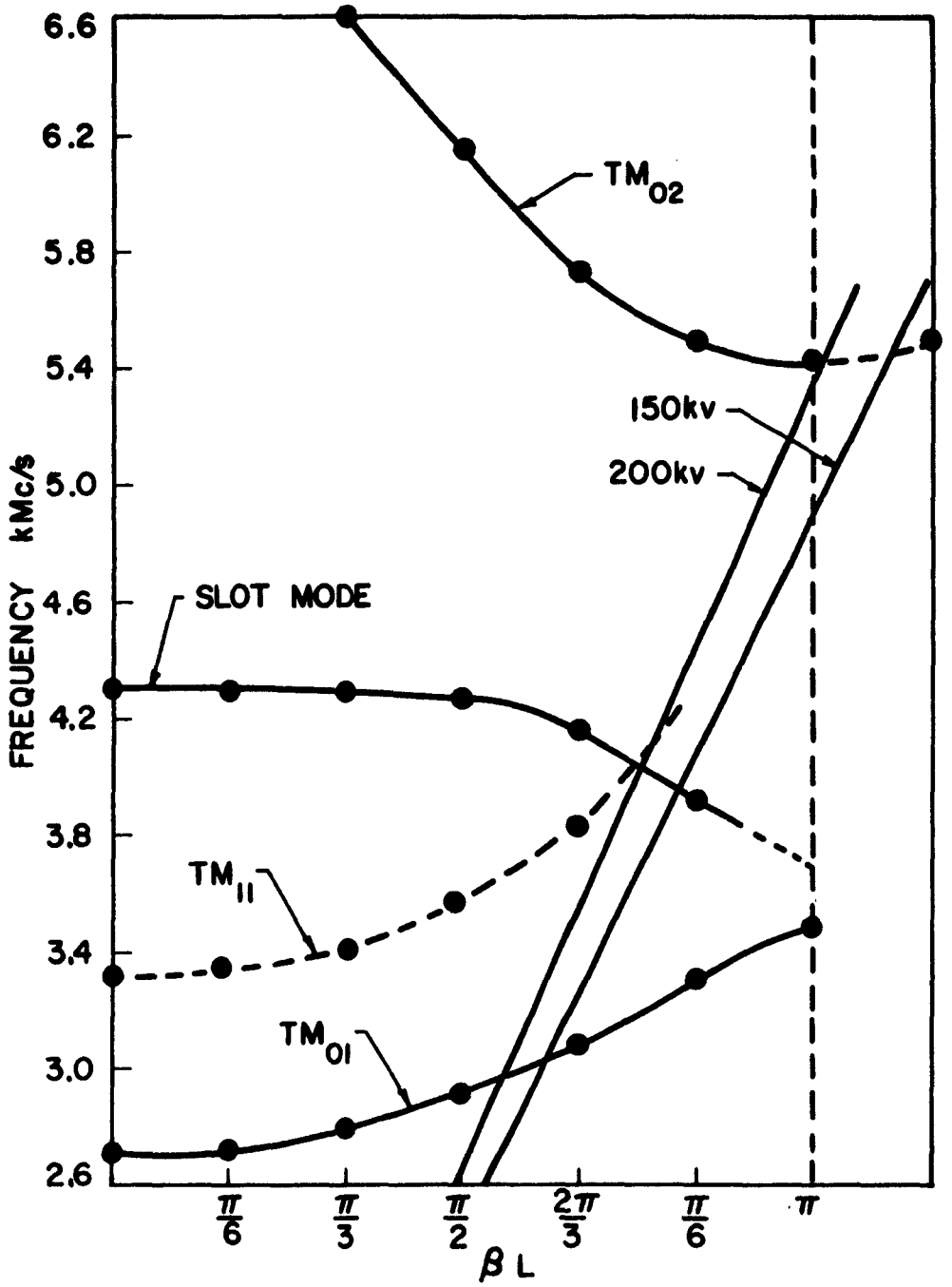

Fig. 7. Measured ω-β characteristics of the final circuit for the 10 megawatt TWT

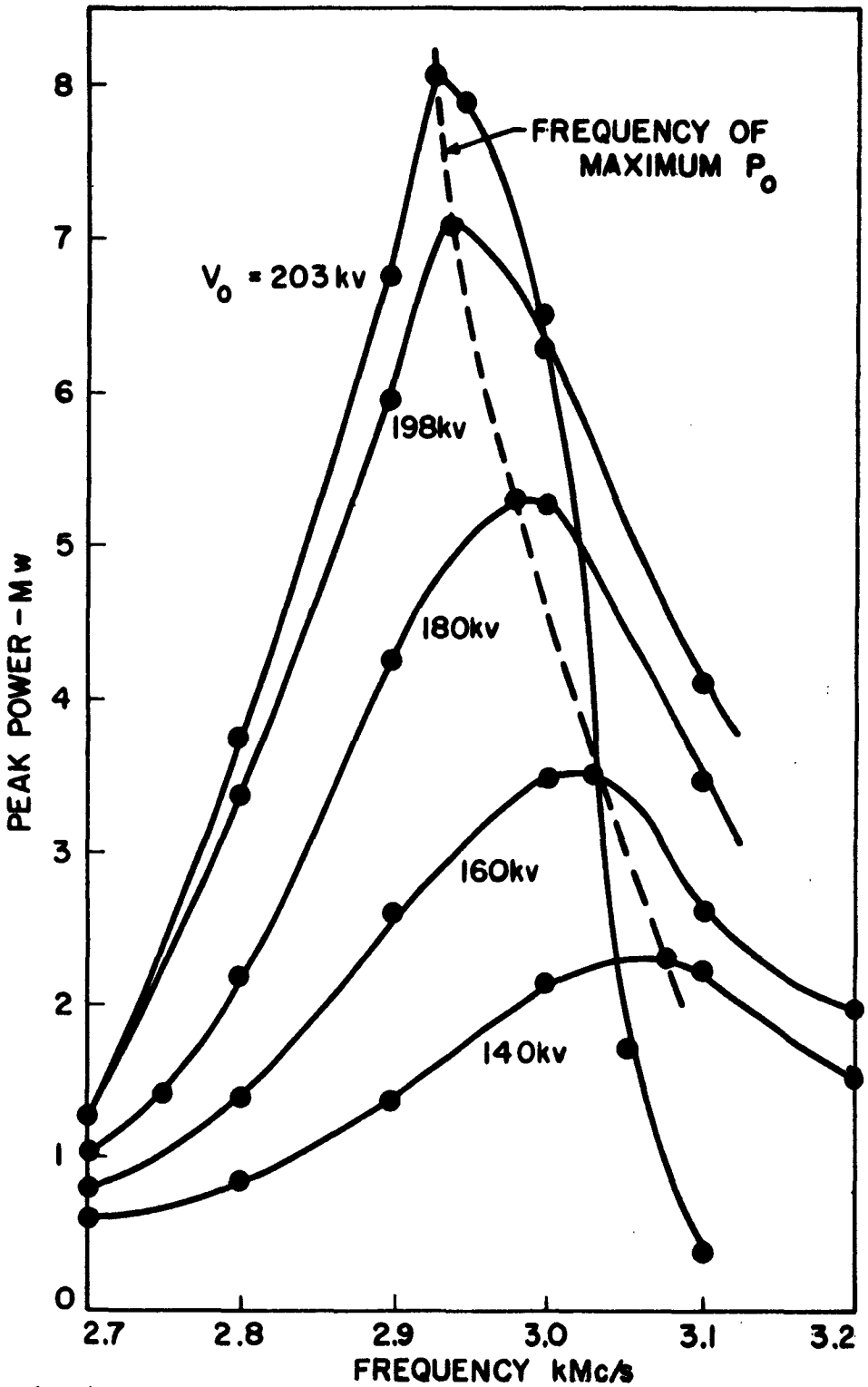

Fig. 8. Peak power output of the 10 mw cloverleaf TWT as a function of frequency at different beam voltages.

Figure 7 shows the measured ω-β characteristic of the final circuit. Note that the upper (TM_{02}) passband may present oscillation difficulties at operating voltages.

The first tube[3,4] was designed to operate at 200 kv with a perveance 2×10^{-6} electron gun. It consists of three sections, each comprised of eleven identical cavities. The first model so constructed exhibited violent oscillations at the lower cut-off of the TM_{02} passband, so a modification consisting of additional attenuation was made. This attenuation was essentially uniform in the central section, but was tapered from about 2-1/2 db/cavity down to zero in four cavities such that two cavities from the input and output couplers were loss free. The result, of course, was a considerable reduction in efficiency, the price of stability.

Since the beam in this amplifier is well into the relativistic region it was desirable to check performance over a fairly wide voltage range to see if any improvement in efficiency could be observed at higher voltages. It can be shown from a simple ballistic analysis, assuming that the same change in beam velocity at saturation occurs in the relativistic beam as well as in the nonrelativistic beam, that the efficiency should increase by the factor

$$\eta_{rel}/\eta = 1 + 3X/2 + X^2/2 \quad ,$$

where

$$X = eV_0/m_0c^2 \quad .$$

This result also assumes that the frequency of maximum power output remains constant as the voltage increases, a condition not true in practice since the synchronization frequency decreases as the voltage is raised. The interaction impedance, therefore, also increases, which tends to improve the efficiency somewhat although not a great deal in this tube because the initial value of the gain parameters, C, is relatively high, and the variation of efficiency with C above this point is slight.

Values of power output up to 8 mw peak were obtained as shown in Fig. 8. Efficiency as a function of beam voltage is shown in Fig. 9. The measured efficiency improvement is greater than that predicted from purely relativistic considerations for several reasons. Optimization of the focus fields, choice of reference voltage, and the assumption of constant impedance are all factors, but we can at least conclude that the predicted trend is apparent.

The additional loading for oscillation suppression caused a downward shift in the ω-β characteristic, so it is difficult to ascertain the proper value of impedance to use in computing the gain and efficiency. Measured values of small signal gain as a function of voltage lie about halfway between those calculated, above that assuming constant impedance

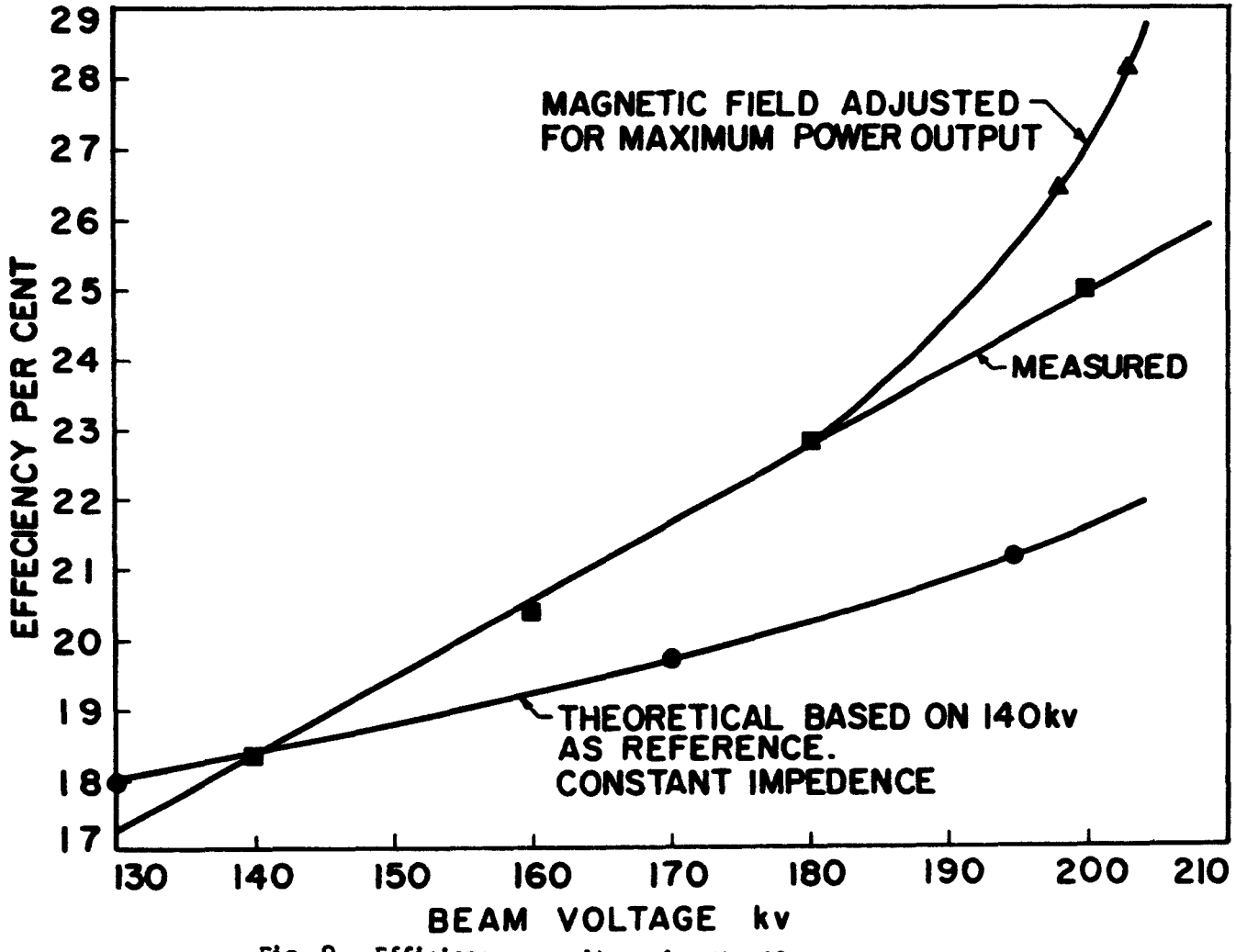

Fig. 9. Efficiency vs voltage for the 10 mw cloverleaf TWT

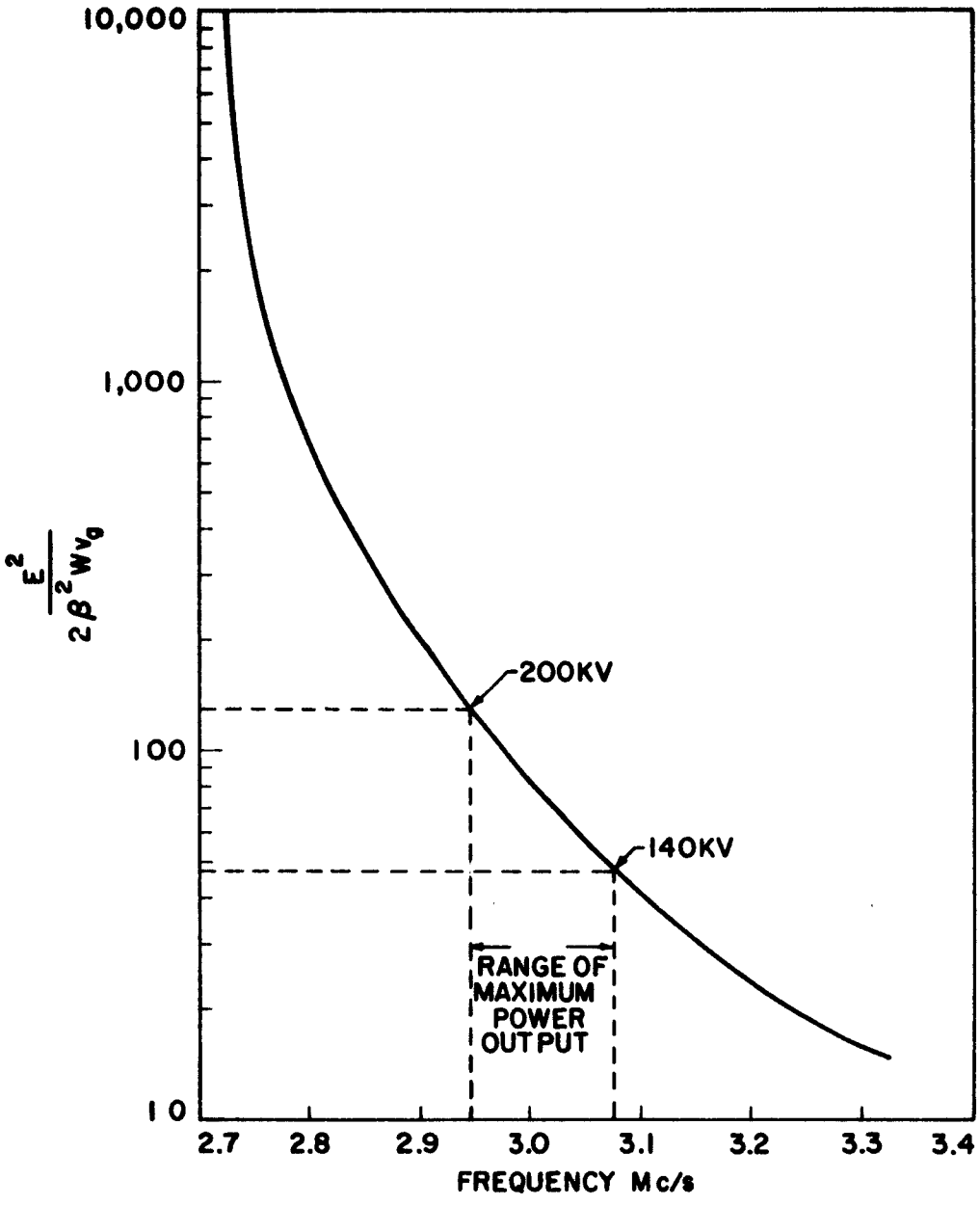

.Fig. 10. Pierce impedance vs. frequency for the 10 mw TWT

and below that obtained using the value at the frequency corresponding to maximum power output. Thus, we conclude that the range of impedances at maximum power output should be lower than those shown in Fig. 10.

There were no detectable oscillations up to 200 kv, so if the efficiency can be improved, the tube should easily develop 10 mw with saturation gain of 40 db. The bandwidth is less than expected, but should be considerably improved by optimization of the various circuit parameters, C , QC , and attenuation. Average power capabilities are unknown due to the lack of a suitable modulator to make such tests. Suffice it to say that with no cooling of the tube body or attenuators and with as high as 30% beam interception at the tube output under full power conditions, over 2 kw of average power was obtained continuously for several hours, with no noticeable decrease in performance.

THE CENTIPEDE TWT

An S-band high power traveling-wave tube using the centipede circuit has given the following performance data:[5] three megawatts peak power, 30 per cent efficiency, 30 db small signal gain, and approximately 18 per cent, 3 db saturated bandwidth (from 2600 and 3100 Mc/sec at 120 kv. Typical data provided by the first tube of this type is given in Fig. 11 for different operating voltages. The periodic elements of this tube consist of a number of reversed loops which afford negative mutual coupling between cavities and result in a forward-wave fundamental mode for the operating band of the tube. The measured cold bandwidth is approximately 40 per cent. A number of the tube components, including the individual sections, are shown in Fig. 12. The total tube consisted of 28 sections--14 sections in the input end, a lossy ceramic sever, and 14 sections in the output half of the tube. The drift tube diameter was 3/4 in. and the beam perveance was 1.65 micropervs. During the initial tube test, oscillations were observed at 4600 - 4700 Mc/sec, which were attributed to the higher frequency loop backward-wave mode in addition to the pulse-edge oscillations at the upper cut-off of the operating band. At the completion of the first tests, the tube was taken apart and reassembled incorporating lossy ceramic attenuators in the form of disks between the sections which were so located that the loop mode was attenuated more than the passband frequencies. This eliminated the oscillations in the loop mode for 120 kv operations and also reduced the efficiency by 3 or 4 per cent due to the increased attenuation in the operating band. Other tube performance characteristics were not appreciably affected.

THE SELECTIVE ATTENUATION OF HIGHER ORDER MODES IN MEGAWATT TWT'S

In order to avoid the limiting effects of stability of tube performance, a number of different methods have been used in the tubes previously discussed; e.g., by using severs, by placing lossy ceramic attenuators appropriately to provide differential attenuation, and by tapering the

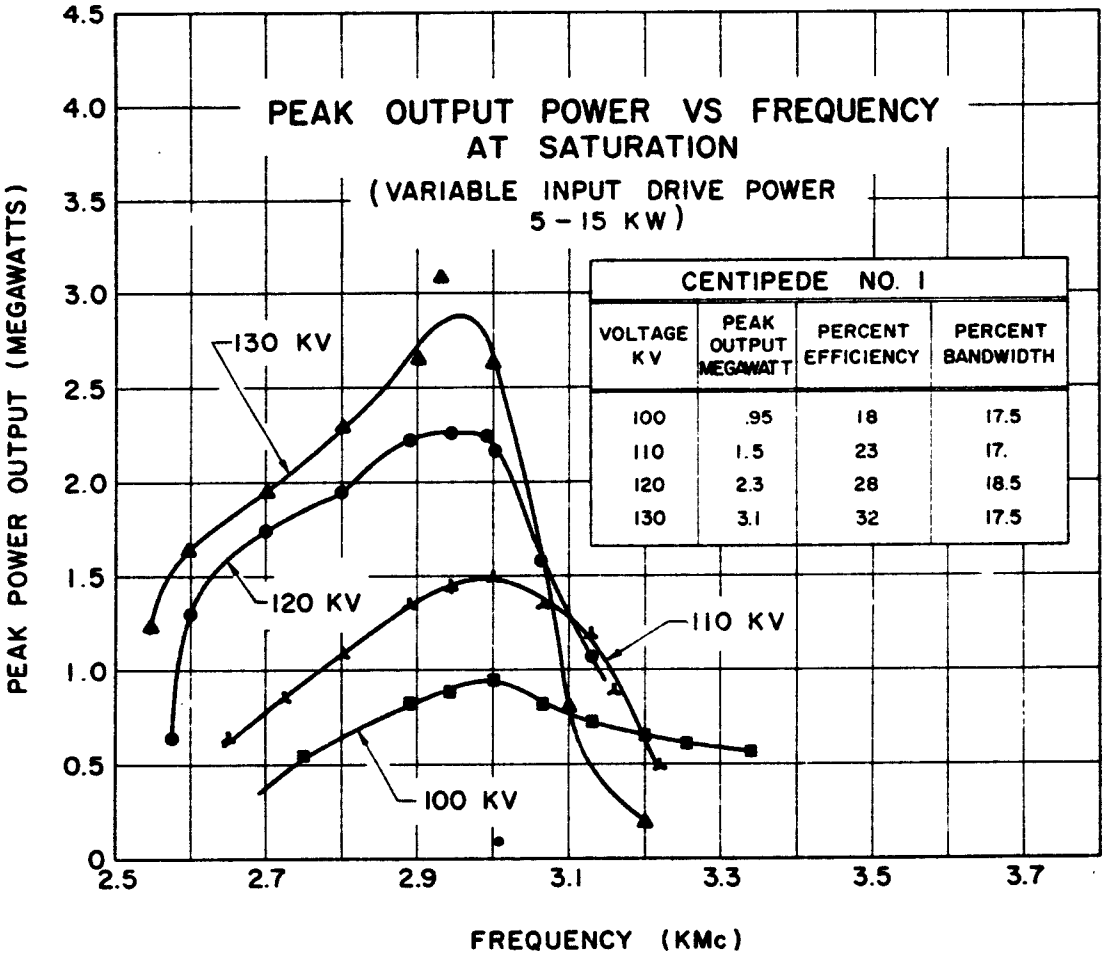

Fig. 11. Peak power output vs frequency for the centipede TWT

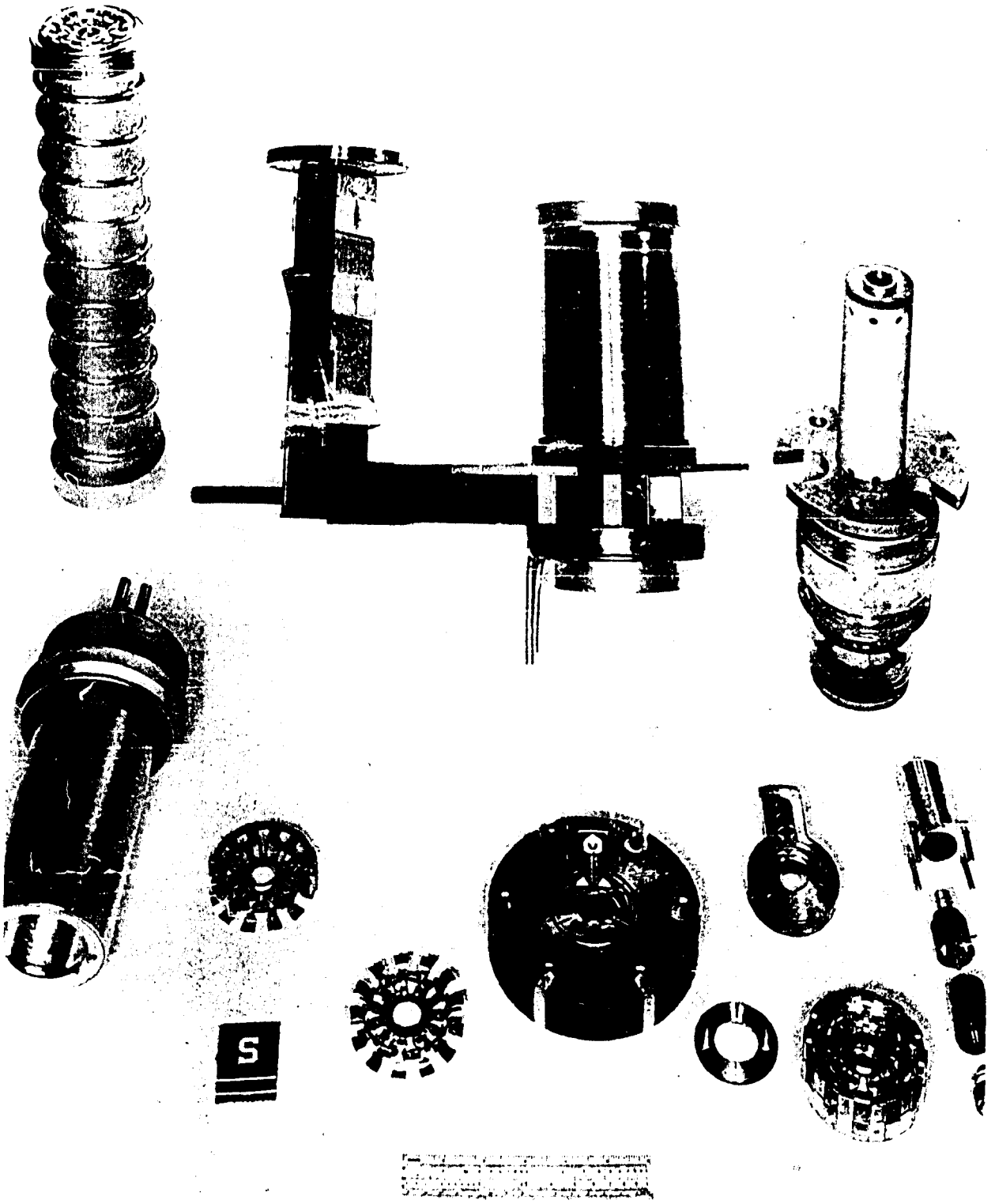

Fig. 12. Severed tube components for the centipede TWT

velocity of the circuit. Another approach, which has been investigated by calculations and cold tests, is the selective coupling of the troublesome modes into an external uniform guide by means of common slots between the periodic structure and guide.[3,4,6] A typical setup showing the manner in which the structure is coupled to an external guide by the coupling slots is shown in Fig. 13. A dispersion diagram of the centipede circuit is shown in Fig. 14. Also shown are the dispersion diagrams of the coupled uniform guides. For the coupling to the backward-wave loop mode the slots are in alternate sections. This is shown by the curve labeled "waveguide (A)." For the coupling to the forward-wave fundamental mode as well as the loop mode, the slots are in each section (waveguide (B)). The waveguide width is adjusted for the proper cut-off frequency, and the guide is loaded with dielectric to adjust the phase velocity. The slot resonant frequency is altered to vary the amount of coupling by changing the slot length. Measurements using the loop mode coupler show that complete power transfer can be obtained with as few as two slots over a narrow frequency region around the slot resonance. Slots in the circuit have also been used to couple the loop mode frequencies into an external lossy region (no waveguide). For this case, four slots per section have given a minimum of 1.5 db per section over a 500 Mc frequency range compared to the 0.7 db per section required for stability. This plot of attenuation vs frequency is shown in Fig. 14. This kind of attenuation can also be achieved with the attenuation in a waveguide with a preselected cut-off frequency above the operating frequency range. Waveguide (B), which couples to the circuit in the operating passband as well as the upper loop mode, would allow the upper cut-off of the operating band to be appropriately attenuated. Calculations show that the coupling of this guide to the growing wave of the structure and beam introduces negligible attenuation to the operating mode (typically, 3 db attenuation for 30 db total gain at synchronism) due to the nature of the coupling in the presence of a growing wave; i.e., negative attenuation of the beam-circuit wave.

With the above methods of coupling and attenuating the undesired modes and frequency regions, not only can tube stability be achieved but perhaps a more important feature is that the attenuators can be in the cut-off region at the operating frequency range. Thus the attenuators will not be exposed to the high peak and average powers during tube operation. This approach should permit the tube performance characteristics of these types of tubes to be optimized without the previous limitation of stability requirements.

ACKNOWLEDGEMENT

The research reported in this document was supported in whole or in part by the Rome Air Development Center, Air Research and Development Command, United States Air Force, under Contracts AF 30(602)-1844 and AF 30(602)-2575.

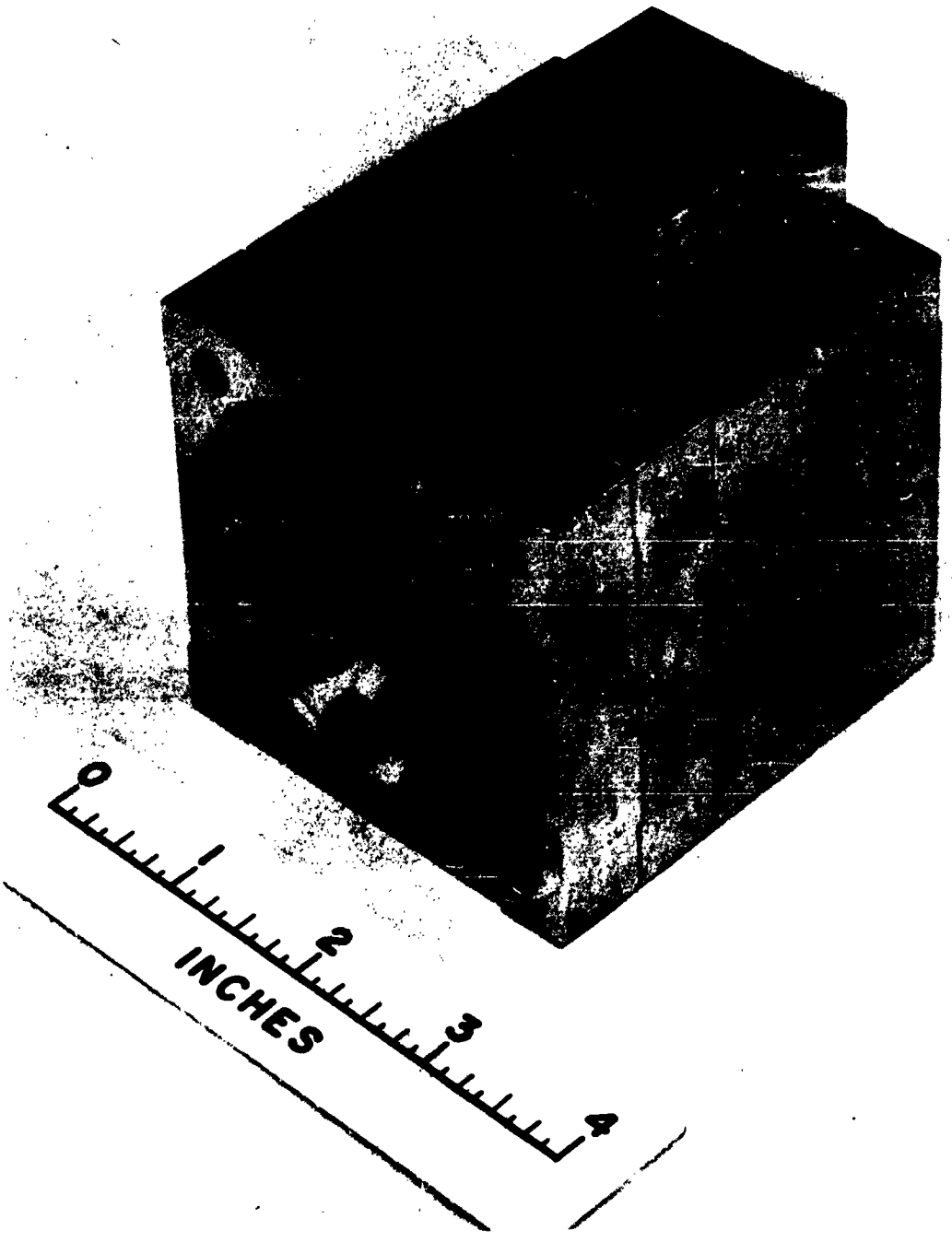

Fig. 13. The centipede circuit and an external waveguide coupled by slots.

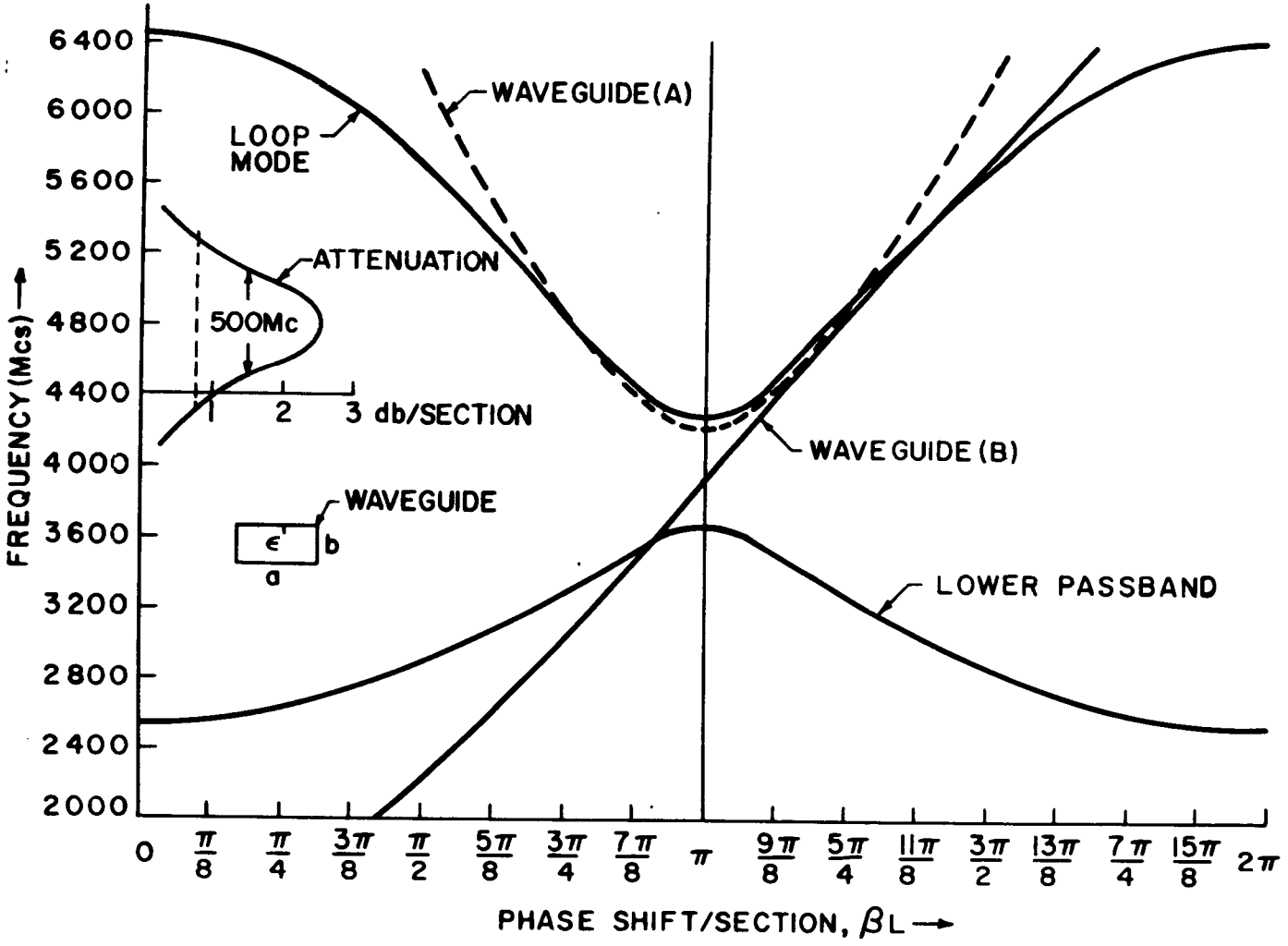

Fig. 14. The $\omega\beta$ diagram of a centipede circuit with the dispersion curves of rectangular waveguides.

LIST OF REFERENCES

1. M. Chodorow and R. A. Craig, "Some New Circuits for New High Power Traveling-Wave Tubes," Proc. IRE 45, 1106-1118 (1957).

2. M. A. Allen, "Coupling of Multiple-Cavity Systems," Microwave Laboratory Report No. 584, Stanford University, Stanford, California (1959).

3. A. First and Second Annual Reports for Contract AF 30(602)-1844, "Development of High Power Broadband Tubes and Related Studies," Microwave Laboratory Report No. 773, Stanford University, Stanford, California (1961).

   B. Proceedings of the International Congress on Microwave Tubes, Munich (1960):

   (1) M. A. Allen, G. S. Kino, C. B. Williams, "A New Circuit for a Wide-Band High Power Traveling-Wave Tube."

   (2) M. Chodorow, R. A. Craig, C. C. Lo, "Tapered Traveling-Wave Tube."

   (3) R. A. Craig and Y. Hiramatsu, "A Pulsed 10-Megawatt Traveling-Wave Tube Amplifier."

4. Third Annual Report for Contract AF 30(602)-1844, "Development of High Power Broadband Tubes and Related Studies," Microwave Laboratory Report No. 854, Stanford University, Stanford, California (1962).

5. M. Chodorow, A. F. Pearce, D. K. Winslow, "The Centipede High Power Traveling-wave Tube," Microwave Laboratory Report No. 695, Stanford University, Stanford, California (1960).

6. Quarterly Memoranda Nos. 1, 2, and 3 for Contract AF 30(602)-2575, "Multimegawatt Broadband Microwave Tubes," Microwave Laboratory Report Nos. 881, 903, and 933, Stanford University, Stanford, California.

A MEGAWATT X-BAND TWT AMPLIFIER WITH 18% BANDWIDTH

By

T. Roumbanis and J. Needle of Sylvania Electric Products Inc.
and D. K. Winslow of Stanford University

INTRODUCTION

A high-power X-band TWT has given over a megawatt peak power with more than 12% bandwidth. The slow-wave structure is a loop-coupled cavity circuit, known as the centipede, in which the coupling between sections is obtained primarily by the negative mutual inductance of reversed loops, providing a forward fundamental phase-velocity. The structure provides a cold bandwidth of 35%, and an interaction impedance comparable to that of the cloverleaf structure. X-band was chosen in order to exploit the wide bandwidth capability of the centipede circuit in a new frequency range.

The capability of the centipede circuit had already been demonstrated at S-band by Chodorow, Pearce and Winslow. They achieved 3 megawatts of pulsed power, a peak efficiency of 30%, a saturated half-power bandwidth of 18% and a saturated gain of 26 db. They employed an electron gun perveance of 1.65×10^{-6} using a beam voltage of 130 kv.

The X-band Sylvania-sponsored project was aimed at developing a broadband tube for sophisticated radar and communication systems which would enable considerable frequency agility. High average power capability was another important goal.

DESIGN OBJECTIVES

The TWT was designed for 1.8 megawatts of peak power, a peak efficiency of 30%, a saturated half-power bandwidth of 18% from 8.3 to 10.0 Gc, and a saturated gain of 30 db. The beam voltage was to be 130 kv with a beam current of 47 amperes, giving a perveance of 1×10^{-6}. The average r-f power was to be greater than 10 kw.

PRELIMINARY WORK

The geometry for the centipede elements was initially determined by scaling from the Stanford S-band design. Techniques were developed for the accurate manufacture of X-band centipede elements, and for the precise measurement of the velocities of propagation and the interaction impedances of the various modes. These measurements provided necessary information for calculation of the tube parameters.

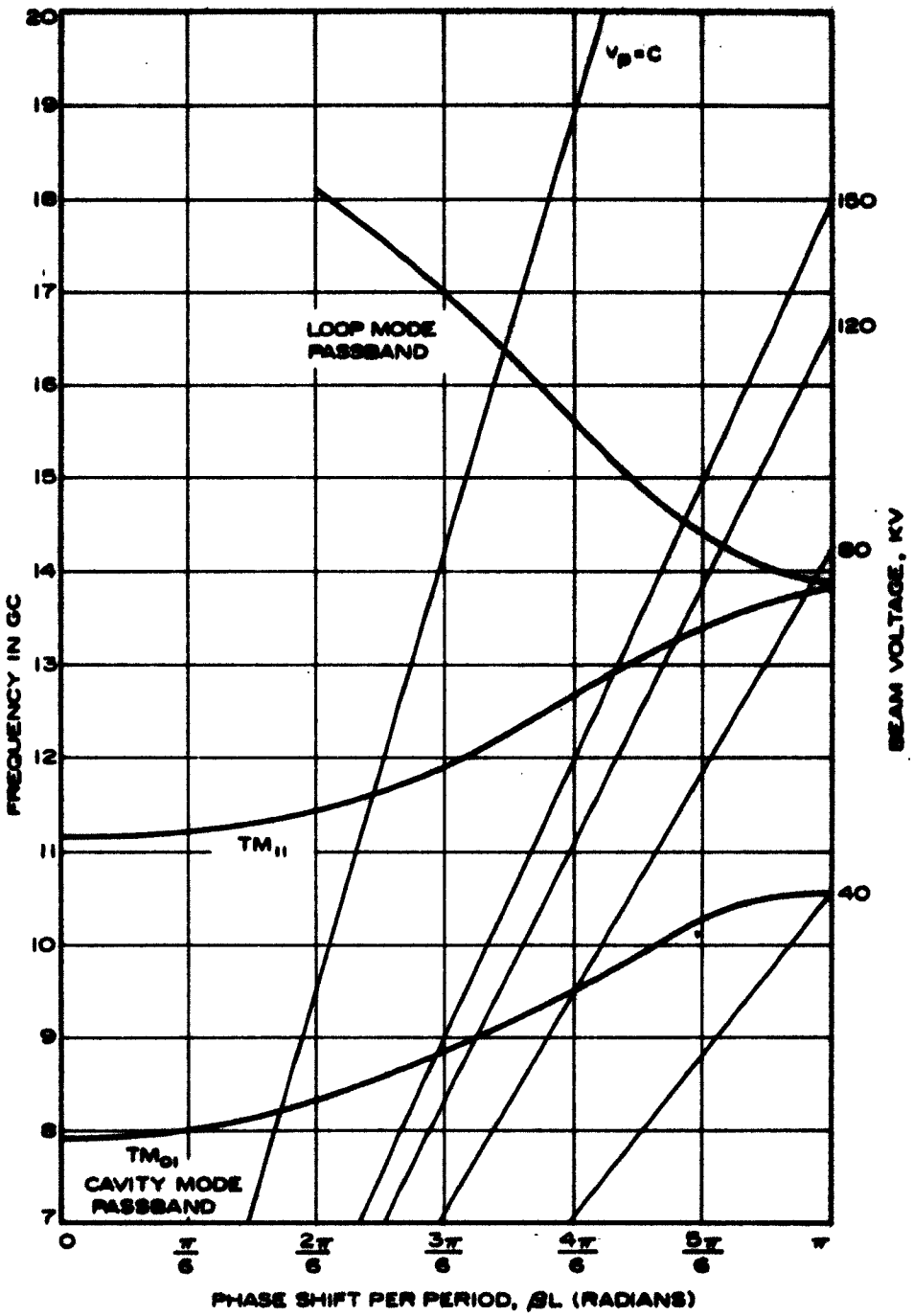

Figure 1. Frequency versus Phase Shift

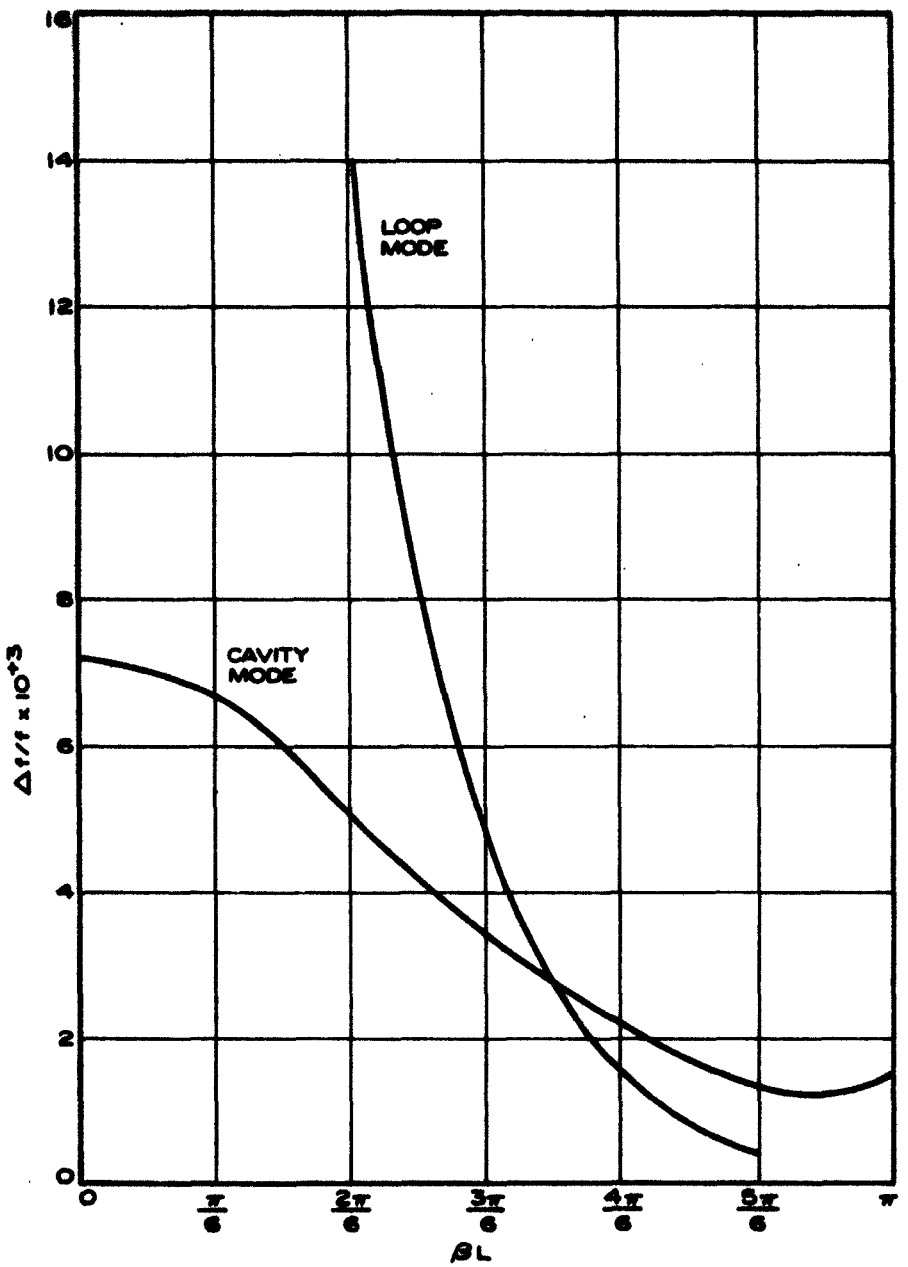

Figure 2. Relative Interaction Impedance ($\Delta f/f$) versus Phase Shift per period (βL)

Beam

Voltage	130 kv
Current	47 amp
Radius	0.1125 inch
Brillouin Magnetic Field	1050 gauss

Small Signal Gain Calculations (Pierce's Notation)

f(Gc)	9.0
βL	1.822
γa	1.085
K_{av}	27.0
QC	0.078
C	0.135
b	0.786
X_1	0.848
1+Cb	1.106
BC	5.65
BCN(gain/period)	1.64
Efficiency (reduced)%	35

Figure 3.
Tube Design

Some of the results of cold test measurements are presented in Figure 1, which shows the velocities of propagation of the various modes. The cold measurements were made by employing sweep oscillator techniques on resonant cavities comprised of centipede elements. The resonances were identified by perturbing the field in various ways. The lowest mode is the TM_{01} cavity mode, which provides the principal interaction field. The next higher is the TM_{11} which, having no E field on the axis, can be ignored, and the top one is the loop mode. The following results were obtained by adjusting the inner diameter of the centipede cavity wall, and the positions, sizes, and shapes of the loops: The TM_{11} mode was almost removed from the operating band; a cavity mode cold bandwidth of approximately 35% was achieved; and adequate separation was provided between the loop mode and the cavity mode to prevent mode inversion and to lessen the possibility of backward-wave oscillations. The voltages marked on the frequency versus phase shift plot correspond to phase velocities or beam velocities which have been corrected for relativistic values.

In Figure 2, the interaction impedance is shown in terms of the relative frequency perturbation $\Delta f/f$ versus phase shift. The frequency perturbations were taken with a 30-mil-diameter sapphire rod. Note that the impedance of the loop mode goes to zero at π radians phase shift per period. This eliminates the possibility of band edge oscillations in this mode.

Figure 3 shows the results of conventional calculations of the tube parameters at the mid-band frequency (9.0 Gc) based on the cold test results. For an efficiency of 30%, a beam voltage of 130 kv and a peak r-f output power of 1.8 megawatts, the required d-c beam power is 6 megawatts and the perveance is 1×10^{-6}. The resulting beam current is 47 amperes. Note that $\gamma a \cong 1$, and the interaction impedance K averaged over the beam is 27 ohms.

The structure length was based on a desired small-signal gain of 35 db and a saturation gain of approximately 30 db. Calculations assumed a small-signal gain of 1.5 db/structure period.

TUBE COMPONENTS AND ACCESSORIES

The centipede elements are approximately 1/16 inch thick in the beam region, with a calculated average r-f power-handling capability greater than 10 kw. A major effort was required to develop techniques for manufacturing centipede elements to the appropriate dimensions and tolerances.

The required attenuation was obtained with two severs. As shown in Figure 4, each sever region consists of a short circuit and drift tube terminated with lossy ceramic rings and Kanthal-coated centipede elements. The drift tube length is approximately 1/40 of a plasma wavelength. The Kanthal adds approximately 3/4 db loss to each centipede element, which in turn lowers the phase velocity over the cold bandwidth except at the π-mode end, where it increases the phase velocity. The stainless steel tube shown in Figure 4 serves as a vacuum envelope and an alignment jig for the centipede element.

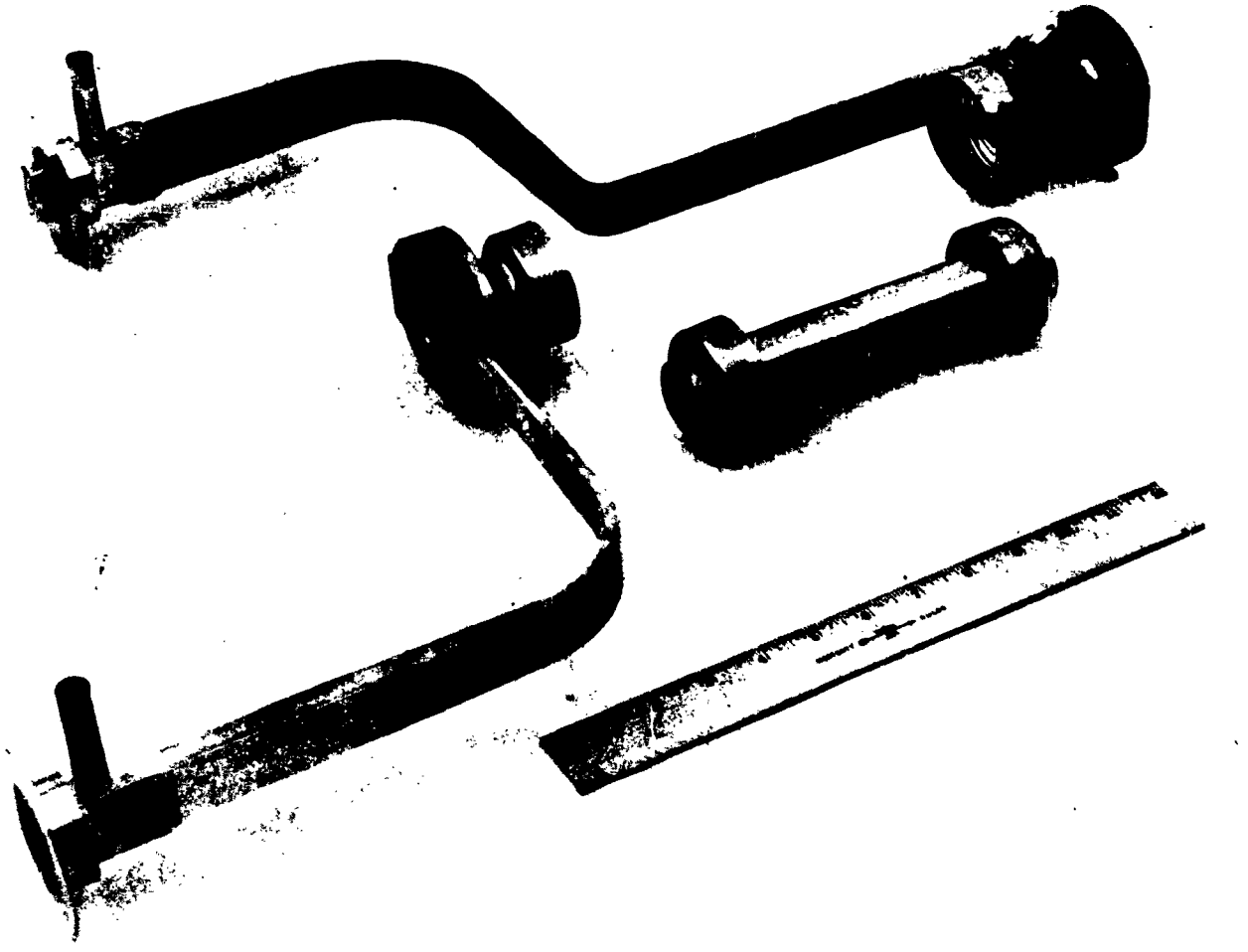

Figure 5. R-f Input and Output Waveguide and Couplers.

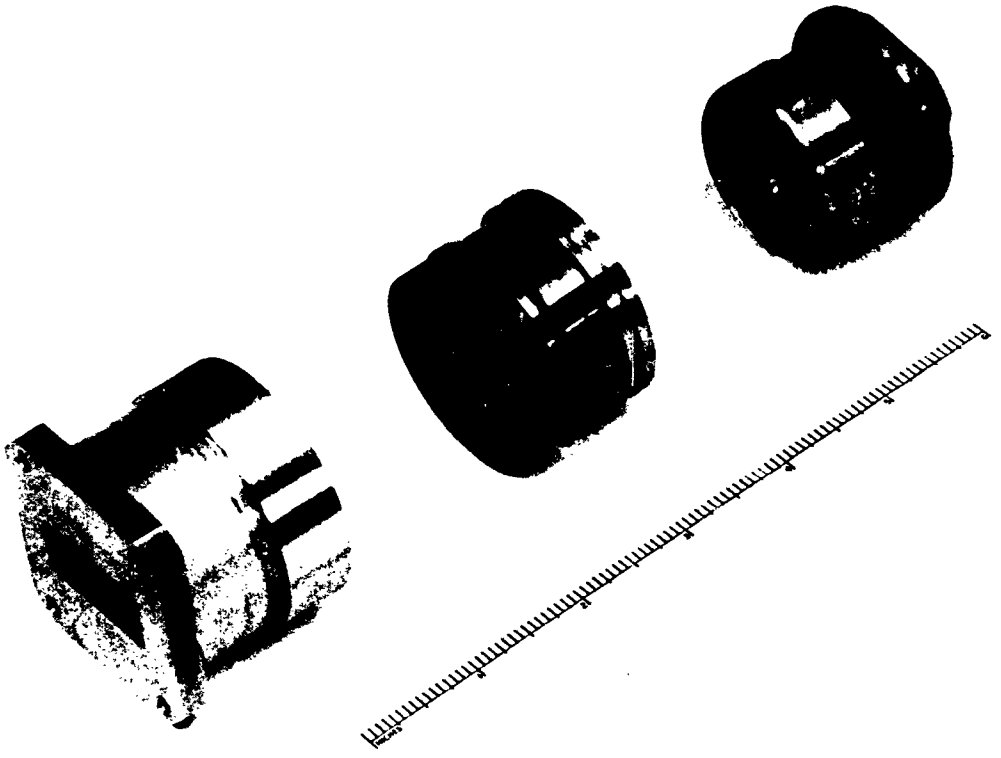

Figure 6. R-f Waveguide Window used for Input and Output

The r-f input and output couplers shown in Figure 5 consist of reduced height rectangular waveguide transforming to a coaxial section and thence to the slow-wave circuit. Dimensions of waveguide and coaxial sections were designed to avoid propagation of higher order modes in the operating band and to avoid multipactor effects. The VSWR of the couplers was maintained at less than 2:1 over the operating band, including the π-mode. The VSWR is less than 1.5:1 over a large part of the frequency band. The coupler performance was considered satisfactory in the loop mode from 13.5 to 15.5 Gc. The waveguides, tapering from reduced height X-band to large X-band size, were electroformed to the coupler and to the windows, to eliminate the need for brazing.

Figure 6 shows the input and output windows. The window configuration, known as a waterfall design, consists of a large X-band rectangular waveguide at either end, transformed to a circular section in the center. This window is rated at approximately 2 kw, with pressurizing and gas flow for cooling and for ion-sweeping across the window face. The bandwidth of the window (with a VSWR less than 1.2:1) covers the hot bandwidth of the tube up to and including the π-mode.

The present electron gun, shown in Figure 7, is a convergent-flow diode gun, using a dispenser-type cathode. The beam diameter and the perveance are lower than the designed values. The operating perveance is 0.66×10^{-6}, giving a cathode loading of 6.6 amps/cm^2 at 130 kv. A second gun, with a perveance of 1.2×10^{-6} has been tested and will be used in the next tube.

The collector, shown in Figure 8, was designed for space-charge beam divergence with acceptable heat distribution at high average powers. The coolant flows around a double-start thread and the whole collector is insulated from the tube body for monitoring collector current.

A pre-focus coil is used in the cathode region. The main focusing coils were designed to provide a flux density of 2500 gauss. The tube envelope, r-f couplers, and focusing coils are all liquid cooled.

TUBE DESIGN, ASSEMBLY, AND PROCESSING

The tube was designed to permit easy modification or replacement of the major components. Figure 9 shows a completed tube ready for processing. The tube was evacuated by a diffusion pump system which was subsequently valved off by a bakable valve. The tube is now continuously pumped with a VacIon appendage pump.

TUBE TEST

The d-c beam pulses have a 2-microsecond flat top, and rise and fall times of less than 0.5 microsecond. The beam voltage and current are measured on an oscilloscope with an appropriate capacity divider and a current transformer. The collector pulse current is read as a voltage drop across a 2-ohm non-inductive resistor. The average collector power, measured by a calorimeter, agrees closely with power calculated from the collector pulse current, beam voltage, pulse length, and pulse repetition rate (usually 60 to 100 pps). Figure 10 is a block diagram of the input driver chain, and Figure 11 is a diagram of the output power monitor and measurement chain.

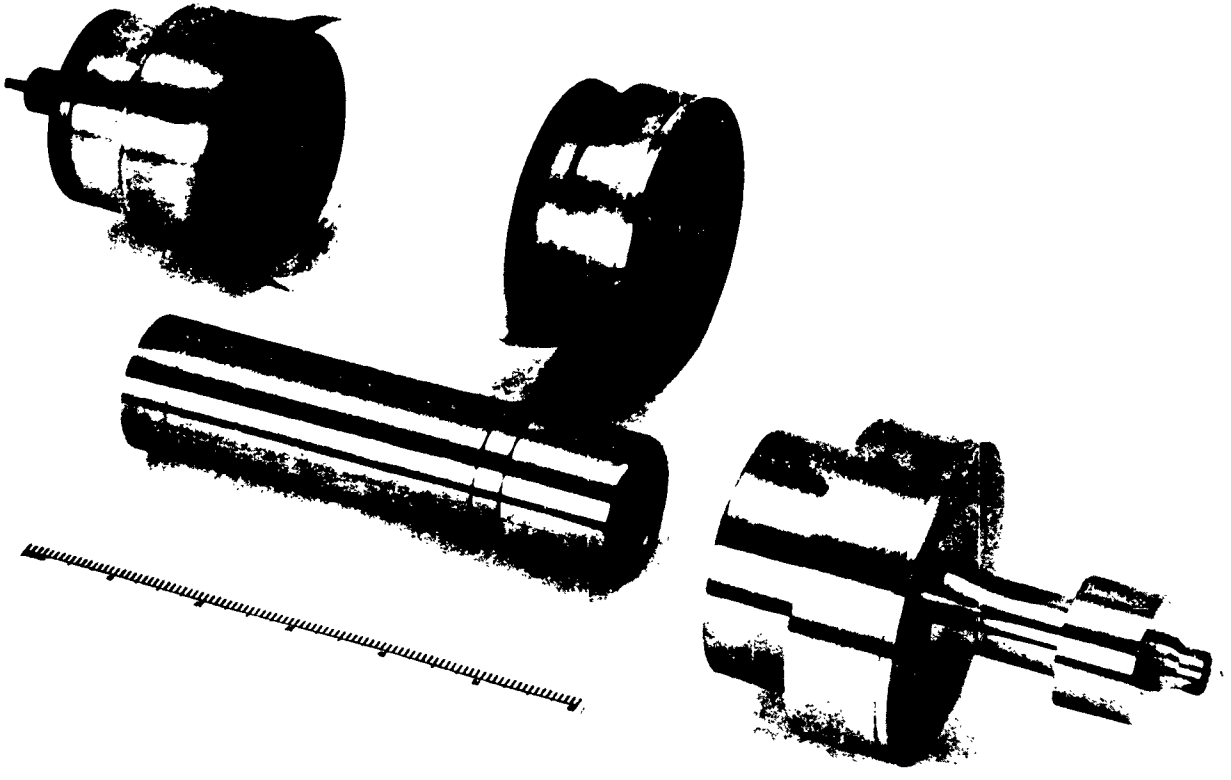

Figure 7. Electron Gun Components.

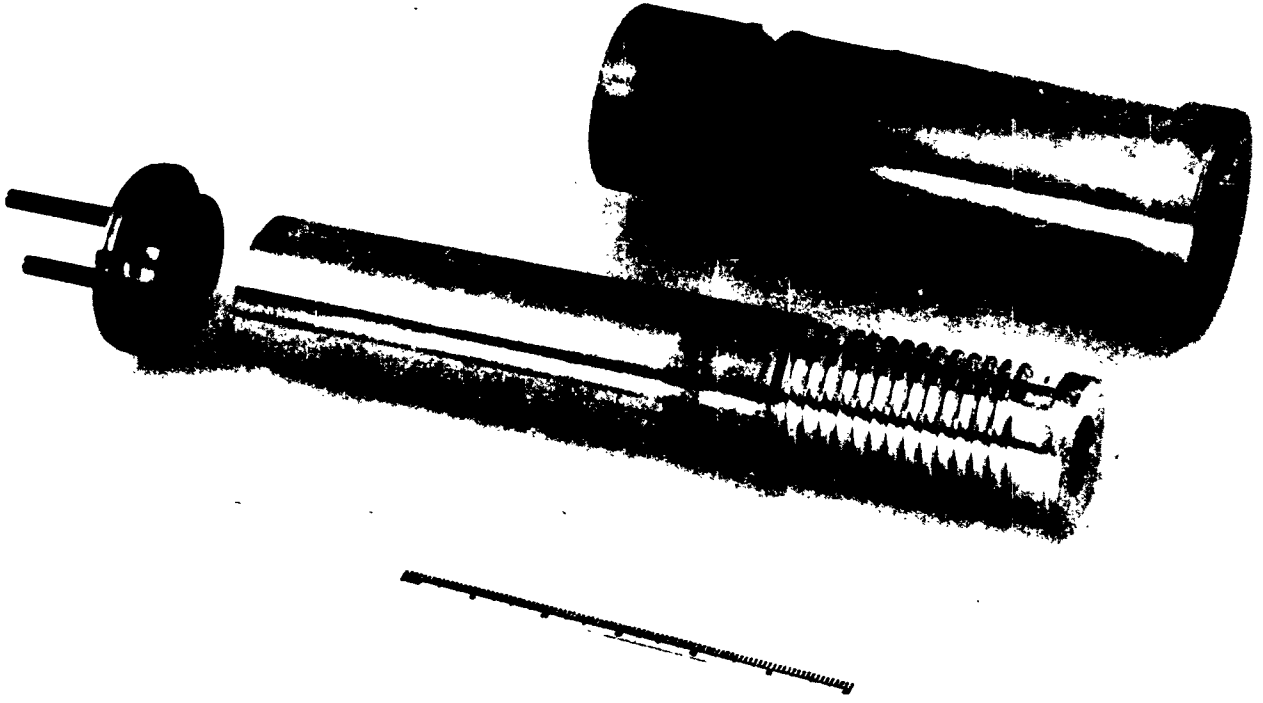

Figure 8. Water-cooled Collector Components.

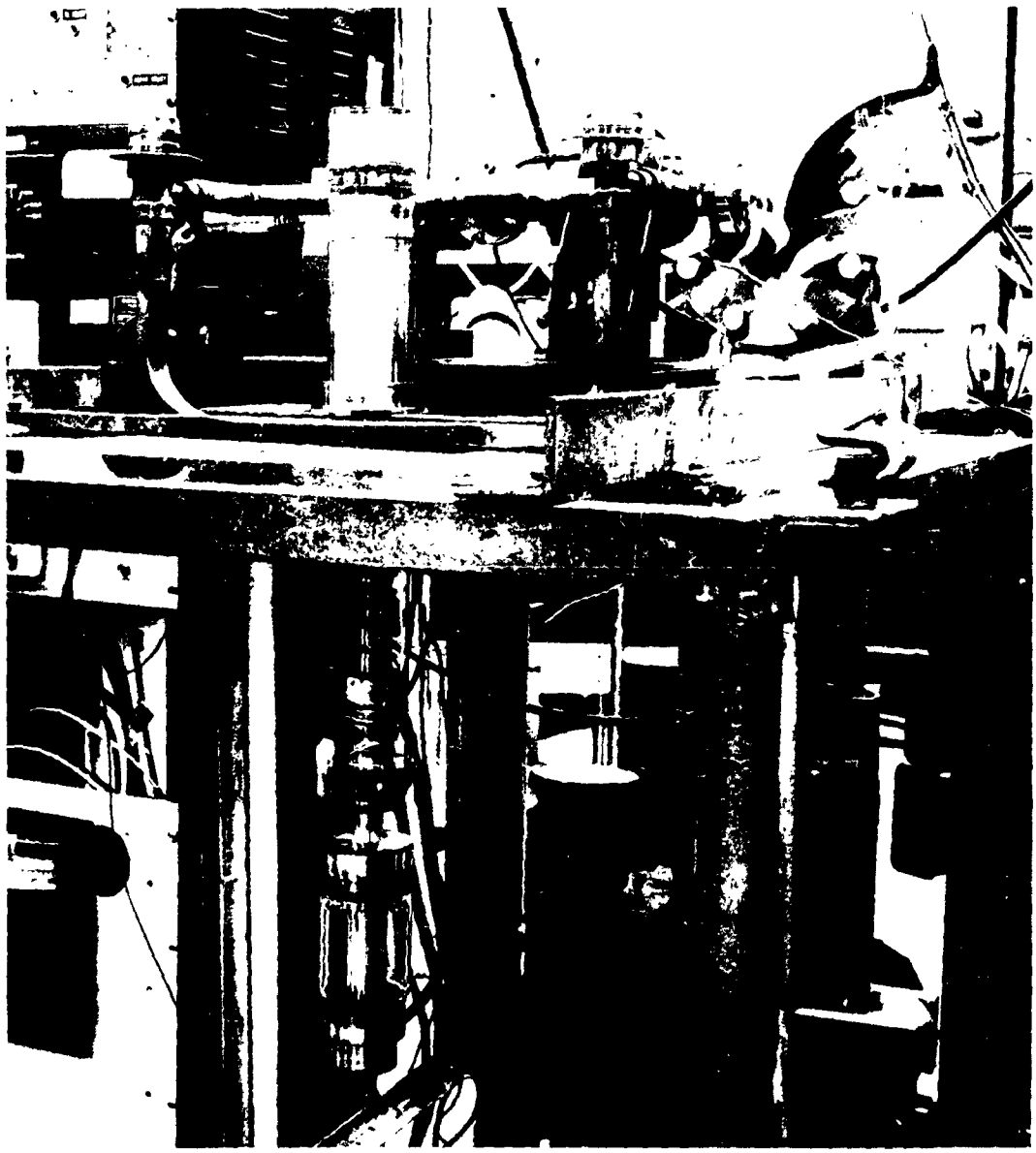

Figure 9. SYT-4341 ready for final processing.

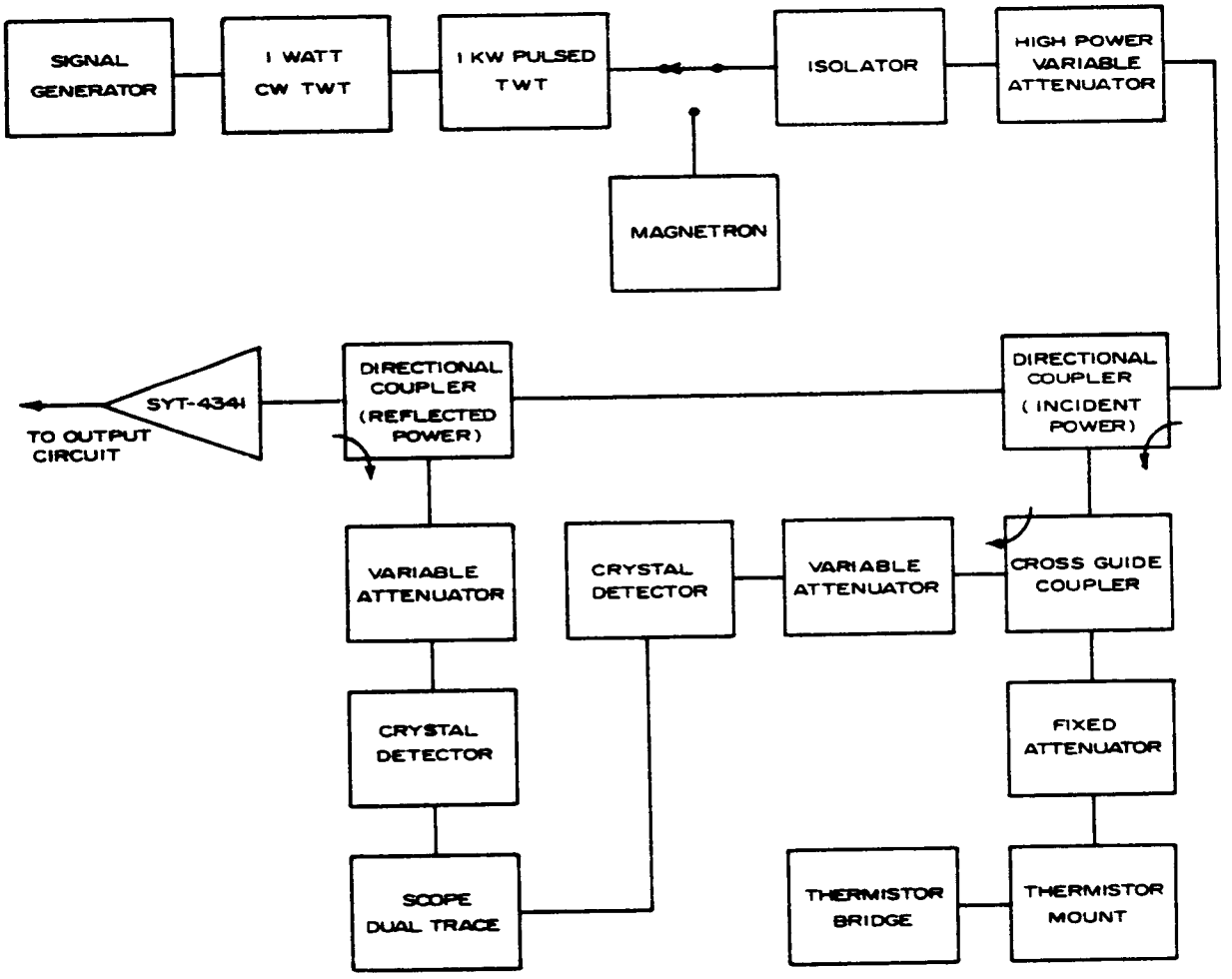

Figure 10. Block Diagram of Input Driver Chain.

Excellent beam transmission (over 95%) has been achieved under saturation conditions. The required focusing fields for saturated power have averaged between 1450 and 1700 gauss (approximately 1 1/2 times the Brillouin value) for beam voltages up to 150 kv. No cavity-mode band-edge oscillations, loop-mode backward-wave oscillations, or regenerative oscillations have been observed.

Figure 12 shows all of the data taken up to this time. Saturated power was measured at 120, 140, and 150 kv at various frequencies in the range 8.5 to 9.5 Gc and should be accurate to within $\pm$ 10%. The focusing fields were optimized for each reading. At 150 kv a peak-power of 1.15 megawatts was obtained with a peak efficiency of 24% calculated from the calorimeter readings. At 120 kv the estimated saturated 3db bandwidth is 15 to 18%. This is based on the measurements in the frequency range from 8.5 to 9.5 Gc and the extrapolation of the curve for the higher frequencies.

The initial results from the first tube are completely satisfactory. The second tube, under construction, will incorporate a tapered output and a higher perveance electron gun. These improvements should allow the second tube to provide 1.8 megawatts peak power with an efficiency of 30% and a saturated bandwidth of 18%.

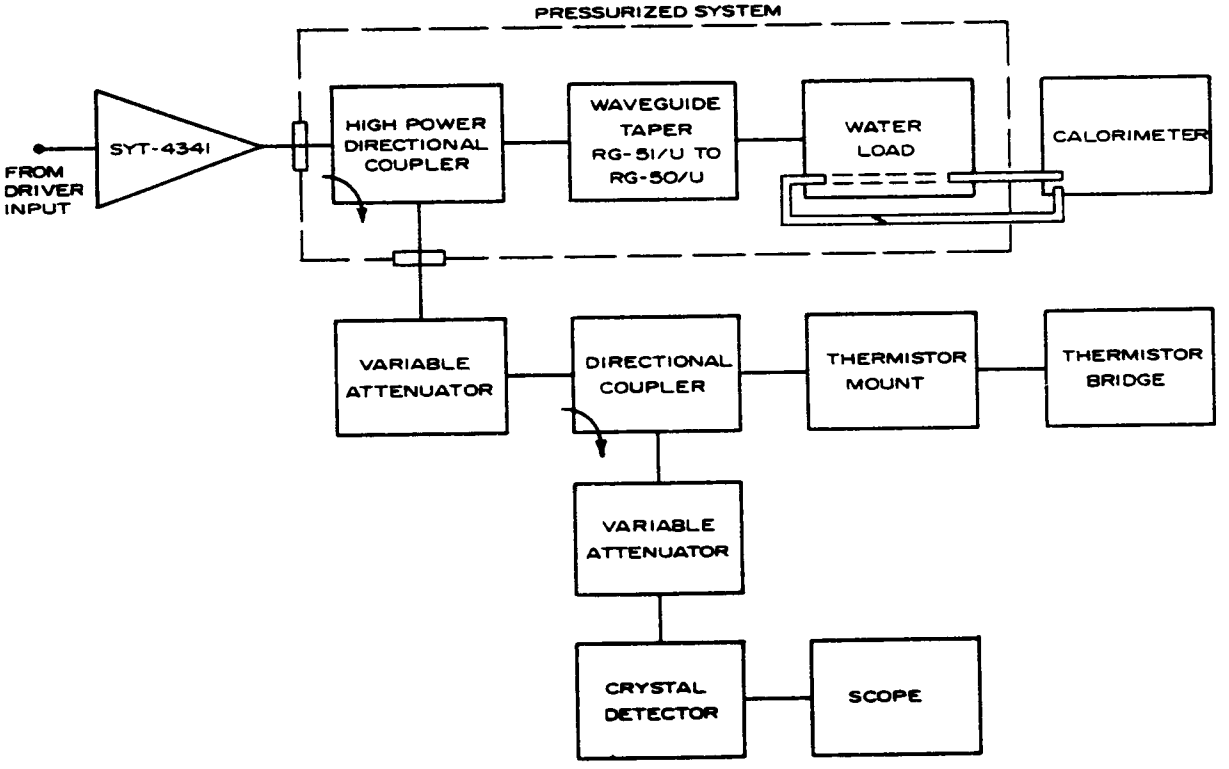

Figure 11. Output Power Monitor and Measurement Chain

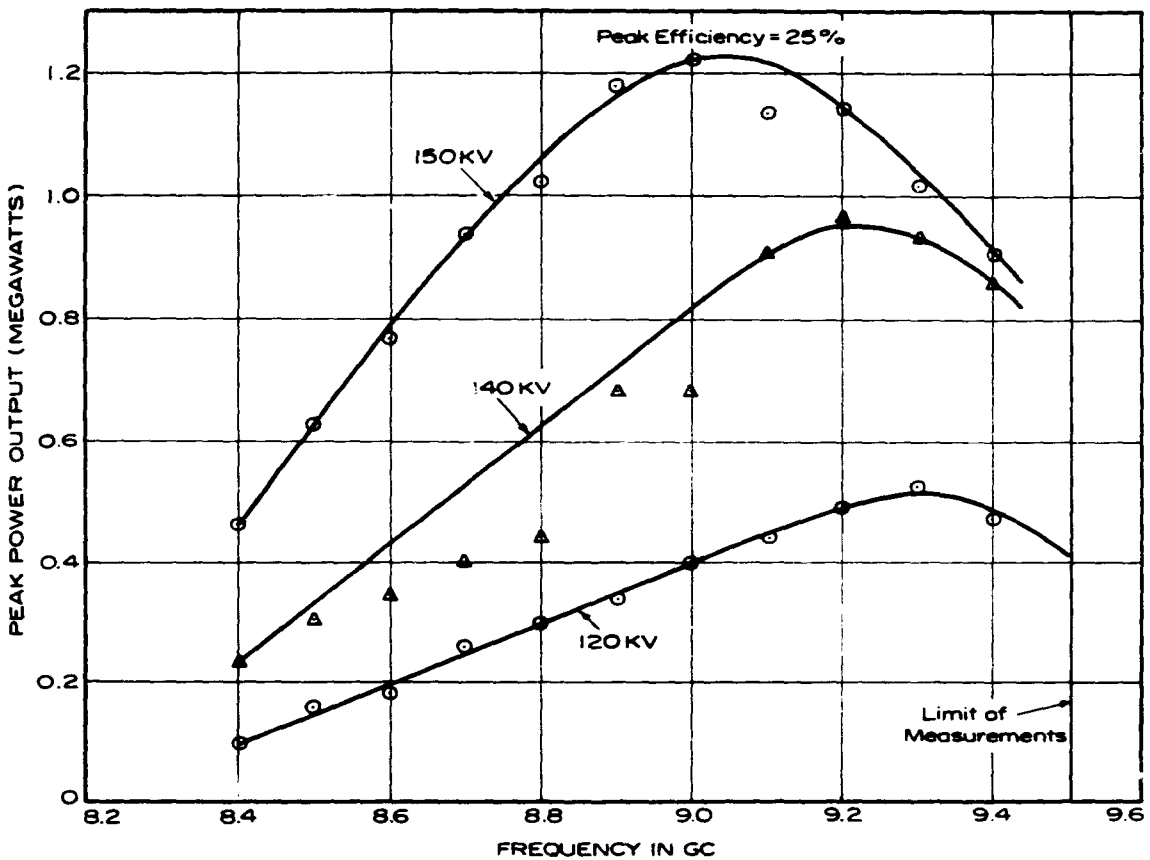

Figure 12. Peak Output Power versus Frequency at Saturation

HIGH POWER CW AMPLIFIER FOR 50-56 Gc FREQUENCY RANGE

By

John E. Nevins, Jr.

Hughes Research Laboratories

I. Introduction

During the past several years a research program devoted to developing the millimeter wave tube technology has been conducted at the Hughes Research Laboratories. The program whose primary objective is to apply this technology to high power CW amplifiers and oscillators has been jointly sponsored by the Bureau of Ships, Nobsr 81198, and the Hughes Aircraft Company. The subject of this paper is one development of our program, a high power CW amplifier designed to operate in the 50-56 Gc frequency range.

Initially when this program was started, a set of objectives were laid out to act as guide posts and seemingly would be a significant advance in the state-of-the-art. Of course the chosen frequency range has possible system applications, but more important, it was a branching off point where the tube technology which we were familiar with was not adequate.

The paramount problems are the formation of a well-controlled electron beam and the fabrication of tube parts that could be assembled to extreme tolerances. The success of our efforts in these areas when combined have resulted in tube performance that significantly surpassed our original objectives and is just the prelude to more substantial results.

The CW amplifier has produced powers in excess of 150 watts when operated as a forward-wave oscillator, with efficiencies greater than 30 percent. The first series of amplifiers were narrow-band (4 percent) low gain (17 db); however, the bandwidth has been increased in the latest versions. Depressed collector operation has increased the over-all efficiency in excess of 30 percent when the electronic efficiency was 8-10 percent.

Higher powers and increased gain will be obtained when increased gun perveance and multiple sections internally terminated are utilized.

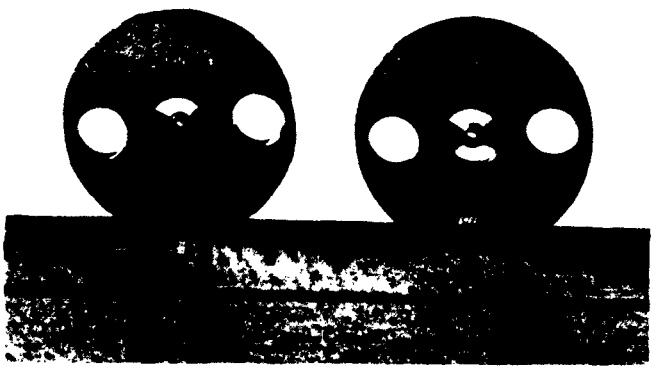

Fig. 1. A typical coupled cavity section.

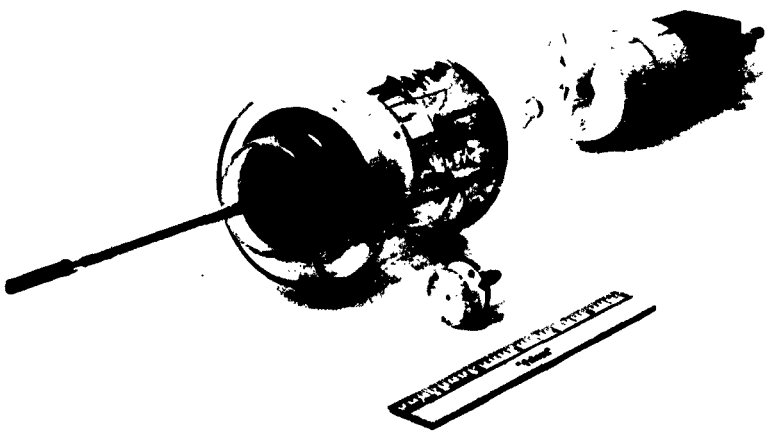

Fig. 2. The four times scale beam tester.

II. General Discussion

When the study was initiated, the hope was to build an amplifier with CW capability producing 50 watts of average power, 20 db gain, 10 percent bandwidth and as high an efficiency as possible. The initial design called for an electron gun whose perveance was 0.1×10^{-6} to operate at 10 KV with a nominal beam diameter of .015". At the perveance and voltage chosen, the power density in the beam is approximately 0.9 megawatt/cm^2 and an average beam power is 1 kilowatt. Of course, the beam diameter of .015" is a nebulous dimension in that the thermal velocities play an important role due to the large area compression. It is necessary to over focus the beam with a magnitude field greater than the Brillouin field and scalloping of the beam occurs.

The cathode loading of 1.0 amp/cm^2 was a conservative choice and as a result requires a relatively large area compression. If one were to use a 2 amp/cm^2 cathode loading, the area compression would be reduced accordingly and the beam would be more easily focused; however, the gun would not be easily scaled to higher frequencies which was the intention.

Another factor that critically affects the electron optics are the exacting tolerances. Dimensional tolerances such as the focus cup to cathode spacing are extremely important and are of the order of .002". The assembly and alignment of gun and circuit are exacting when you realize that the beam will follow a helical path if not centered in the magnetic field, and translaminar streams originating at the cathode rim due to improper positioning of the cathode will effectively enlarge the electron beam. When you consider that the rf circuit drift tube is .020" in diameter, focusing and tube construction must be excellent if beam interception is not to limit the tube performance.

The decision as to the preferred rf circuit to be used was based on two factors, heat dissipation and low voltage operation. Good heat capacity requires not only heat conductivity but a maximum amount of metal volume in the circuit. Low voltage is desirable for CW operation because it allows the maximum current for a fixed power dissipation. The coupled cavity circuit meets these two requirements most adequately since it is a very massive copper structure and the coupled cavity operates on the (+1) space harmonic. Pictured in Figure 1 is a typical cavity section. An aggregate of such circuit sections are stacked together to form the rf structure. The doubly re-entrant coaxial cavities are coupled by a slot in the transverse wall which is oriented 180 degrees with respect to the adjacent slots.

One might consider that such an rf structure would be too difficult to fabricate and assemble at 5 mm; however, it is possible and moreover economical when proper tooling and mechanical design are utilized.

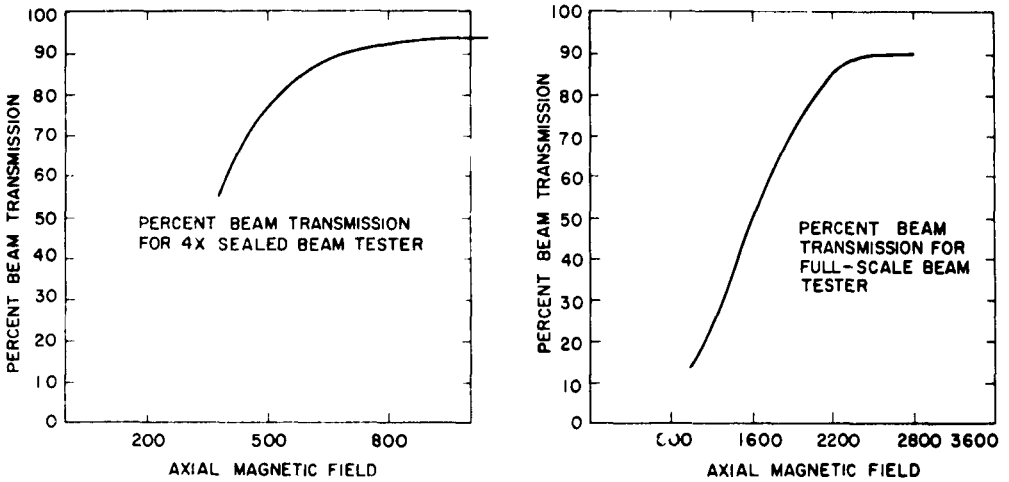

Fig. 3. A plot of percent beam transmission as a function of magnetic field for the 4x scaled gun tester and the full-scale gun.

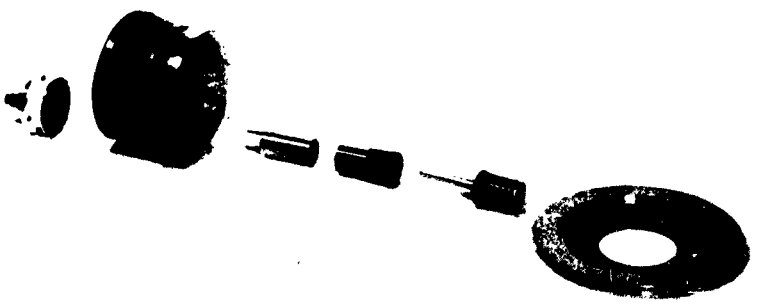

Fig. 4. Full scale beam tester.

III. Component Design and Operating Data

Electron Gun

The 0.1 microperve electron gun was designed using standard methods and constructed to four times the full scale. By so doing the gun could be tested in both electrostatic and magnetic demountable equipment as well as in a glass beam tester. The electrostatic tests gave the measurement of current density as a function of axial distance so that position of the beam minimum could be determined. The current density measurements also can indicate translaminar electron streams which may enlarge the beam. This was not the case with our gun.

Once the beam minimum is located the gun was tested in a 4 times scale beam tester shown in Figure 2. A drift tube of .080" simulated the rf circuit. By moving the beam tester with respect to the solenoid pole piece and by eliminating cathode flux with a bucking coil, the transmission characteristics illustrated in Figure 3 were obtained. Ninety percent beam transmission at approximately 700 gauss was achieved.

A full scale beam tester was assembled which consisted of a block of copper one inch in length with a .020" diameter drift tube machined through it and the necessary pole pieces. Because of alignment problems and a slight curvature of the drift tube, the effective drift tube diameter was reduced to .019". The beam transmission achieved with this arrangement is shown in Figure 4. Ninety percent beam transmission was achieved with 2800 gauss.

Because of the thermal spreading of the beam there is a tail on the current distribution; this fact has been demonstrated by previous authors and also measured in our experiments. The beam as it travels through the tube will scallop due to over-compensation of the space charge forces. The beam images the cathode with a near uniform current distribution and then scallops in. Because of this thermal spread, it is impossible to get 100 percent transmission without increasing the drift tube diameter to the detriment of the tube's rf performance.

RF Circuit

There are a number of components such as vacuum windows, circuit transitions, and elbows that have to be designed. Most of the design was accomplished at low frequencies and then scaled to the 50-60 Gc range.

The vacuum window that has been used consisted of a .001 mica disc approximately .200" in diameter which was placed in a recess machined in a stainless steel flange. A copper washer was also placed in the recess and compressed between two flanges. The copper washer so compressed formed a vacuum seal and also rf tuned the window. The typical VSWR of the window is less than 1.08:1. The assembly is shown in Figure 5. The window assembly has withstood bakeout temperatures greater than 500°C and pressures of eleven atmosphere.

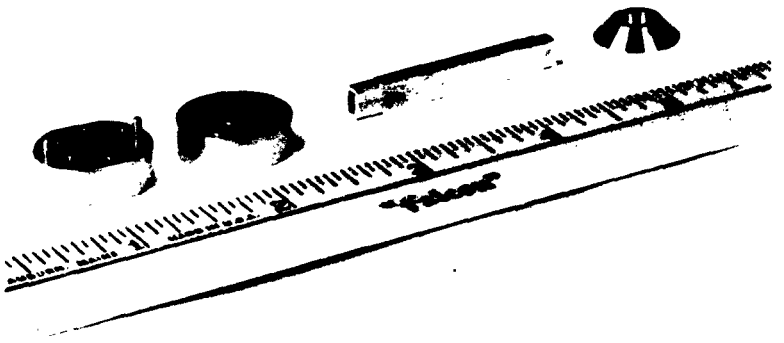

Fig. 5. Millimeter-wave vacuum window assembly.

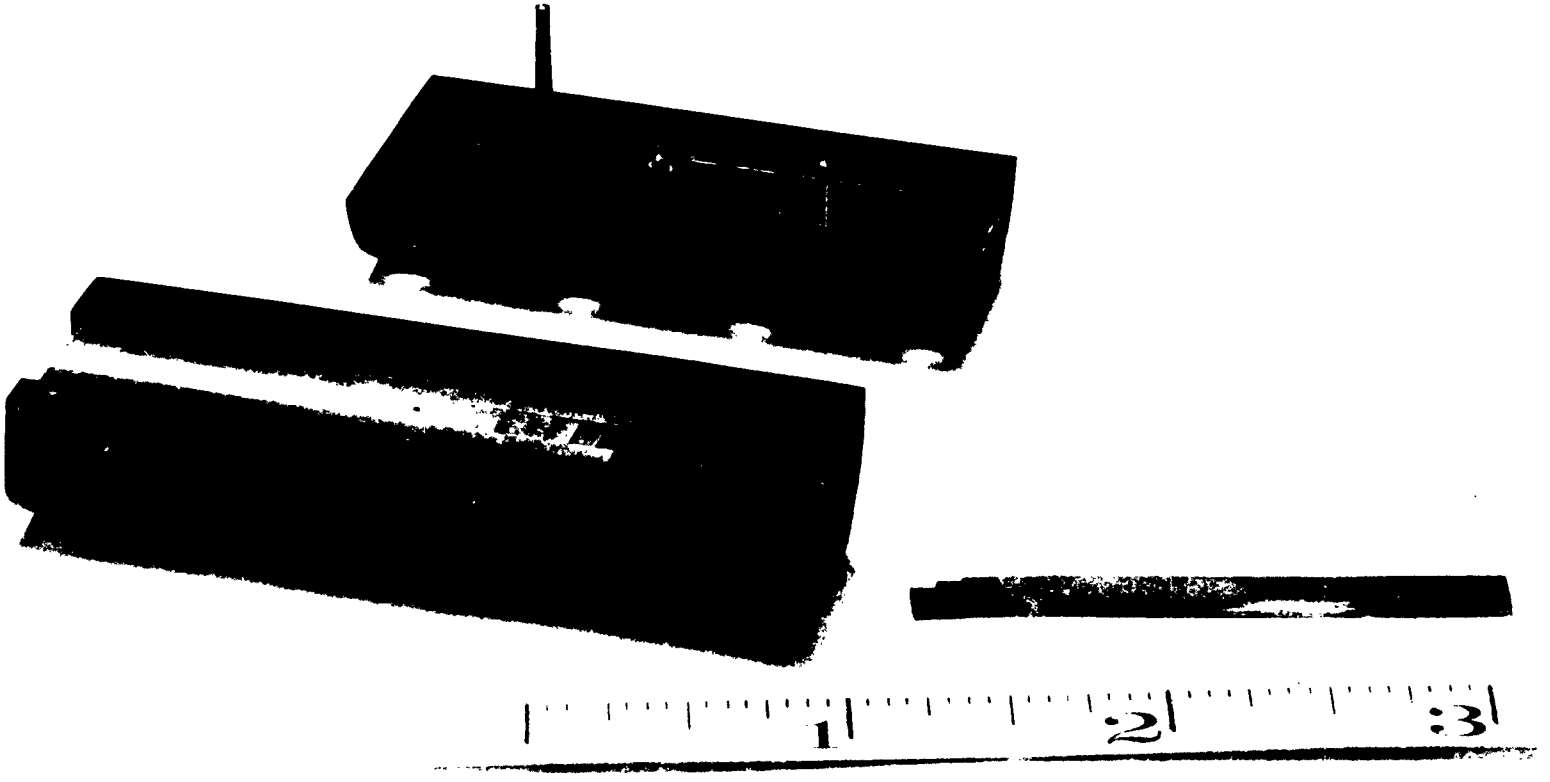

Fig. 6. Millimeter-wave match section assembly.

The rf transition to the coupled cavity circuit was constructed from a step transformer, a length of narrow height waveguide, and an adjusted iris cut in the side wall of a half cavity section. Typical X-band match sections had a VSWR less than 1.5:1 over a 15 percent bandwidth. The VSWR deteriorates as the transition is scaled a factor of 6 times to the 50-60 KMC frequency range and the maximum VSWR is increased to 1.7:1. Figure 6 shows the circuit transition assembly. Recent improvements in the match have reduced the VSWR to less than 1.5:1 over the frequency band of interest.

The basic circuit sections were fabricated in a number of ways. Hobbing the part was attempted and after a number of design changes a cavity section could be formed that only required a lapping operation to restore the crowning of the section to the required flatness. Although this method of forming the basic cavity was developed to a final design, machining techniques were used to make our cavity sections. Using proper tooling, the cavity sections are machined on an instrument lathe, with all dimensions indexed from two alignment holes that are initially punched in a circuit blank. The coupling hole is punched in the form of a sector. The dimensions are listed below.

Cavity depth	.024"
Cavity OD	.109"
Cavity ID	.034"
Beam Hole	.020"
Circuit Period	.036"
Cavity Gap	.0068"

The tube when assembled is aligned by means of stainless steel tubing which passes through circuit sections, match sections, pole pieces and electron gun anode. Usually after assembly the effective beam hole diameter is reduced to .0195" from .020".

Pictured in Figure 7 is a tube assembly.

Operating Data

The initial design of the amplifiers was completed at X-band frequencies, and scaled to operate at 50-56 kMc. One aspect of the design could not be scaled and that was circuit loss. The estimates of loss were of the order of 0.5 db per cavity based on data obtained from X-band amplifiers. Actually, the loss was 0.1 db per cavity or less, which unfortunately reduced the expected electronic bandwidth of the amplifier. Since tooling and the match sections were completed, the tubes were assembled with a predicted small signal bandwidth of 4 percent. The data to be presented was for this design. Subsequently, we have increased the bandwidth to 8 percent by increasing the coupling between cavities. One factor that works against wide bandwidth is the low value of C, (Pierce's gain parameter) which is of the order of 0.03.

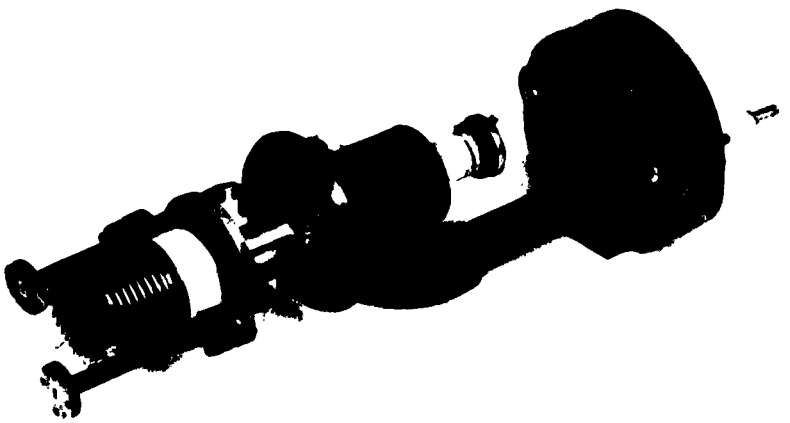

Fig. 7. A millimeter-wave power amplifier.

Fig. 8. The millimeter-wave power amplifier and driver tube mounted in solinoids.

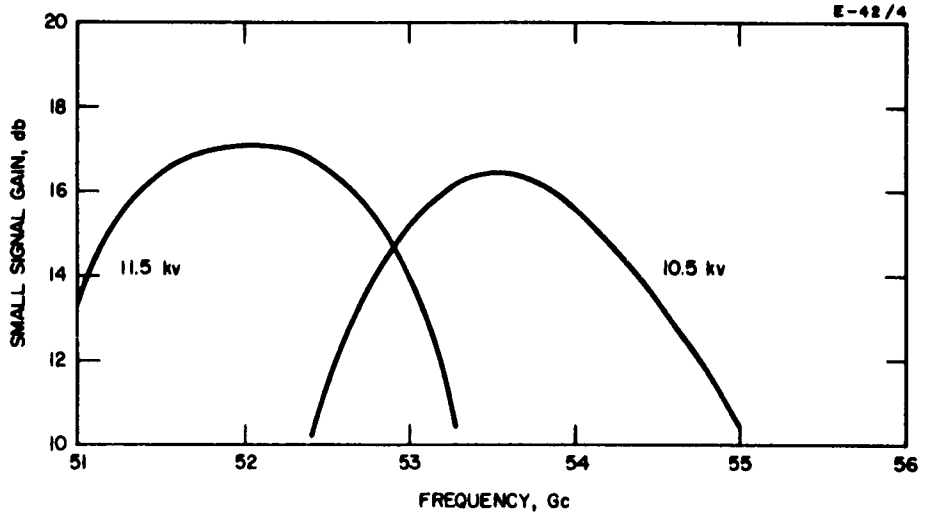

Fig. 9. The small signal gain of the HAV-1.3 millimeter-wave power amplifier.

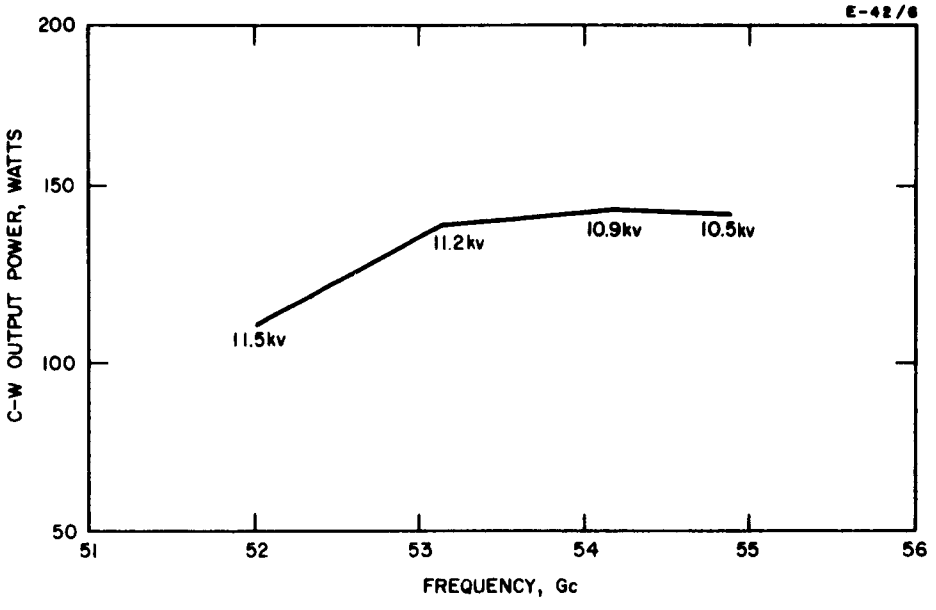

Fig. 10. The efficiency of the HAV-1.3 when operated as self-excited oscillator.

Figure 8 shows the power amplifier mounted in the solenoid with a second tube operating as a forward-wave oscillator driver. The small signal gain of the tube is shown in Figure 9 for several values of beam voltage. The maximum gain was 17 db.

The tube could not be driven hard enough to get saturated power output measurements. No adequate driver tube was available. The maximum output power when driven by a pulsed source was 100 watts and the tube gain was still quite linear. In order to get a measure of the output power capability, the tube was operated with a feedback network and made to oscillate at several frequencies by varying the beam voltage. Shown in Figure 10 is the CW output power as a function of frequency when the tube is operated as a forward-wave oscillator. This power measurement is the power delivered to a load, and does not include the power in the feedback loop or the additional loss due to the increase in surface resistivity of the waveguide due to heating. The waveguide temperature was 80°C.

The tube is operated with a depressed collector. The electronic efficiency was approximately 8 percent and the system efficiency approximately 30 percent. Shown in Figure 11 is the system efficiency when the measured power output is compared to total DC power input. The values of efficiency presented are lower than actual for the reason quoted in regard to output power. I might add that since this data was taken the operation of our collectors has been improved by use of transverse magnetic fields in the collector region, which reduce secondary electron back currents.

The amount of collector depression is a function of rf power output. Plotted in Figure 12 is the percent beam transmission as a function of collector depression. When there is no input drive power, the collector can be depressed to 95 percent without the beam transmission decreasing appreciably. The tube was operated at 75 percent depression which reduced the beam transmission to 88 percent when maximum output power was achieved.

The tube has been operated in a permanent magnet. The beam transmission was the same as with a solenoid; however, the collector could not be depressed adequately. The one difficulty with the magnet design was the presence of large leakage fields at the collector. When the collector voltage was depressed, the body current increased excessively. Figure 13 shows the tube and magnet package.

IV. Conclusion

The traveling-wave tube amplifier that has been described in this paper has demonstrated that by utilizing excellent electron optics and refined tube assembly techniques very high CW power can be obtained at millimeter frequencies. With further developments in severed high gain tubes and improved beam optics, the results presented in this paper will be extended not only in tube performance but also to increased frequency.

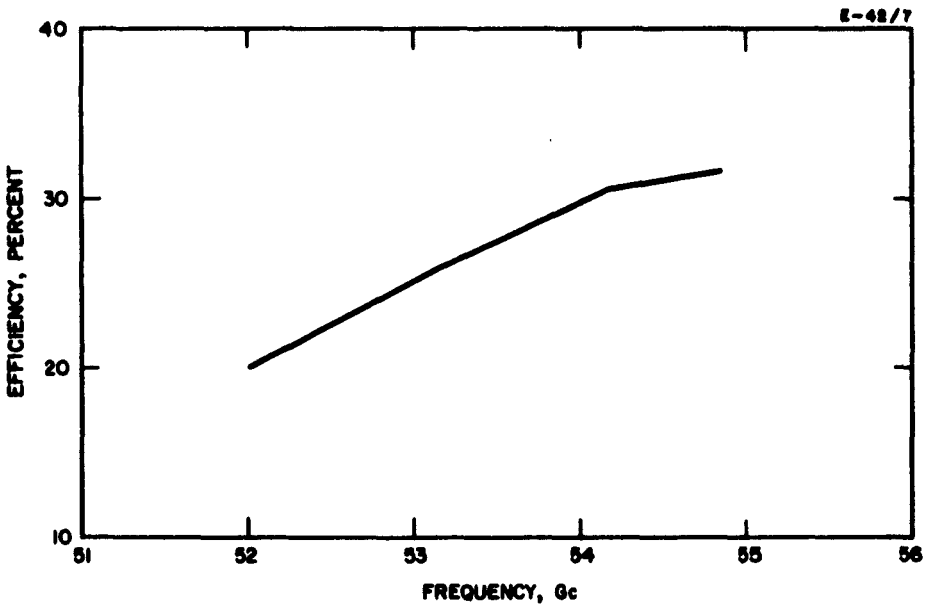

Fig. 11. C-w output power of the HAV-1.3 when operated as self-excited oscillator.

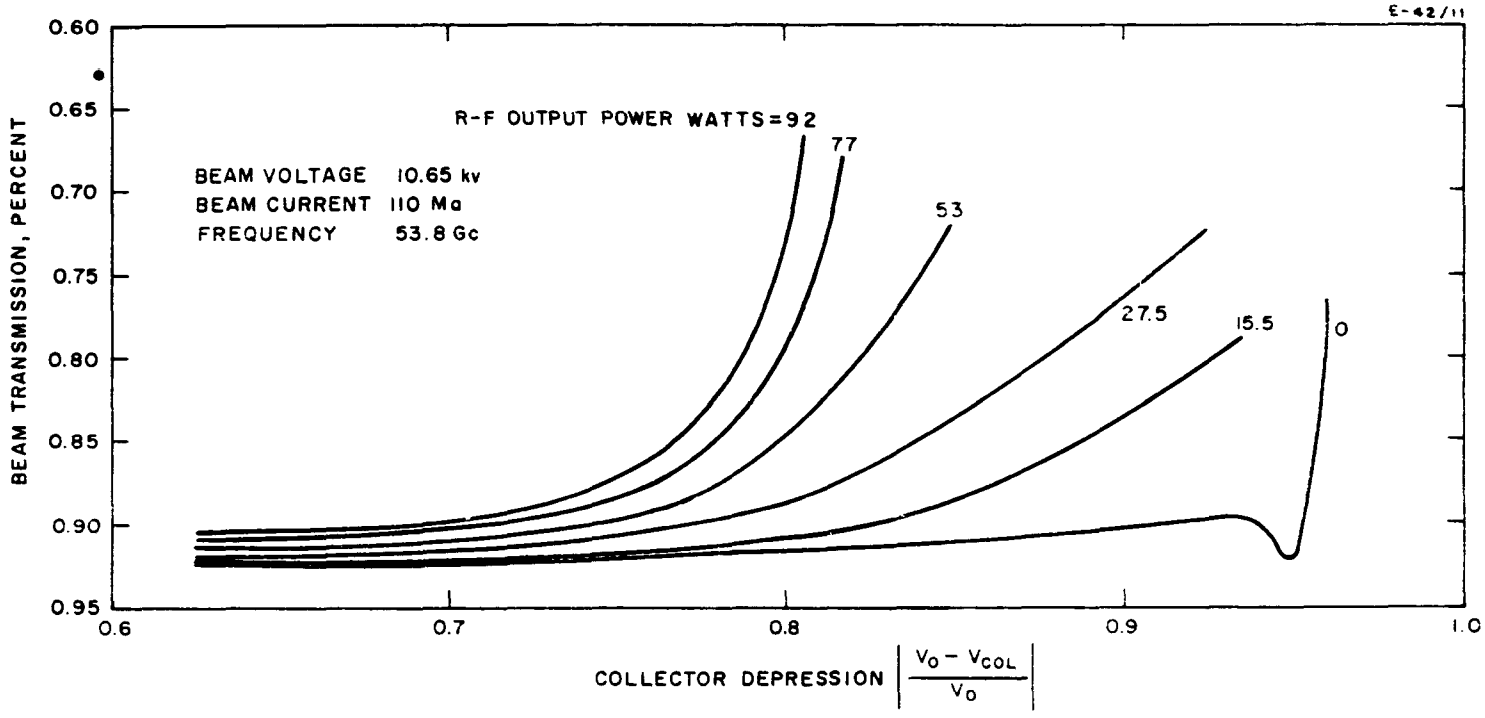

Fig. 12. A plot of the collector characteristic with various levels of r-f driver power.

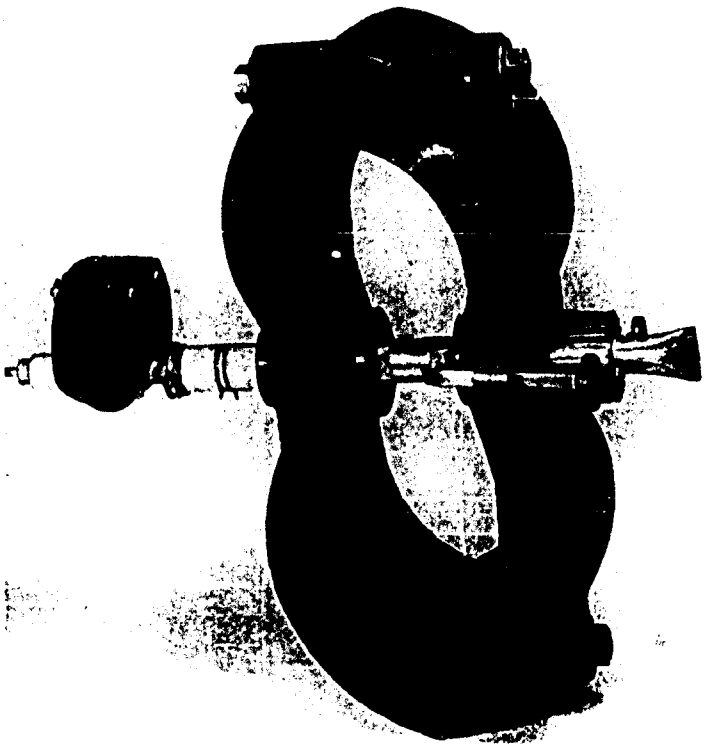

Fig. 13. The permanent magnet and millimeter-wave power amplifier.

A 100 GC HIGH-POWER BACKWARD-WAVE OSCILLATOR*

By

James W. Sedin

Watkins-Johnson Company
Palo Alto, California

The objective of the work to be described is to take a really significant step in the direction of achieving very high power at very high frequency by conventional beam tube techniques. The objective specifications of the particular tube being developed are shown below in Fig. 1. The WJ-225 is a backward-wave oscillator designed to produce 100 kw peak power and 1000 watts average power at 100 Gc. This frequency and power level does not represent an ultimate limit but rather an achievable goal that is an order of magnitude greater in peak power and 2 orders of magnitude greater in average power than existing tubes. The tube operates at voltages up to 200 kv and beam currents up to 11 amperes.

* The research reported here was performed under Contract No. AF 33(616)-8369 and was sponsored by:

Aeronautical Systems Division
Electronic Technology Laboratory
Air Force Systems Command
United States Air Force

DEVELOPMENTAL SPECIFICATION

PERFORMANCE	Typical
Power output	100 kw peak 1 kw average
Frequency range	98-101 Gc
Efficiency	5 percent
ELECTRICAL REQUIREMENTS	
Beam voltage	150-200 kv
Beam current	11 a
Heater power	80 watts
MECHANICAL	
Length	30 inches
Diameter	3 inches
Weight	30 pounds

Fig. 1 - WJ-225, 100 Gc high power voltage tunable backward-wave oscillator.

The reason for developing a backward-wave oscillator, which has perhaps questionable value in systems applications, is that the over-all cost of the development is considerably lower than it would be for an amplifier since no rf driver and associated hardware and test equipment is required. The basic development problems associated with beam formation and focusing, circuit construction, and rf breakdown are similar for an oscillator or an amplifier.

An experimental tube has been constructed that has produced of the order of 100 kw peak power and 50 watts of average power. Oscillations have been measured from 94.2 to 101.3 Gc.

In the following sections, the basic tube design will be summarized and the individual components of the tube will be described. Test results obtained on the experimental tube will be presented and the direction of the continuing effort outlined.

Tube Design

The basic problems encountered in designing tubes for very high frequencies are that the circuit structures become extremely delicate and difficult to construct with sufficient accuracy, and the current density required from the cathode becomes large. Both of these problems are greatly eased by designing for high voltages and lower currents because the dimensions of the beam hole and the circuit period increase with the electron velocity and the current density required from the cathode decreases inversely as the square of the voltage for a fixed beam power, at least where relativistic effects are unimportant. In fact, the only parameter that does not improve with a decreased perveance is the interaction parameter C and therefore the efficiency and gain per unit length. Fortunately, for very high power tube designs it is possible to get reasonable C factors with relatively low perveances.

The tube that we have designed utilizes a perveance 0.125×10^{-6} beam at voltages up to 200 kv. The cathode loading at 11 amperes beam current is only 1.5 amperes/cm^2. The circuit used is a simple disc-loaded waveguide operated on the first backward space harmonic just past π phase shift per section. The disc-loaded waveguide is geometrically simple and easy to construct accurately and is extremely rugged thermally. Figure 2 is a photograph of the first experimental tube. There are no high power windows on this tube. The rf power is dissipated in vacuum loads and sampled by means of a 40 db directional coupler. The tube is a very high power tube by any scaling rule. It is frequently assumed that the maximum rf power that can be achieved at a particular frequency is given by the relation

$$P_f^2 = \text{constant.}$$

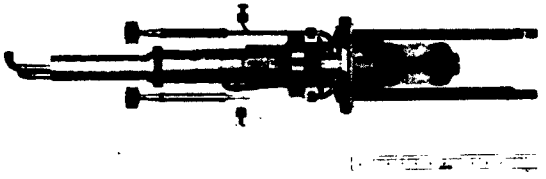

Fig. 2 - WJ-225, experimental 100 Gc backward-wave oscillator.

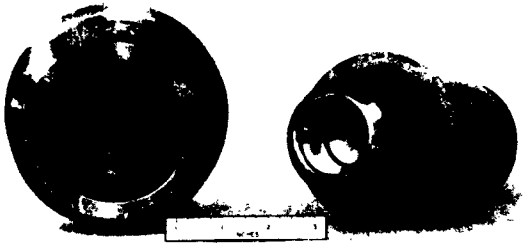

Fig. 3 - High convergence perveance 0.125 x 10^{-6} electron gun.

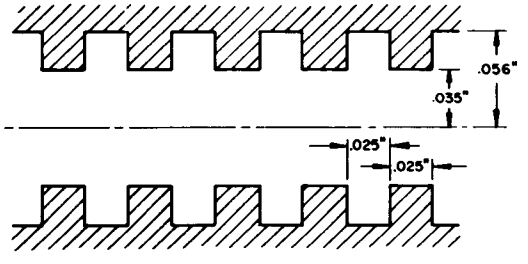

Fig. 4 - Dimensions of the disc-loaded waveguide circuit.

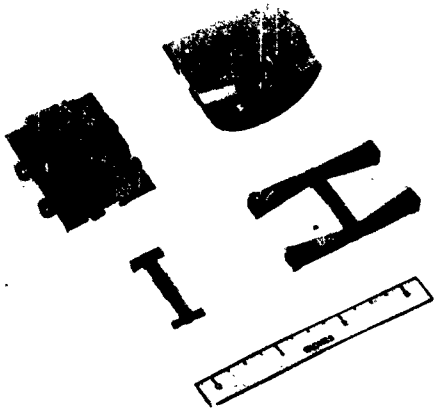

Fig. 5 - Electroformed disc-loaded waveguide and cooling block.

If this rule is used and the fact that the efficiency of the BWO is about a factor of three below that of an equivalent amplifier, this tube corresponds to a 30 megawatt tube at X-band

The Gun

Figure 3 is a photograph of the electron gun. The cathode diameter is 1.2 inches and the circuit drift tube diameter is 70 mils. The beam formed by this gun was measured to be 40 mils diameter at 14 kv and is probably about 13 mils diameter at 200 kv. The area convergence from 1.2 inches to 40 mils is 900. An 11 ampere beam 40 mils in diameter has a current density of 1350 amperes/cm^2. Beam transmission was consistently better than 94.5 percent through a 70 mil drift tube 1.25 inches long.

The Circuit

Figure 4 is a cross-sectional drawing showing the dimensions of the disc-loaded waveguide circuit. The dimensions are not particularly small and the circuit is extremely rugged thermally. A single circuit disc could withstand about 1/2 percent beam interception on a 5 microsecond pulse at 200 kv. The circuit is matched to two waveguides on each end. The double waveguide match reduces the peak power that must be transmitted by the waveguide and it loads the output cavity more symmetrically than would be possible with a single waveguide match. The entire circuit and matching waveguides was electroformed in one piece. In this way it was possible to hold very close tolerances on the circuit dimensions and circuit loss was reduced to a minimum because all braze joints were eliminated. Figure 5 is a photograph of an electroformed circuit. The internal circuit dimensions were held to within ±0.2 mils. Each match cavity contains 4 eight mil diameter pins located 4 mils away from the cavity wall. These pins were located in the mandrel and electroformed in place.

The ω-β diagram for the disc-loaded waveguide is shown in Fig. 6. The circuit dimensions are such that the γa of the beam hole at 200 kv, which corresponds to a frequency of about 101 Gc, is 1.9. At 140 kv, which corresponds to a frequency of 99.6 Gc, $\gamma a = 2.34$. At 110 kv, which corresponds to a frequency of 98 Gc, $\gamma a = 2.64$. The impedance of the first backward space harmonic is shown in Fig. 7. It decreases very rapidly as the beam voltage is decreased. Nevertheless, $C = 0.041$ at 200 kv and $C = 0.019$ at 140 kv. Our experience with high power oscillators at lower frequencies would lead us to expect efficiencies of 5 to 10 percent. The circuit structure is about 1.2 inches long which is just enough for start oscillation at 140 kv.

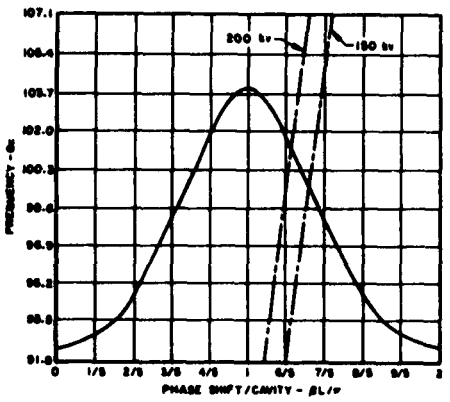

Fig. 6 - Disc-loaded waveguide ω-β diagram

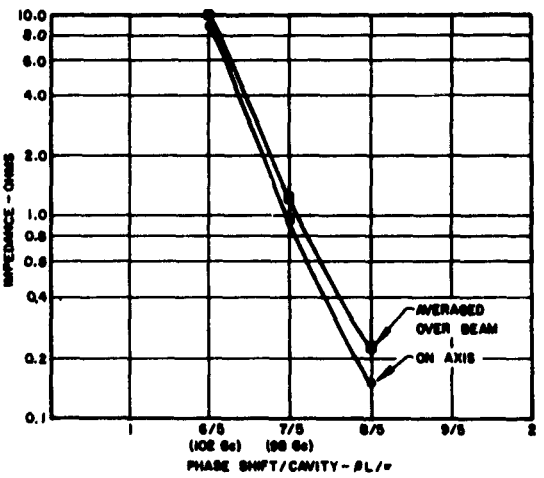

Fig. 7 - Impedance of the first backward-harmonic of the DLWG.

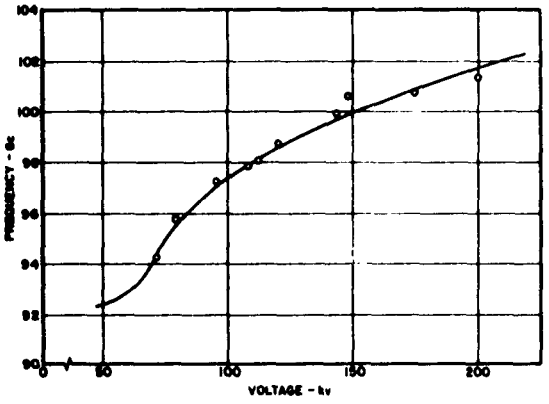

Fig. 8 - WJ-225 tuning curve.

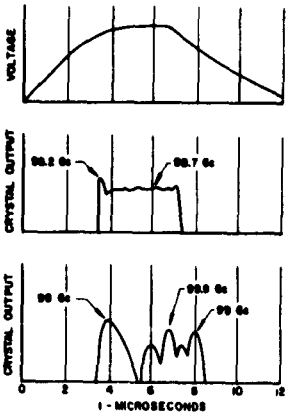

Fig. 9 - Applied voltage pulse and typical rf output pulses from experimental tube No. 1.

Output Waveguide

The output waveguide tapers from 0.025 x .080 inch at the circuit to .122 x .122 inch square guide. On the output arm the waveguide goes to a 40 db directional coupler and then a high power vacuum load which was constructed by spraying stainless steel onto an aluminum mandrel and electroforming copper over the sprayed stainless steel. The load is water cooled. A mica compression seal window is used on the low power arm of the directional coupler. The terminations on the collector end of the circuit are also sprayed stainless steel loads.

Collector

The collector is a simple copper bucket, 1.2 inches ID and 19 inches long. The over-all length of the tube is 30 inches.

Test Results

The first tube was tested at voltages up to 200 kv. Figure 8 is a tuning curve for the oscillator. The rf output pulse was extremely ragged, consisting of a series of spikes of power at different frequencies. Figure 9 shows the applied voltage pulse and typical rf output pulse shapes. The applied voltage pulse has a very long rise and fall time because the tube presents a high impedance load and there is not sufficient current available to charge the stray capacities rapidly. When the tube was examined after tests had been completed, it was discovered that braze materials had flowed into the waveguide and brazed the matching pins solidly to the cavity wall at the collector end of the tube. This would account for the fact that the tube did not tune smoothly. It would also account for the fact that oscillations were observed at voltages below which the tube would normally oscillate.

The peak powers as measured with a calibrated crystal ranged as high as 160 kw. Efficiencies ranged up to 29 percent. The most accurate measurement made during early testing was 74 kw at an efficiency of 9.6 percent. During later tests, power measurements were made with a calorimeter and the results compared with the crystal readings. Readings made with the calorimeter actually gave higher powers than those measured with the crystal so there is reason to believe the initial power measurements are not greatly in error.

As the testing progressed, the beam transmission and the power output decreased and the rf pulse shape deteriorated further. After the initial tests at low duty cycle were completed, the duty cycle was increased. The maximum average rf output power as measured with the calorimeter was 50 watts at 99 Gc. This occurred at a beam duty cycle of 0.0037. The average rf output power was low because the peak power had decreased by the time this measurement was made and the rf pulse length was only a fraction of the applied beam pulse. The beam duty cycle was

increased to 0.006 at about 160 kv at which point the circuit was destroyed. The average beam power was nearly 8 kw and the beam transmission was only 90 percent at this time. The first 5 or 6 cavities of the circuit were destroyed by peak heating effects.

To summarize, the significant results of the tests are:

1. The tube oscillated from 94.2 to 101.3 Gc
2. Peak rf power of the order of 100 kw was measured.
3. An average rf power of 50 watts was measured at 99 Gc.
4. A beam of nearly 8 kw average power was passed through the circuit before it was destroyed.

Plans for Continuing Work

The major design change that we are making in the next tube is to modify the electron gun so that it will produce a larger diameter beam that will be easier to focus. We would also like to have the beam minimum occur further from the anode so that the pole piece can be tapered to reduce the leakage magnetic field. A larger diameter beam will result in better interaction and more rf output power.

A second change that we plan to make is to use a silicon carbide loaded glaze rather than a sprayed stainless steel waveguide termination. The directional coupler will be eliminated and the mica window placed after the silicon carbide loss.

We hope to begin work on a TE_{01} circular mode high power window in the near future.

CHARACTERISTICS OF HIGH PERVEANCE HOLLOW BEAM GUNS FOR SUPER-POWER TUBES*

By

R. D. Harris

Litton Industries
Electron Tube Division

This paper concerns some of the characteristics of the generation and focusing of large diameter, high perveance hollow beams, and some test results from the guns we have built. Studies of two distinct types of guns were undertaken to produce the hollow beams; the first, a magnetron-injection type gun[1] and, second, electrostatically focused Pierce-derivative type guns. Most of the work to be reported here will be on the magnetron injection gun.

Magnetron Injection Gun Design Method

The magnetron injection guns were designed from a planar analytical formulation, similar to that reported by Kino and Taylor at the 1961 Electron Tube Devices Research Conference and later published.[2] The equations of space-charge flow

$$\begin{aligned} \frac{d\vec{v}}{dt} &= -\eta\vec{E} \quad -\eta \quad \vec{v} \times \vec{B} \\ \nabla^2\phi &= -\rho/\varepsilon_0 \\ \nabla\cdot\vec{J} &= 0 \\ \vec{J} &= \rho\vec{v} \end{aligned} \tag{1}$$

1 - J. Hull, U.S. Patent 2,632,130; November 28, 1947.

2 - G. S. Kino and N.J. Taylor, IRE Trans. on Elect. Devices, Vol ED-9, pp 1-11, January, 1962.

* - Work accomplished under Signal Corps Contract No. DA 36-039 SC-87313.

can be solved in cartesian coordinate for the case of a flat cathode in the (x,z) plane, two uniform components of magnetic field (B_y and B_z), and one-dimensional electric field (E_y). See Fig. 1 for the basic geometry and Appendix a for a definition of symbols. The solution to this hypothetical flow is given in parametric form, and in terms of the initial normal velocity ($\dot{y}_o$) in equations 2, 3, and 4.

$$X = \frac{\eta J_c}{\epsilon_o \omega^3} \sin\theta \frac{u^2}{2} + \frac{\cos\theta\,(1-\cos u)}{\omega}\left[\frac{\eta J_c}{\epsilon_o \omega^2} - \dot{y}_o\right] \qquad (2)$$

$$Y = \frac{\eta J_c}{\epsilon_o \omega^3} \sin^2\theta \frac{u^3}{6} + \frac{\dot{y}_o u}{\omega} + \frac{\cos^2\theta(u-\sin u)}{\omega}\left[\frac{\eta J_c}{\epsilon_o \omega^2} - \dot{y}_o\right] \qquad (3)$$

$$Z - Z_o = \frac{\eta J_c}{\epsilon_o \omega^3} \sin\theta\cos\theta \frac{u^3}{6} - \frac{\sin\theta\cos\theta}{\omega}(u-\sin u)\left[\frac{\eta J_c}{\epsilon\omega^2} - \dot{y}_o\right] \qquad (4)$$

Examination of the equations will indicate that an additional simplification is possible if ($\dot{y}_o$) is made equal to $\frac{J_c}{\epsilon_o \eta B^2}$. For convenience in the remainder of this paper this quantity will be defined as the term Δ. This approximation seems quite good if the magnetic field is large and current density is small because the term Δ is then of the same order of magnitude as the thermal velocities. For $J = 0.5$ A/cm^2 and $B = 1500$ gauss, Δ would be equivalent to 0.06 volts. On the other hand, if the magnetic field is below 1000 gauss Δ becomes very large, namely in the order of volts. For example, if $J = .5$ (A/cm^2) and $B = 600$ gauss the equivalent voltage for Δ is 2.23 volts. This latter value is very unrealistic for initial velocities and certainly cannot be expected in physical guns.

The problem then arose as to how critical is the choice of this flow parameter Δ. A partial answer can be obtained by comparing the trajectories when $\dot{y}_o$ equals zero and when $\dot{y}_o$ equals Δ. Equations 5, 6, 7, and 8 result and are plotted in Fig. 2.

(1) $\dot{y}_o = 0$

$$Y_1 = \mathrm{Sin}^2\,\theta \frac{u^3}{6} + \cos^2\theta\,(u - \mathrm{Sin}\,u) \qquad (5)$$

$$Z_1 = \mathrm{Sin}\,\theta\,\cos\theta\,\left(\frac{u^3}{6} - (u - \mathrm{Sin}\,u)\right) \qquad (6)$$

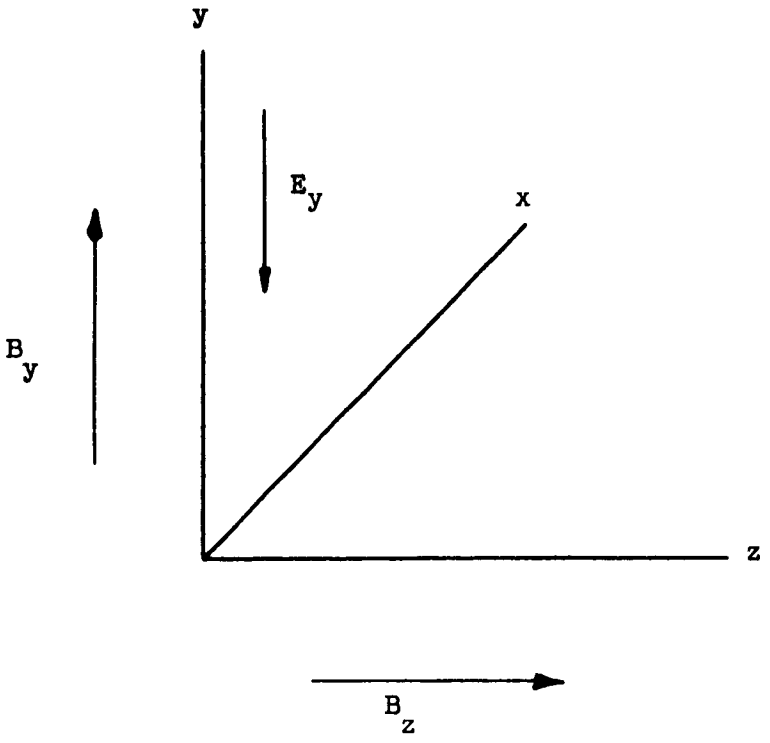

Fig 1 - Coordinate System For The Space-Charge Flow

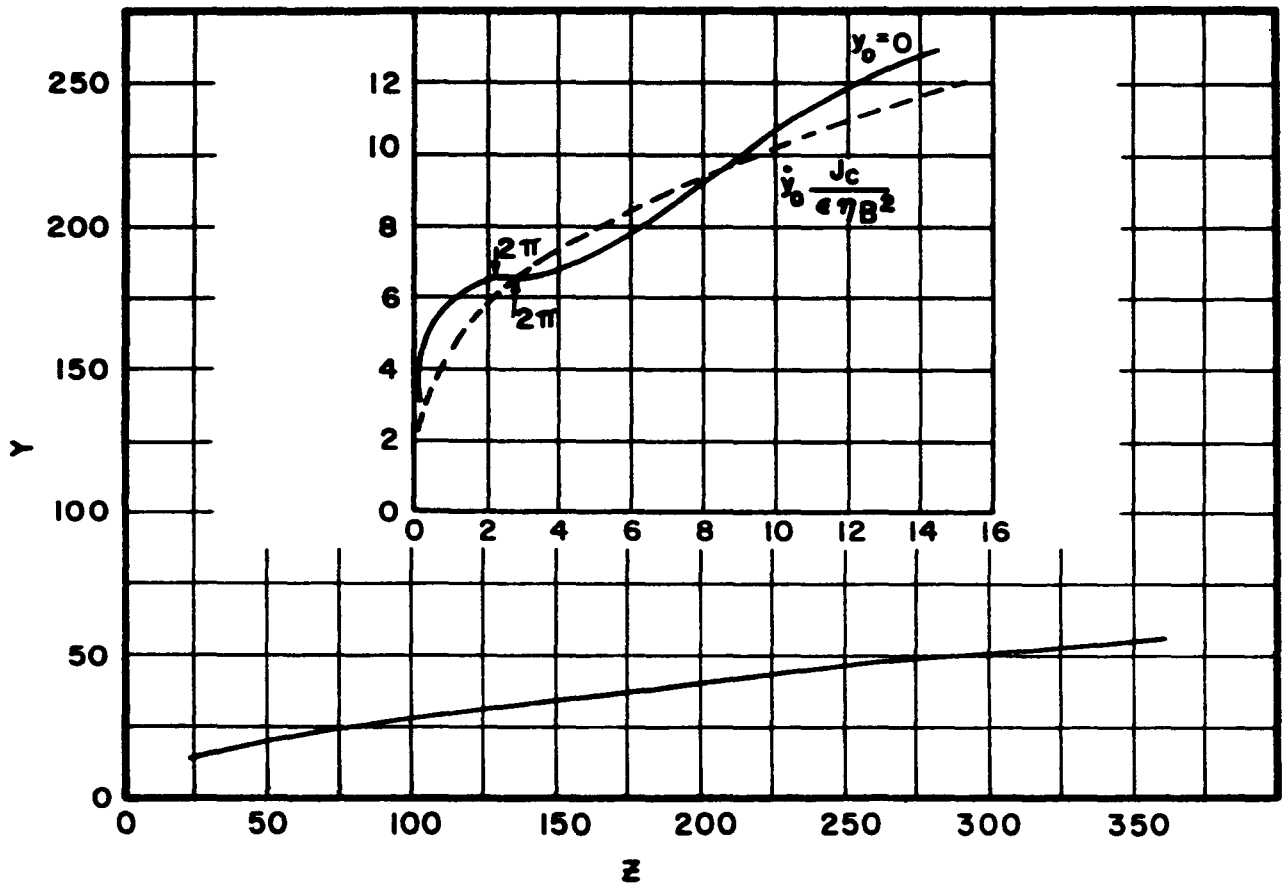

TRAJECTORIES IN THE Y-Z PLANE FOR
0 AND $J_c/\epsilon\eta B$ INITIAL VELOCITIES

Fig. 2

(2) $\dot{y}_o = \Delta$

$$Y_2 = \sin^2\theta \frac{u^3}{6} + u \tag{7}$$

$$Z_2 = \sin\theta \cos\theta \left(\frac{u^3}{6}\right) \tag{8}$$

The two solutions are very close for small values of the angle theta (i.e., the angle of the magnetic field). The largest error occurring for small values of u, normalized time. For values of initial normal velocity between zero and the ideal value the trajectories lie between the two curves. The equations in Fig. 2 are plotted on a scale corresponding to the physical length of the guns which have been built. If one neglects the effect on the (y.z) trajectories of the initial transverse velocities then since zero initial velocity is not a true statement of thermal velocities, the assumption of a unique value Δ as the initial velocity seems to be adequate for design purposes. The noise aspects of this assumption have not been investigated.

Accelerator Design

The planar equations of space charge flow can best be utilized in the design of an axisymmetric electron gun by letting the x, y and z coordinate axis correspond to the θ, r and z cylindrical coordinate respectively. Then we can consider the planar flow infinite in the x direction and can find the electrode surfaces outside this flow by the method described by Kirstein[3]. The treatment employs the method of analytic continuation to find equipotentials outside the beam. Fig. 3 shows some equipotential surfaces calculated by this method. The axisymmetric accelerator (modulating anode) was determined by first placing the planar gun model (i.e., the cathode, zero-potential electrodes and accelerator) on the (x,y) planar Litton Precision Resistance Network Analogue and measuring the space charge free fields at the cathode. The geometry was then placed on the (r,z) Axisymmetric Litton Precision Resistance Network and the accelerator position varied until the field values at the cathode were the same as the planar case. The cathode was tilted (i.e., made in shape of a truncated cone) so that a uniform axial field would produce the proper magnetic components at the cathode surface. Fig. 4 shows a typical gun geometry. The gun design requires that the cathode current density and the magnetic field be

3 - P. T. Kirstein, Proc. IRE, Vol. 46, pp 1716-1722, Oct. 1958.

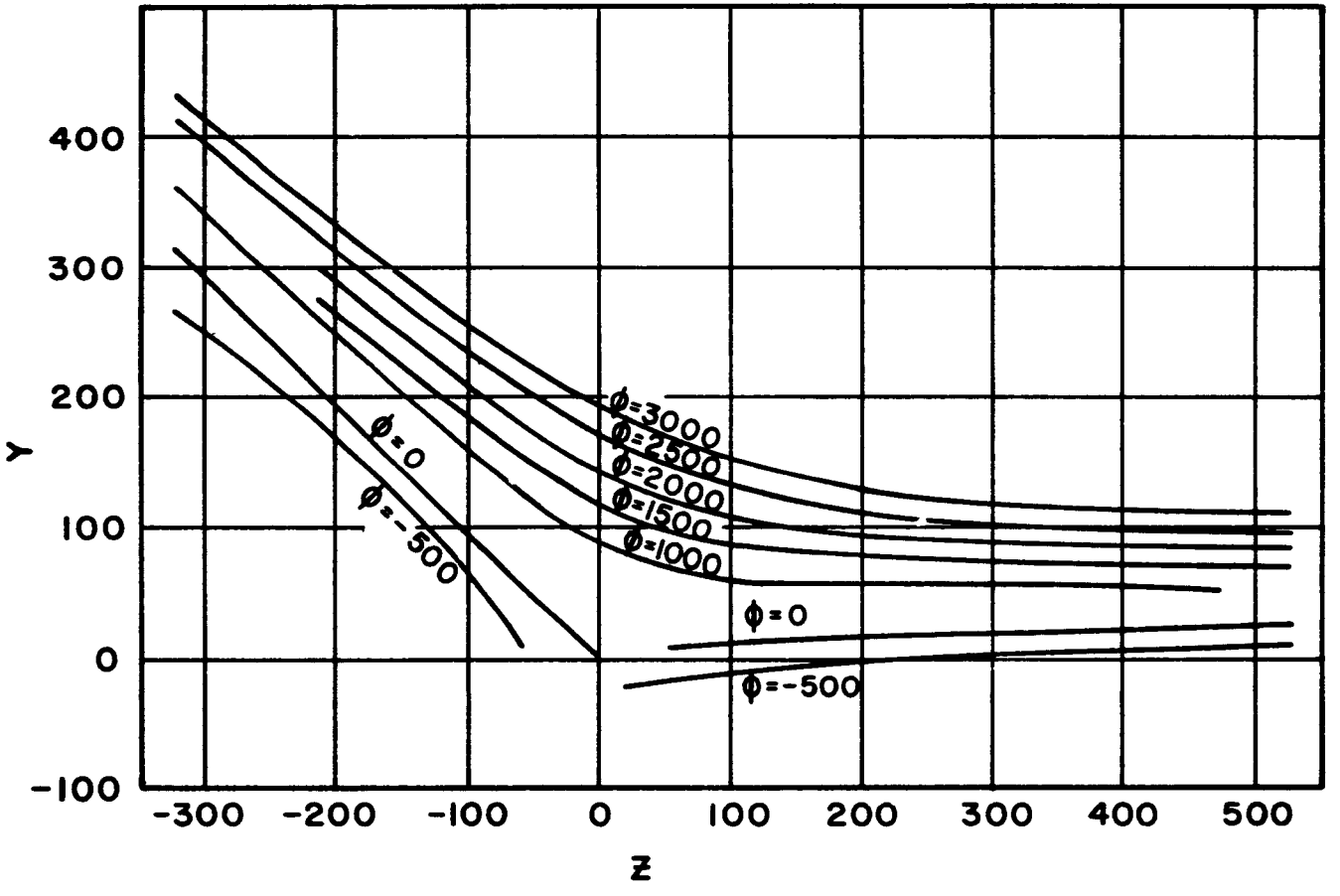

EQUAL POTENTIAL SURFACES IN Y-Z PLANE

Fig. 3

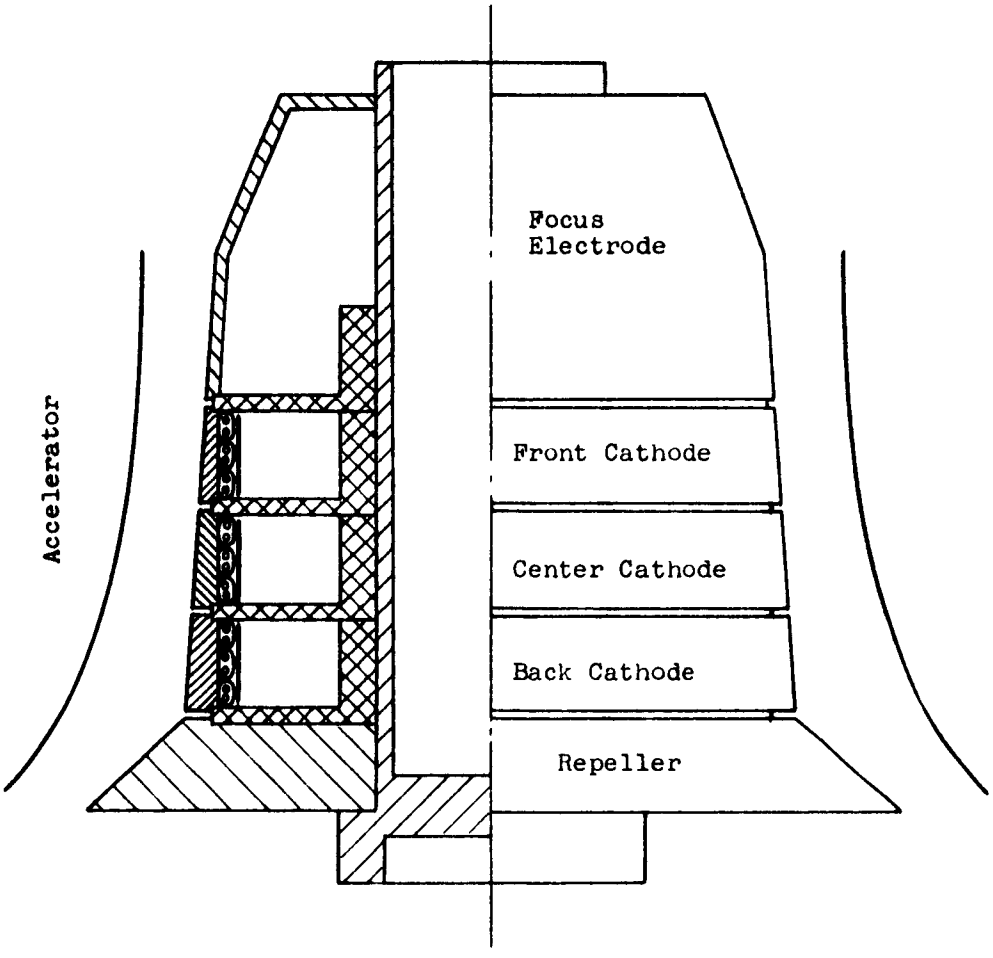

2" DIAMETER MAGNETRON INJECTION GUN CATHODE

Fig. 4

specified in order to reduce the normalized equipotential to a physical accelerator. It is possible to raise the perveance of the gun if additional magnetic field is available. To see this fact one can calculate an approximate radius at a constant Z value for the equipotentials shown in Fig. 3, and then use this radius together with the largest cathode radius in the Hull magnetron cut-off equation. The magnetic field value thus obtained can be plotted against the gun perveance. Fig. 5 is a plot of perveance versus cut-off field for a two-inch diameter cathode, one inch long, and having cathode loading of 0.5 amps/cm^2. The larger the value of perveance desired, the greater will be the magnetic field necessary to cut off the accelerator current. For a given gun with fixed accelerator dimensions the perveance decreases with increased magnetic field. However, the increase in perveance from a reduction of accelerator diameter more than compensates for the decrease in perveance caused by the increased magnetic field required to cut-off current to the reduced diameter accelerator.

For example, in the two-inch gun mentioned above the perveance of a 3300 volt electrode was 41 μpervs with a Hull cut-off magnetic field of 650 gauss. A 4400 volt electrode, a different equipotential line which will give the same current flow, would have a perveance of only 27 μpervs and a magnetic cut-off field of 533 gauss. Thus, by increasing the magnetic field 20% we have been able to increase the perveance 50%.

There is obviously one other way to increase the perveance and that is to increase the length of the cathode while keeping the accelerator voltage constant. For the case above, the cathode length would need to be increased 50%. It appears that this scheme soon reaches the point of diminishing returns. Uniform cathode loading requires the accelerator to have a continually decreasing diameter toward the exit of the gun. In addition, the beam is continually increasing in diameter and if the gun is too long a higher potential must be used and/or a higher value of magnetic field to prevent current interception. Both of which decrease the perveance.

A quantitative feeling for the values of magnetic field strengths we have been discussing is readily available from one of the guns mentioned above. The perveance 41 gun had a beam diameter of 2.09 inches, thickness .120 inches, and the beam was injected into a 6000 volt drift tube of 3.6 inch diameter. The beam is thin with respect to the beam diameter and the assumption can be made that the space charge density is constant and the axial velocity variation small across the beam. The beam voltage can then be determined from equation 9,

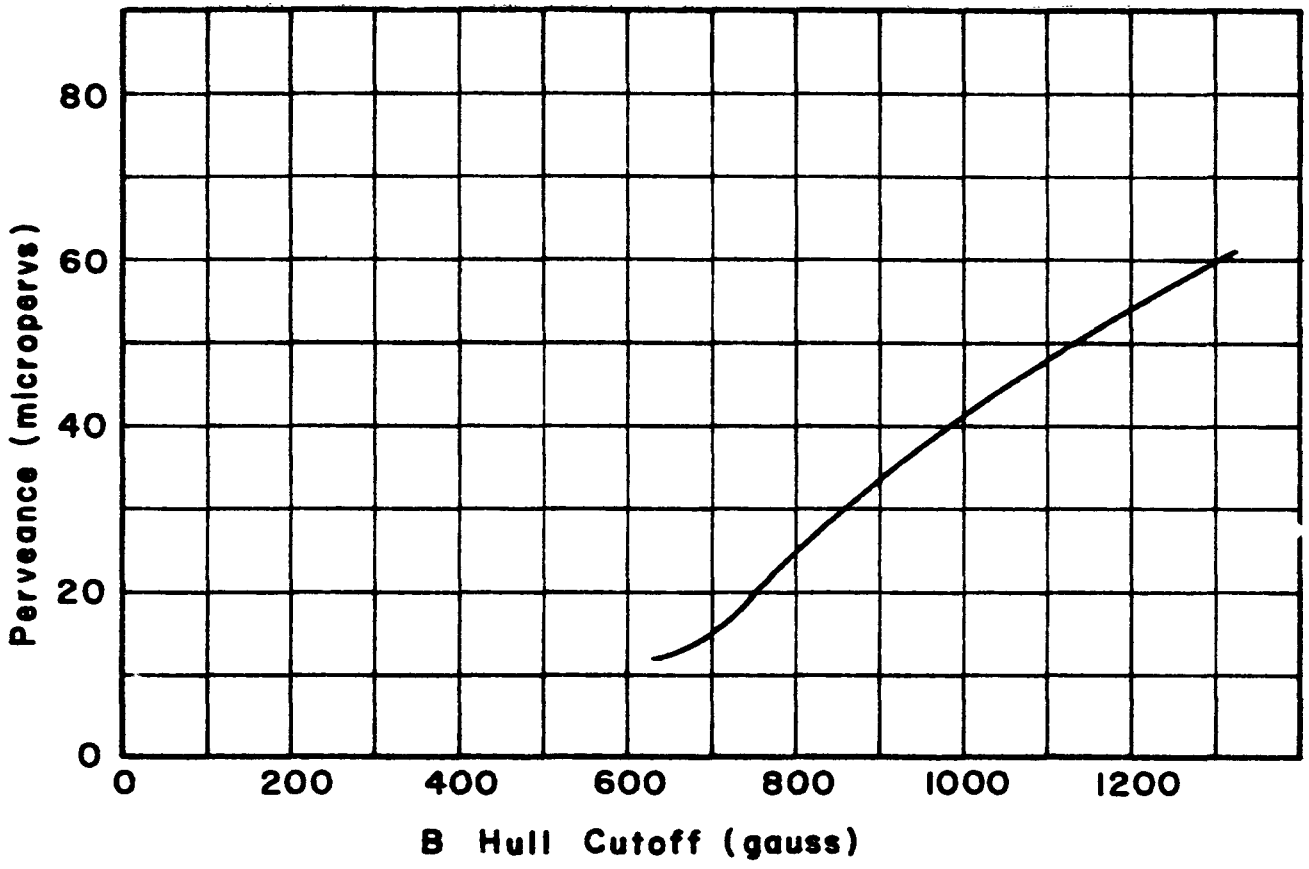

GUN PERVEANCE VERSES ACCELERATOR
CUTOFF MAGNETIC FIELD

Fig. 5

$$\phi_{DT} - \phi_B = \frac{I}{33 \times 10^{-6}\ \phi_B^{\frac{1}{2}}} \left[\frac{1}{2} + \ln \frac{r_{DT}}{r_b} - \frac{r_a^2}{r_b^2 - r_a^2} \ln \frac{r_a}{r_b} \right] \quad (9)$$

where r_b is the beam outside radius and r_b is inner radius. Inserting in the above mentioned values yields a beam voltage of 3650 Volts. This value in turn can be substituted in the formula for a Samuel magnetic field

$$B_S = \frac{I^{\frac{1}{2}}}{1.205 \times 10^3\ (\phi_a)^{\frac{1}{4}}\ r_b \left[1 - \frac{r_a}{r_b}^4 \right]^{\frac{1}{2}}} \quad (10)$$

to give 200 gauss. The magnetic field required to cut off accelerator current in the experimental tests was just under 800 gauss; or 4 times the hollow-beam Brillouin value. For perveance-30 guns the magnetic field has been about 50% greater than design value and 25% greater than Hull cut-off value. As the perveance is decreased the magnetic field can also be lowered. Kino and Taylor[2] operating a gun with a perveance of 10 μpervs, were able to reduce the magnetic field down to Brillouin values.

Generally, "immersed" magnetically focused beams have sufficient stiffness between 1.5 and 2 times Brillouin magnetic field strength to give satisfactory tube operation. But once the hollow beam has been formed in a magnetron injection gun any change in the magnetic field will change the beam diameter. Therefore, if the cathode and drift tube diameters are approximately the same, the magnetic field value above the cathode must be continued the length of the tube. The extreme stiffness of these high-perveance beams provides a favorable condition for super-power applications. Whenever cathode loading is a problem, one can make larger diameter cathode and then magnetically converge the beam in diameter to fit the circuit. In one test the diameter was reduced 20% without affecting the beam thickness.

Focus Electrode Considerations

Applications of beams to super powers require that a minimum of the total energy be in the rotational form because rotational energy is not useful for interaction and also is difficult to recover in depressed collectors. Rotational energy inside the magnetron gun can be as high as 30% of the total energy. Even with a post acceleration region, where the beam is presumed accelerated in the axial direction only, the percentage of rotational power in the beam is excessive for super powers. An experiment was conducted to determine the amount of rotation in a magnetron injection gun beam. A small

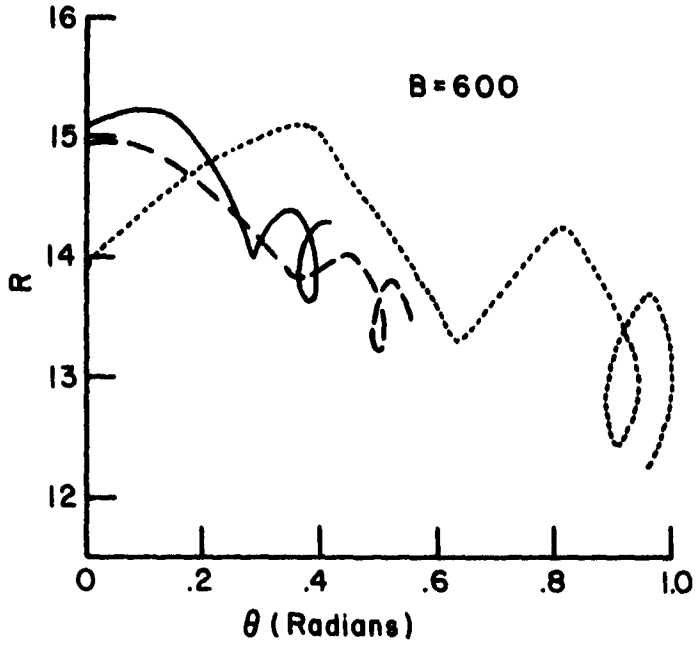

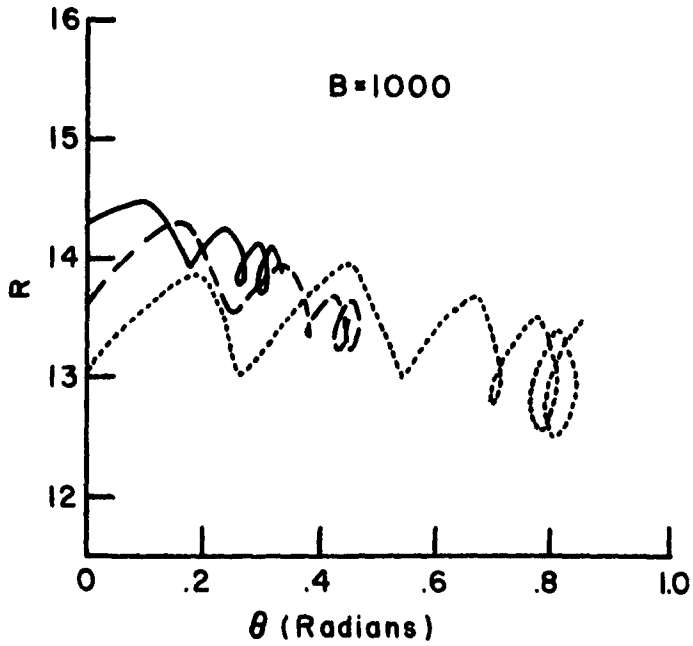

R-θ PLOTS OF TRANSITION TRAJECTORIES

Fig. 6

wire was placed through the diameter of the beam close to the exit of the gun and the beam then observed on a movable carbon screen. The screen was capable of axial movement corresponding to four ripple wavelengths. Calculations indicated that if the beam was rotating around the axis a certain amount of rotation would be detectable. However, there was no observed rotation and the distortion of the wire shadow was almost negligible. These results seemed to indicate an immersed focused condition. The next step was to trace some electron trajectories on the Litton Precision Resistance Network Analogue. The trajectories were plotted with space charge simulated in the gun region, but without space charge in the transition region. Although there is at present, still considerable difficulty in accurately plotting the trajectories in crossed-electric and magnetic fields with the network board (in particular, the scale of these plots is too small for really good accuracy) the results do yield a valid description of the general type of motion involved. Fig. 6 shows plots of R versus θ for trajectories of electrons emitted from the front, back, and middle of the cathode, as they emerge from the gun. Not shown is the electron rotation inside the gun region, but is rotation around the axis as in a magnetron. The electron rotates between 50 and 90 degrees, depending upon its initial position, before leaving the gun. As the electric field decreases from the high value between accelerator and front focus electrode at the gun exit, the beam shrinks in diameter due to the stronger magnetic forces and the motion changes from rotation around the axis to rotation around a flux line. Thus, the beams produced from magnetron injection guns of perveances greater than 20 μpervs are ultimately in a magnetically "immersed focused" condition when passing through the circuit. Although guns with perveances less than 20 μpervs have not been studied, it is believed that the same focusing mechanism holds for them. Fig. 6 also shows the decrease in the cycloid amplitudes due to an increased magnetic field. Fig. 7 is an R-θ plot for different drift tube voltages (i.e. axial velocity values).

One magnetron injection gun, designed according to the design procedure here presented, has been placed in a very-high-power klystron. The gun perveance was designed for 25 μpervs and has been operating at 28 μpervs. The beam transmission with no rf drive is over 99% up to 30 megawatts beam power. Original design values for the beam were 10 megawatts at 180 KV. Operating at saturated gain and 8 megawatts the transmission is 97% with 40% tube efficiency.

The amplitude of the ripple on convergent magnetically-confined flow electron guns is dependent upon the position and direction of entry into the uniform magnetic field region. It should then be expected that the ripple in a beam generated by magnetron injection gun would depend upon the transition geometry. Three different front focus electrode shapes were

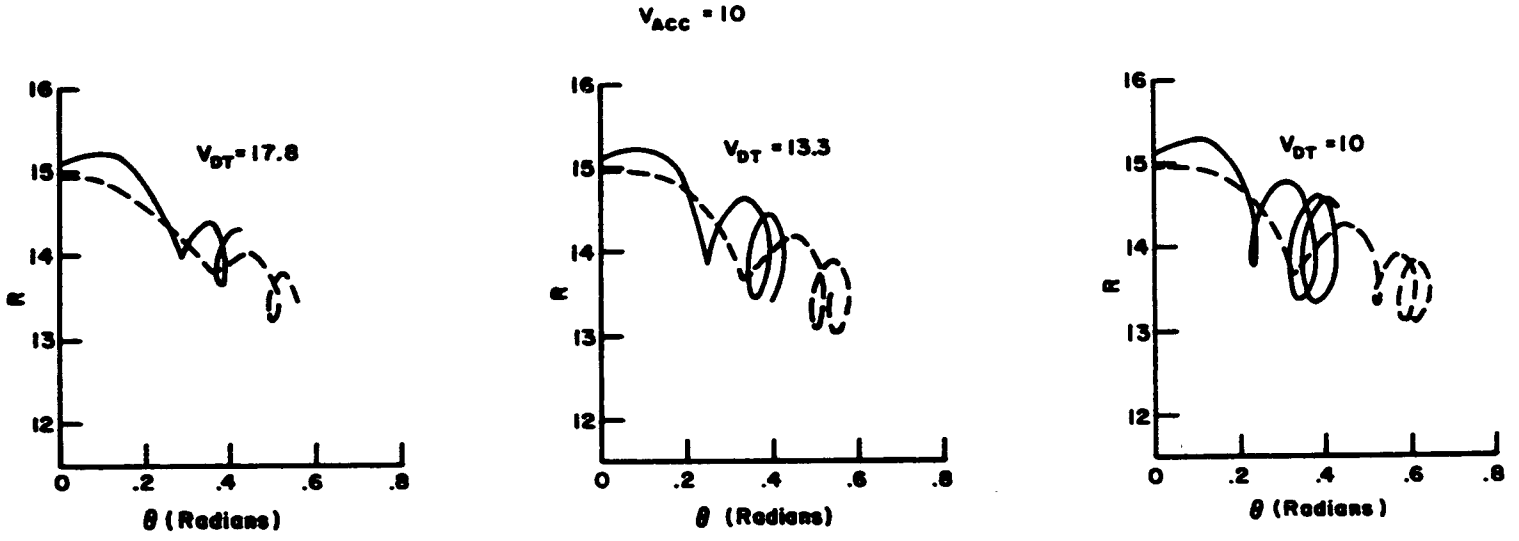

R-θ PLOTS OF TRANSITION TRAJECTORIES

Fig. 7

placed on the resistance network analogue, and electron trajectories were traced through the transition region to see the effect on the beam. The electrodes consisted of a round dome, a blunt nose, and a linear tapered nose. The trajectories from either end and middle of the cathode are shown in Fig. 8 for the blunt and tapered front focus electrodes. The trajectories for the round and tapered noses are approximately the same and only one case is given. The blunt nose produces a 10% beam ripple. The radius of the focus electrode is 12.9 units. The trajectories are plotted space charge-free, but since all are approximately in phase the only effect of space charge inclusion would be to spread the trajectories apart where they are bunched together. The ripple on the beam from the tapered nose is about 8% but since the trajectories are out of phase the inclusion of space charge would very greatly smooth out the ripples. There is, however, another characteristic of the plots which should be considered. If the axial velocity versus axial distance is plotted, as in Fig. 9, we see that the electrons slow down as they leave the gun for the cases of the round and tapered focus electrodes. There is a space charge build-up for the particular drift tube voltage indicated at the gun exit which reduces the beam current. Note also that for lower drift tube voltages the potential depression is even greater and the beam current less. The variation of beam current with drift tube voltage for two magnetron injection guns is shown in Fig. 10. The slope of the curves is relatively constant up to the point where all the gun current is pulled away and down the tube. Higher values of drift tube voltage result in end emission from the front cathode section and decreased slope of the curve. The cathode axial loading uniformity also deteriorates. For normal applications the space charge build-up will reduce slightly the gun perveance if the transition from gun to tube is not properly designed. In addition, because of the excess charge, more magnetic field is required to cut off the accelerator current. This charge build-up is evident in switch tubes utilizing magnetron injection guns. The ideal current-voltage characteristic of switch tubes is flat to the knee of the curve, as in a pentode, but in switch tubes using magnetron injection guns the current starts decreasing slowly before this knee is reached, if the collector voltage is decreased below a certain level. This is because of the excess charge at the gun exit. The value of collector voltage at which this change of slope occurs depends upon the specific design of the tube.

Inverted Magnetron Gun Considerations

An inverted magnetron injection gun (cathode radius greater than accelerator radius) is also being investigated for the production of hollow beams. It can be shown[4] by analyzing the

4 - Quarterly Report No. 4, U. S. Army Signal Corps Contract No. DA 36-039 SC-87313.

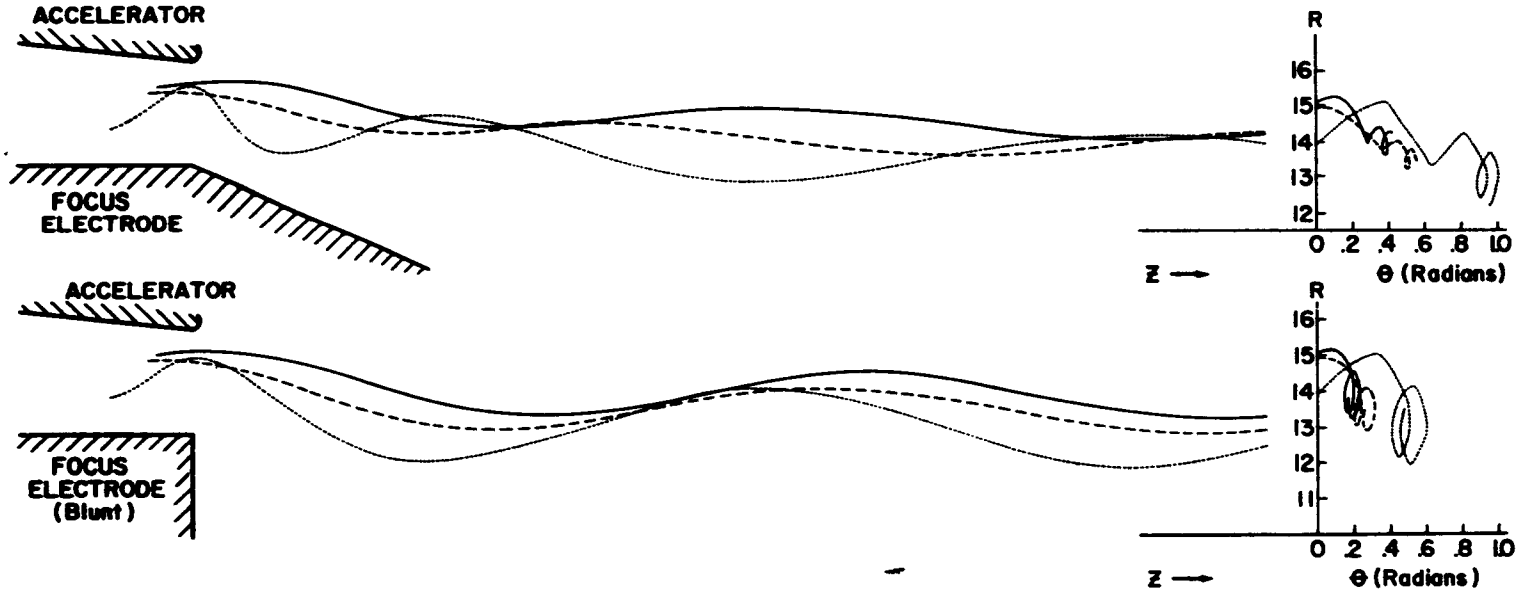

TRAJECTORY PLOTS THROUGH THE TRANSITION REGION

Fig. 8

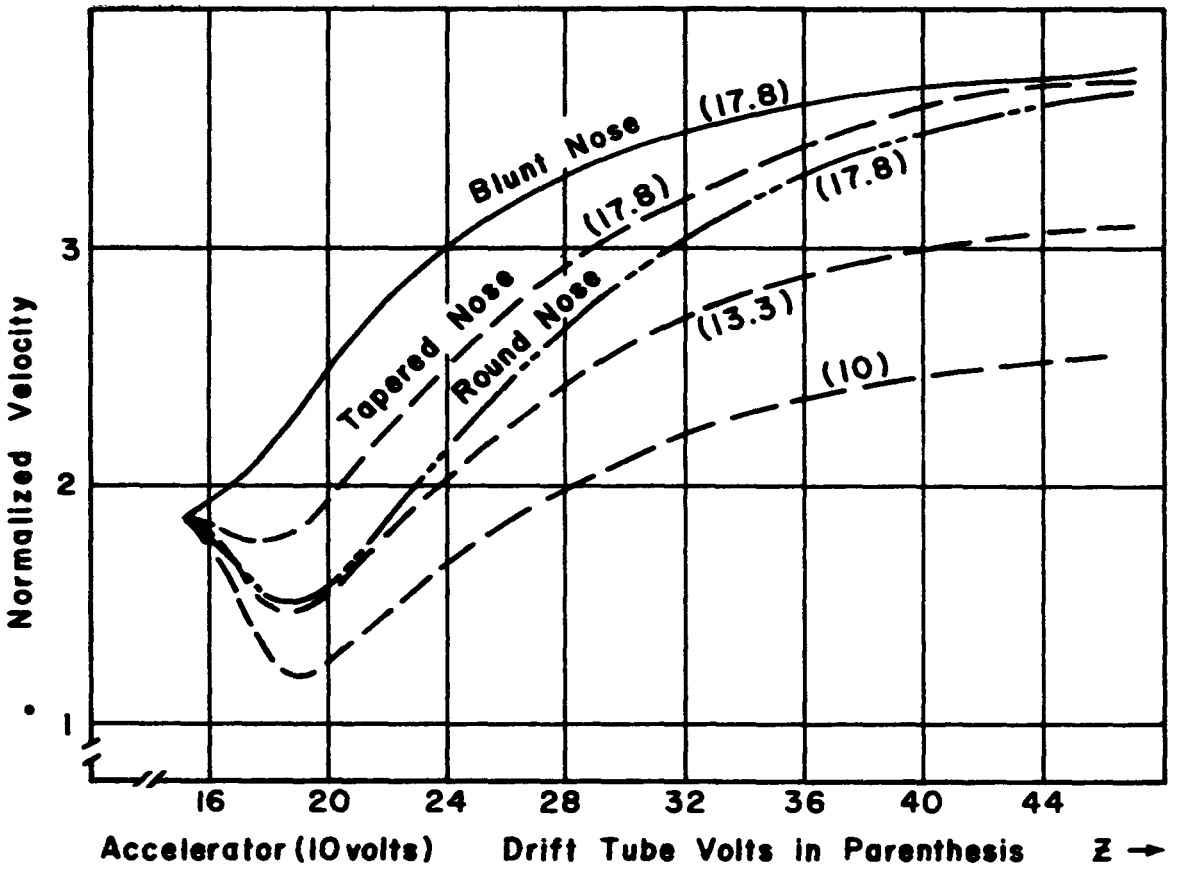

AXIAL VELOCITY VERSES AXIAL POSITION
THROUGH THE TRANSITION REGION

Fig. 9

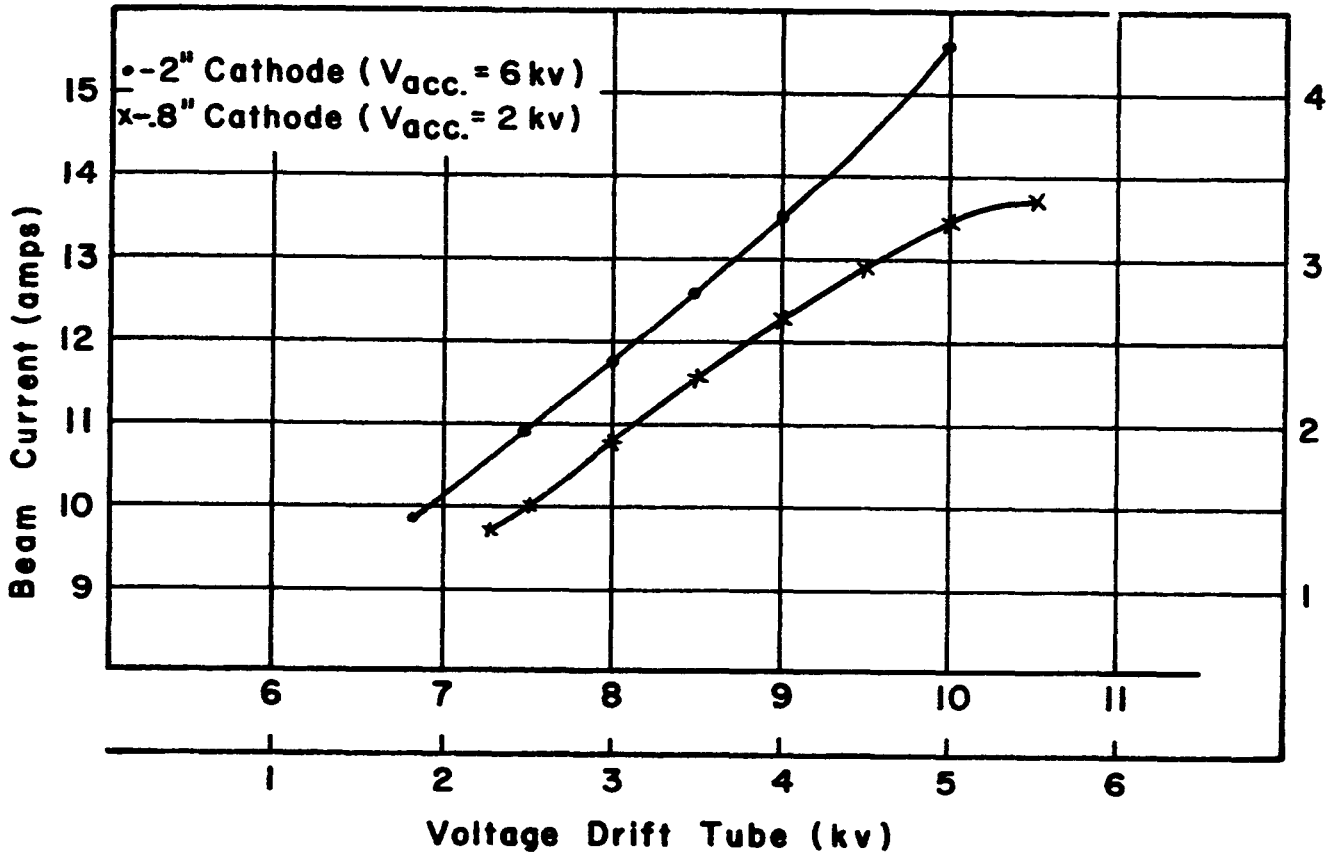

BEAM CURRENT AS A FUNCTION OF DRIFT TUBE VOLTAGE

Fig. 10

focusing forces, that in a uniform magnetic field the inverted gun produces a beam of the same diameter as a conventional gun, if both cathodes are the same size. The inverted gun has the proper geometry to utilize the fringing field of a solenoid to an advantage. By allowing the magnetic field to fringe through the gun region, a stronger magnetic force is produced in the direction to push the electrons out of the gun. In addition, if the flow is laminar the electrons from the back of the cathode form the inner beam diameter, and must not rotate for proper focusing. The inner beam edge would then be at the ultimate diameter of the flux line which passed through the back of the cathode, which would be at a smaller diameter in a fringing field than in a uniform field. Thus, there is no advantage over a conventional gun in a uniform magnetic field, but in a fringing magnetic field the inverted gun has a natural convergence mechanism. In cases of high cathode loading, this convergence would allow the designer to increase the cathode diameter, lowering the cathode current density, and still have adequate beam current.

Electrostatic Gun

An electrostatically focused hollow beam gun is the second approach to the high perveance beam generation. The gun is designed on the resistance network for a beam perveance of 15 μpervs, a beam voltage of 100 KV and an area convergence of 25. The space charge flow is electrostatically focused inside the gun region. For rotational energy considerations the beam outside the gun is "immersed" focused. Fig. 11 is a schematic of the various electrodes and the beam profile. This gun is now in testing.

Recognition is given to the U. S. Army Signal Corps under whose support and sponsorship this work has been undertaken.

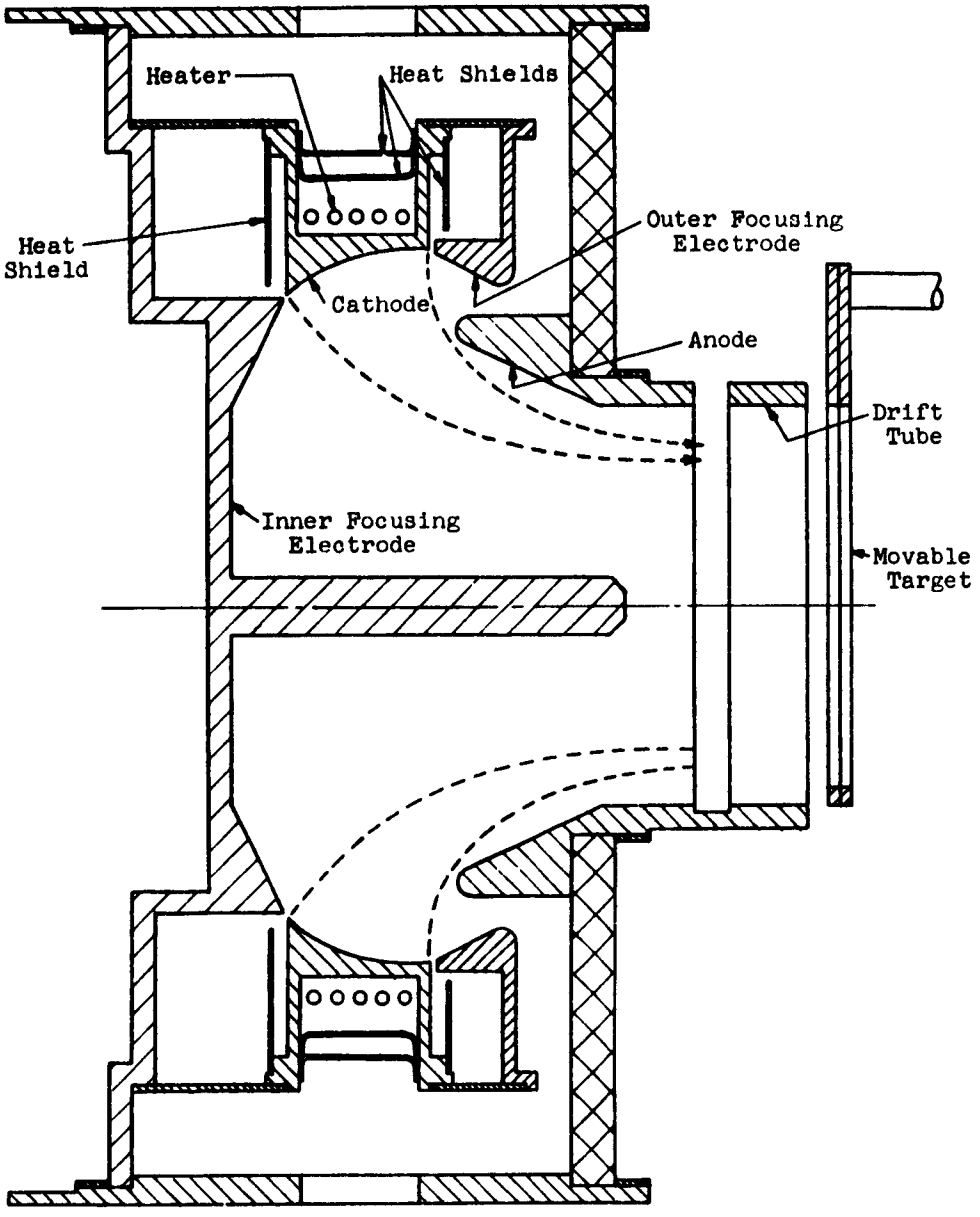

COMPLETE ELECTROSTATIC HOLLOW BEAM GUN

Fig. 11

Appendix A
Definition of Symbols

η = e/m (charge to mass ratio of electrons)

B = magnetic field

J_c = cathode current density

ϵ_o = permativity of free space

ω = ηB

u = ωt = normalized time

θ = arctan (B_y/B_z)

$\dot{y}_o$ = initial normal velocity

A_o = $\eta J_c/\epsilon_o \omega^2$

X,Y,Z,R = normalized coordinates

r_a = beam inner radius

r_b = beam outer radius

Φ_B = average beam voltage

APPLICATION OF MAGNETRON INJECTION GUNS IN HIGH-POWER MICROWAVE TUBES

By

William E. Waters

Microwave Electronics Corporation
4061 Transport Street
Palo Alto, California

I. INTRODUCTION

It has been known for many years that the use of a dense, radially-thin, hollow electron beam in an O-type microwave tube will result in RF performance which is superior to to that which can be achieved with a solid round beam. For example, in a traveling-wave tube, the use of a high-density hollow beam results in a stronger interaction between the electrons and the electromagnetic wave traveling on the circuit. With suitable design it is possible to greatly increase the beam-to-circuit coupling (i.e., obtain a higher value of the Pierce interaction parameter C) over that obtained with a conventional solid beam, yet at the same time minimize problems associated with longitudinal space-charge debunching (i.e., avoid problems associated with high values of QC). In multicavity klystron amplifiers the use of a thin hollow-beam accomplishes two desirable objectives; first, the gap coupling coefficient is increased, resulting in a higher electronic conversion efficiency, and second, the RF beam susceptance is increased. It is well recognized that any design change which increases beam susceptance will, if properly exploited, result in increased RF bandwidth of a klystron.

A major problem, which has prevented full exploitation of the attractive possibilities of hollow-beams in high-power microwave tubes, has been the lack of a systematic design procedure for satisfactory electron guns.

II. GENERAL DESCRIPTION OF GUN

During the past three years much progress has been made in the development of design procedures for a type of hollow-beam electron gun known as a "Magnetron Injection Gun," or MIG for short. Figure I illustrates a typical

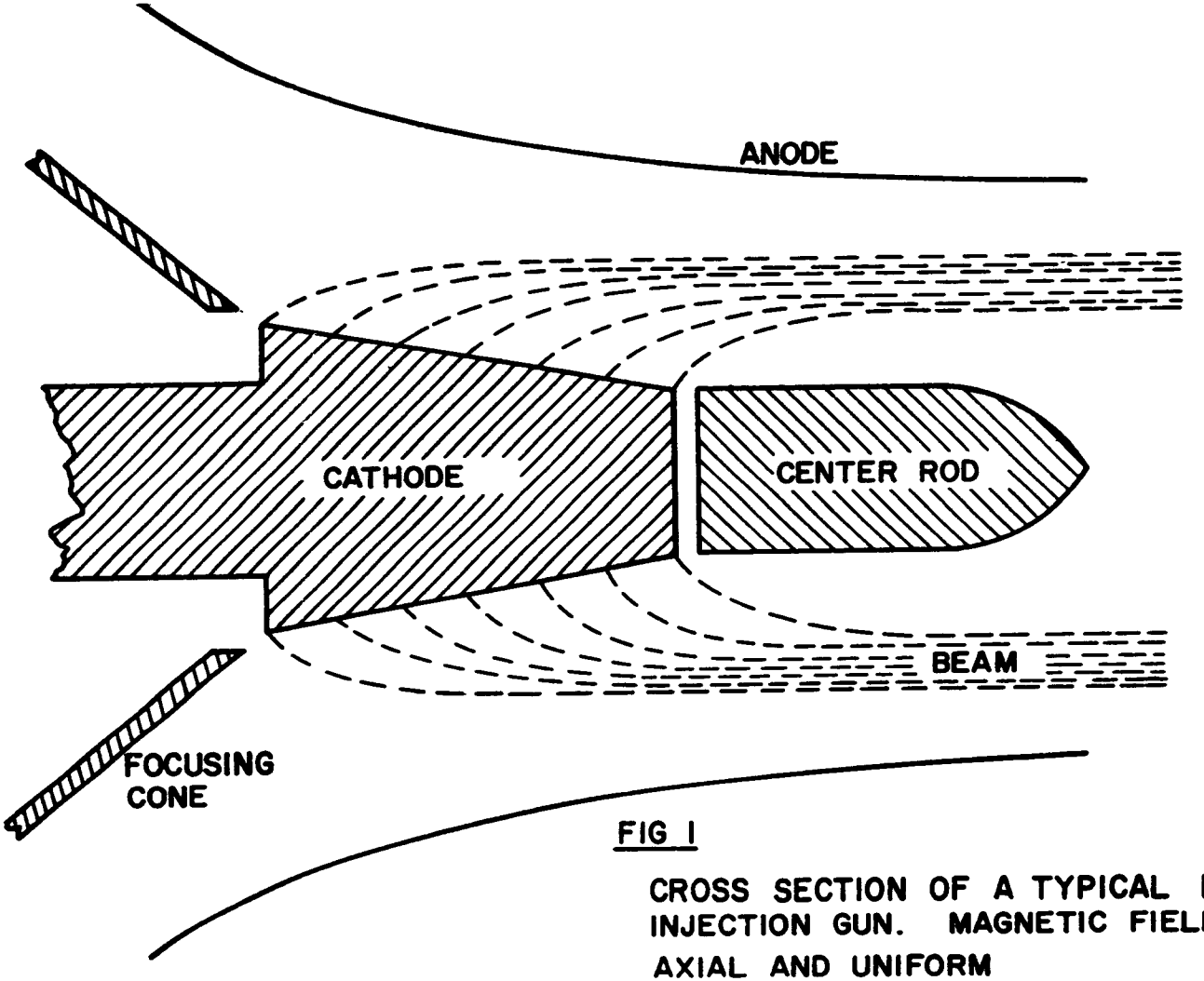

FIG 1

CROSS SECTION OF A TYPICAL MAGNETRON INJECTION GUN. MAGNETIC FIELD IS AXIAL AND UNIFORM

gun in cross-section. The cathode is a section of a cone, and emission arises from the conical surface. In its most usual form, the gun is immersed in an approximately uniform axial magnetic field, which may be generated either by a solenoid or with permanent magnets of suitable design. Surrounding the cathode is a curvilinear beam-forming anode, also often called the modulation anode. The purpose of this anode is to create an electric field in the vicinity of the cathode, so as to draw off a space-charge limited current on the one hand, and to impart an ordered longitudinal motion on the other, thereby causing the beam to be ejected from the gun.

In Figure 2, we have depicted in schematic form the basic features of an electron optical system employing an MIG; in an actual microwave tube, the electrode labelled "drift tube" would be replaced by an RF interaction circuit, such as a sequence of klystron cavities, a helix, or a coupled-cavity slow-wave circuit. The magnetic field has been depicted as axial and uniform; however, there is no theoretical reason to prevent the use of other configurations of magnetic field, such as field-reversals, or even periodic permanent magnetic fields. In fact, PPM focusing of a 5 watt CW X-band amplifier using an MIG has been used with a high degree of success by the author, at Microwave Electronics Corporation.

III. PROPERTIES OF A BEAM PRODUCED BY AN MIG

A. Radial Thickness.

It is possible to demonstrate that a hollow electron beam, which is injected from a gun into a focusing system such as a uniform or periodic magnetic field, will remain hollow only if a finite magnetic field strength exists at and near the cathode surface. An MIG satisfies this requirement, in view of the fact that the cathode is immersed in a magnetic field. It may further be demonstrated that, in a uniform field, the inner diameter of the hollow-beam will be equal to the diameter of the small end of the conical cathode. The outer diameter of the beam, far from the cathode, will exceed the diameter of the large end of the cathode because of the presence of a finite amount of space-charge in the beam. By proper choice of the cathode half angle, the magnetic field strength, and the cathode emission density, one may arrive at designs in which, at one extreme, the outer beam diameter, and hence the radial thickness of the beam is determined almost entirely by the amount of beam current, and at the other extreme almost entirely by the shape of the cathode and the flux lines. The designer also possesses a large degree of control over the transit time of electrons through the gun; this is a very important consideration relating to the noisiness of the beam. Very briefly it may be stated that, to reduce beam noisiness, the transit time of the electron through the gun should be as small as possible; this is most easily accomplished by increasing the half angle of the cathode. In guns intended for high power tubes, a reduction of transit time through the gun also reduces the likelihood of back bombardment of the cathode; this effect is believed to be a major contribution to excess noise.

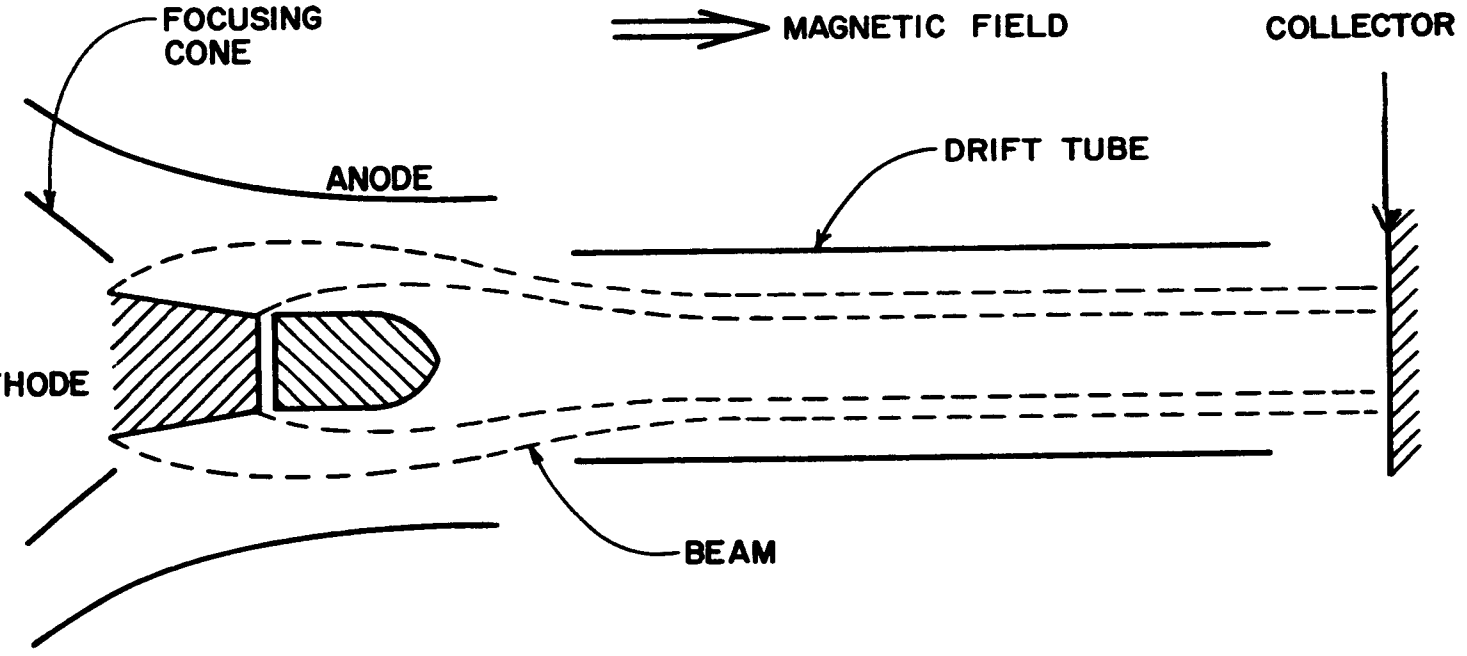

FIG 2

COMPLETE O-TYPE ELECTRON OPTICAL
SYSTEM UTILIZING MAGNETRON INJECTION GUN

B. Cathode Area Consideration.

Consider the surface areas of (a) one end of, and (b) the cylindrical surface of, a cylinder of diameter d and axial length ℓ, as depicted in Fig. 3(a). The end area is $\pi d^2/4$, and the cylindrical area is $\pi d\ell$. These areas are equal if $\ell = d/4$; it is clear that a cylinder having these proportions would be considered very "short." The design of an MIG is straightforward even for a conical cathode whose length is eight (8) to ten (10) times the base diameter, as depicted in Fig. 3 (b). However, the surface area of a cone having base diameter d and axial length is smaller than a corresponding cylinder by the ratio $\frac{1}{2}\left[1+(d/2\ell)^2\right]^{\frac{1}{2}}$ for a cone half angle less than about 20° (a rather large angle for an MIG) this ratio is very nearly 1/2. Despite this apparent disadvantage, the conical cathode is easily designed to possess a much larger emitting area than would a disk having the same diameter. This is a consideration of paramount importance for any electron gun which is to be immersed in a magnetic field.

C. Property of Confined Flow.

The fact that the cathode is immersed in a magnetic field may be summarized by the statement that the space-charge flow arising from an MIG is a type of confined flow. To the tube designer this statement means that, well beyond the gun, i.e., in the RF interaction region, in order to maintain a beam having a given diameter, voltage and current, a higher magnetic field will be required than if the cathode were completely shielded from magnetic flux. The advantage to be gained from the higher magnetic field is stiffer beam focusing, a characteristic which is extremely desirable in high-power O-type microwave tubes, in which radial debunching made possible by low-beam stiffness can be a serious problem.

D. Convergence and Perveance Definitions.

The beam area convergence and gun perveance which may be designed into an MIG can both be high. To a first approximation, for gun designs in which the radial thickness of the emergent beam is determined only slightly by space-charge, the area convergence is very nearly equal to the reciprocal of the half-angle of the cathode, provided that angle is less than about 30°. For extremely small angles, and in the limit, for a cylindrical cathode, the radial thickness of the emergent beam will be determined largely by space-charge and by thermal emission velocities of the electrons. We have built and tested a gun in which the calculated area convergence was 220 in the absence of thermal velocities; an approximate treatment including thermal velocities predicts that the convergence should be some 10% smaller.

One must proceed cautiously in speaking of the perveance of the beam generated by an MIG, as there are several equally-usable definitions of perveance. Referring to Fig. 1, it is seen that, in the vicinity of the cathode, each electron rather quickly moves outward to a position of constant

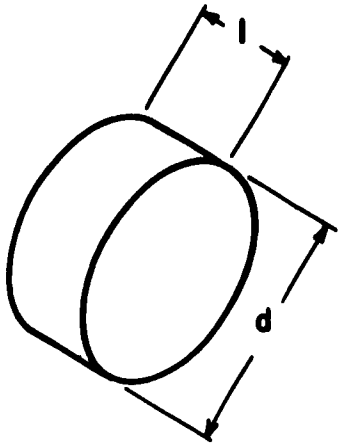

FIG 3a

SHORT CYLINDER, $l = \frac{d}{4}$

SURFACE AREA OF END AND SIDE ARE EQUAL

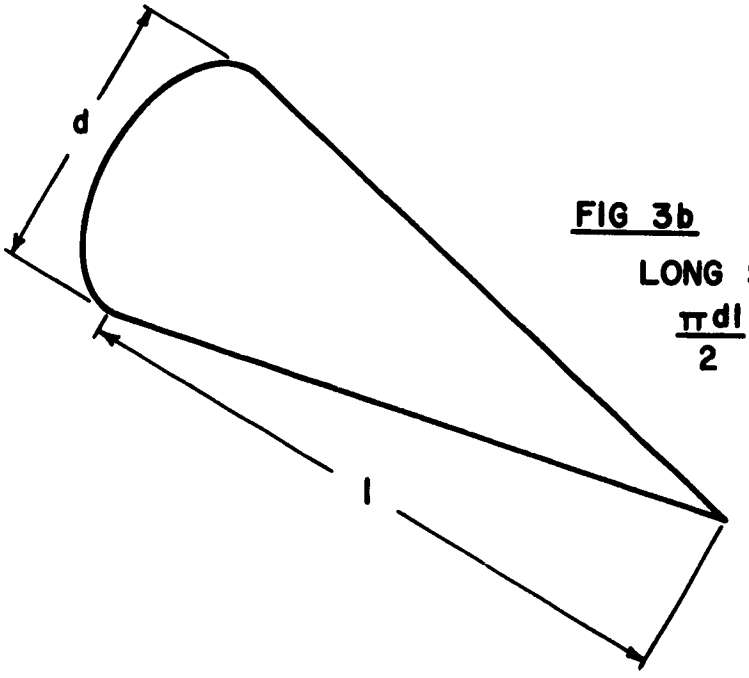

FIG 3b

LONG SLENDER CONE,

$$\frac{\pi d l}{2}\left[1+\left(\frac{d}{2l}\right)^2\right]^{1/2} = \text{AREA}$$

radius; because such motion has resulted in the cutting of magnetic flux, an appreciable portion of the kinetic energy will be associated with motion around the axis, and the remaining kinetic energy will be associated with longitudinal motion. Finally, far from the cathode the entire beam may have been accelerated to a potential greatly different from that existing in the gun proper. Thus, one may define the perveance of the beam in the interaction region (drift tube) to be the current divided by the 3/2 power of the drift tube potential (this is defined to be the interaction perveance). In the gun itself, the perveance may be defined in terms of the anode potential (anode perveance), the total potential in the beam (total gun perveance), or the potential associated with longitudinal motion only (longitudinal perveance).

It is possible to show that the total gun perveance can be as high as, but no higher than, 44.4 micropervs; similarly, one may show that there is no upper limit to the longitudinal perveance. We have built a number of different guns having total perveances between 10 and 38 micropervs; the gun mentioned previously, having an area convergence of 220, possessed an anode microperveance of 19, and a calculated total microperveance of about 28. In this gun the cathode was cylindrical, and the emergent hollow-beam thickness was determined primarily by space-charge, with thermal velocities supplying a small correction.

E. Absence of Electrode Interception.

In addition to being capable of high area convergence and high perveance, a further extremely attractive characteristic of an MIG is that, with proper design, theoretically correct electrodes which will actually produce a given flow pattern need not intersect the electron trajectories. Thus, no interception of current will occur on any electrode of a well designed MIG. The gun may be thought of loosely as a magnetron operating below its cutoff parabola, so that no current reaches the anode. One may contrast this type of behavior to that of a conventional convergent gun, a so-called "Pierce Gun," particularly of the gridded variety. In such guns, the grid and anode may both intercept appreciable current. Secondly, theoretically the anode surface should intersect the beam; the problem of compensating for the hole in the anode, in a practical design, is notoriously well-known.

For purposes of comparison the important characteristics of an MIG and a conventional convergent gun are formulated in Table I.

TABLE I

COMPARISON OF MAGNETRON INJECTION GUN AND PIERCE GUN

Characteristic	Magnetron Injection Gun	Pierce Gun
Maximum Perveance	44×10^{-6}	$5 \text{ to } 6 \times 10^{-6}$
Area Compression	220 or greater	100 to 200
Cathode Magnetic Field	Yes	No
Grid Interception	No Grid	4% to 15%
Anode Interception	0	1/4% to 3%
Application to Hollow-Beam Generation	Excellent	Poor
Type of Beam Compression	Longitudinal	Radial
Cathode Subject to		
(a) Back Bombardment	Possibly	No.
(b) Ion Bombardment	No	Yes
Required Design Tools	Tabulated Data Only	Tabulated Data plus Electrolytic Tank

IV. STATE OF DEVELOPMENT OF MIG THEORY

The state-of-the-art pertaining to design procedures for MIG's is highly advanced. Apparently the first solution of the necessary space-charge equations, for the special case of a conical cathode in a uniform field, was derived by the author, while working at the Diamond Ordnance Fuze Laboratories, about three years ago. Soon afterward a more general type of solution, still utilizing a conical cathode, but permitting the radial and longitudinal components of the (axially-symmetric) magnetic field to be given by an infinite number of combinations of Legendre polynomials, was derived by P. T. Kirstein.[2]

Finally, a theoretically-exact method for calculating the shapes of electrodes which will actually produce a given flow pattern was developed in detail by K. J. Harker at Stanford University.[3] Additional work on the theory of MIG's, and/or numerical solution of both the space-charge flow equations and the electrode design problem, have been carried out by various workers.[4] A number of major publications on the subject have been, or are soon to be, published.[1,4,5] A new theoretical treatment of thermal velocities have been developed by Kirstein;[6] this theory is currently being adapted in detail to MIG's.

V. CONCLUSIONS

In the preceding discussion we have reviewed the basically important properties of a magnetron injection gun, with particular reference to a high-power microwave tube. We have shown that it is possible to design such a gun to produce a dense hollow-beam, that the gun perveance can be approximately an order of magnitude higher than that attainable with a conventional convergent gun, that no current interception is to be expected on any gun electrode, particularly the anode, that high current convergence is possible, and finally, that the available literature relating to the theory and design of magnetron injection guns is, or soon will be, in an advanced state.

VI. REFERENCES

1. Waters, W.E., "Magnetron Guns-An Exact Theoretical Treatment," Diamond Ordnance Fuze Laboratories, Technical Report No. TR-843, 27 April 1960.

2. Kirstein, P.T., Jour. Elec. and Control VII, 417 (1959).

3. Harker, K.J., Jour. of Appl. Phys., 33, 1861 (1962)

4. At the International Congress on Microwave Tubes, held at The Hague, Sept. 3-7, 1962, papers relating to various aspects of magnetron injection gun theory, design, measurements of characteristics, and applications were read by N. Taylor, Varian Asscoiates; B. Arfin, Eitel-McCollough; A. Sutherland and V. Dryden, Sperry-Rand Corp., Gainesville; A. Bers, MIT Lincoln Laboratory; J. Lind, Raytheon Corp., Spencer Laboratory; and A.H.W. Beck, Cambridge University. Proceedings of the Congress will be published in April, 1963.

5. V. Dryden, Jour. of Appl. Phys., October 1962.

6. Dr. Kirstein's paper was read at the tube congress held at The Hague.

THE CURRENT AND VELOCITY DISTRIBUTIONS IN A VELOCITY-MODULATED, BRILLOUIN-FOCUSED ELECTRON BEAM

By

A. S. Gilmour, Jr.

School of Electrical Engineering
Cornell University
Ithaca, New York

ABSTRACT

From the extensive analytical studies of Brillouin electron beams since World War II, the theoretical small signal behavior of these beams is well understood. Until recently, however, there was very little experimental data, which could be used to verify the theoretical predictions. This paper presents the results of measurements of the small signal r-f current and velocity distributions in a Brillouin-focused electron beam and compares these results with those predicted by theory.

The beam analyzer used to make the measurements, and the state of the d-c Brillouin beam are described in order to emphasize the care that was taken in producing the beam. Some of the important features of the beam analyzer are: (1) its capability to be pulse operated at beam voltages up to 10 kv and beam currents up to 1 ampere; (2) a multipurpose nonresonant probe that may be positioned so as to make d-c and r-f current and velocity measurements at any point in the electron beam; (3) a ball valve placed between the electron gun and the drift region, which makes it possible to keep the cathode at pressures below 1×10^{-7} Hg at all times, including periods when the drift tube is exposed to air and when changes are being made in the beam-measuring apparatus; and (4) a beam-scanning and recording scheme which eliminates the necessity for taking point-by-point measurements in the beam. Some of the effects, such as those of stray magnetic fields, that were eliminated in perfecting the beam are shown by electron beam cross sections taken with an automatic recorder. Plots are given of the cyclotron wavelength, scallop wavelength, and beam diameter as functions of the magnetic focusing field and the beam voltage.

The first r-f results presented are small signal measurements taken with the magnetic focusing field adjusted for minimum scalloping (less than 2 per cent). The velocity standing-wave pattern on the beam (obtained by placing negative potentials on the Faraday cage to stop the electrons) is shown to behave very much like the standing-wave pattern on a lossy transmission line with the maxima decreasing slightly as a function of distance. The minima of the pattern are shown to be greater than the d-c velocity of the beam and to vary with distance. Surprising enough it is found that a confined flow theory

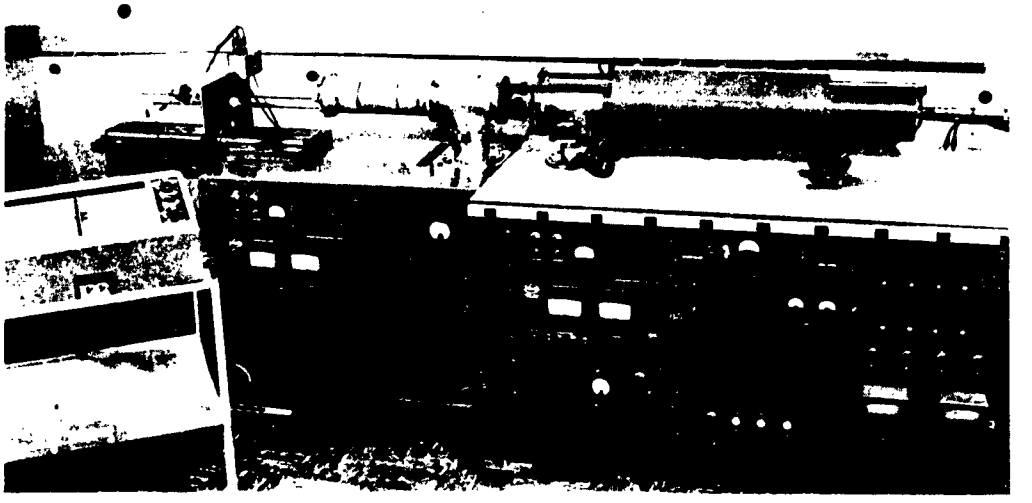

Fig. 1. Beam analyzer.

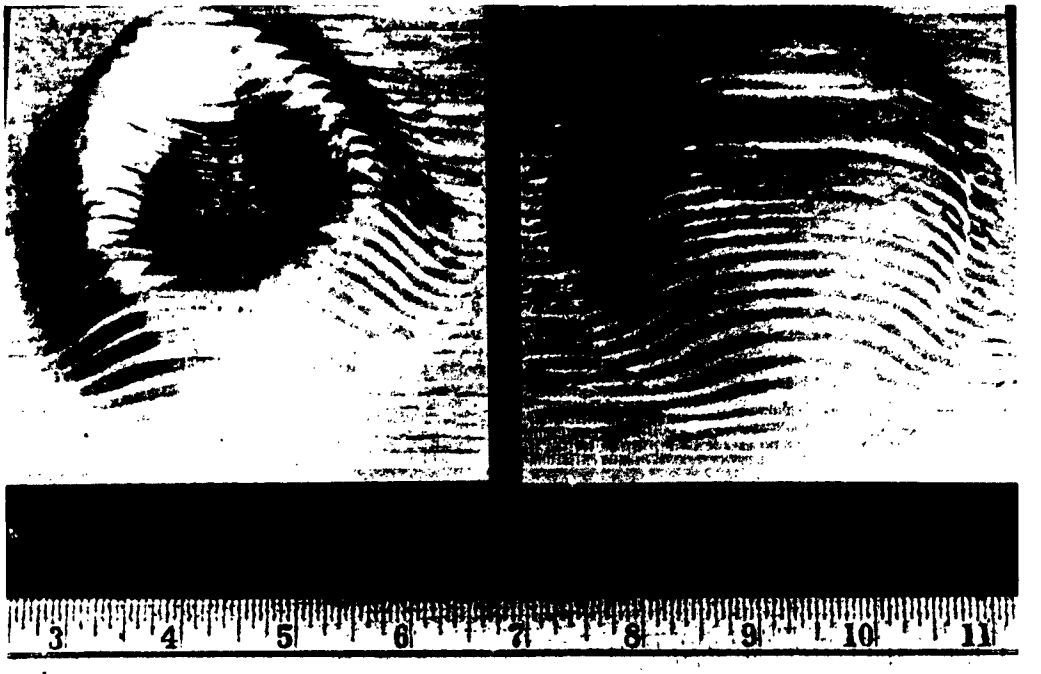

Fig. 2. Electron beam cross sections taken before and after solenoid and electron gun were magnetically shielded.

which includes the effects of higher-ranking waves predicts the behavior of the velocity pattern on the Brillouin beam. Data showing the small signal distribution of the r-f current on the beam is then presented and agree well with the predictions of Brillouin-flow theories; that is, the r-f current is found to be concentrated at the edge of the beam in the form of a surface current. The amplitude of the surface current density is shown to be nearly constant, while the thickness of the current ring varies as a function of distance along the beam.

I. INTRODUCTION

In recent years, many experimental and theoretical studies have been made of the current distribution in velocity-modulated electron beams. The major drawback of the experimental investigations has been that no careful examination was made of the state of the direct-current beam before modulation. A knowledge of the state of the unperturbed beam is important, because most theories that describe the r-f behavior of a beam are based on an ideal beam; i.e., one that is laminar, free from scalloping or other variations in the axial direction, and having a charge density that is constant in the radial and angular directions. Since the major purpose of this study was to compare theoretical predictions with the actual beam behavior, it was necessary to produce a beam that approximated the ideal beam as closely as possible. Moreover, it was desirable to produce a beam similar to those used in commerical linear-beam tubes, so that any results obtained would have a direct bearing on the design and operation of commerical tubes.

II. DESCRIPTION OF ANALYZER

Shown in Figure 1 is a photograph of the beam analyzer used in this study. The electron gun, a Pierce gun with a micro-perveance of 1.15 normally operated at 5400 volts, is contained in the short cylindrical magnetic shield attached to the upper right-hand side of the analyzer. This gun was obtained from a Sperry STL-100 traveling-wave tube which was one of five donated to the School of Electrical Engineering at Cornell by the Sperry Gyroscope Company. The vacuum chamber in which beam measurements were made was surrounded by the focusing solenoid which is the long large-diameter cylinder in the upper right corner of the picture. A ball valve was used between the electron gun and the beam measurement region. When in the open position, the valve permitted the beam to pass through the ball. When the valve was closed, changes could be made in the measuring apparatus without affecting the oxide-coated cathode of the electron gun, since the gun was maintained at pressures below 1×10^{-7} mm Hg by an ion pump. It is estimated that the drift tube was opened to air more than 50 times during the course of the study without damaging the cathode. Motion inside the primary vacuum system was accomplished by using polished stainless steel rods that passed through O-ring vacuum seals. By using the secondary vacuum system shown to the left, pressures lower than 5×10^{-7} mm Hg could be maintained in the primary system, including periods when the rods were being moved into the vacuum system.

The magnetic field in the solenoid rose from zero to the average value on the axis of the solenoid in an axial distance of less than one beam diameter and then varied less than 2 per cent as a function of axial position. It was found that stray magnetic fields, even though they were only a few per cent of the main solenoid field, had large effects on the beam. Figure 2 shows

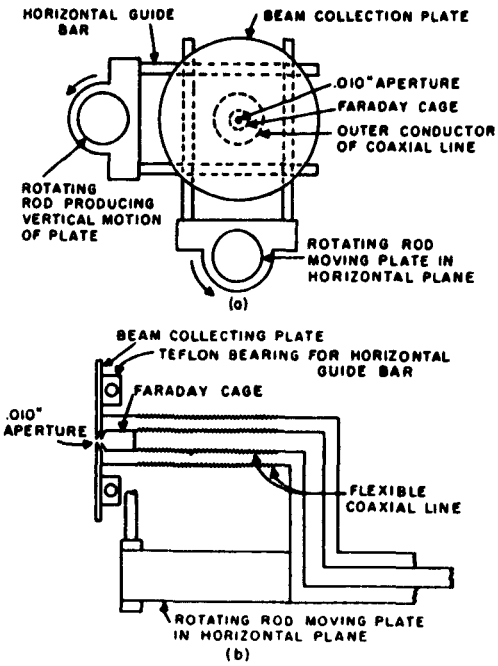

Fig. 3. Simplified sketch of beam-scanning mechanism inside beam analyzer.

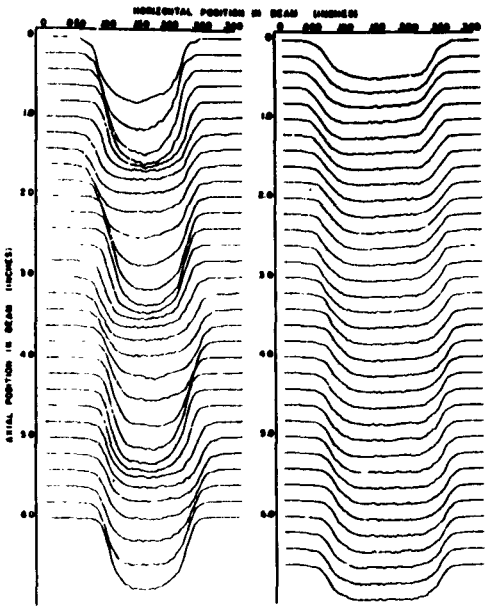

Fig. 4. Sample data from which beam characteristics are obtained.

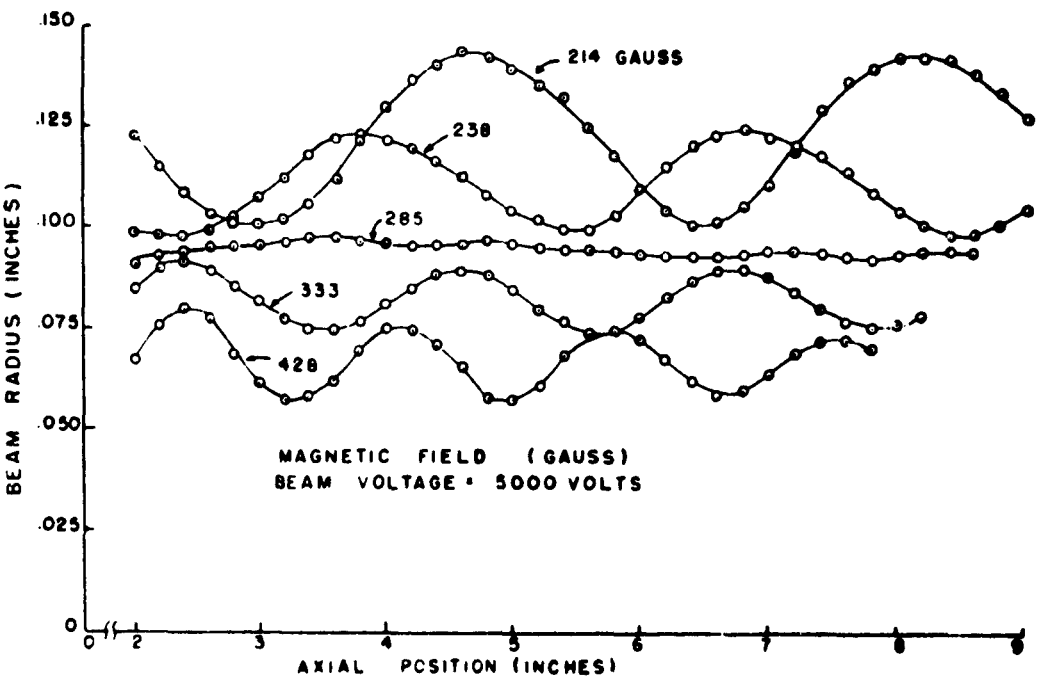

Fig. 5. Beam radius versus axial position.

electron beam cross sections taken before and after the solenoid and the electron gun were magnetically shielded. After shielding, the magnetic field in the cathode region was found to be less than one-half percent of the field in the drift tube and was reasonably uniform over the cathode surface.

Figure 3 shows the part of the beam-scanning mechanism inside the analyser. Most of the electron beam was collected by the beam-collecting plate, which was carbonized to reduce the emission of secondary electrons. A small portion, however, was allowed to pass through the 0.010-inch aperture in the center of the plate to a Faraday cage attached to the end of the center conductor of a coaxial line. The electron current from the cage went through a coaxial vacuum feed-through in the bottom control rod to an indicating device outside the analyzer. The collecting plate was positioned in the plane perpendicular to the axis of the solenoid by rotations of the two control rods. As is shown in the sketch, the plate could be moved horizontally by rotating the bottom rod. Vertical motion was produced in a similar manner by rotating the side rod. Although rotational motions were converted to translational motions in positioning the cage, they could be considered to be linear, since the distances moved were small compared to the length of the lever arms.

III. D. C. BEAM PROPERTIES

To determine how well standard Brillouin beam theories define the behavior of a Brillouin beam of the type used in linear beam tubes, data similar to that shown in Figure 4 were taken on the STL-100 beam. These data were obtained by recording the current from the Faraday cage at various axial positions in the beam as the cage was moved horizontally across the beam on a beam diameter. The curves in Figure 4b are the beam profiles for a beam voltage of 5 kv and a magnetic field level that produced very little scalloping. The curves in Figure 4a were also taken at 5 kv, but the magnetic field was 1.33 times the value required for no scalloping. The periodic variations in the widths of the profiles indicate the scalloping of the beam. Shown in Figure 5 are the 5-kv beam radii containing 95 per cent of the beam current as functions of the axial position in the drift tube and of the magnetic field. Notice that at 285 gauss, which is within 2 per cent of the computed Brillouin flow value, the beam diameter varied less than 2 per cent.

Shown in Figure 6 is the center position of the beam as a function of magnetic field and axial position. Motion of the beam center position is thought to have arisen from a misalignment of the cathode. In taking data, it was interesting to observe that when complete cross sections of the beam were taken as a function of the axial position, the center position was found to move in the clockwise direction about the axis of the solenoid when the current flowed through the solenoid in one direction and in the counterclockwise direction when the solenoid current was reversed.

Figure 7 shows the wavelengths of the motion of the center of the beam (cyclotron wavelength) and the scallop wavelengths as functions of the magnetic field and the beam voltage for the beam from the STL-100 gun. Table I compares the values of the cyclotron wavelength at 200 gauss obtained from Figure 7 with the calculated values.

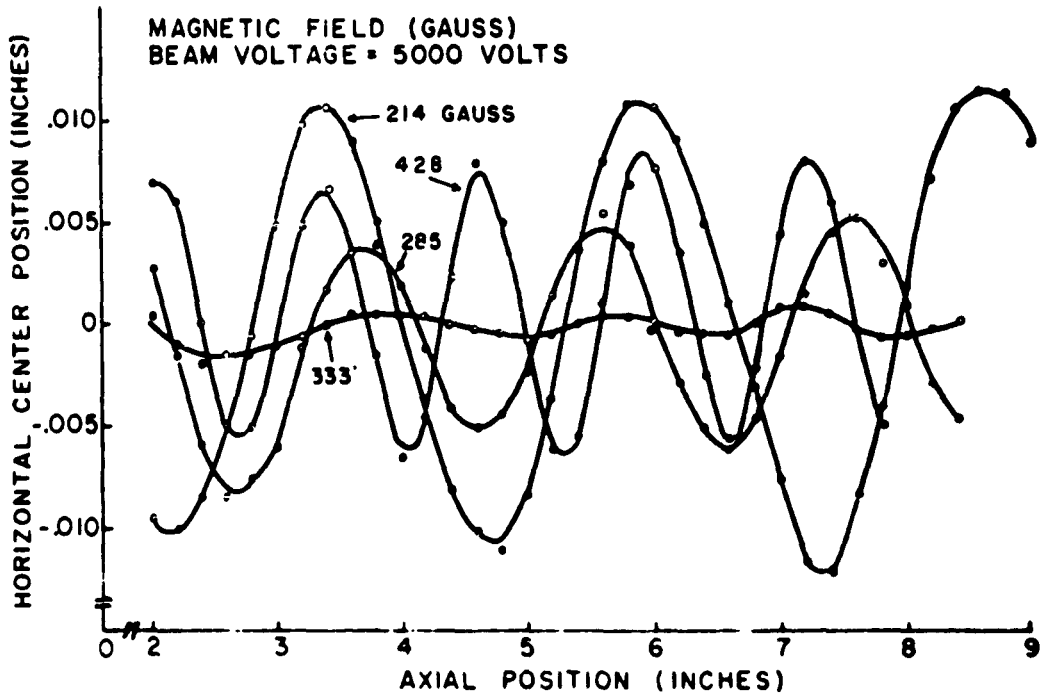

Fig. 6. Horizontal center position versus axial position.

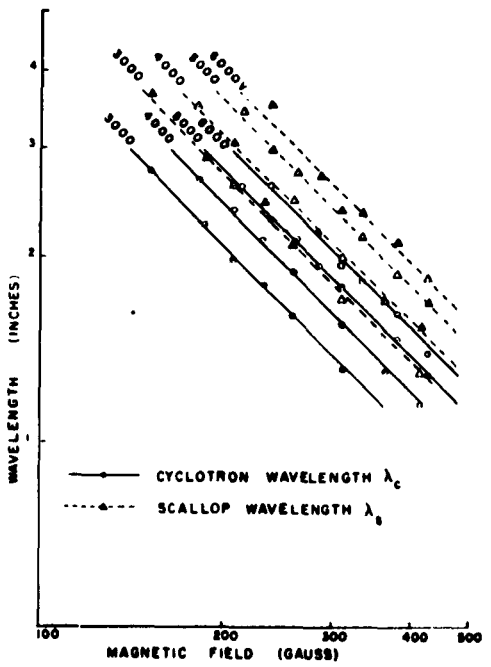

Fig. 7. Cyclotron and scallop wavelengths versus magnetic field.

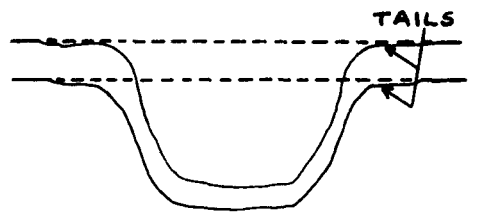

Fig. 8. Beam profiles showing low current-density "tails." (Taken at two points spaced 0.2 in. on axis of beam.)

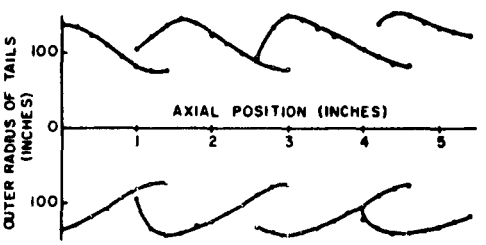

Fig. 9. Outer radius of profile "tails" versus axial position in beam.

Table I. Experimental and Calculated Cyclotron Wavelengths

Beam Voltage	λ_c from Figure 7 (inches)	Calculated λ_c (inches)
6000	3.08	3.06
5000	2.77	2.79
4000	2.45	2.50
3000	2.09	2.16

For the calculated values, the velocity variation along the axis of the drift tube was taken into account. This variation was small, amounting to less than 1 per cent when the collector was near the gun end of the drift tube, and amounting to about 5 per cent when the collector was more than one drift-tube diameter from the gun end. The calculation of the velocity variation as a function of distance is given in detail elsewhere.

The scallop wavelength curves nearly lie along straight lines having a slope of -1, therefore the flux in the cathode region was small. Because of this, the scallop wavelength should have been related to the cyclotron wavelength through $\lambda_g = \sqrt{2}\lambda_c$. The ratio λ_g/λ_c obtained for the STL-100 beam was 1.31 instead by $\sqrt{2}$ which represents an error of about 7 per cent. This error is thought to have been caused partially by a small amount of flux linking the cathode and partially by the electrons in the low current density "tails" shown in Figure 8. These "tails" were found to move into and out of the beam in the manner shown in Figure 9, which is similar to the arrow development in an electron beam described by Johnson. Since the tails were outside the beam in regions where the bulk of the beam was scalloping outward, and inside the beam in regions where the beam was scalloping inward, they could have altered the space-charge force in the beam so as to reduce the scallop wavelength from $\sqrt{2}\lambda_c$ to $1.31\lambda_c$.

Shown in Figure 10 is the equilibrium radius of the beam as a function of the magnetic field. The data points represent the average beam radii that contained 93 per cent of the beam current and the straight lines give the beam radii predicted by theory. The error between the two is less than 3 per cent. The 95 per cent diameter was found to be greater than the theoretical value by about 6 per cent and the 90 per cent diameter was found to be less by about 6 per cent.

IV. R. F. BEAM PROPERTIES

The first r-f measurements made on the Brillouin beam were of the velocity modulation on the beam resulting from a doubly-reentrant cavity tuned to 1940 mc and driven at various signal levels. The method used to measure the peak velocity of the electron beam was that of applying a negative potential to the Faraday cage which was just large enough to repel the electrons approaching the cage from the aperture in the movable beam collector. Since the current to the cage dropped rapidly from a constant value to zero as the cage potential was varied from the beam voltage plus a few volts to the beam voltage minus a few volts (see Figure 11), small changes in the beam velocity could be easily detected by observing the curve of the cage current versus voltage. The reason the curve of current versus voltage did not have a sharper cut-off than shown in Figure 11 is because the "beam voltage" was a

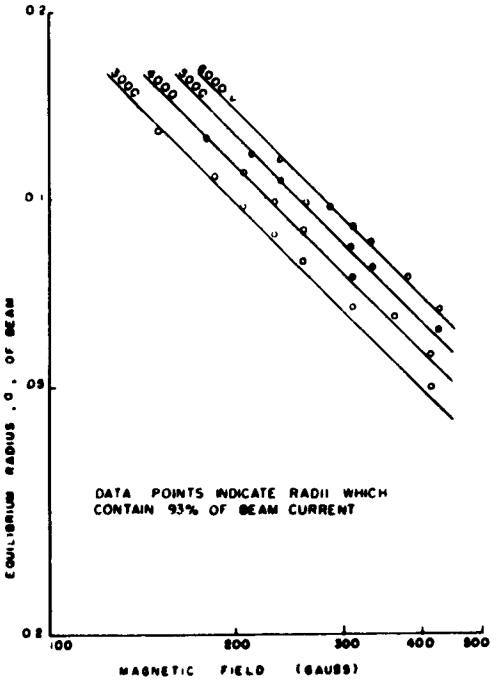

Fig. 10. Equilibrium radius versus magnetic field.

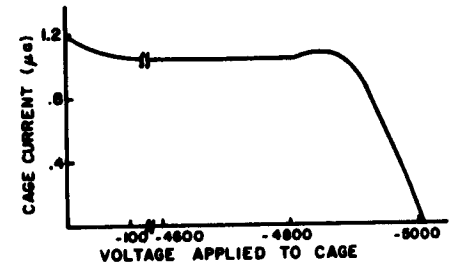

Fig. 11. Current-voltage characteristic for Faraday cage.

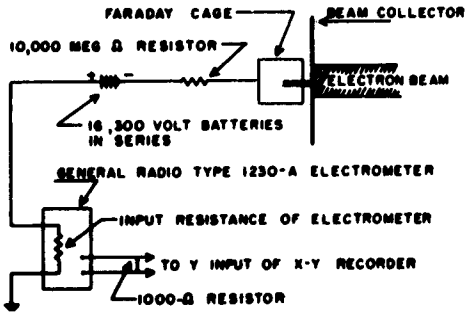

Fig. 12. Circuit used to provide peak beam-velocity indication to X-Y recorder.

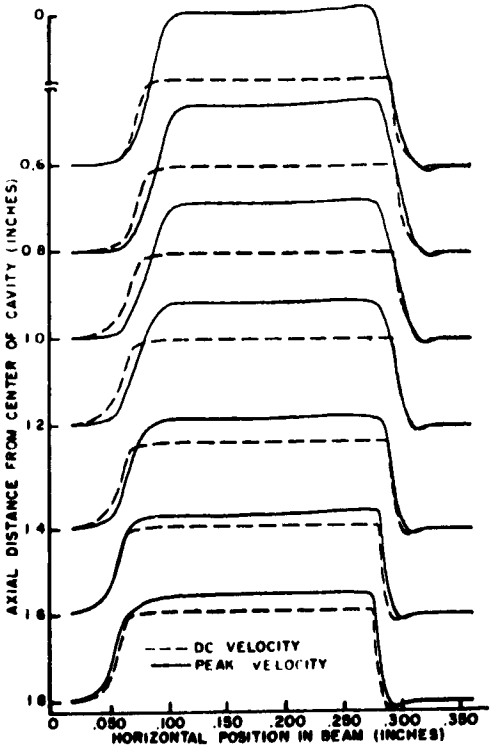

Fig. 13. D-C and peak beam velocities as a function of the axial and the radial positions in beam.

16.7μ sec duration pulse (rise time = .2μsec, fall time =.3μ sec) applied to the cathode of the beam tester, and the pulse droop was about 50 volts.

To make automatic recording of the velocity possible, the circuit shown in Figure 12 was devised. This circuit is essentially a voltage divider in which a fraction of the current approaching the cage was used to build up a bias voltage across the 10,000 MΩ resistor in series with the input resistance of the electrometer. This bias voltage in turn repelled the remaining part of the current approaching the cage and returned it to the beam collector. Sixteen 300-volt batteries were used to provide a cage bias just below the d-c beam voltage of 5000 volts. Therefore the voltage required across the 10,000 MΩ resistor was the difference between 4800 volts and the voltage equivalent of the peak velocity of the beam. At a beam voltage of 5000 volts, the bias current required was .02μa, which represented only two per cent of the total current of 1μa passing through the aperture under Brillouin flow conditions. As can be seen in Figure 11, the cage potential at a cage current of .02μa was essentially the peak voltage in the beam. When velocity modulation was applied to the beam, the peak velocity of the beam increased, therefore the current necessary to bias the cage increased. In addition, the voltage-current characteristic became more sloping, so that with 500 volts of modulation on the beam, the bias current was .07μa and the error in measuring the peak voltage was about 5 per cent. This error could have been reduced by using a resistor larger than 10 kMΩ, but then the time constants involved would have been too large to permit data to be taken in a reasonable time interval.

The input resistance switch of the electrometer was normally set on the 10^8-ohm position so that the voltage into the electrometer was .01 of the voltage across the 10 kMΩ resistor. The output current from the electrometer was passed through a 1000Ω resistor to provide a voltage input to the X-Y recorder.

Data, similar to that shown in Figure 13, were obtained by recording the d-c and the peak r-f beam velocities at various axial positions in the beam as the Faraday cage was moved horizontally through the beam diameter. This data was taken at drive levels ranging from α = .015 to α = .30. In all cases, it was found that the variations in the peak velocity as a function of the radial position in the beam were small. In particular, under small-signal conditions (Figure 10 is a good example), the peak r-f velocity as a function or radius was found to be nearly constant.

As a result, the velocity of the entire beam was very nearly that shown by the curves in Figure 14. These were obtained by moving the cage to the center of the beam and by plotting the peak velocity as a function of axial position. The important points to notice about the standing waves shown in Figure 14 are (1) that at small-signal levels, the second velocity maxima is greater than the first, and succeeding maxima decrease as a function of distance, (2) that the nulls do not reach the d-c beam level, and (3) that at large-signal levels the amplitude decreases rapidly, and the shape of the

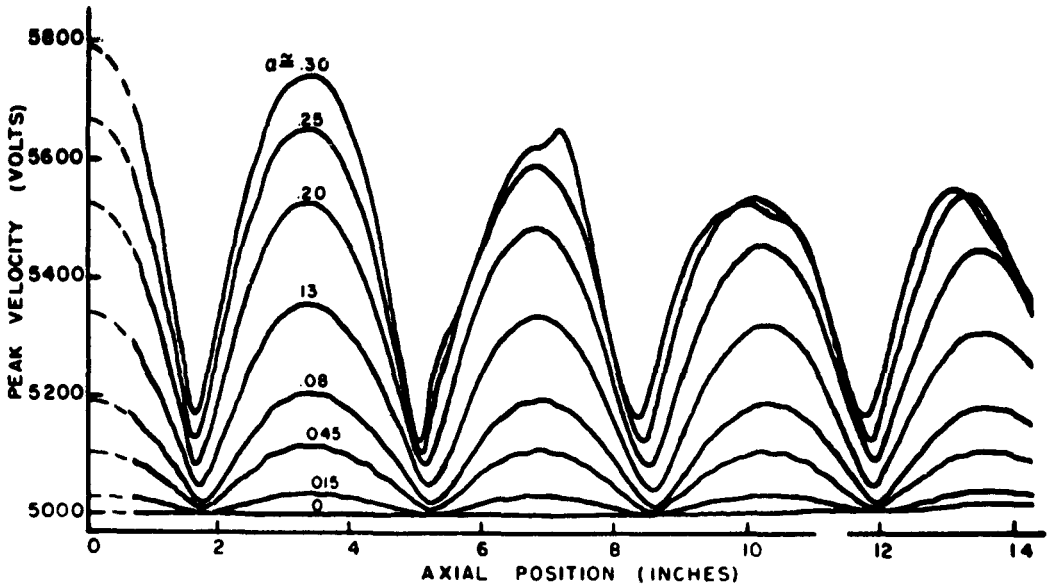

Fig. 14. Peak beam velocity as function of axial position and R-F drive level for Brillouin flow conditions.

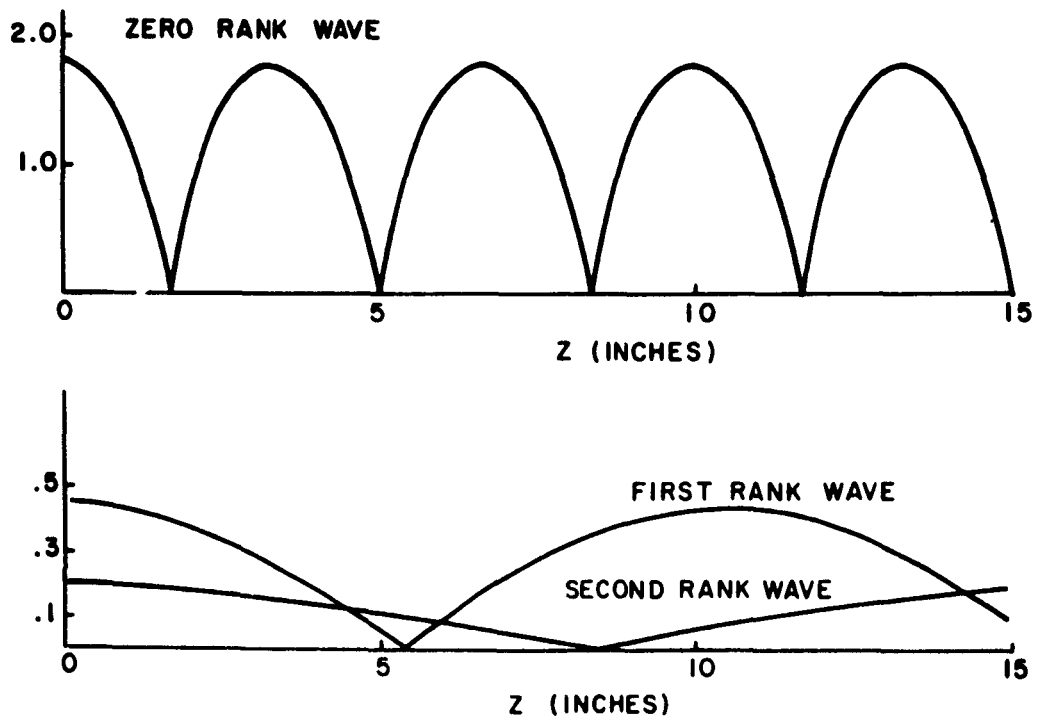

Fig. 15. Amplitudes of zero-, first- and second-rank velocity waves.

standing-wave pattern deviates considerably from a series of half sinusoids. It is interesting to observe that the first two of these items can be explained with confined flow space-charge wave theory containing the effects of higher ranking waves. The zero-, first-, and second-rank waves are shown in Figure 15 and the sum of these waves is shown in Figure 17. The total velocity is shown by the solid curve and it is seen that the higher-rank waves cause the second velocity maxima to be greater than the first and that succeeding maxima decrease with distance. It must be noted, however, that the initial increase in the maxima is larger than that found experimentally. The percentage decrease in the succeeding maxima is predicted to be about 8 per cent by the confined flow theory, and is found to be closer to 10 per cent in the experimental results. The ratio of the minimum to the maximum velocity is predicted to be 0.14 and this is the same as the average of the small-signal experimental results. The major difference between the predicted and actual minima is that those shown in Figure 17 are not all at the same level, whereas the minima resulting from the small-signal measurements are all at the same level.

At large-signal levels, Figure 14 shows that there is no initial increase in the velocity maxima. Also the percentage decrease in the maxima is nearly 20 per cent as compared to 10 per cent at small-signal levels. Since the shape of the standing-wave pattern is no longer a series of half sinusoids at high-signal levels, it is to be expected that at least a second-order theory would be required to analyze these results.

In addition to the Brillouin beam investigation, measurements were made of the peak electron velocities in a scalloping d-c beam, which was velocity modulated. Plots of the beam velocity as a function of axial position and of drive power for a magnetic field 25 per cent greater than the Brillouin value are shown in Figure 18. With the exception of the decrease in wavelength, these curves are not much different from those shown in Figure 14 for the Brillouin flow case.

A plot of reduced plasma half-wavelength as a function of the magnetic field is shown in Figure 19. The slope of the line fitting most of the data points is -0.45. However, at 200 gauss, the slope changes to -1 and the reduced plasma half-wavelength becomes equal to the scallop wavelength. The explanation for this must be that the periodic d-c electric field, which is caused by the d-c scalloping of the beam, forces the regions of high electron density resulting from the velocity modulation to move into the regions of low density on the scalloping beam. This action is similar to the pulling of the frequency of an oscillator by a resonant circuit, where the reduced plasma frequency corresponds to the oscillator frequency and the d-c scalloping beam corresponds to the resonant circuit.

Plots of the beam velocity as a function of axial position and of drive power for magnetic fields 25 per cent and 35 per cent below the Brillouin value are shown in Figures 20 and 21. The effect of the d-c beam minima on the velocity curves in Figure 20 is to depress the right-hand side of each half sinusoid. In Figure 21, where the reduced plasma half-wavelength is shown equal to the scallop wavelength, the right-hand sides of some of the half sinusoids are actually depressed to the minima of the velocity standing wave by the d-c beam minima.

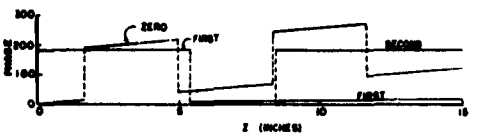

Fig. 16. Phase shift relative to $\omega t - \beta_e z$ for the zero-, first-, and second-rank velocity waves.

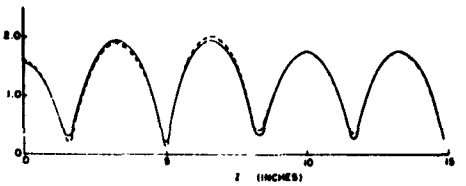

Fig. 17. Sum of zero-, first-, and second-rank velocity waves.

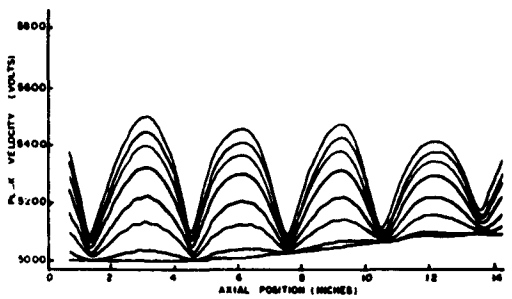

Fig. 18. Peak beam velocity as function of axial position and of R-F drive level for a magnetic field 25 per cent greater than Brillouin value.

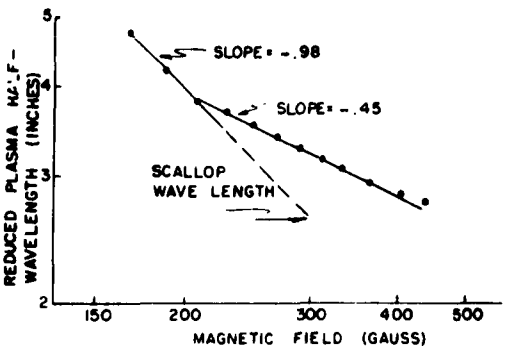

Fig. 19. Plot showing locking of plasma oscillation onto D-C scalloping of beam.

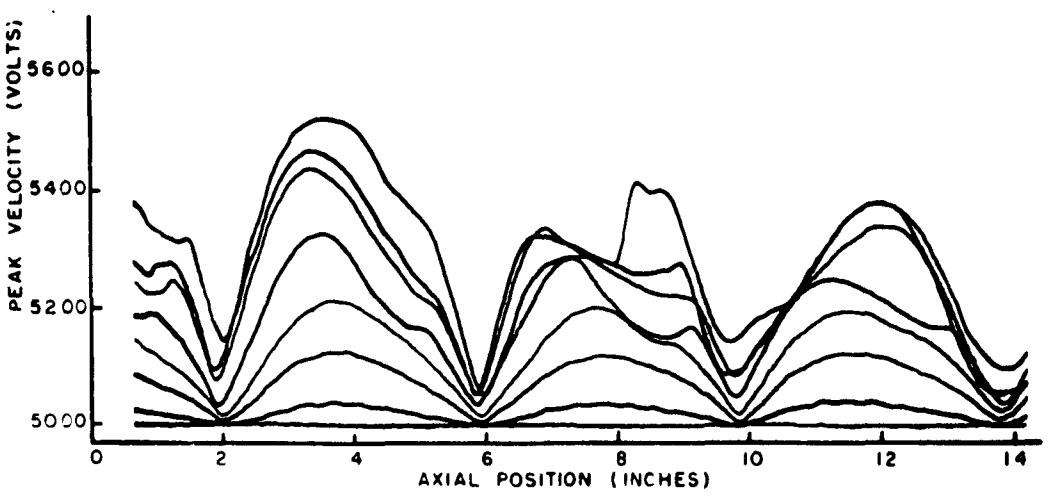

Fig. 20. Peak beam velocity as function of axial position and of R-F drive level for magnetic field 25 per cent lower than the Brillouin value.

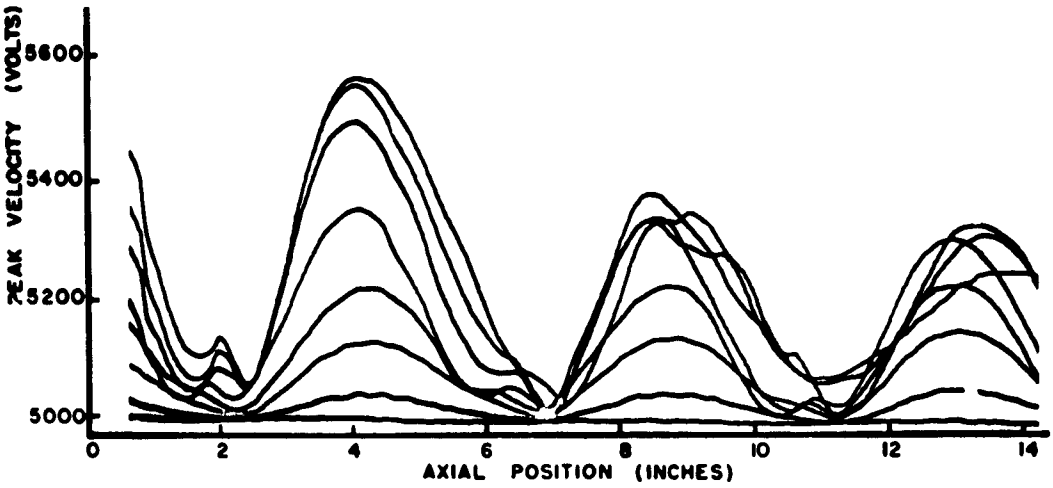

Fig. 21. Peak beam velocity as function of axial position and of R-F drive level for magnetic field 35 per cent lower than the Brillouin value.

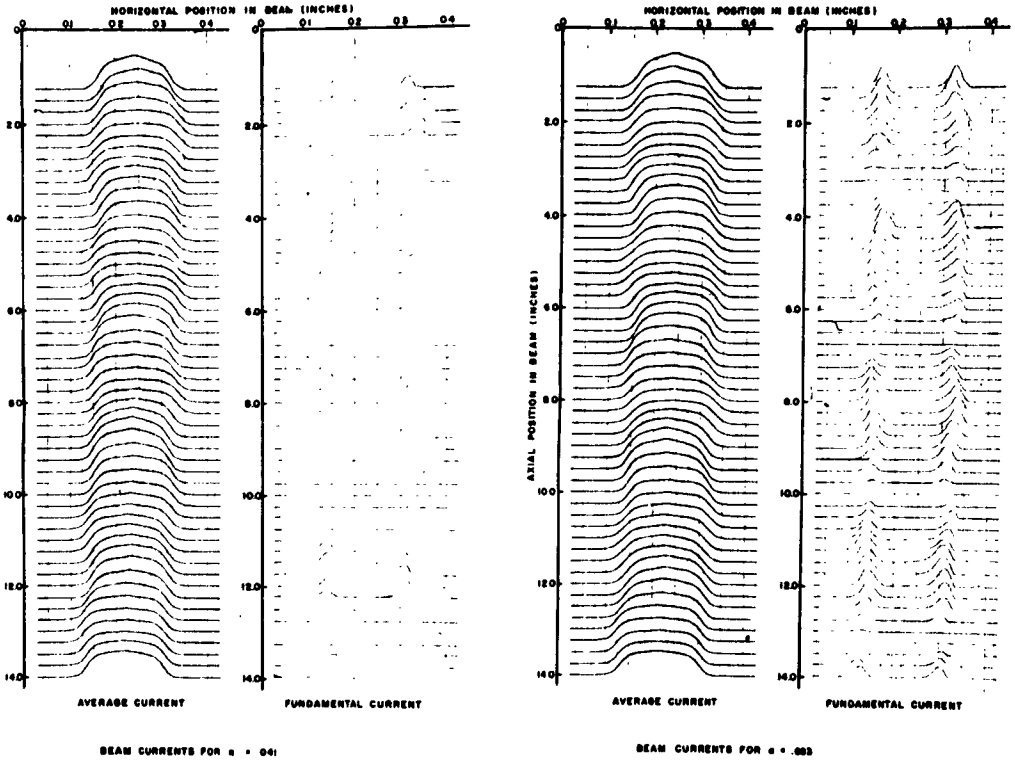

Fig. 22, 23. Average and fundamental current density plots as functions of the horizontal and axial positions on the Brillouin Beam.

Measurements were made of the fundamental current in the Brillouin beam by using the non-resonant coaxial probe shown in Figure 3. Figure 22 shows average and fundamental current density plots as functions of the horizontal and axial position in the Brillouin beam for a depth of the modulation of $\alpha = .041$. The average current plot is similar to the d-c Brillouin flow plot since the r-f drive level was not high enough to cause the beam to change appreciably. The fundamental current data displays the surface current shell that is predicted by Brillouin beam theories to result from modulation by a gridless gap cavity. The center plane in the gap in the cavity is indicated by the zero axial position point. Notice that the current density becomes zero at a distance of 3.3 inches from the cavity and that the zero repeats every 3.3 inches, which is the reduced-plasma half wavelength. These zeros occur at the maxima of the velocity standing wave and the points of maximum current density occur at the minima of the velocity wave as is predicted by theory. Shown again in Figure 23 are curves of the average and the fundamental current densities, but these were obtained for $\alpha = .083$. The major observations to be made here are; (1) that the average current contours are widened slightly by the r-f current wave and (2) that both the amplitude and the width of the fundamental current contours have increased. The increase in the width of the current ring is understandable from the simple Brillouin flow theory which assumes the d-c current density as a function of radial position is rectangular in shape. The increase in amplitude of the current ring, however, stems from the fact that the d-c current density as a function of radial position is more nearly trapezoidal than rectangular in shape. This effect has been observed and reported by Donald K. Winslow at Stanford University.

V. CONCLUSIONS

In conclusion, it may be said that the most important new development in the beam analyzer described here is the ball valve between the electron gun and the drift tube. This valve has made it possible to carry out a large number of measurements in a single electron beam, even though the drift tube was opened to air numerous times for alterations to be made in the beam-scanning apparatus.

The beam formed through the use of the analyzer was very nearly an ideal Brillouin beam since the density of the magnetic flux in the cathode region was less than one-half per cent of that in the drift region, and since the beam scalloped less than 2 per cent when the magnetic field was within 2 per cent of the calculated Brillouin flow value. The RF behavior of this Brillouin beam, both in terms of velocity and current agreed with the theoretical predictions very well.

VI. ACKNOWLEDGMENTS

This work is part of a study of the RF characteristics of electron beams which is being conducted under the sponsorship of the Rome Air Dev. Center of the Air Res. and Dev. Command, USAF (R.F. Transmitter and High Power Tube Branch).

MEASUREMENT OF THE SURFACE TEMPERATURE OF A SOLID UNDER ELECTRON BOMBARDMENT

By

Elliot Silverman

Lincoln Laboratory,* Massachusetts Institute of Technology

One severe limitation in the generation of super high power is the evaporation of materials from surfaces subjected to high intensity pulsed electron beam bombardment. The kinetic energy of the beam impinging on the surface is converted into thermal energy resulting in local heating of the material to high temperatures. The metal vapors liberated can limit peak power output by

a) inducing vacuum voltage breakdown
b) coating insulators within the tube vacuum with metal
c) cathode poisoning
d) changing critical dimensions of the RF structure.

Heat generated by a pulse of a few microseconds duration appears as surface heating of the metal since the time constant for heat flow away from the surface may be long compared to the pulse duration. Surface damage due to the thermal stresses produced by the pulsed heating may result even at power levels insufficient to cause melting.

A program has been in progress at Lincoln Laboratory to obtain quantitative information on the temperature rise of materials under various conditions of pulsed electron bombardment. Of particular interest is the single pulse heating of the metal.

This paper will first review the analytical results obtained, then describe briefly the series of experiments conducted to measure the surface heating and finally will make a comparison of the predicted and measured surface temperatures for the metals investigated.

A theoretical solution of the heat flow problem has been made by Dr. G. Vibrans of our laboratory. The energy distribution with depth has been calculated and inserted as a distribution of heat sources in an appropriate solution of the heat-conduction equation. The single pulse surface

*Operated with support from the U. S. Advanced Research Projects Agency.

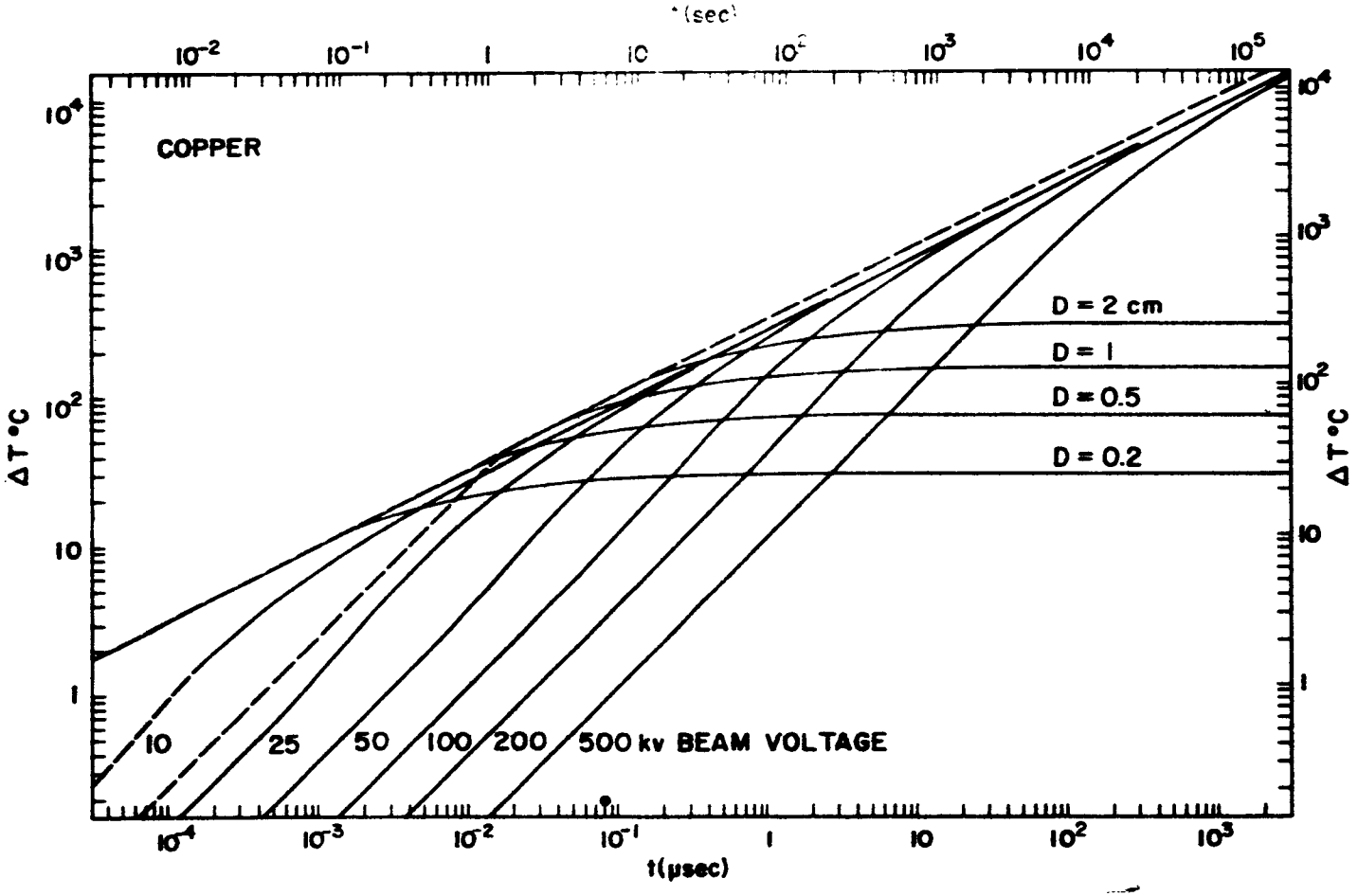

Fig. 1 SURFACE TEMPERATURE vs TIME FOR OFHC COPPER

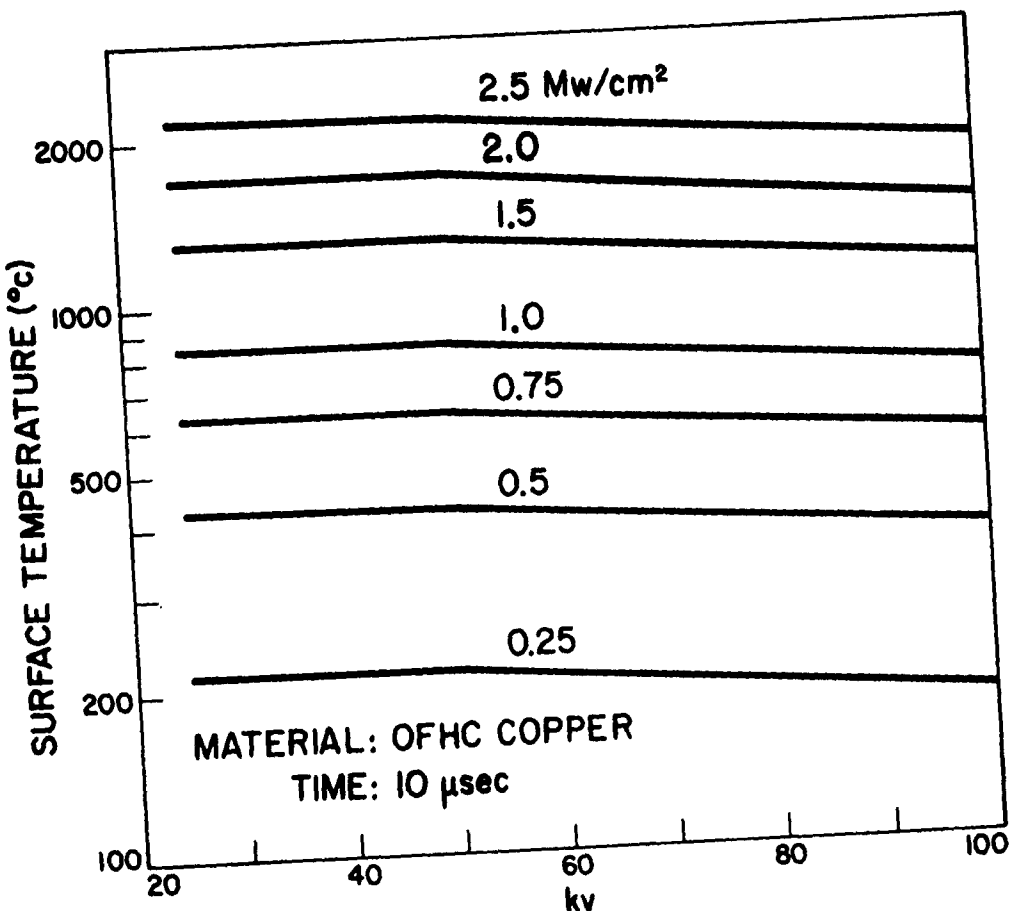

SURFACE TEMPERATURE vs BEAM VOLTAGE FOR CONSTANT BEAM POWER DENSITY

ch8-180

Fig. 2.

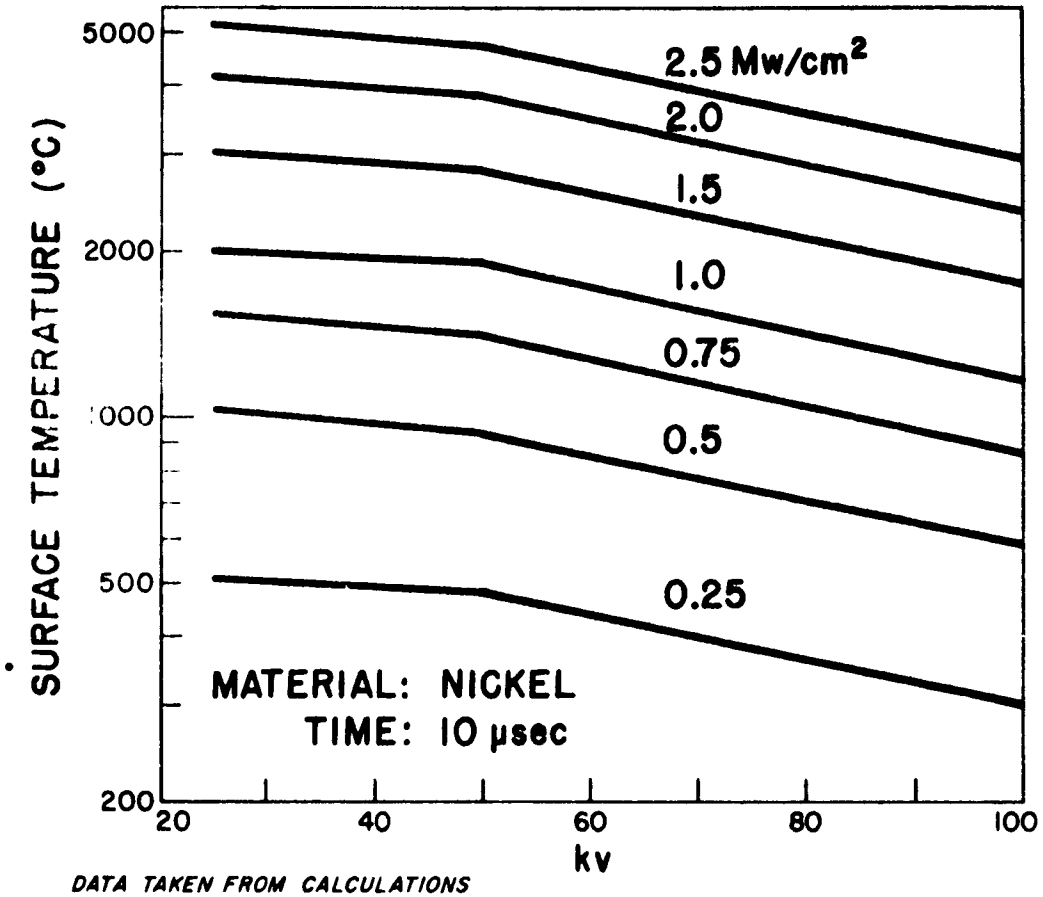

DATA TAKEN FROM CALCULATIONS BY G. VIBRANS

SURFACE TEMPERATURE vs BEAM VOLTAGE FOR CONSTANT BEAM POWER DENSITY

CVF-181

Fig. 3

temperature vs. time for any solid is plotted in one diagram with pulse voltage as the parameter. The analysis shows that materials with high thermal conductivity, specific heat and density will exhibit the lowest transient temperature rise. For our initial investigation, OFHC copper, nickel and chromium were studied.

In Fig. 1 we have plotted the predicted single pulse surface temperature vs. time for OFHC copper with pulse voltage as parameter. The four horizontal lines do not apply to this analysis. The peak power density assumed is 1 Mw/cm^2. This curve shows how the temperature first rises linearly with time, then goes through a transition and finally approaches the square-root law. However, as can be seen from the curves, 200 kv electrons at 10 μsec are still in the transition part of the curve.

For comparison, the volume heating temperature rise derived on the assumption that the beam energy is uniformly distributed over a depth equal to the practical range of 25 kev electrons is shown as a dashed line with slope 1 near the left corner of the chart. However, if one assumes that all the energy is dissipated at the surface of a semi-infinite slab, one obtains the well known $\sqrt{\text{time}}$ curve shown as a dashed line with slope 1/2. As seen from these curves the predicted temperature is always less than the idealized volume and surface heating curves at any given voltage.

Since the calculated temperature rise is directly proportional to the beam power density impinging on the target, one may calculate for any assumed time interval, a family of curves with power density as parameter.

In Fig. 2 we have plotted the predicted surface temperature as a function of pulse beam voltage for beam power densities between 0.25 Mw/cm^2 and 2.5 Mw/cm^2 assuming a pulse duration of 10 μsec, the pulse duration used throughout our experiments. The material is OFHC copper. It is interesting to note that the surface temperature decreases slowly for higher pulse voltages due to penetration of the electron beam into the metal. No consideration of the thermodynamic phase change of the metal is included in this analysis and therefore surface temperatures exceeding the melting point are predicted.

A similar group of curves are plotted for nickel and chromium and are shown in Fig. 3 and Fig. 4 respectively. Here we observe a greater dependency of surface temperature on the pulse voltage.

To investigate experimentally the materials which had been analytically evaluated, a special tube was designed which permitted targets of different materials to be tested within the same vacuum chamber and under the same pulsed conditions. The experimental set-up for observing the temperature rise of the bombarded target is shown in Fig. 5.

Basically the tube is a diode employing a production type VA87 cathode assembly and a water cooled collector. Beam perveance is 1.8×10^{-6}. The target assembly consisting of four separate targets is fastened on a copper block which in turn is clamped to the water cooled collector by a clamping shaft. With the tube placed in a horizontal position, and the clamping shaft unlocked, the target assembly is free to rotate 360^{o} about its axis. Any one of the four targets may be chosen by

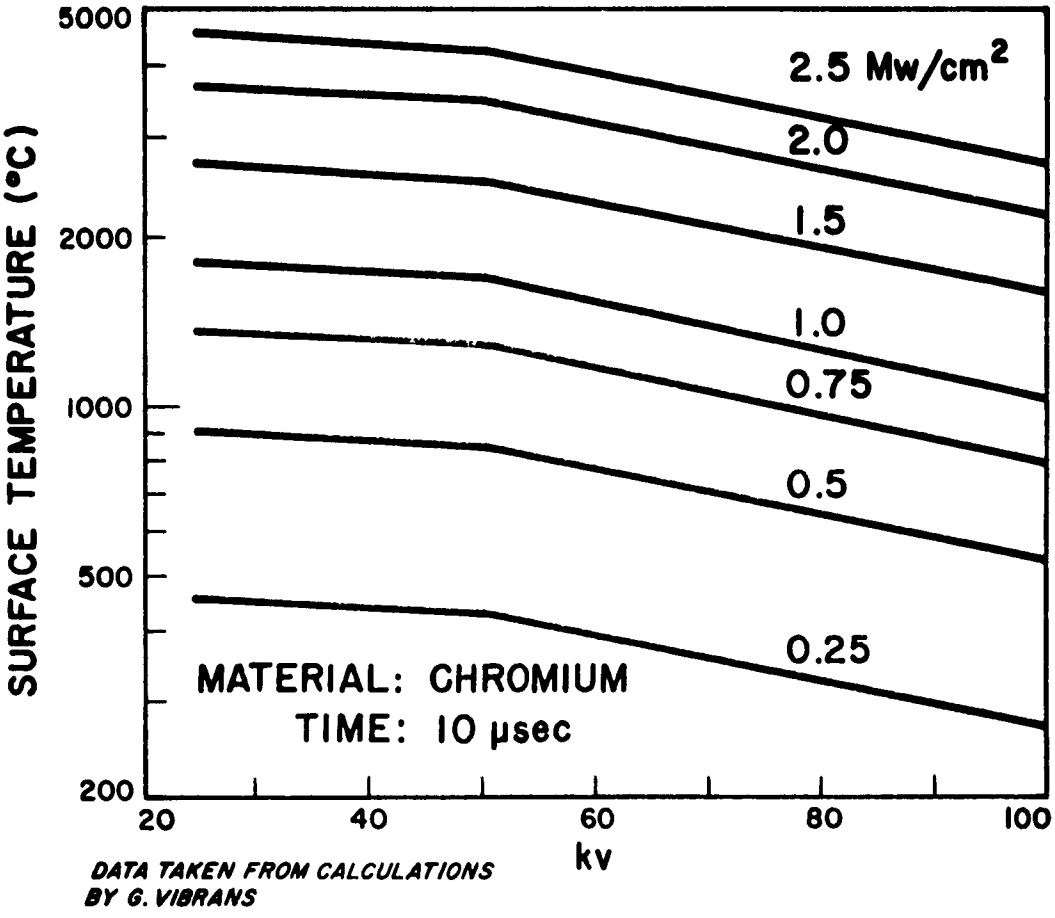

SURFACE TEMPERATURE vs BEAM VOLTAGE FOR CONSTANT BEAM POWER DENSITY

Fig. 4 c48-179

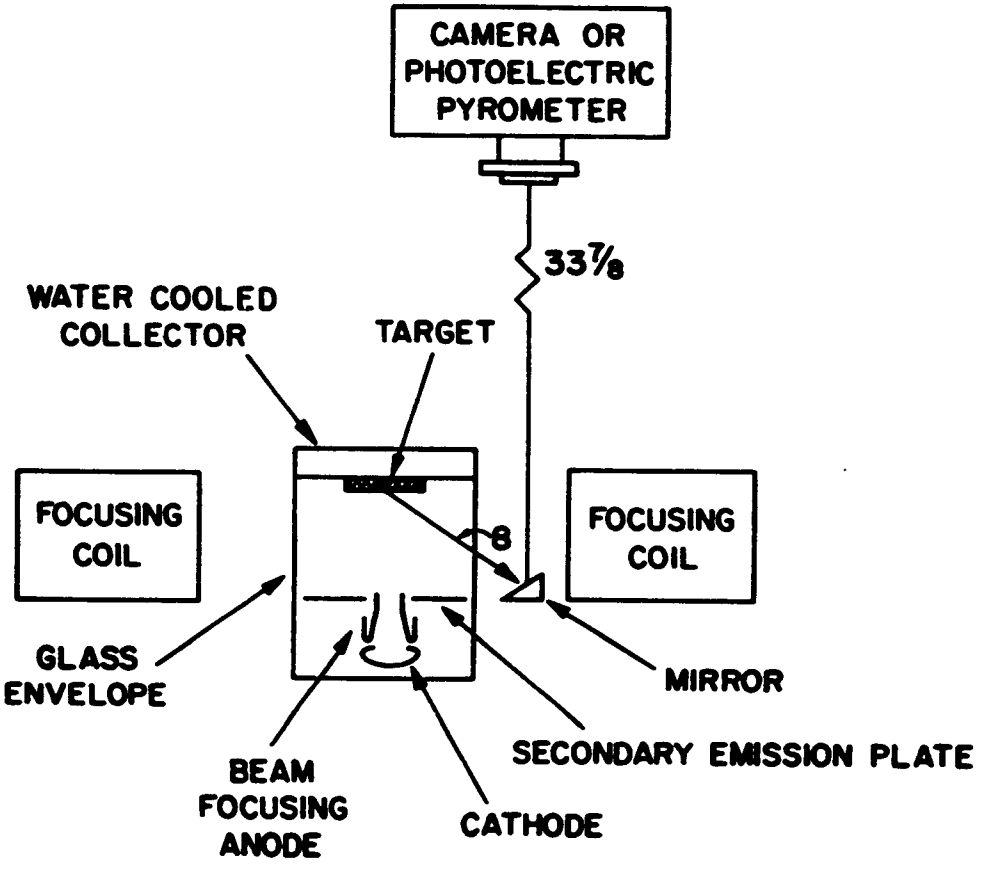

Fig. 5

EXPERIMENTAL SET UP FOR OBSERVING BOMBARDED AREA

simply rotating the tube until the desired target appears in position. The shaft is then locked assuring good thermal contact between the target assembly and water-cooled collector. The tube incorporates demountable vacuum flanges which permit rapid changing of target assemblies. Prior to changing of a target assembly, dry nitrogen is admitted into the tube via the vacuum manifold to prevent poisoning of the cathode when the tube is opened to air. During the course of our experiments, the tube was let down to dry nitrogen and reprocessed three times with no measurable loss of cathode emission. A 5 liter/sec. ion pump is attached to the tube maintaining a steady state vacuum better than 10^{-8} Torr. Interlock circuitry on the pump prevents pulsing the tube if instantaneous pressure exceeds 10^{-5} Torr. during beam bombardment.

Provision has been made in the tube design to observe the target visually during pulse bombardment. A mirror, mounted on the tube base and placed between the focusing coil and tube glass envelope, permits viewing the bombarded surface from a position directly above the lead shield surrounding the tube. Extreme care has been taken to shield both personnel and viewing equipment from the X-rays produced. For temperature measurements the photoelectric pyrometer is placed in position as shown.

A schematic diagram of the photoelectric pyrometer is shown in Fig. 6. An image of the target is viewed through the ocular eyepiece lens and focused by a movable objective lens onto a beamsplitter mirror tilted 45° to the optic axis. Radiant energy from the target passes through the objective lens and strikes the cathode of the 7102 photomultiplier tube. The spectral response of the 7102 photomultiplier is in the infrared region peaking at approximately 0.8 microns. The operator sees a magnified image of the spot through the ocular eyepiece permitting him to focus and position the photoelectric pyrometer on the desired area. Directly in front of the 7102 tube is a long pass interference filter whose cutoff wavelength is 0.7 micron. Undesirable luminescence is filtered out. The output of the photomultiplier is fed through the cathode follower to a dual beam oscilloscope.

The photoelectric pyrometer is calibrated against a commercial optical pyrometer using a tungsten ribbon lamp and a rotating sectored disk.

A typical pulse for copper as viewed at the photomultiplier output for single pulse beam voltages up to 58 kv. is shown in Fig. 7. Both the photomultiplier output pulse and the corresponding target current pulse are shown superimposed. The horizontal time scale is 5 μsec/cm. Above 58 kv a spike appears near the trailing edge of the pulse as shown in Fig. 8.

In a series of repeated experiments, measurements were carried out on both nickel and chromium targets with results similar to that shown in Figs. 7 and 8, with the one difference that the spike now appears at pulse voltages lower than that observed for copper. Plotting only the amplitude of the flat portion of the output pulse from the photomultiplier as a function of the peak pulse voltage, one obtains the curves shown in Fig. 9.

The measured data show no significant difference in pulse tempera-

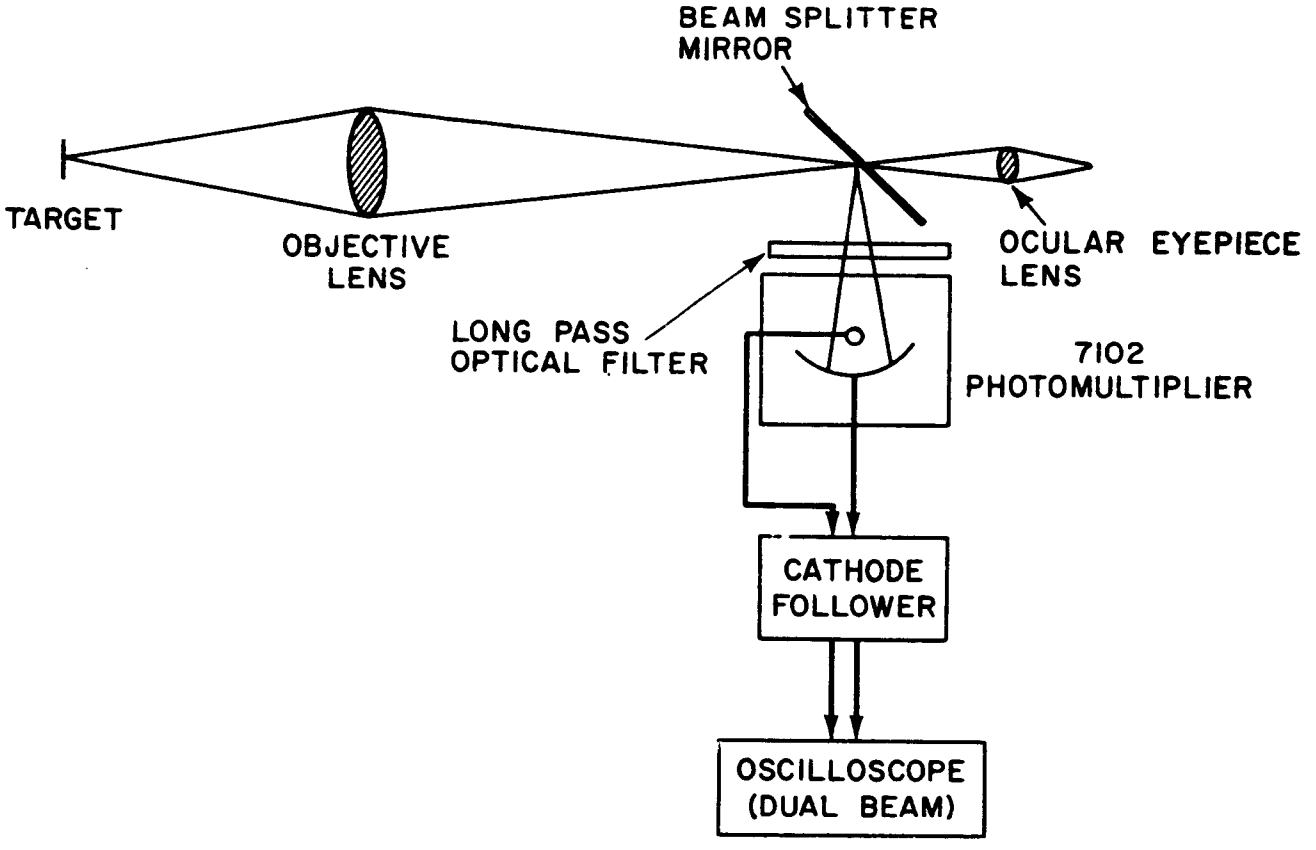

Fig. 6

PHOTOELECTRIC PYROMETER

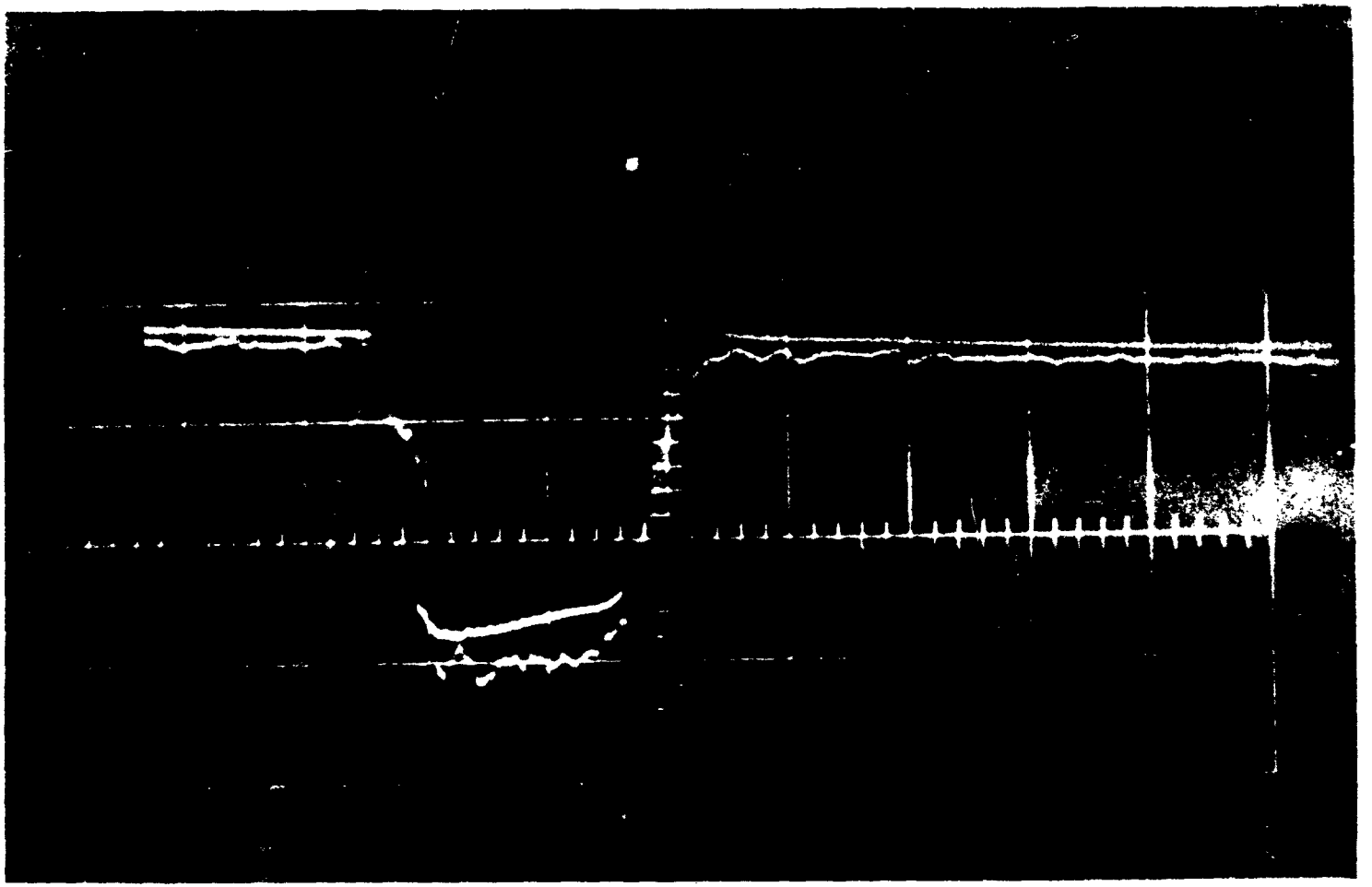

Fig. 7. Photomultiplier output pulse and target current pulse for copper at pulse voltages less than 58 kv. Horizontal time scale 5 us/sec.

ture for the three materials. Theoretical calculations indicate that the temperature rise for copper, under the pulsed conditions used, should be approximately one half that of nickel and chromium. During this investigation it was observed that the bombarded target emitted visible light of greenish color which could not be explained by thermal emission. One concludes that the flat region of the pulse is due to a radiation that is relatively insensitive to the thermal characteristics of the material under bombardment. One possible explanation would be that this light in the visible and the infrared spectrum is part of the bremsstrahlung that one usually observes in the X-ray region of the spectrum, where most of the energy is emitted.

Figure 10 shows the bremsstrahlung intensity as a function of wavelength for 40 kilovolt electrons. Calculations have been made of the bremsstrahlung intensity in the range from 0.5 to 1.0 microns and the results indicate that the radiation in the infrared region is of the same order of magnitude as the black-body radiation for temperatures and voltages in the ranges used during the experiments, and could account for the flat portion of the observed pulse.

Experiments to investigate this radiation were conducted. An additional achromatic objective lens was inserted in line with reflecting mirror mounted on the tube base and the photomultiplier objective lens, increasing the amount of radiation impinging on the photomultiplier. While the copper target was single-pulsed at 0.13 Mw/cm^2 power density, 28 kv pulse voltage, photographs of the photomultiplier pulse were taken with a series of narrow band optical filters interposed. The results show that the radiation is a continuous spectrum within the wavelength limits of the photomultiplier instrumentation (i.e., 0.7 microns - 1.1 microns). Therefore, any attempt to filter out this undesired radiation would also reduce the thermal radiation from the bombarded area.

Since it is shown that the flat portion of the pulse is not related to the thermal radiation, experiments were conducted to investigate the amplitude of the spike above the flat region. The target materials were again copper, nickel and chromium.

As the beam voltage and consequently the beam power density is increased, the ratio of the spike amplitude to flat amplitude also increases as shown in Figs. 11 and 12 for nickel targets. Again, the photomultiplier pulse is shown with the corresponding target current pulse.

In Fig. 11 the pulse voltage was 50 kv corresponding to 0.61 Mw/cm^2 power density and in Fig. 12 the pulse voltage was 58 kv corresponding to 0.87 Mw/cm^2. Horizontal time scale is 5 μsec/cm. While the flat is still discernible on the pulse, its amplitude has been reduced due to the change in scope sensitivity required to view the spike amplitude.

Assuming that the spike is due to the thermal radiation, one converts the spike amplitude to the corresponding temperature. In calculating the measured and predicted temperature, a beam area of 1.41 sq. cm was used based on a beam diameter of 0.53 inches at the target surface.

Figures 2, 3 and 4 showing temperature vs. pulse voltage were

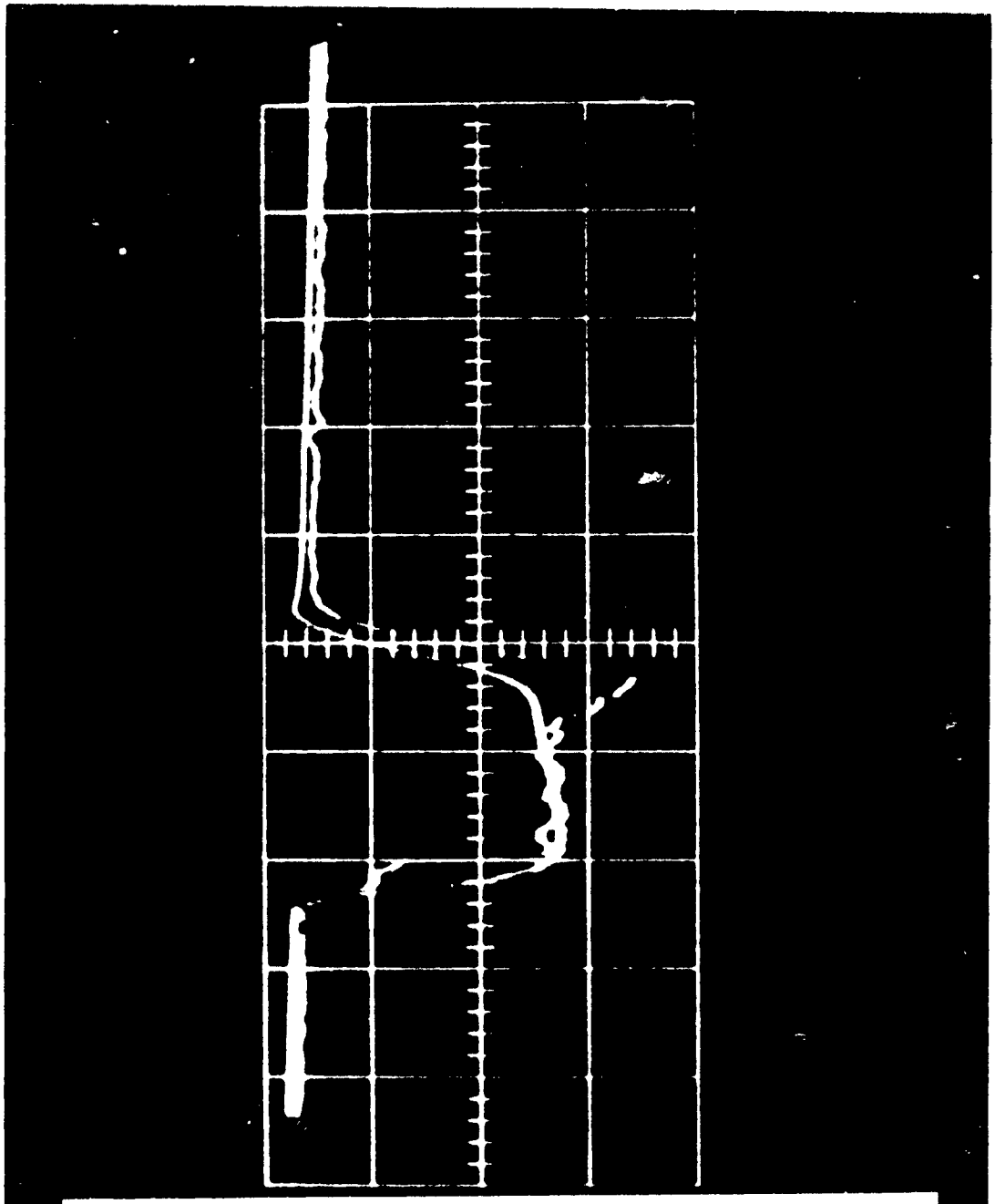

[illegible] multiplier output pulse and target current pulse [illegible] pulse voltages above 58 kV.
[illegible] time scale 5 μs/cm.

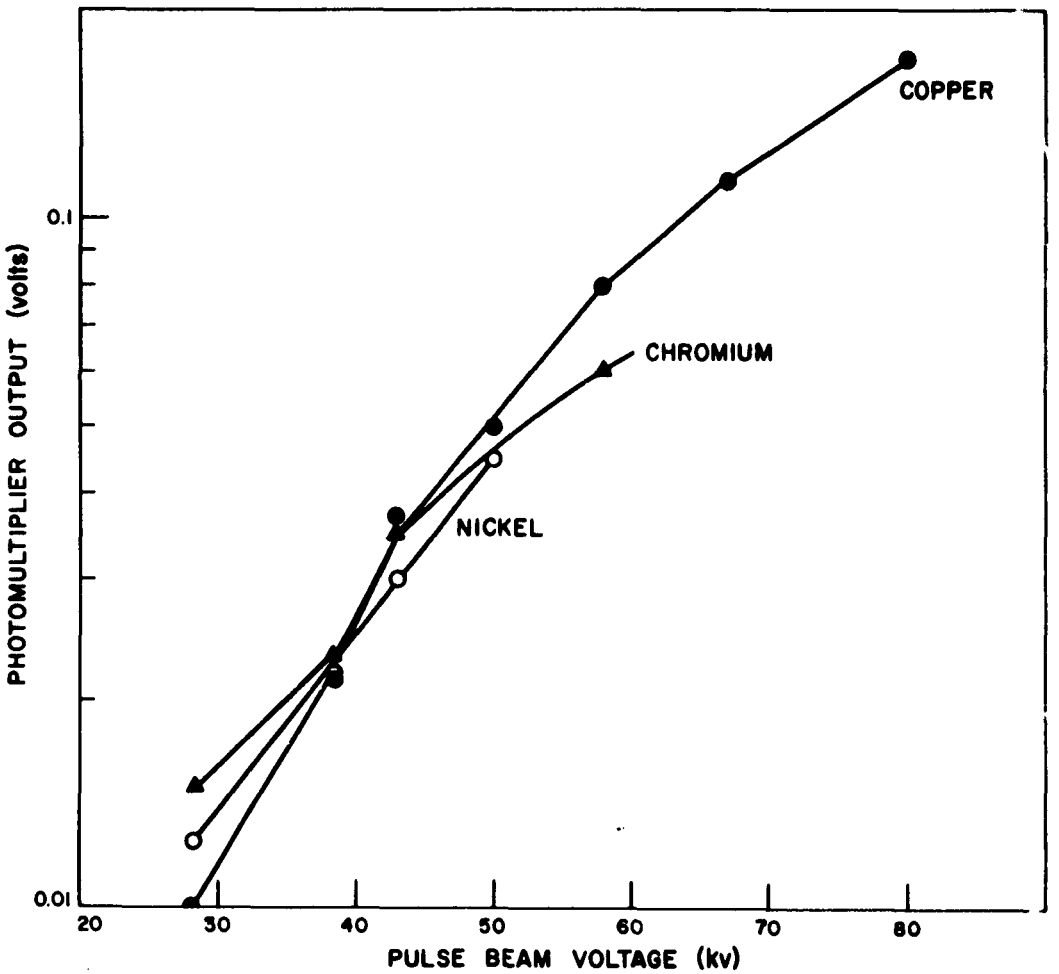

PHOTOMULTIPLIER OUTPUT vs PULSE BEAM VOLTAGE FOR COPPER, CHROMIUM AND NICKEL TARGETS

Fig. 9

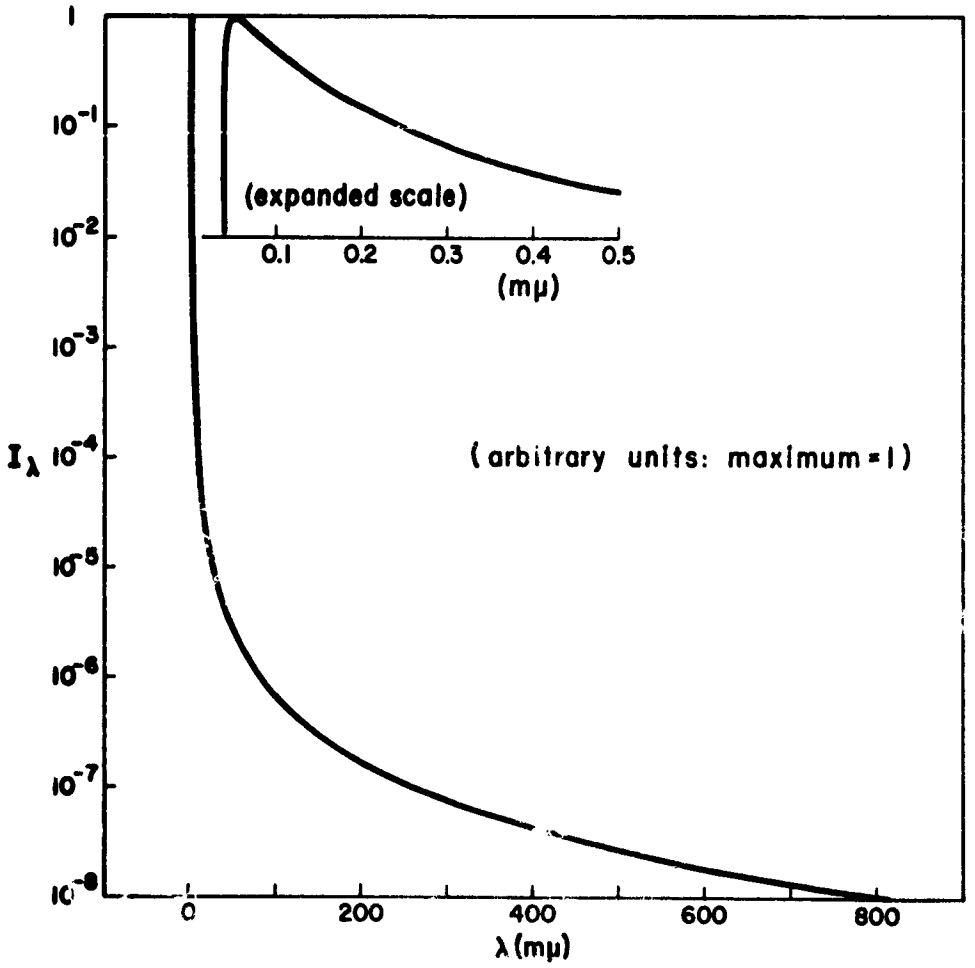

SPECTRAL INTENSITY DISTRIBUTION OF 40 kv X-RAYS

Fig. 10

048-182

calculated assuming constant beam power density. Replotting these curves for the three metals, taking into account that the beam density impinging on the target varies as (voltage)$^{5/2}$ power, one then obtains the predicted temperature for copper as shown in Fig. 13. The pulse duration is 10 μsec. The measured temperatures are shown as open points. The beam power density at 38 kv is 0.28 Mw/cm^2 and at 85 kv - 2.25 Mw/cm^2. The experimental data agree within 30 per cent of the predicted temperatures.

Here we observe that at voltages above 75 kv the measured temperature does exceed the melting point of copper. One possible explanation would be that the surface doesn't melt during this short pulse duration but is superheated.

The predicted and measured temperatures for nickel are shown in Fig. 14. Here we observe a close agreement between the measured and predicted data.

The predicted and measured surface temperature for chromium are shown in Fig. 15. Again the measured data are represented by the open points.

As stated previously the beam area used in our calculations was based on a beam diameter of 0.53 inches. The experimental arrangement for measuring this diameter is shown in Fig. 16.

Since the bremsstrahlung intensity is directly proportional to the peak current density at any point on the beam, one may obtain a beam profile by scanning a blue sensitive photomultiplier tube across the bombarded spot. An achromatic lens (focal length 10 inch) and a second mirror were inserted as shown in the diagram. The lens was placed at a distance from the target to produce a 1:1 image/object size ratio. The image was focused on a 0.025" pinhole aperture mounted directly on the photomultiplier whose spectral response peaked at 0.44 microns. A curve showing the photomultiplier output as a function of radial distance is plotted in Fig. 17. One observes that the beam current density is relatively uniform over the beam diameter.

It should be pointed out that while the photomultiplier output pulse does indicate the instantaneous heating for a single pulse duration, it is averaged over the beam diameter. Experiments are in progress at [illegible] laboratory to measure the instantaneous temperature for a single pulse as a function of the radial distance across the beam.

Cumulative effects of many repetitive pulses on the surface damage have also been investigated. A photograph of a copper target bombarded at a 300 pulse per second rate, 28 kilowatt pulse voltage, 0.13 Mw/cm^2 beam power density, 10 μsec pulse duration and for a total of 10,000 pulses is shown in Fig. 18. Physical damage to the target is quite evident after only 33 seconds of pulse bombardment corresponding to 10^{-1} sec. of actual beam on time.

The component parts of the impulse heating tube are shown in Fig. 19, namely, the cathode, water cooled anode, sight glass assembly,

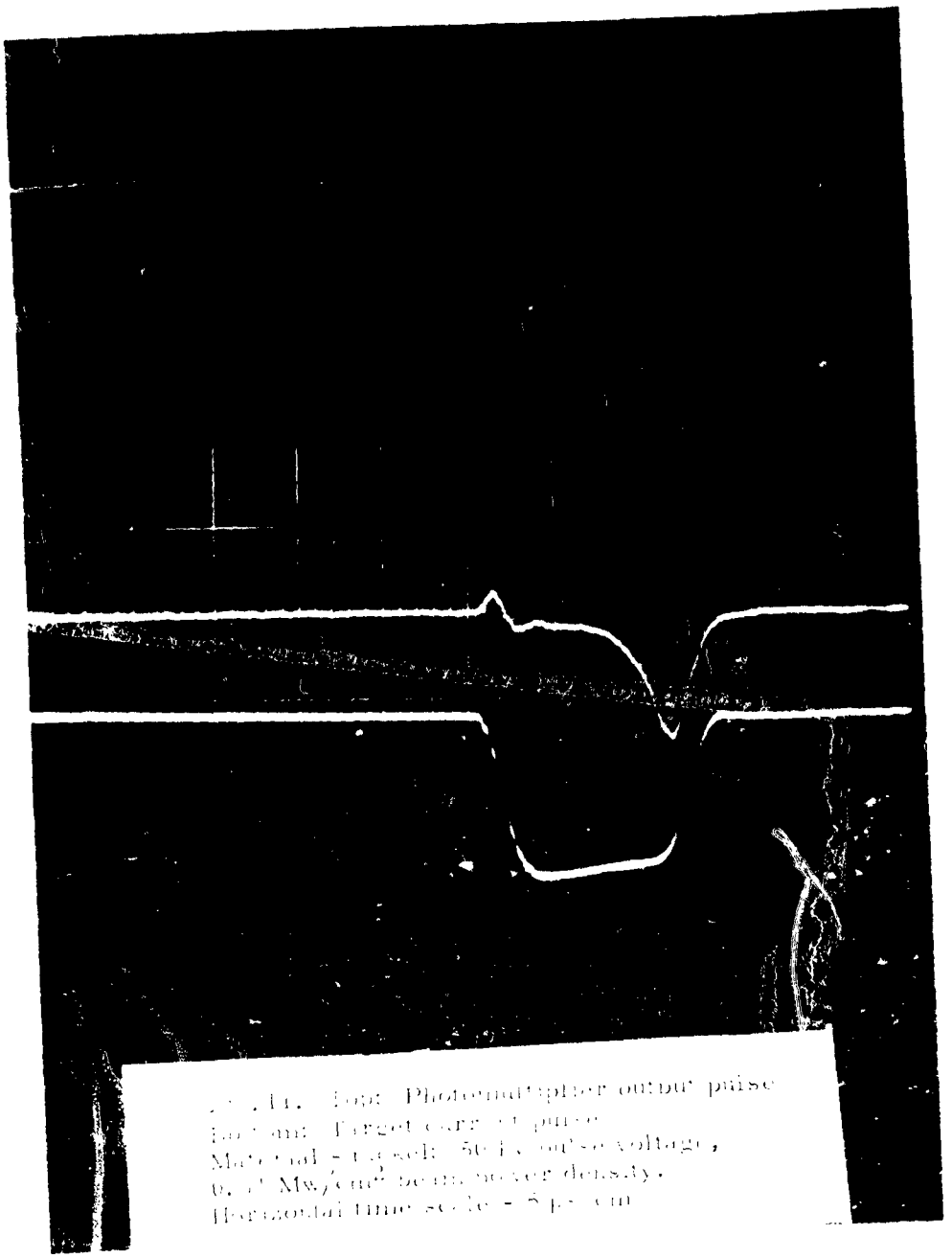

Fig. 11. Top: Photomultiplier output pulse
Bottom: Target current pulse
Material - Lucite; Top: pulse voltage,
0.1 Mw/cm² beam power density.
Horizontal time scale - 5 μs/cm

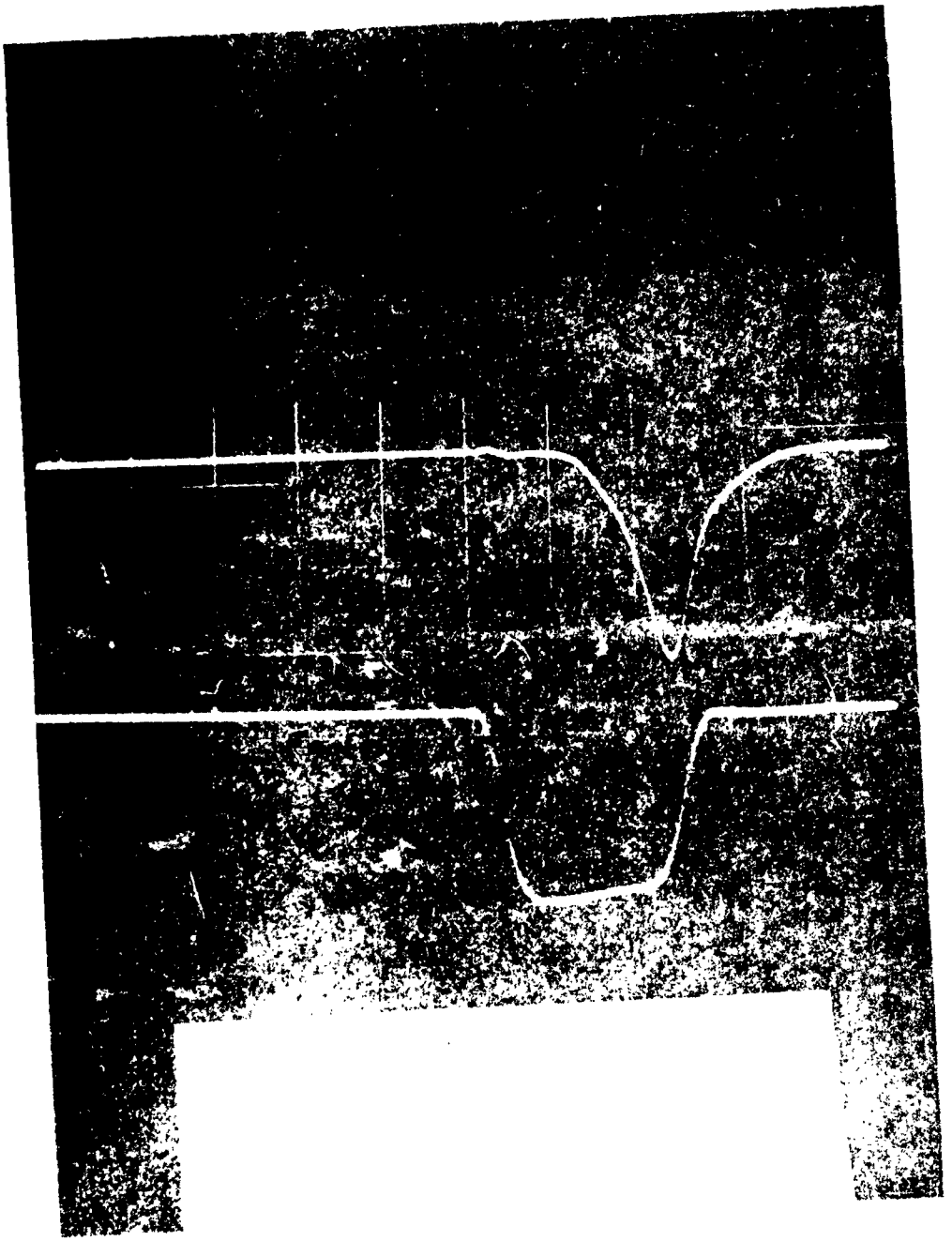

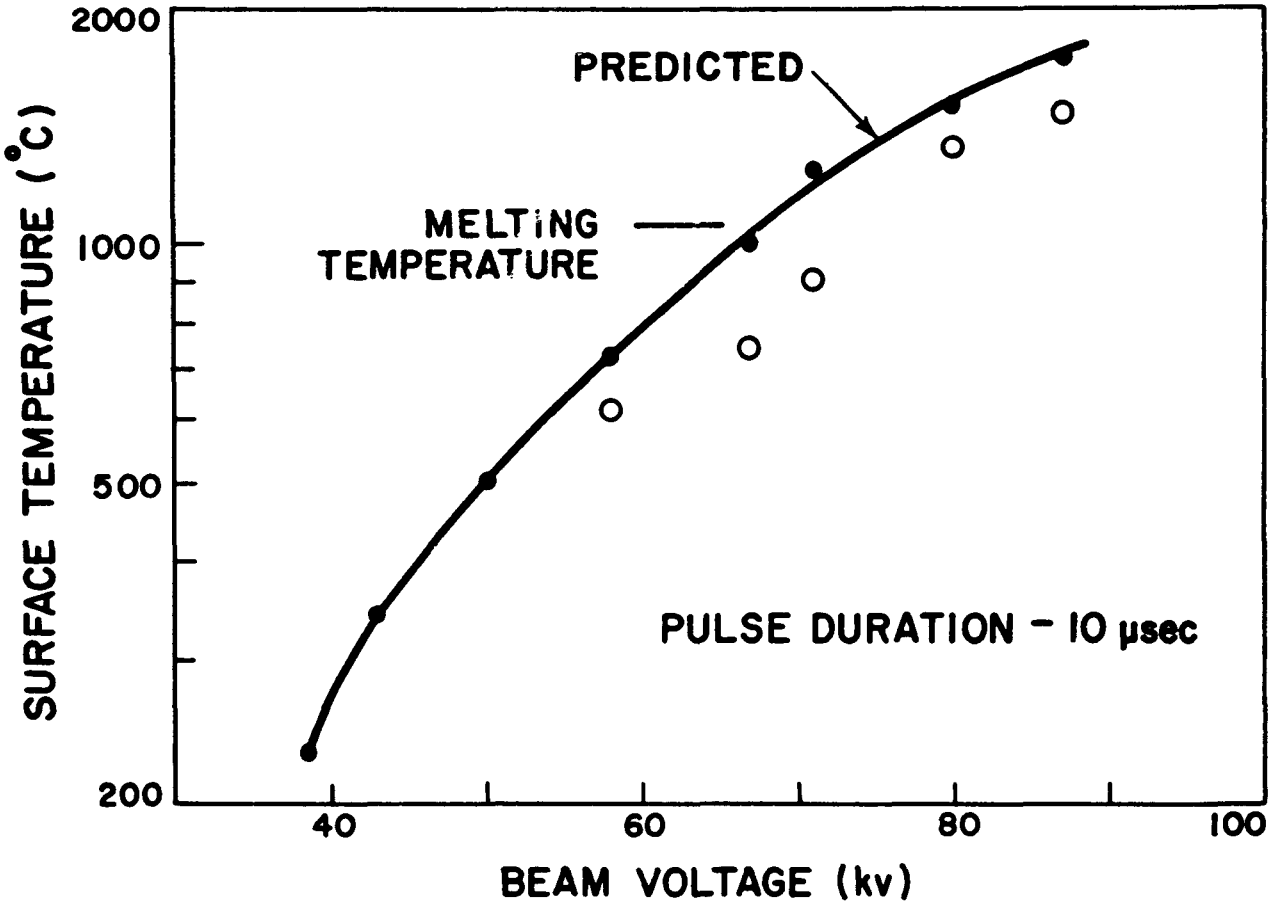

PREDICTED AND MEASURED TEMPERATURE RISE
vs BEAM VOLTAGE FOR COPPER

Fig. 13

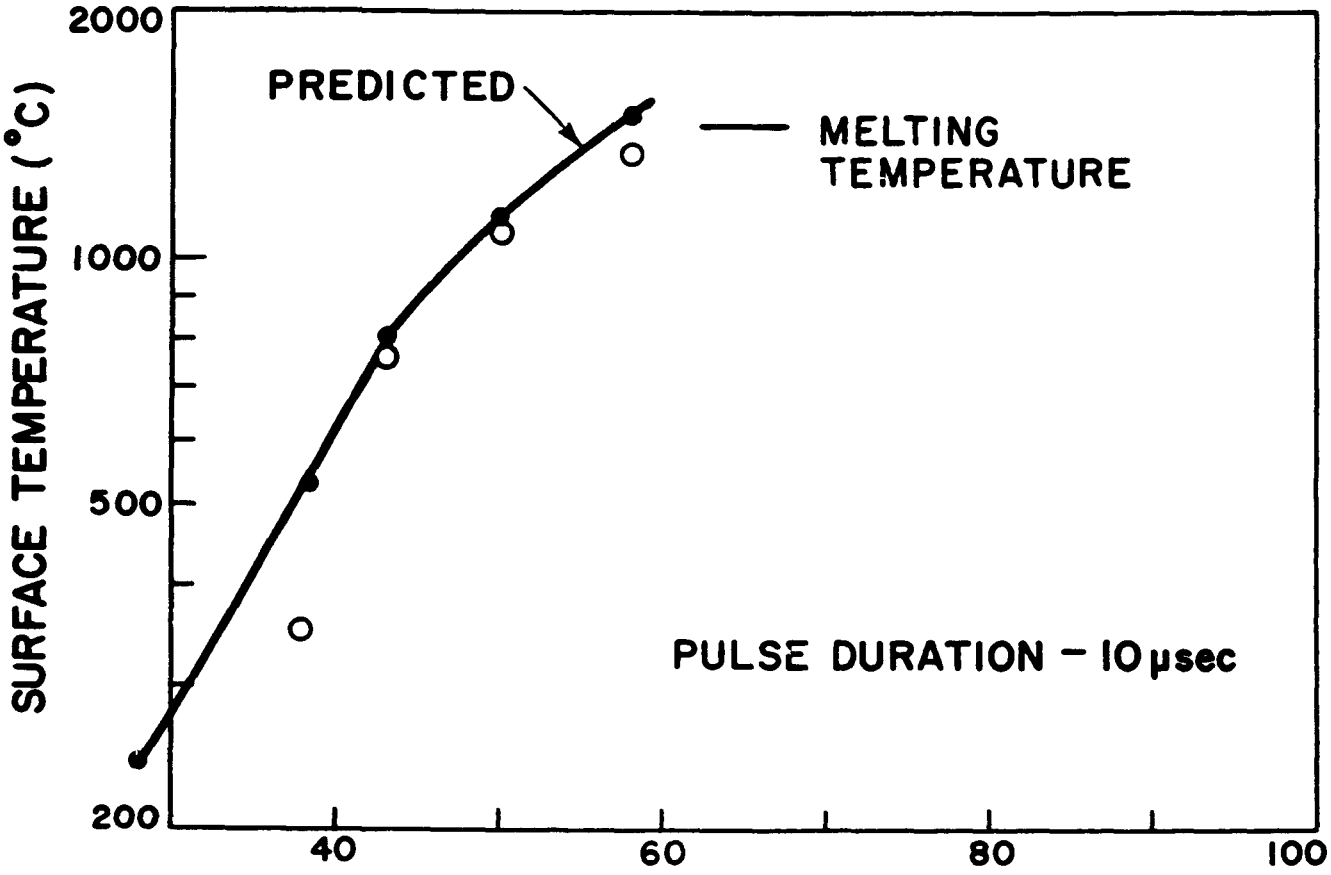

Fig. 14 PREDICTED AND MEASURED TEMPERATURE RISE vs BEAM VOLTAGE FOR NICKEL

der :ountable flanges, water cooled collector and target assembly.

Figure 20 shows the test setup used during these experiments. Shown in the photograph are pulse modulator, DC power supply, pulse transformer, photoelectric pyrometer placed in position over the lead shield, focusing magnet and auxiliary viewing equipment.

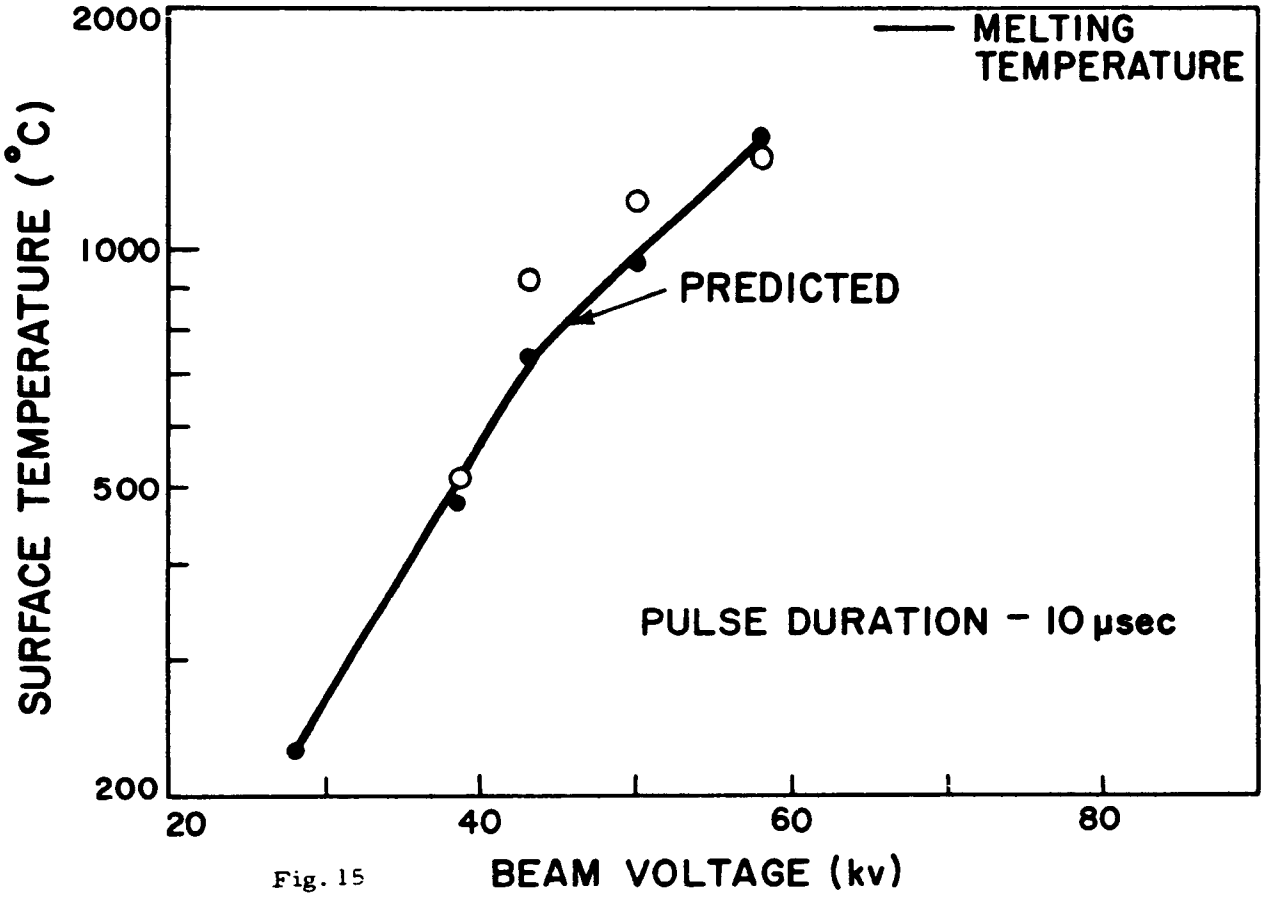

Fig. 15 PREDICTED AND MEASURED TEMPERATURE RISE vs BEAM VOLTAGE FOR CHROMIUM

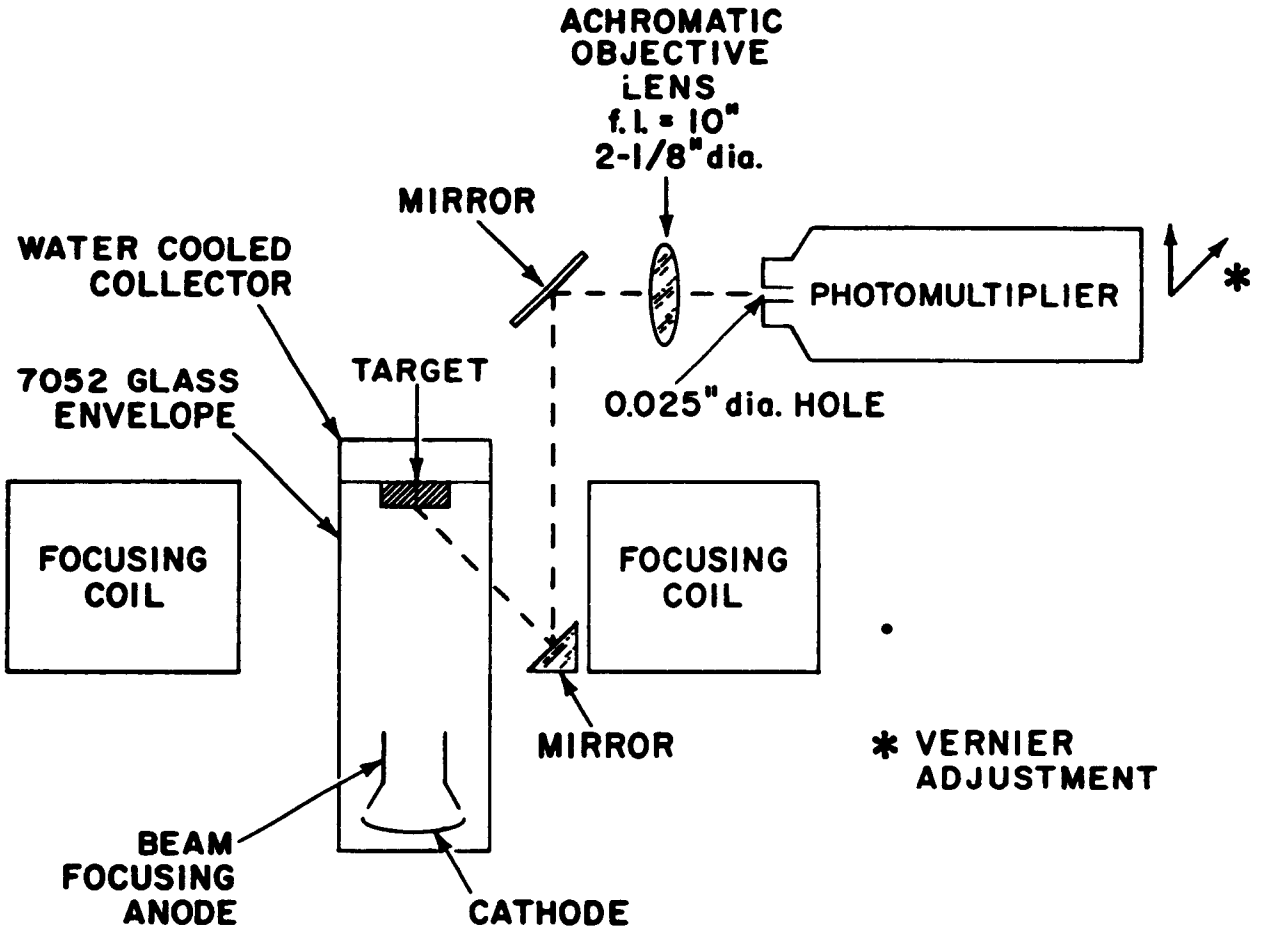

Fig. 16 EXPERIMENTAL SETUP FOR MEASURING BEAM PROFILE

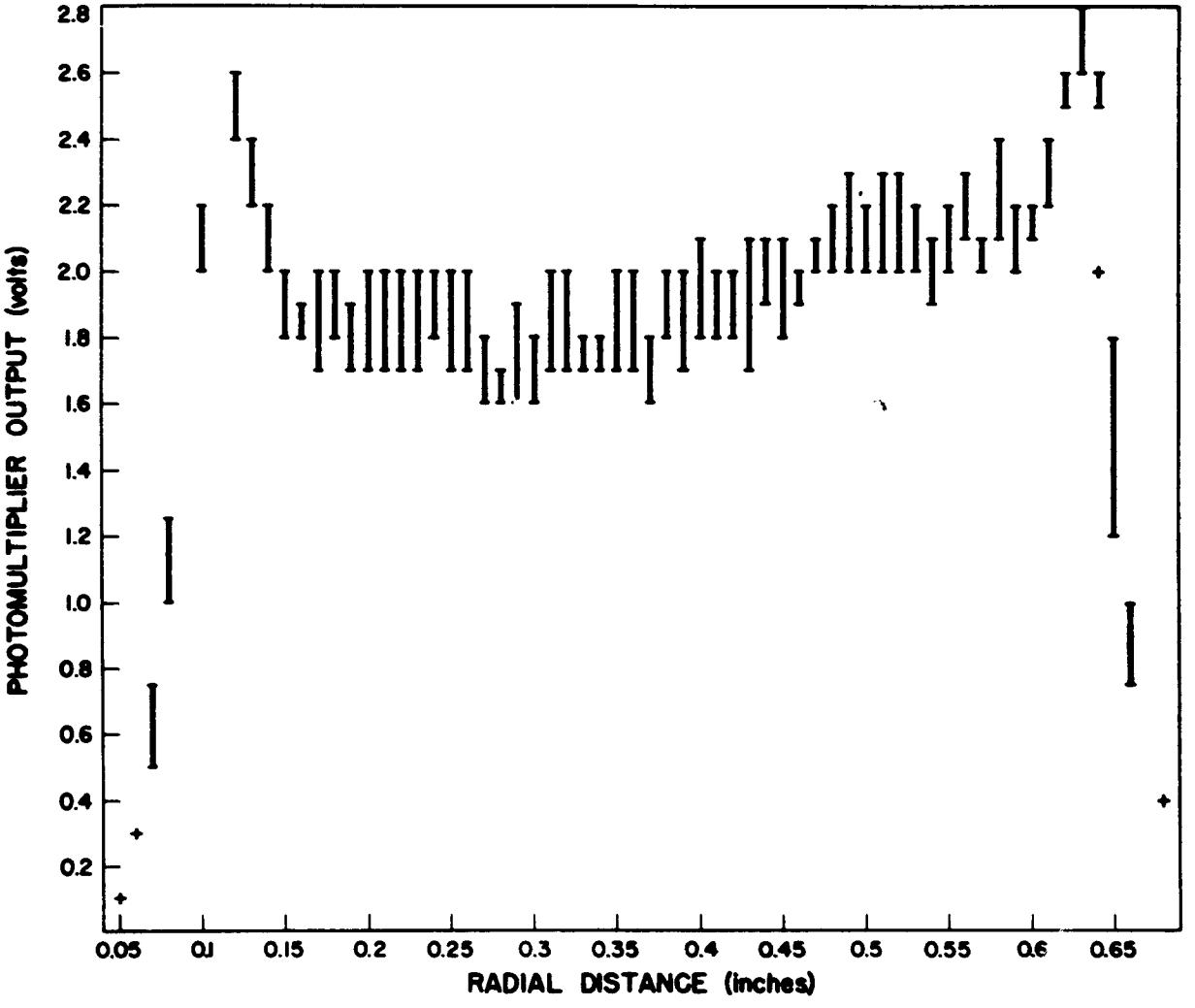

Fig.17 BEAM PROFILE TAKEN AT 52 kv PULSE VOLTAGE

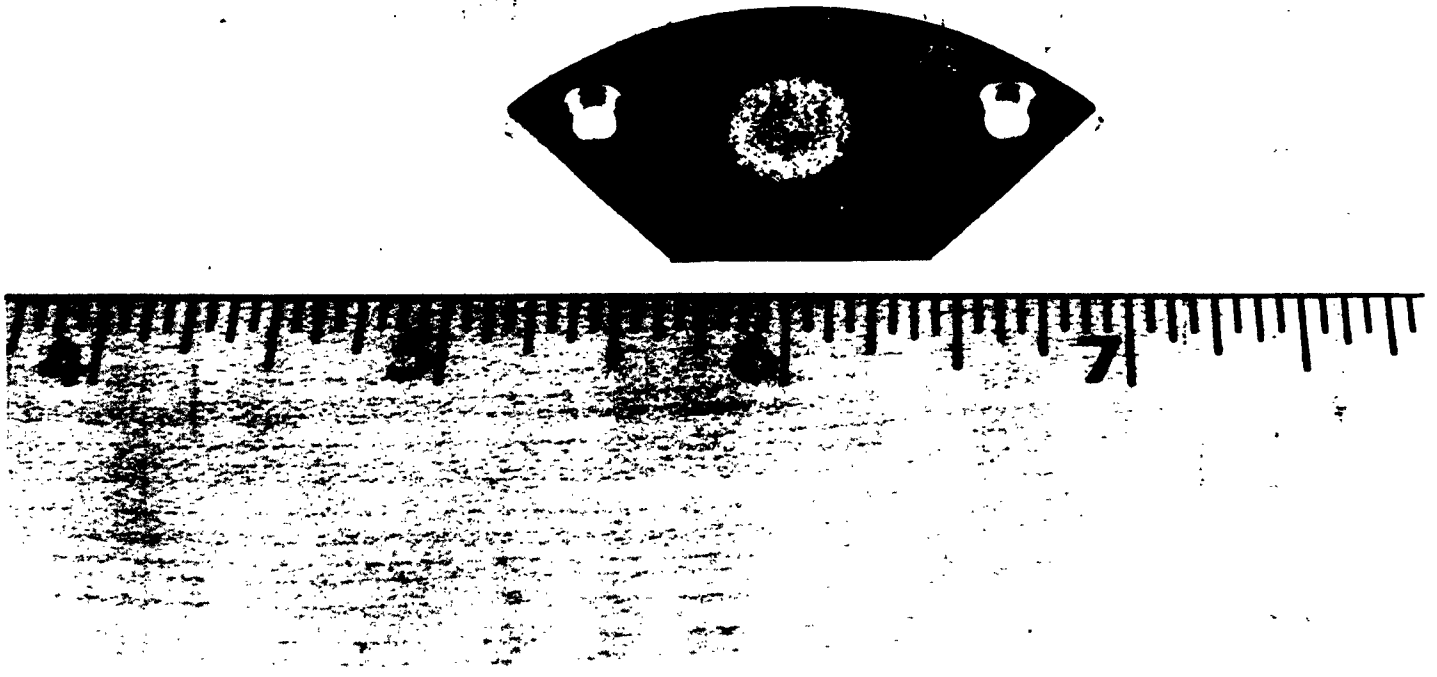

Fig. 18. Photograph of copper target bombarded 10,000 pulses at 300 pps rate, 28 kilovolts pulse voltage, 0.13 Mw/cm^2 beam power density, 10 μsec pulse duration.

Fig. 19. Component parts of impulse heating tube.

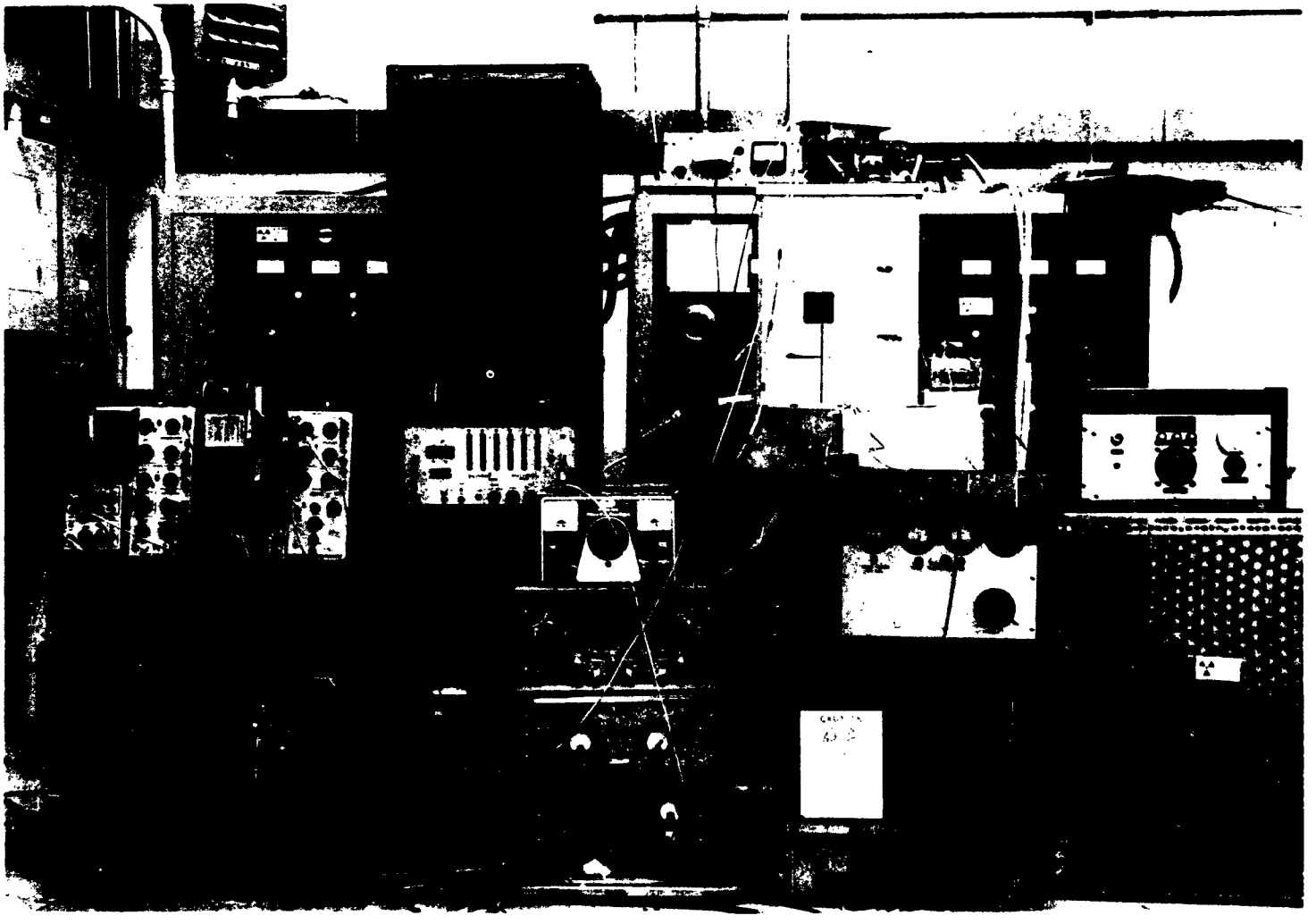

Fig. 20. Photograph of experimental test set up.

DESIGN FOR A BROADBAND, S-BAND VERY HIGH POWER CROSSED-FIELD AMPLIFIER

By

P. N. Hess and G. P. Kooyers

Litton Industries
Electron Tube Division

Previous work on injected-beam crossed-field amplifiers has resulted in tubes having broad bandwidth, high power output, good efficiency and moderate gain. Until recently, most of the work on this type of device was done on tubes of circular geometry. Such geometry limits the gain of the amplifiers because of the many possible modes of rf feedback from output to input. Recent work on the linear form of such amplifiers has greatly reduced the feedback problem and, when coupled with severed circuit techniques, has put the injected-beam crossed-field amplifier in the same high gain class as the conventional O-type traveling-wave tube and the multiple-cavity klystron.

A typical two-section, linear, injected-beam amplifier is shown diagrammatically in Fig. 1. Note the individual sections of slow-wave structure separated by a severed drift region and the depressed collector at the output end. With single sever tubes such as this, stable saturated gain of 25 db is easy to achieve. A representative tube is shown in Fig. 2. It is a 1 KW CW, X-band amplifier having 25 db gain and 30% bandwidth. The electronic interaction of tubes of this type is well understood and the operational characteristics, both small-signal and saturated, very accurately predicted by a large-signal analysis which has been developed[1]*. This design tool is commonly used to design such tubes for any desired frequency and power level within the capability of the device. The most recent work on this linear tube has resulted in the achievement of section-to-section isolation of more than 40 db over 50% bandwidths. Therefore, multi-section tubes can be built with saturated gains as high as desired

*Numbers refer to references listed at the end of this paper.

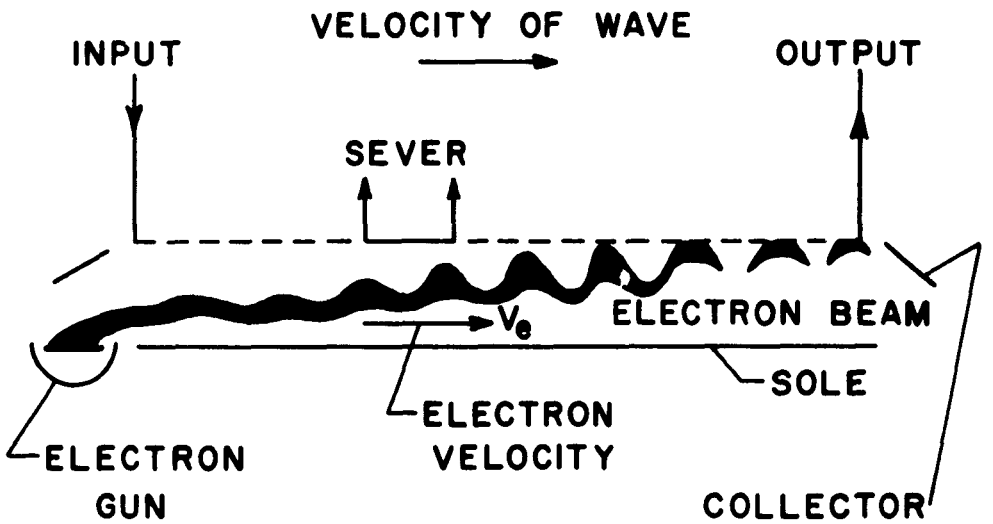

DIAGRAMMATIC SKETCH OF
INJECTED-BEAM CROSSED-FIELD AMPLIFIER
(BIMATRON)

Fig. 1

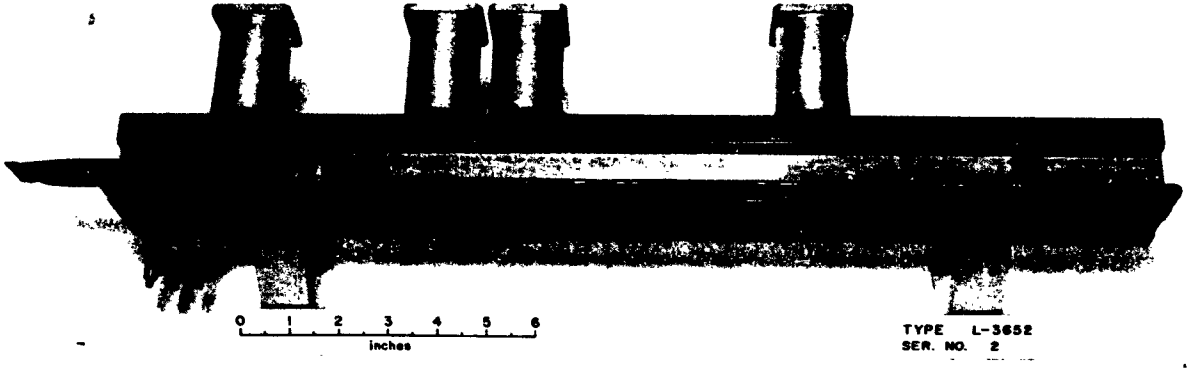

HIGH GAIN, X-BAND, 1 KW, CROSSED-FIELD AMPLIFIER

Fig. 2

without the problem of oscillation instability in the absence of rf drive. The only remaining limit in the gain of this tube now is the noise figure of the crossed-field guns. Tests which we have made indicate that saturated gain of 40 db should be possible with noise levels similiar to that of other high gain broadband amplifiers.

Crossed-field amplifiers of the injected-beam type may be operated either pulse or CW. The perveance one can use in this device is about the same as that commonly used in klystrons or traveling-wave tubes, and in order to achieve high peak power in this device one must use the same relatively high voltage which one must use for high pulse power linear beam tubes.

Concurrent with the progress in injected-beam crossed-field amplifiers, there has been similiar progress in distributed-emission amplifiers. To achieve high peak power, it is desirable to use this type of interaction where the beam perveances are typically one to two orders of magnitude greater than injected-beam crossed-field amplifiers or linear beam devices.

As in the case of injected-beam tubes, most of the earlier work has been done with tubes of circular design where rf feedback limits the gain and bandwidths to moderate values. The advantages of the linear format apply to this type of crossed-field amplifier as well as to the injected-beam type. A typical example is shown diagrammatically in Fig. 3. Distributed-emission crossed-field amplifiers have achieved pulse power output of hundreds of kilowatts at X-band with 10-12 db gain and 20% bandwidths.

In addition to their high peak power capability, distributed-emission tubes have the further advantage of cold-cathode operation if some means of starting the secondary-emission process is included. The advantage of this Class B type operation, especially in a linear, non-reentrant device which does not oscillate in the absence of drive, lies in the simplicity of the dc power supplies; no pulse modulator is needed.

The most recent advancement in the magnetron amplifier field has been the idea of combining these two devices in the same vacuum envelope. The result will be a very high power amplifier capable of high gain, broad bandwidth, high efficiency and Class B operation. In addition, the injected-beam acts as the secondary-emission trigger for the high power distributed-emission section and greatly reduces starting jitter compared to ordinary distributed-emission devices. A diagrammatic sketch is shown in Fig. 4. Note the section of injected-beam amplification giving high gain, the sever and build-up section and the final section of distributed-emission amplification. Note, also, that all electrodes operate from

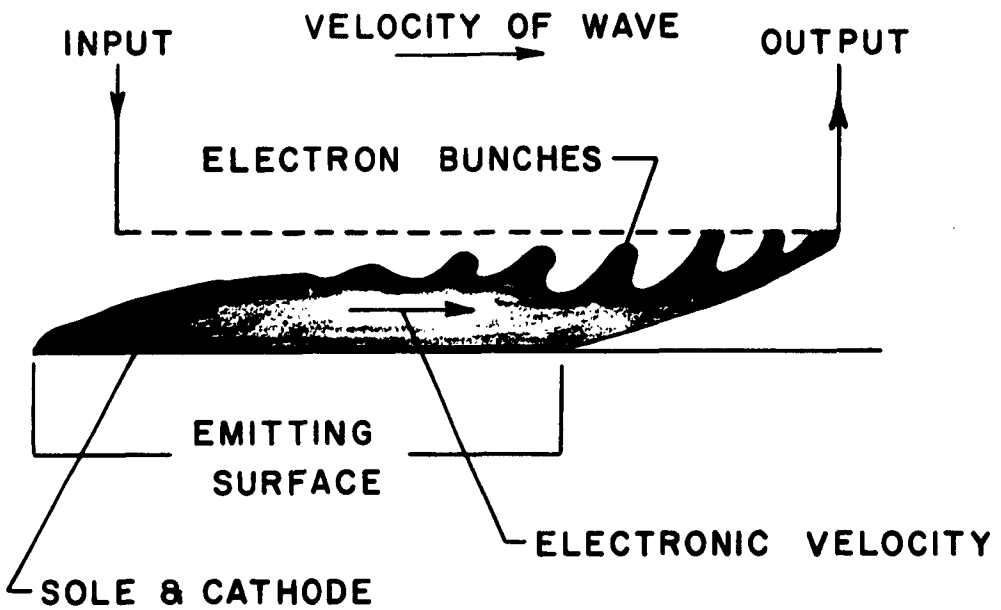

DIAGRAMMATIC SKETCH OF THE
FORWARD-WAVE DISTRIBUTED EMISSION
CROSSED-FIELD AMPLIFIER
(DEMATRON)

Fig. 3

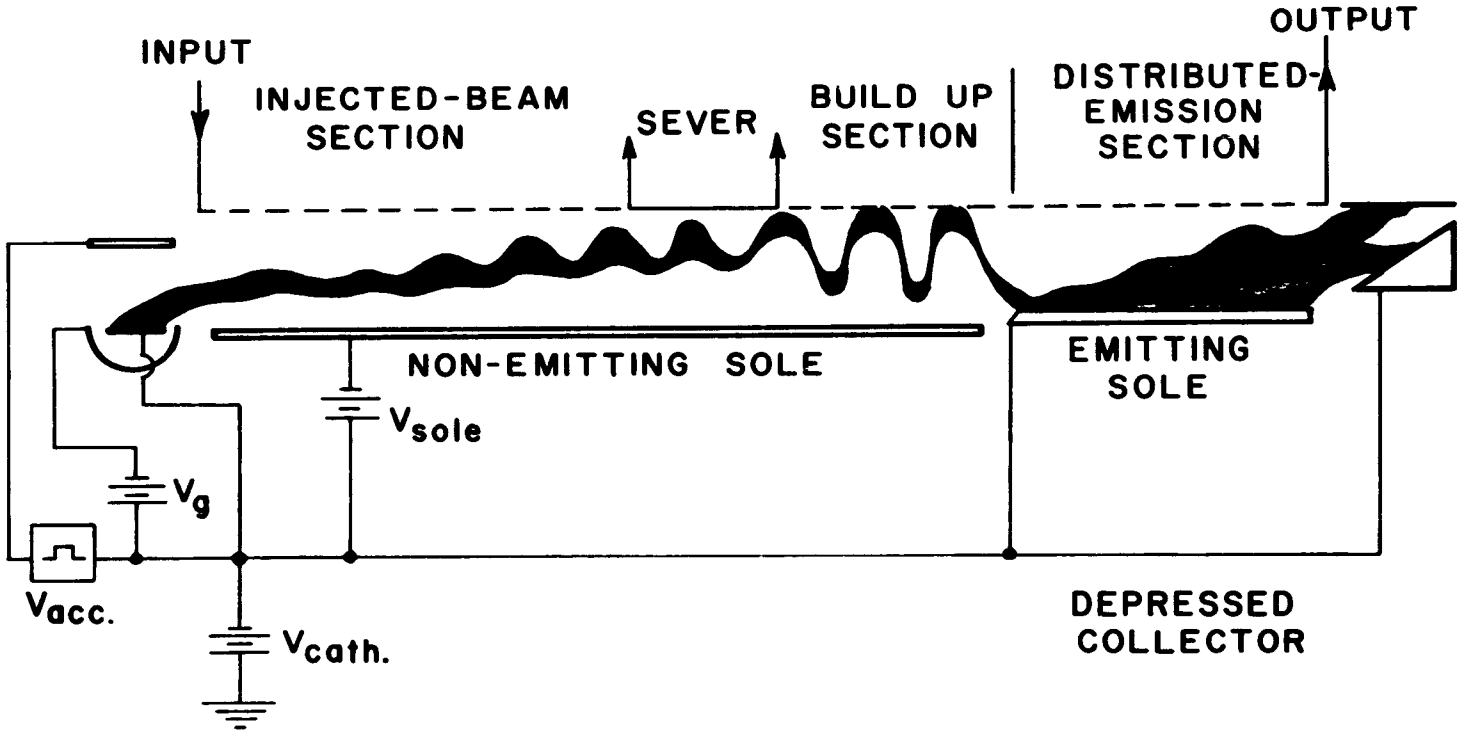

DIAGRAMMATIC SKETCH OF THE COMBINATION CROSSED-FIELD AMPLIFIER (BIDEMATRON)

Fig. 4

a dc power supply except the accelerator of the injected-beam gun. Thus, only a non power-consuming pulser is needed for complete pulse operation of the tube.

The remainder of this paper will describe the electrical and mechanical design features of a combination injected-beam, distributed-emission amplifier recently started and having the following specifications as a goal:

Peak power	10 megawatts
Average power	200 kilowatts
Pulse length	200 μ seconds.
Center frequency	2800 mc/s
Bandwidth	25%
Gain	35 db
Efficiency	70%

Electrical Design

The injected-beam portion of the amplifier has been designed according to the large-signal computer analysis previously mentioned. The only difference between the design procedure for the injected-beam portion of a combination tube and a conventional injected-beam tube is the requirement that the design be compatible with the distributed-emission section of the combination. In the present case, this means only that both cathodes operate at the same potential. In general, it could mean equal beam velocities, equal structure impedance or perhaps equal electronic efficiencies.

In the present design it was desired to limit the length of the injected-beam section to that length which would cause the beginning of saturation at the desired input power level. In this way, maximum rf energy is carried across the sever on the beam and is available to drive the distributed-emission section. The peak power output from the first section is plotted vs. length of interaction in Fig. 5. Note that the build-up section beyond the sever re-establishes the circuit wave at a high power level before distributed-emission interaction takes place. Within this build-up section a portion of the injected-beam is collected on the slow-wave structure. Other electrons find themselves in an unfavorable phase position and move towards the sole electrode. It is these uncollected electrons which initiate the secondary-emission from the distributed-emission cathode. In this specific design, the power level at the beginning of the distributed-emission section is 500 KW representing a power gain to this point of 23 db.

It is not necessary that the slow-wave structure pitch be the same on both sides of the sever. Indeed, in the specific design to be presented, the two structures are of

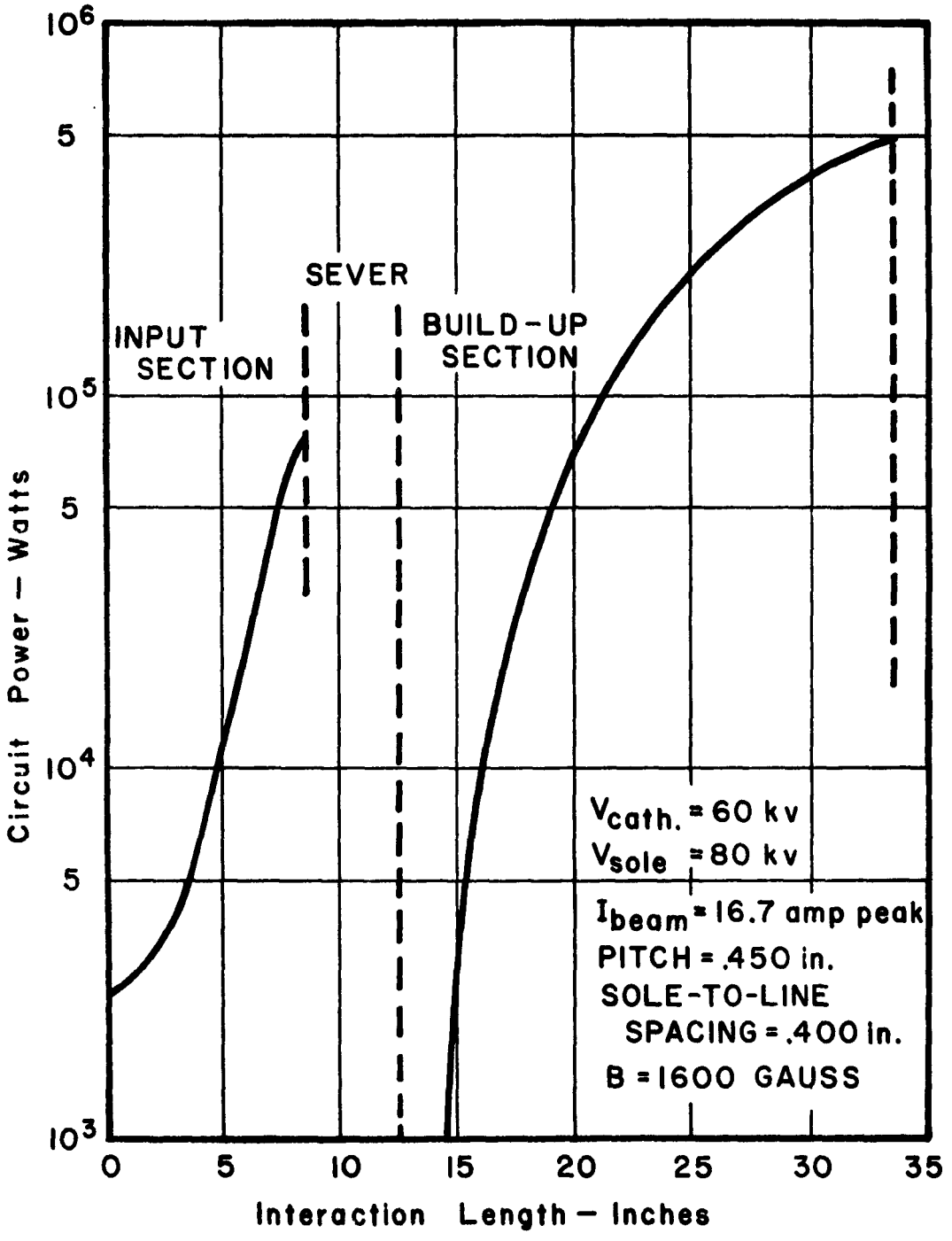

Fig. 5 COMPUTED CIRCUIT POWER vs LENGTH INJECTED-BEAM SECTION

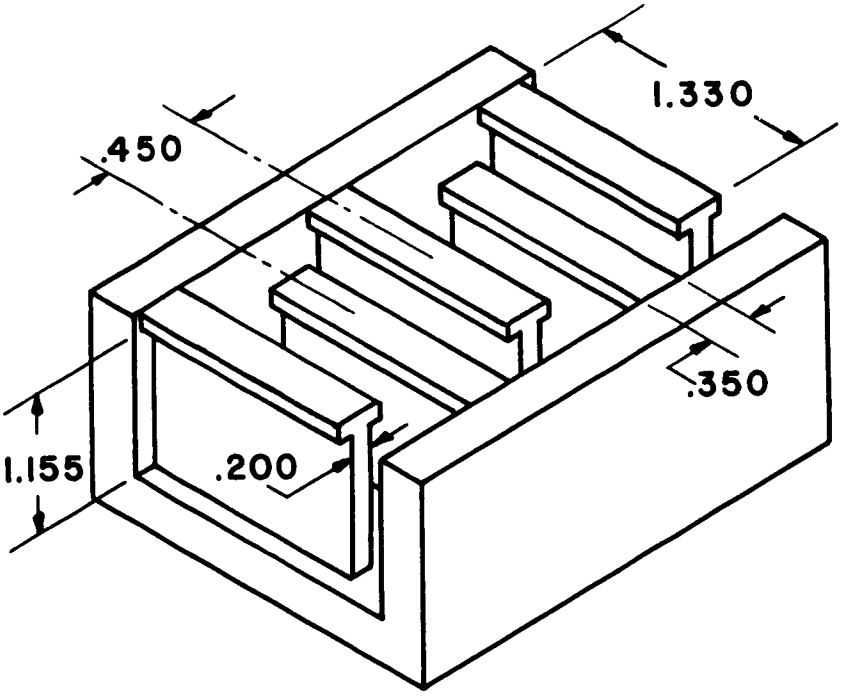

NOSED SPLIT-FOLDED
WAVEGUIDE STRUCTURE

Fig. 6

different types and have different impedances. The velocity of the beam may be adiabatically changed across the sever region to match any structure wave velocity by gradual tapering of either the electric field or the magnetic field.

For the present design, the input injected-beam section of the amplifier uses the slow-wave structure shown in Fig. 6. It is a fundamental backward-wave structure with excellent thermal dissipation properties, good bandwidth and relatively high space-harmonic interaction impedance. The dimensions of the structure for this S-band high power application are as shown in the figure. We call this structure the split-folded waveguide.

The slow-wave structure used in the build-up and distributed-emission sections is shown in Fig. 7. It is similiar to the previous structure except that the vane tips are continued across the structure to the opposite side. It also is a fundamental backward-wave structure. For the same frequency range, this structure is approximately one and one-half times larger than the split-folded waveguide and has a second space-harmonic interaction impedance about two-thirds as large. Its advantage lies in its large size and thermal dissipation ability. If necessary, liquid cooling can be provided at the vane tips. This structure has been named the slot-coupled vaned structure. Its dimensions for the present application are shown in the figure.

The distributed-emission section of the tube is designed to provide an additional 13 db gain, raising the peak power level from 500 KW to 10 MW and the average power level from 10 KW to 200 KW. In order to handle the structure dissipation at this power level, it is necessary to spread the electron collection over a large area. One must limit the average dissipation/unit area to a relatively low value so that the impulse heating associated with the relatively long pulse lengths (200 μ seconds) does not become excessive. In the present design, this is accomplished by a tapered interaction impedance. The interaction is allowed to proceed from the beginning of the distributed-emission section to an intermediate level at constant impedance and exponential power growth. When the exponential power growth has reached the value corresponding to the allowable dissipation per unit area, the interaction impedance is lowered so as to maintain this level of power operation at a constant value. This impedance taper is continued to the output end of the distributed-emission section. Hence, over an extended length of interaction, the power growth is linear and the structure dissipation is constant.

This design approach is illustrated in Fig. 8. Note that constant-impedance interaction takes place to a circuit power level of 3.5 MW. At this point the average dissipation/unit area is 235 watts/cm^2. Linear power growth is then employed

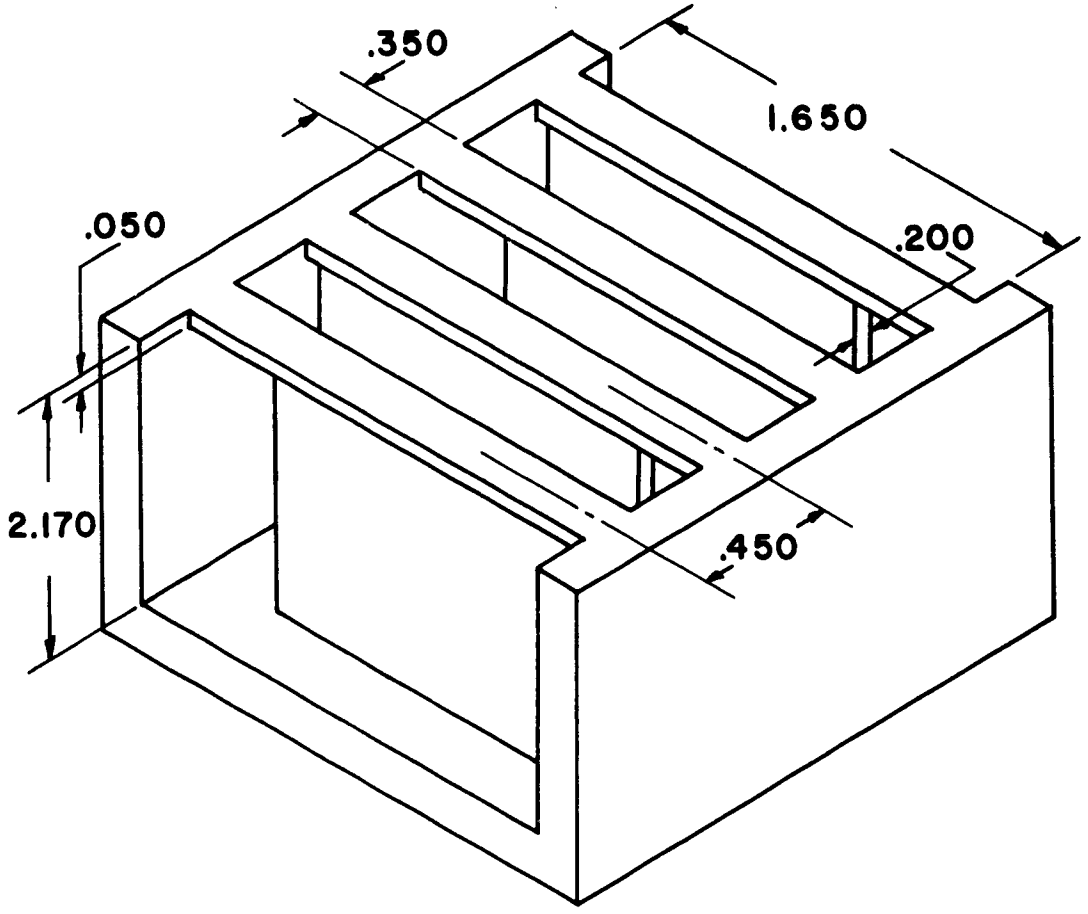

SLOT-COUPLED VANE STRUCTURE

Fig. 7

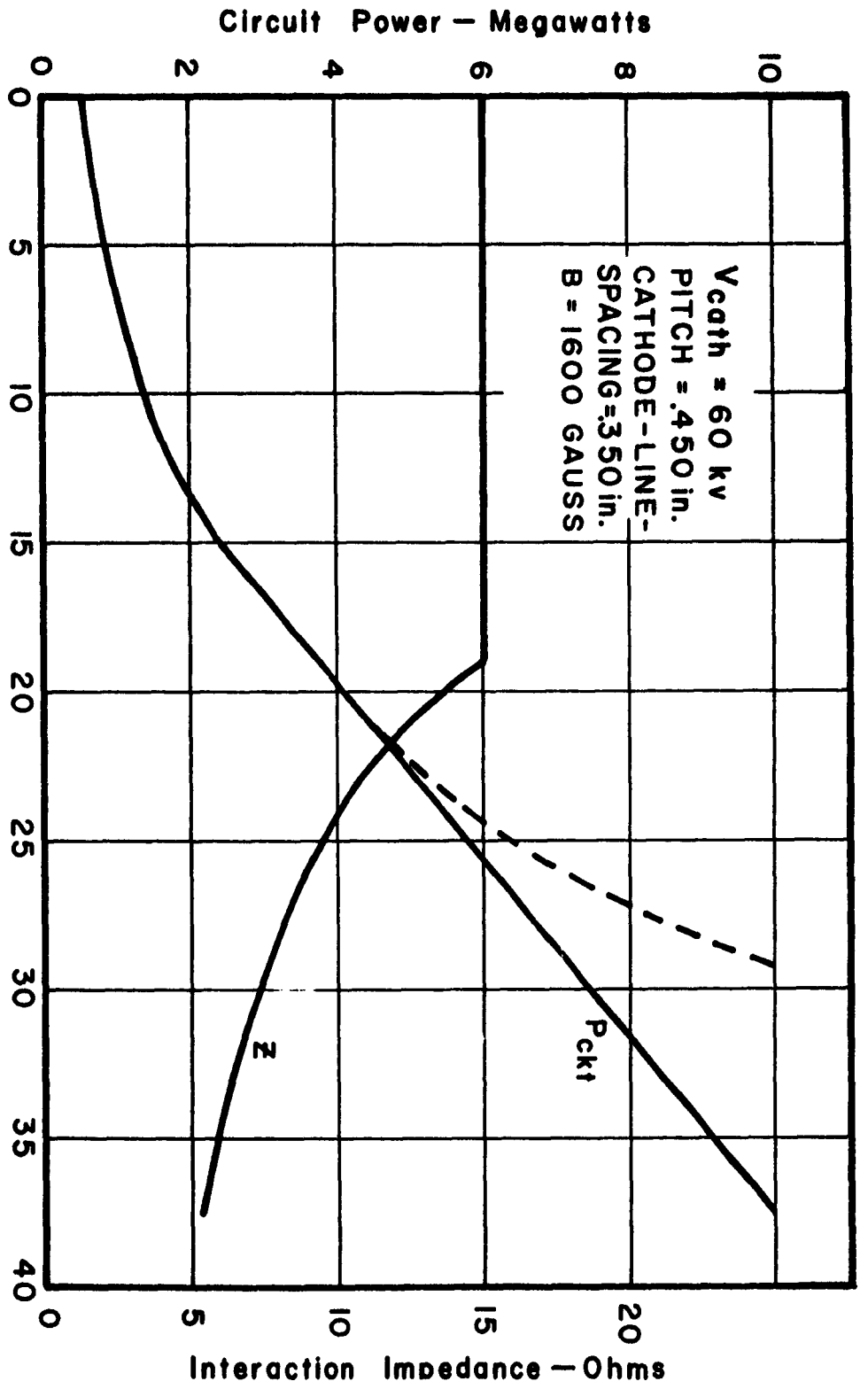

Fig. 8 CIRCUIT POWER AND IMPEDANCE vs LENGTH

at this dissipation level to the desired 10 megawatts at the output. The mid-band impedance of the structure is 15 ohms at the beginning of the taper. It varies inversely proportional to the distance to a value of 5.2 ohms at the output.

The impedance of this structure may be varied with no degradation of either synchronous velocity or dc focusing by changing the geometry of the slots between cavities. Since the impedance is lowered progressively towards the output, the synchronous bandwidth will increase beyond the desired 25%.

Two general methods have been used to arrive at the electrical design of the distributed-emission section shown in Fig. 8. The first is a large-signal computer analysis similiar to that already described for the injected-beam interaction. It has been recently presented by G. P. Kooyers of our Laboratory[2]. Experimental verification of all phases of this analysis has not yet been completed. For this reason, an "equivalent" magnetron analysis previously developed[3] was also used to check the design. This approach is based upon subdividing the crossed-field amplifier interaction space into a number of incremental lengths which are then replaced with equivalent magnetrons. Under conditions of identical dc electric and magnetic fields, identical rf fields and identical dimensional parameters, the electronic interaction process is the same in any distributed-emission tube whether it is an amplifier or an oscillator as long as the gain through the incremental length is small. In addition, under these conditions, the same real and reactive power per unit area will be delivered to the rf wave in the amplifier or the oscillator. This approach is valid for the large-signal regions of interaction. Obviously, in the present design, it is valid for all regions except the initial bunching region where the injected-beam triggers the distributed-emission cathode.

It is again noted that the foregoing design employs a linear format. Such a geometry allows severed-circuit techniques and secondary-emission triggering by the injected-beam of the first section; however, it precludes the possibility of reentrant beam operation. It has already been noted that non-reentrant beam, crossed-field amplifiers allow higher stable gain and wider bandwidths than their reentrant beam equivalents; however, their efficiency will be less unless the energy in the spent beam is recovered. Fortunately, this can be accomplished by a relatively simple depressed-collector. Such a device is simple because all electrons enter it at the same axial velocity and because, in crossed-field focused beams, no electrons can be turned around and returned to the interaction space.

Previous work on depressed collectors for injected-beam amplifiers has resulted in improvements in efficiency by factors of 1.3 to 1.5. These collectors were designed on the basis of a known electron potential distribution at the

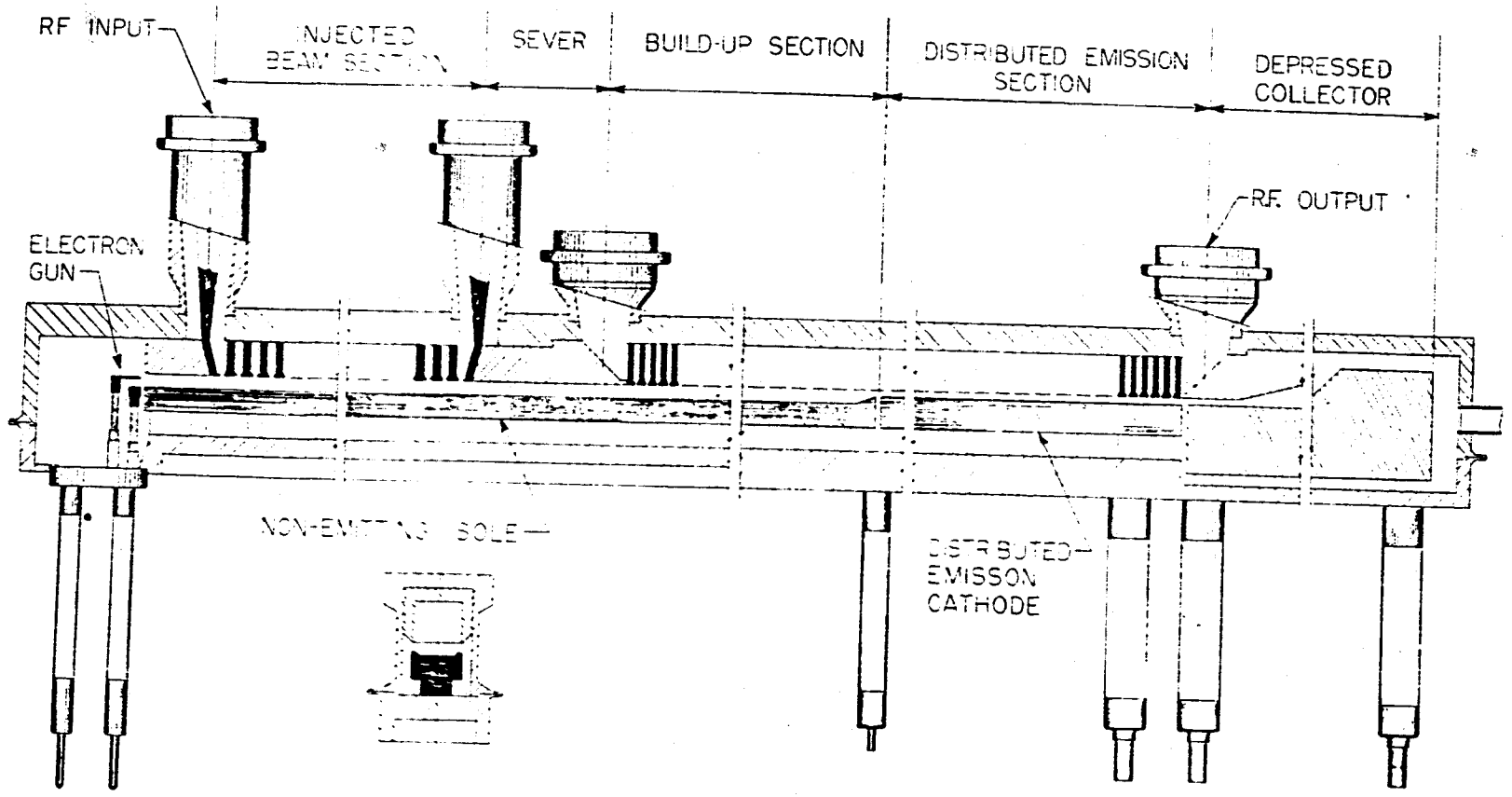

MECHANICAL DESIGN S-BAND CROSSED-FIELD AMPLIFIER

FIG. 9

collector entrance plane(4). The large-signal analysis of injected-beam interaction was used to determine this potential distribution. Similiar work is currently in progress for the distributed-emission interaction. We are confident that the efficiency can be made comparable to reentrant beam devices by a suitable depressed collector.

Mechanical Design

The mechanical design of the amplifier is shown in Fig. 9. From left to right is shown the injected-beam gun, the input rf coupler, the first section slow-wave structure, the first section output rf coupler, the sever and the sever termination, the build-up section, the distributed-emission section with slow-wave structure and emitting sole, the rf output coupler and, finally, the depressed collector. Details of the mechanical design are evident from the figure.

Of particular importance are the rf couplers and the waveguide windows. The injected-beam section which uses the split-folded waveguide structure makes use of a scaled version of the ridged waveguide coupler and window used on the Litton X-band crossed-field amplifier. Typically, such couplers provide a match through the tube whose VSWR is better than 1.5 to 1 over 40% bandwidth. This match is measured at the input coupler with all other couplers terminated with matched loads. At X-band, the windows and couplers have operated without cooling at 600 KW peak power and 1500 watts average power. The scaled version will be completely adequate for the first section of the S-band amplifier. The details of this window are shown in Fig. 10.

Several approaches are being considered and evaluated for the output window design. The scaled window already described is one of the more promising. For the high average power requirement the alumina will be replaced with beryllia. A heat flow calculation based upon the geometry shown indicates a temperature gradient of less than 100°C for 200 KW average power flow when the outside of the window is held at ambient by water cooling. This is well below the run-away point and indicates that dielectric loss heating will not be a problem. No multipactor problems or other electron bombardment problems have been encountered with this window at X-band and none are anticipated in the present design.

It is presently planned to use a Charles "short" gun for the injected-beam. However, the cathode loading for 200 μ second pulses is quite high, being on the order of 7 amps/cm^2 For this reason, we are also designing a Kino gun for this part of the beam.

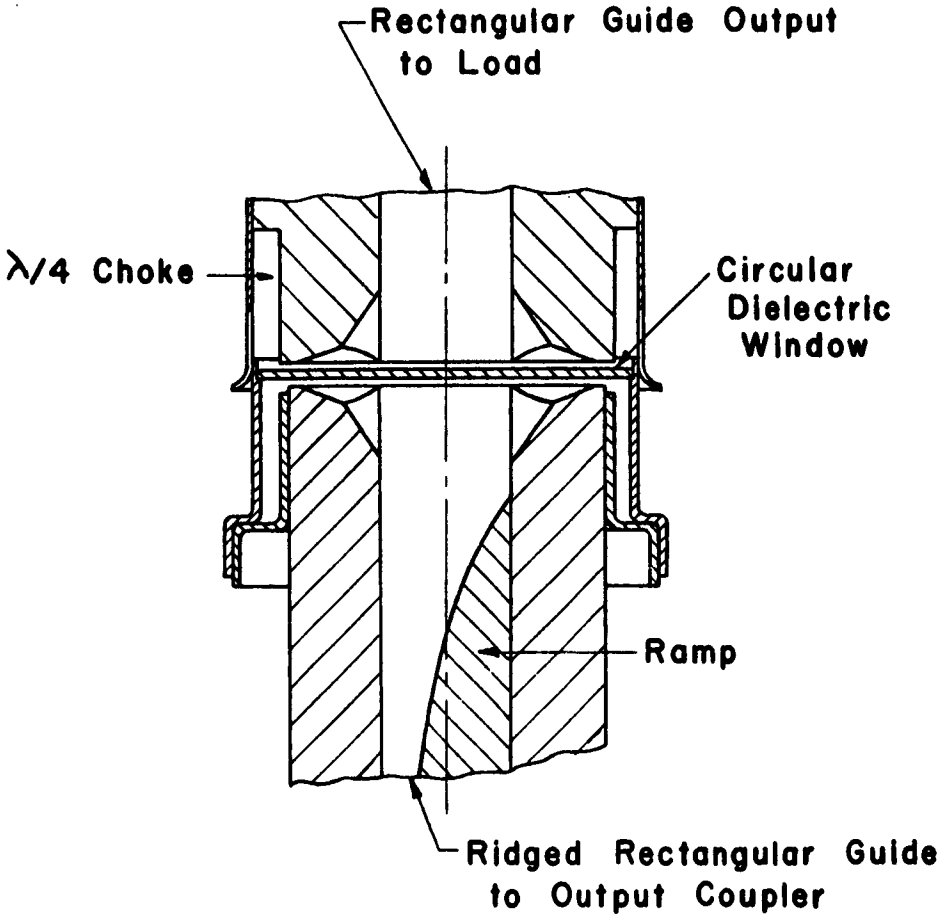

BROADBAND HIGH POWER
OUTPUT WINDOW DESIGN

Fig. 10

The distributed-emission cathode is made up of several segments of Phillips-type cathode material. We have previously found that a "warm", i.e., well-below thermionic-emission temperature Phillips cathode makes an excellent secondary-emission cathode. Initially, heaters will be included but heat sink designs will eventually make them unnecessary.

The present design is a laboratory model and will be tested in an electromagnet. However, the basic design is amenable to packaging in permanent magnets with very little additional work.

The program outlined in this paper has just gotten under way. We have demonstrated both the injected-beam interaction and the non-reentrant distributed-emission interaction separately at much higher frequencies. We are confident that the specifications for this amplifier will be met within the two and one-half years programmed for the development.

The authors gratefully acknowledge the support of the Rome Air Development Center under Contract No. AF 30(602)2792.

References

(1) J. F. Hull and G. P. Kooyers, "Experimental and Theoretical Characteristics of Injected-Beam Type Forward-Wave Crossed-Field Amplifiers", International Conference on Microwave Tubes, Munich, Germany, 1960.

(2) G. Kooyers and O. Buneman, "Large-Signal Analysis of Distributed-Emission Magnetron Amplifier", Electron Devices Research Conference, University of Minnesota, 1962.

(3) G. E. Pokorny, A. E, Kushnick and J. F. Hull, "The Dematron - A New Crossed-Field Amplifier", IRE Transactions, PGED, Vol. ED-9, No. 4, July, 1962.

(4) E. K. Shaw, G. P. Kooyers, P. N. Hess and G. E. Pokorny, "A Study of Depressed Collectors for Crossed-Field Amplifiers", Final Report, Air Force Contract No. AF 33(616)7921.

HIGH-POWER WAVEGUIDE WINDOWS

By

Delos B. Churchill

Sperry Electronic Tube Division
Sperry Rand Corporation
Great Neck, L.I., New York

INTRODUCTION

A waveguide window is a gas pressure barrier that is transparent to the flow of microwave power. For most applications, a window must be absolutely vacuum tight. Practical considerations require that it also be rugged, compact, and capable of withstanding high temperatures.

Simple, low-pressure windows for low-power applications were developed early in the microwave art, and their design presents no special problems. The widely used glass and mica windows are inexpensive and easily installed. But window problems have grown with the development of the high-power microwave tubes that use window-sealed output waveguides as integral parts of their vacuum envelopes (Figs. 1, 2, and 3).

Almost every manufacturer of high-power tubes has experienced window failures. The window, frequently an afterthought in the tube development program, has suffered from the improper use of dielectric materials, inadequate sealing techniques, and even a misunderstanding of the microwave network problem involved. In 1959, the Sperry Gyroscope Company was awarded a contract, administered by the U.S. Army Signal Research and Development Laboratory, to investigate waveguide-window failure mechanisms and develop improved windows. This program is presently in its third year. An industry-wide survey disclosed that there had been a very meager exchange of information on window problems and, in consequence, a considerable duplication of effort.

WINDOW TYPES

At least twelve different window configurations have been developed for use on medium-power and high-power tubes (Fig 4). The designer's choice

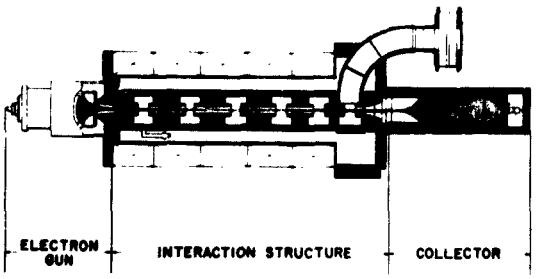

Fig. 1 Pill-Box window on L-band klystron tube.

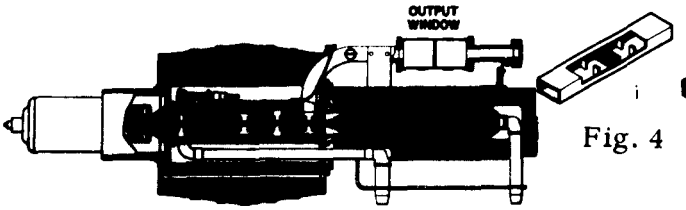

Fig. 2 Thin-disc, filter-type window on S-band klystron tube.

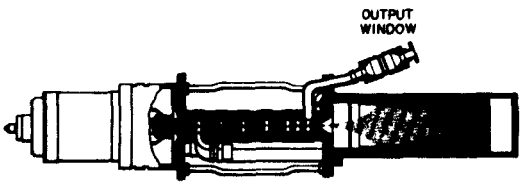

Fig. 3 Double-disc, filter-type window on X-band klystron tube.

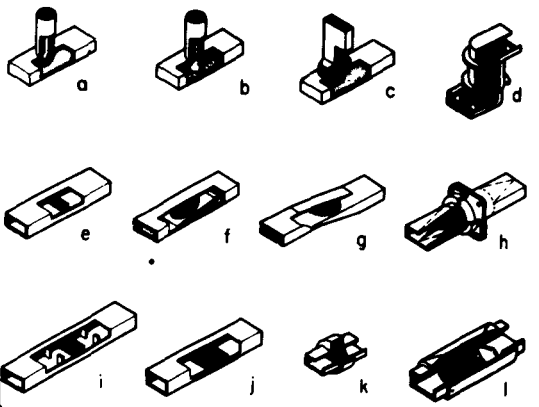

Fig. 4 Currently used window designs.

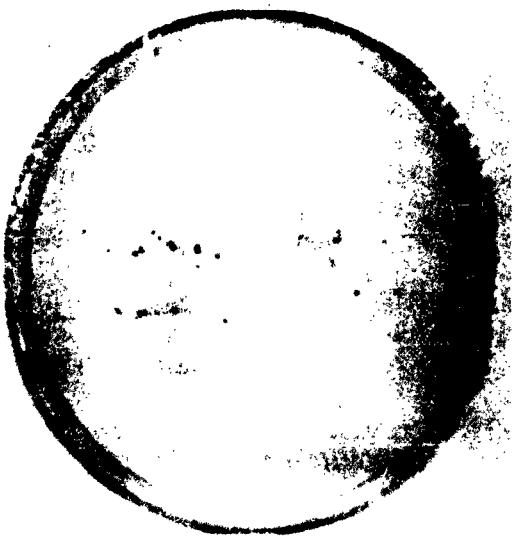

Fig. 5 Punctured window from Stanford linear accelerator, input side.

Incident Surface

is guided by the electrical and mechanical requirements and, necessarily, by the cost of development and fabrication. But cheap windows have caused expensive tube failures, and since reports of window failures became numerous, window materials and configurations have been selected with more care.

The coaxial and waveguide "corner junction" windows (a, b, and c) are commonly used on tubes operating at frequencies below 2 Gc. In terms of power density averaged over the normal waveguide cross section, these windows have only modest power-handling capacity because high local fields are produced at the corners. In the coaxial line-to-waveguide models (a and b) the shape of the dielectric element favors a strong seal. One commercially produced model of the waveguide-to-waveguide corner junction window (c) uses a bowl of high-temperature glass, and has operated successfully on a 5-megawatt L-band for several years. All other window types shown in Fig. 4 have been fabricated.with ceramic dielectric elements.

The type illustrated by sketch (d) deserves special mention. This window, developed in England by Barrington and Hyman,[2] is unusual for its operation in a higher order waveguide mode. The contoured corners are $TE^{\square}_{10} - TM^{0}_{01}$ mode transducers, and the wave impedances of the regions within the circular section, are equalized. The dielectric disc transmits the TM^{0}_{01} mode with a negligible reflective loss over a wide band of frequencies. However, despite its bandwidth, the window has not been widely adapted because of the practical difficulties associated with producing a pure TM^{0}_{01} mode.

Sketches (e, f, and g) illustrate windows that have been widely used on S-, C-, and X-band tubes. The elliptical or circular dielectric plate is brazed to a metal frame that is oriented normal to, or canted with respect to, the axis of power propagation. The disc and frame comprise a resonator; with a suitable choice of materials and dimensions, the resonator Q is low and the window transmits a broad band of frequencies. A great many failures were experienced with self-resonant windows of this type. The electric field at the disc is increased by the condition of resonance, reducing the threshold of arcing. In the canted position, the window is subject to heavy multipactor loading which produces excessive heating. More will be said later about multipactor at windows.

The circular-cone window shown in sketch (h) has very wide transmission bandwidth; but the cost of development and fabrication of this window is relatively high. The dimensions of the cone and the tapered $TE^{\square}_{10} - TE^{0}_{11}$ transitions require careful adjustment and close tolerances. Thin-walled cones of sintered alumina ceramic are commercially available in some sizes. Usually it is necessary to incorporate vanes of lossy material in the circular section to damp out spurious modes. At high power levels, cone windows also are troubled by multipactor loading.

Exit Surface

Fig. 6 Window of Fig. 5, output side.

Transmitted Light

Fig. 7 Window of Fig. 5 photographed by transmitted light.

If the dielectric element fills the waveguide cross section, and its plane surfaces are normal to the waveguide axis, then the principal electric field is continuous through the interfaces, and mode purity is preserved. The simplest window that operates in a pure, dominant mode is the rectangular block window illustrated in sketch (i). A half-wave-thick dielectric block is longitudinally resonant and exhibits a negligible transmission loss at the resonant frequency. However, its bandwidth is narrow unless additional matching elements, such as the irises shown in sketch (i), are inserted. With the proper irises, this window functions as a waveguide filter and has a bandwidth of 20 percent or more. It has been slow in gaining popularity because its bandwidth potential was not appreciated.

Sketch (j) illustrates a broadband version of the rectangular block window that makes use of quarter-wave steps for impedance matching. However, in the regions of the steps, mode purity is lost and the corner fields are high. Consequently, the power-handling capacity is lower than that of the iris-matched block. Once a popular design, this window is now seldom used.

The "pill-box" window of sketch (k) is widely used on high-power tubes covering a large part of the microwave spectrum.The dielectric disc is sealed in a short cylindrical section, and the transitions are essentially flat flanges with small radii on the corners. The broad bandwidth and simple mechanical construction account for the popularity of this window.

Many pill-box windows have failed on tubes due to arcing on the output sides. The thin disc is relatively close to the flange corners, and arcs that start in the load waveguide frequently flash back to the disc surface. In high-average-power applications, a steady arc between the flange corner and the disc causes intense local heating that may crack the disc.

Although simple in appearance, the pill-box window requires careful design for broadband operation. It can operate either in a TE-type mode or in a TM-type mode; broadband models operate in both modes in different parts of the band. TM-mode operation is characterized by normally directed fields at the dielectric surfaces, which leads to multipactor loading at high powers. The relatively abrupt flange corners located close to the disc increase the probability of multipactor.

The last sketch of Fig. 4 illustrates a double-disc window of recent design.[3] Tests have shown that this window has the highest power capability of any of those illustrated, as well as very wide bandwidth. This is a filter-type window, similar in principle to the half-wave-thick block with symmetrical irises. The matching elements are the short, conical transitions, and the pair of discs comprises the half-wave resonator. Nonpropagating modes developed at the transitions decay to negligible amplitudes before reaching the discs. Consequently, the electric field at the

Fig. 8 Photomicrograph of window of Fig. 5.

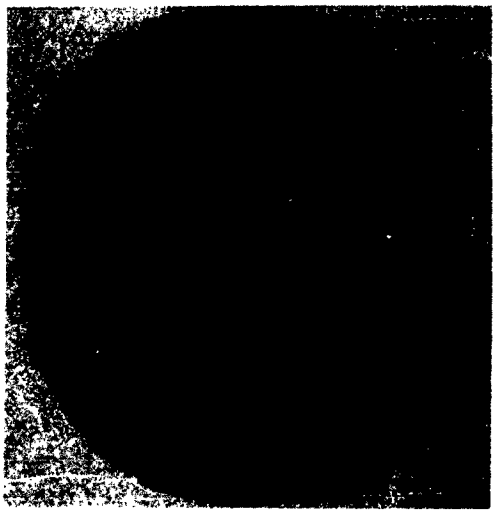

Fig. 9 C-band window punctured in ring resonator tests.

Fig. 10 20X photomicrograph of window of Fig. 9.

dielectric surfaces is essentially that of the pure TE_{11}^{0} mode. With reasonable mechanical tolerances, this window does not require mode suppressors.

The double-disc design has mechanical as well as electrical advantages. The disc thickness is more or less arbitrary, different thickness being compensated by different spacing between discs. Thus, the thickness may be chosen with the principal consideration of optimizing the seal. This usually leads to a disc thickness that is considerably greater than that of the pill-box window, but less than one-quarter wavelength thick. It should also be pointed out that the space between the discs is a gas cell that can be pressurized and pinched off. Thus, if the vacuum seal at the first disc is ruptured, the tube acquires only the gas contained in the cell, which, in many cases, renders the tube salvable.

WINDOW FAILURES

The findings pertaining to window failures will now be summarized. Data were gathered from field and laboratory operation of tubes, as well as from tests with window-sealed, evacuated waveguide sections ("windowtrons") in high-power simulators.

Nearly all the reported instances of failure involved windows that used ceramic dielectric elements. The remainder involved glass and mica windows that were pressed into service beyond their ratings. The most commonly used ceramic body was dense, sintered alumina. Alumina is available with a purity up to 99.5 percent; but, as far as could be determined, the bodies used in the damaged windows ranged only up to 96 percent purity. The predominant form of failure was cracking of the dielectric element. Others exhibited the gross puncture of heavy arcing confined to a small area; and some others had numerous microscopic puncture channels distributed over a larger area. In a few cases the dielectric element was not damaged, but the window lost its transmission capability because a deposit of metal was formed on the inner (vacuum side) surface.

The alumina window of Figs. 5 through 8 was punctured while operating on a 20-megawatt, S-band klystron used to drive the linear accelerator at Standford University.[4] Figures 5 and 6 show the tube side and load side, respectively, and Fig. 7 was photographed by light transmitted through the disc. The large amount of opaque material inside the dielectric body is clearly evident. After this window was sectioned, the material was identified as carbon. Figure 8 is a photomicrograph showing some of the surface craters. Although many of the craters are larger than 0.001 inch, the puncture channels they terminate are much smaller, and wander through the body in various directions.

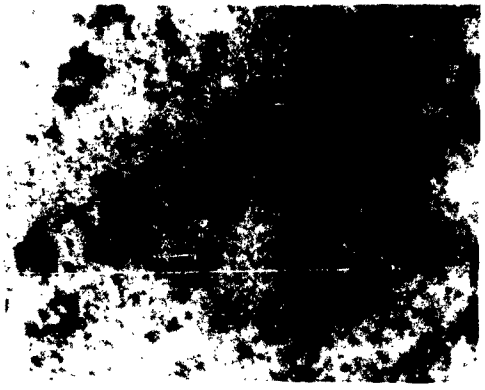

Fig. 11 200X photomicrograph of window of Fig. 9.

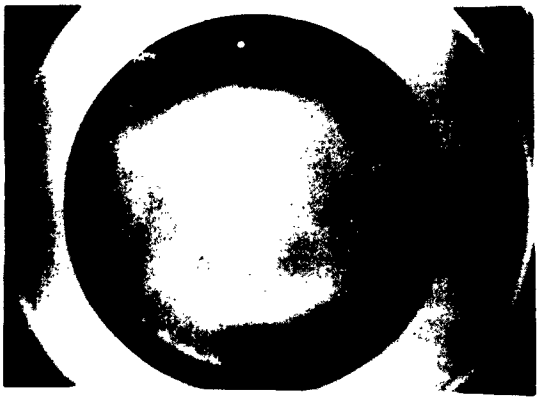

Fig. 12 Sapphire C-band window with metal deposits from arcing.

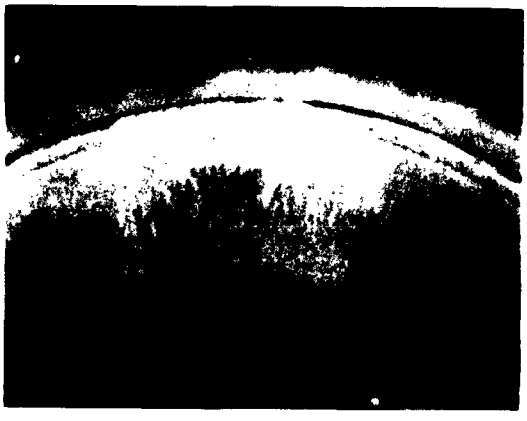

Fig. 13 Window of Fig. 12, showing detail of seal area.

The alumina window of Figs. 9 and 10 was punctured while operating on an evacuated test section in a C-band ring resonator at a peak power level of approximately 5 megawatts.[5] The cratered area was entirely on the vacuum side; the pressurized side showed no evidence of damage. There was no carbon deposit inside the body, but a test with a penetrating dye revealed that the damaged area was porous. The individual craters are very similar to those of the Stanford window.

The polished sapphire window of Figs. 11, 12, and 13 shows a feathery, metal deposit that was produced by vacuum-side arcing. The arc started at the seal and increased in extent as the deposited metal spread over the window surface. The sapphire itself was not damaged, but the window became highly reflective to r-f energy.

Analysis and study of these failures and the circumstances under which they occurred led to the following conclusions. The total heat developed in the dielectric element is always greater than that due to its dielectric loss factor alone. The additional heat is attributed partly to electronic discharge and partly to seal-area losses. At high powers, electronic discharge is the predominant heat-producing mechanism, and involves secondary electron resonance (multipactor) at the dielectric surface. It is not certain whether the metallic walls are involved in the multipactor discharge, or serve only as sources of cold-emitted primary electrons. Windows that operate with a component of the electric field normal to the dielectric surface experience greater multipactor heating. However, there is good evidence that multipactor does occur at the surfaces of ceramic windows having a purely tangential electric field of large amplitude. A theory explaining this finding has been developed, but is beyond the scope of this paper.

The lower the purity of the alumina, the greater is its dielectric loss factor and the more intense is the multipactor discharge at its surface. The latter finding is explained on the basis of the higher secondary-emission coefficients of the various silicates and oxides that constitute the principal impurities. The presence of gaseous hydrocarbons and organic contaminants (particularly vacuum-pump oil vapor) greatly increases the multipactor losses and accelerates the mechanism of charge migration that leads to multiple puncture. Crater formation of the type shown in Figs. 5 through 10 has occurred only to ceramic bodies of lesser purity, and is the result of the excessively high secondary yields of these bodies. Polished crystalline sapphire windows operate at very much lower temperatures than ceramic windows of the same configurations. Attempts to puncture sapphire windows by high-power operation have failed, and none of the windows tested exhibited craters or any other form of erosion.

Arcing at the window seal is a serious problem that requires careful attention to fabrication techniques. The situation that leads to arcing is illustrated by the first sketch of Fig. 14. A large fillet of brazing material forms a strong seal, but it presents a sharp edge to the tangential electric

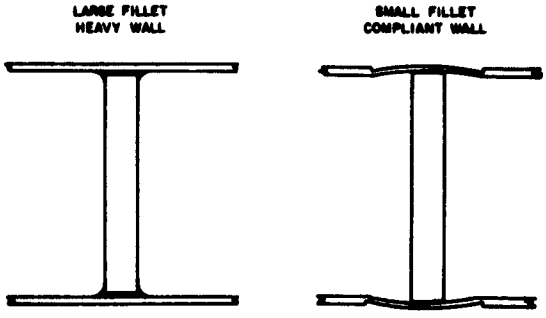

Fig. 14 Sketches showing braze details of edge-sealed windows.

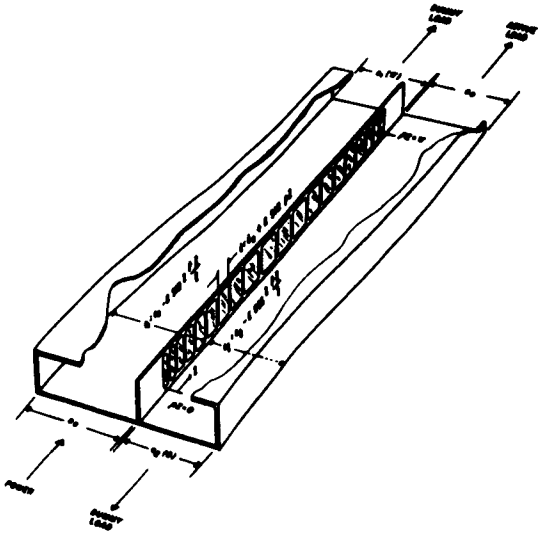

Fig. 15 Proposed coupled-mode window.

field on the window surface. By using a compliant waveguide wall, a tight seal can be formed with a minimum of brazing material confined to the periphery of the window. Owing to the difference in the expansion coefficients of the metal and the dielectric body, and the use of a restraining band (a strip of molybdenum) around the window region during the brazing process, the compliant wall assumes the shape indicated in the second sketch of Fig. 14 after the parts reach room temperature. This shape favors multipactor by distorting the tangential field at the window surface, and should be altered by machining or spinning the wall back to its original shape.

IMPROVED HIGH-POWER WINDOWS

In consideration of the findings of this study, it is concluded that many window failures could have been avoided by choosing better dielectric materials. Some of the favorite window configurations are not wisely chosen for new tubes of increased power. High power-handling capability is provided by windows with a high degree of dominant mode purity, either circular or rectangular, throughout the dielectric-filled region.

A new approach that offers even higher handling capacity is the coupled-mode window illustrated in Fig. 15. This window, based on the principles of total-power-transfer couplers developed by Cook[6] and Fox,[7] has dielectric material located only in regions of low electric field. Consequently, the power density in the dielectric material, which is distributed over a relatively large area, is reduced. A mode of this window has been constructed, and, although it has not yet been tested at high power levels, its transmission characteristics were satisfactory. The principal drawback of this window is its size; nevertheless, for the super-power tubes of the next generation, it may offer a practical solution to the window problem.

REFERENCES

1. Contract No. DA 36-039-SC-78314. The work of this contract was later continued under Contract No. DA 36-039-SC-87389.

2. A.E. Barrington and J.T. Hyman, "A Non-Resonant Waveguide Window", Proc. IEE, 104, Part B; 1958, p. 35.

3. Fifth Quarterly Progress Report, Investigation of Microwave Window Failure Mechanisms and Their Elimination, furnished by Sperry Gyroscope Company to U.S. Army Signal Research and Development Laboratory under Contract DA 36-039-SC-87389, p. 12, par. 4-4a.

4. J. Jasberg and J.V. Lebacqz, "Problems Related to Very High Power Windows at Microwave Frequencies", Advances in Vacuum Science and Technology, Pergamon Press; 1960, p. 667.

5. Fourth Quarterly Progress Report, Investigation of Microwave Window Failure Mechanisms and Their Elimination, furnished by Sperry Gyroscope Company to U.S. Army Signal Research and Development Laboratory under Contract DA 36-039-SC-87389, p. 8, par. 4-1c.

6. J.S. Cook, "Taper Velocity Couplers", Bell System Tech. Jour.; July 1955, p. 807.

7. A.G. Fox, "Wave Coupling by Warped Normal Modes", Bell System Tech. Jour.; July 1955, p. 823.

SUPERPOWER RESONANT RING

by

Floyd O. Johnson

Varian Associates

ABSTRACT

This paper deals with the problems of designing and testing of a superpower waveguide traveling wave resonant ring. Certain design criteria were established which required that the circuit be operable to at least 50 megawatts peak and 1 megawatt average, the waveguide evacuable to 10^{-6} Torr or better and pressurable to 3 atmospheres. The circuit would be tunable over a 10 per cent band in WR 340 waveguide in order to allow tuning by frequency variation. A minimum power gain of 25 was required.

Test results are given showing the highest power obtained to date with a long duty cycle is 80 megawatts peak and 580 kilowatts average. Short duty cycle operation has resulted in peak powers up to 225 megawatts. Gains in excess of 100 times the power input have been measured. Results of waveguide pressurized with Freon 12 are also given.

A new waveguide vacuum flange design is discussed and is shown to be a most reliable seal as well as a properly functioning, low loss, waveguide joint.

Certain high power tube output window test results are given with one window performing well up to 60 megawatts peak and 300 kilowatts average power. It is expected that continuing experiments with this circuit will be performed at power levels far in excess of 50 megawatts peak and up to 1 megawatt average.

I. INTRODUCTION

Traveling wave ring resonators applied in microwave testing are barely a decade old but are finding a continued increase in acceptance and use. Varian Associates now has two such ring circuits, one in WR 112 (X-Band) and one in WR 340 (S-Band). Figure 1 is a photograph of the WR 340 ring as it now exists. The purpose of this paper is to present some of the considerations in its design along with pertinent test results on waveguide components, such as high power vacuum tube output windows.

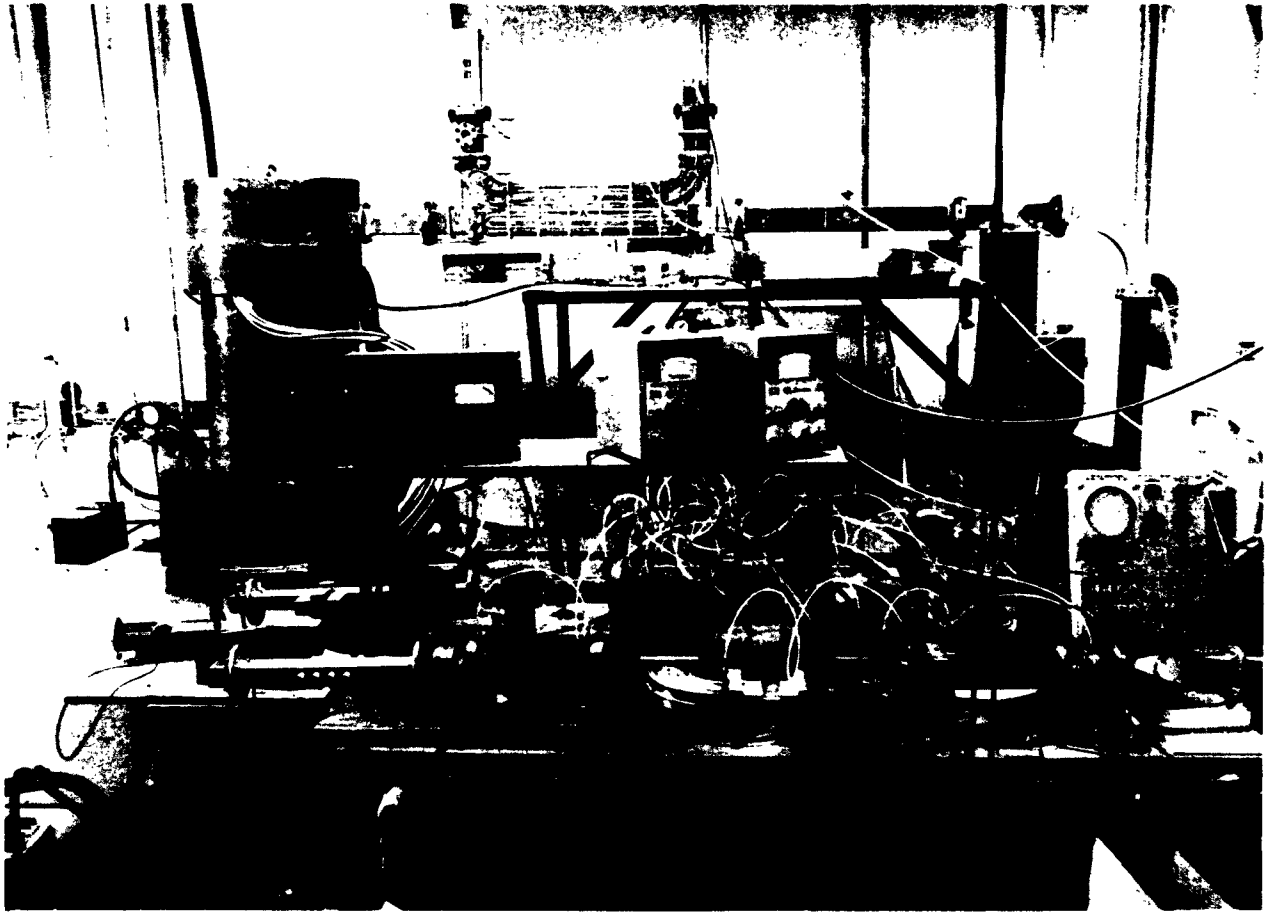

FIGURE 1
"SUPER POWER RESONANT RING"

The initial power level design goal was 50 megawatts peak, 1 megawatt average simultaneous transmission. This power level is substantially higher than that which had been achieved and therefore raised several major considerations in the ring design. These are waveguide evacuation or pressurization, waveguide component cooling, effect of power losses and impedance mismatch, ring driving source, bandwidth and also instrumentation just to name several of the broader problems involved.

II. DESIGN CRITERIA AND TEST CONDITIONS

A. Attenuation

As pointed out by S. J. Miller,[1] attenuation is one of the major considerations in a high gain ring circuit. After careful consideration of practical materials such as brass, aluminum, silver plating and copper, OFHC copper was chosen as being the best despite its obviously poor mechanical strength characteristics in the annealed state. At 2700 Mc, the low end of the desired band, losses theoretically are .004 db per foot. Estimated ring length was 18 feet maximum with a minimum of 6 flange connections, each with approximately .003 db loss. Total calculated loss came to 0.1 db which, as results given later will show, was very conservative.

Subsequent calculation of the voltage coupling coefficient for the optimum gain indicated a 17 db coupler should be used. As overcoupling would be advantageous if the losses should exceed the estimated amount, the sidewall directional coupler decided upon was to have 15 db coupling.

B. Ring Evacuation and Pressurization

Because of the high power capabilities desired for this circuit, the rated 4 megawatts (100 per cent safety factor) in air at atmospheric pressure must be increased. The waveguide must be able to withstand a pressure differential. The WR 340 OFHC waveguide chosen for this project had a 1/8 inch wall which would bulge out as much as 0.10 inch with 1 atmosphere of pressure. Therefore, stainless steel reinforcements were designed to hold the waveguide dimensions within tolerance with a pressure greater than 3 atmospheres.

The use of an evacuated ring posed a different set of problems. A vacuum of 10^{-6} Torr or better was considered adequate for high R.F. voltage testing, but, to obtain this vacuum required that all components be completely sealed and built from low vapor pressure materials, i.e. an all metal system. An all metal R.F. and vacuum waveguide flange (described later) was designed which could also withstand bakeout to at least 500°C and still be vacuum tight. Subsequent tests have shown that this flange is as good as the waveguide itself in handling high power.

All published information on resonant rings indicate that it is most desirable to have a system which includes a means of varying the input coupling along with the

---

1. S. J. Miller, "The Traveling Wave Resonator and High Power Microwave Testing," Microwave Journal, Vol. 3, No. 9, pp. 50-58, September 1960.

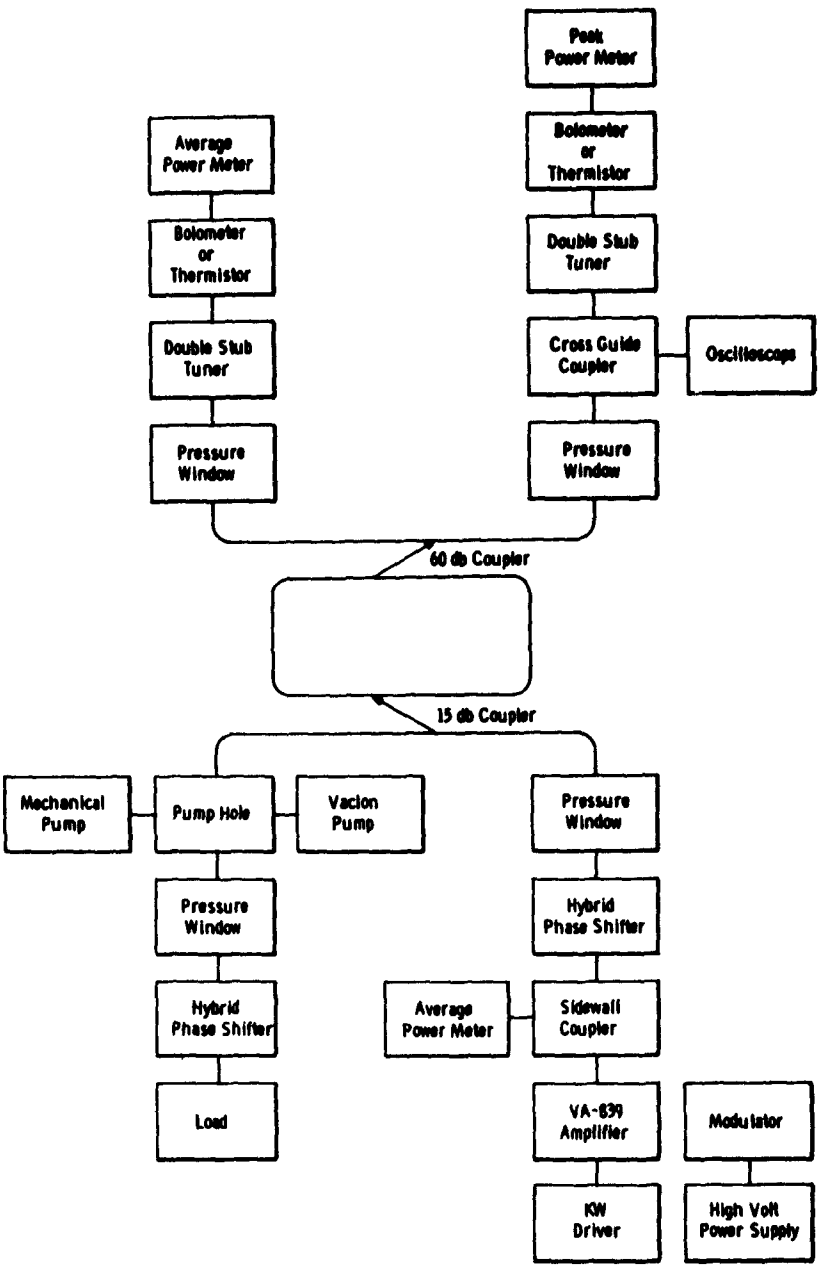

FIGURE 2
TRAVELING-WAVE RESONANT RING BLOCK DIAGRAM

phase and the impedance in the ring. Because of the very difficult task of designing continuously variable, vacuum tight components to vary these parameters and at the same time handle 50 megawatts of peak power, it was decided to make the ring as simple as possible. The coupling was fixed, phase variations used to resonate the circuit were abandoned in favor of tuning by frequency variations and the need for variable impedance matching eliminated by design of nearly reflectionless components.

Reference to the ring circuit block diagram in Figure 2 will show the entire system as used to obtain much of the experimental data.

C. Waveguide and Component Cooling

Initial estimates of expected losses (.1 db) when transmitting 1 megawatt of average power indicated that about 1.2 kw (1200 joule/sec) of energy would be dissipated per foot of waveguide. Due to the high thermal conductivity of copper, removing this energy in the form of heat was considered to be no problem. The waveguide reinforcement previously mentioned served as self jigging for 1/4 inch O.D. water cooling tubing brazed to the side of the waveguide.

Calibrated flow rate meters and thermometers were provided to monitor the temperature rise and thus give the heat dissipation in the windows being tested.

D. Ring Driver and Instrumentation

A broadband driver for this circuit was needed because of the decision to use frequency variation tuning rather than selecting an exact frequency and then tuning the ring to resonance with a phase shifter. Also, with a power gain of only 25, it would require having a tube delivering 2 Mw peak and 40 kw average power. All of these requirements, with the exception of average power, are provided by the Varian VA-839 which delivers 5 Mw peak at 10 kw average. This tube has been used as the driver for all of the tests to date.

A 60 db, high directivity, sidewall directional coupler was built to sample ring power. Although at full power, 80 db coupling would have been an optimum value, a compromise was made in order that the circuit could be used at lower power levels as well. Additional 20 db padding of the 60 db coupler fulfills the full power requirements.

Pressurization or evacuation of only the high power ring portion was accomplished with the use of broadband pressure windows capable of passing as much power as the VA-839 can deliver. It is imperative that the VSWR of these windows be very low so that the circuit operation is not upset by spurious responses due to high random phased reflected power.

E. Waveguide Vacuum Flange

Because of the need for an all metal, bakeable waveguide system, a waveguide vacuum flange was developed. A cross sectional drawing showing the assembly is shown in Figure 3. With this type of seal, the standard cover flange dimensions and

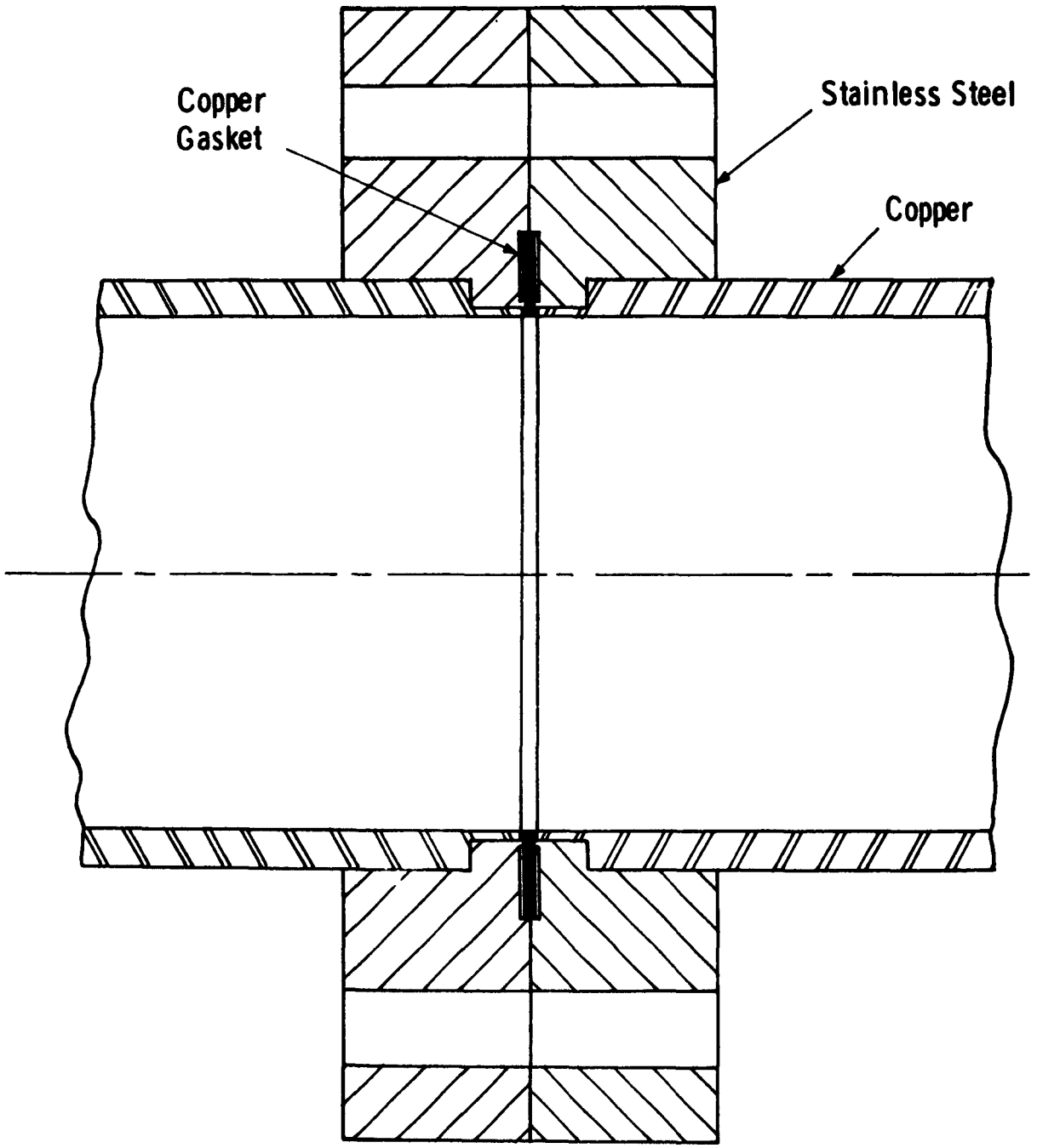

FIGURE 3
WAVEGUIDE-VACUUM FLANGE ASSEMBLY

hole layouts can be maintained. If necessary or desirable, this type of flange can also be mated with a standard cover flange by simply using a gasket one half as thick as normal.

Losses in both standard cover flange connections were measured by a method given in a Varian Technical Memorandum and in an article published by F. Johnson.[2] The vacuum flange was measured to have less loss than the cover flange connection at the lower end of the band as seen in Figure 4. This of course might be expected because the R. F. currents are localized to the immediate vicinity of the seal whereas in a cover flange currents can exist anywhere on its face. These flange connections have been found to be completely reliable after repeated use and repeated high temperature heat cycling.

III. EXPERIMENTAL RESULTS

A. Low Power Performance of the Ring Circuit

Initial experiments with the ring circuit once it was assembled, were at relatively low power levels. During the preliminary preparations for these experiments, careful attention was paid to directional coupler and attenuator calibration. Frequencies at which the circuit is resonant can be calculated knowing the physical length of the waveguide run. Without any test piece, the minimum ring length is 8.7 feet and is resonant at 3 frequencies within the driver tubes bandwidth. With a maximum of 1 kilowatt peak power (.01 duty cycle) available the ring tuning was established after various trials. The most successful tuning method is described as follows.

After the desired frequency has been selected, all the power sampling thermistors or crystals must be tuned at that frequency to introduce minimum standing waves in the ring. For example the two output arms of the sampler coupler are terminated with thermistors. These terminations must be reflectionless at the operating frequency and are made to look so by the use of double stub or slide screw tuners.

The next step in the tuning procedure is to maximize the forward power by varying the frequency. A hybrid phase shifter in the input coupler loaded arm, is then tuned to minimize the ring reflected power. These last two adjustments interact and therefore must be repeated alternately until optimum performance is achieved. If the loaded arm were reflectionless, this method would probably not work because no small reflected wave could be sent back with the proper phase to cancel the internal reflected wave in the ring.

Depending on frequency of operation, duty cycle and care in tuning the low level power gains measured ranged from 40 to 120. One consistent result also reported

---

2. F. O. Johnson, "Measurements of Very Small Losses in Waveguides," Microwaves, p. 16, August 1962.

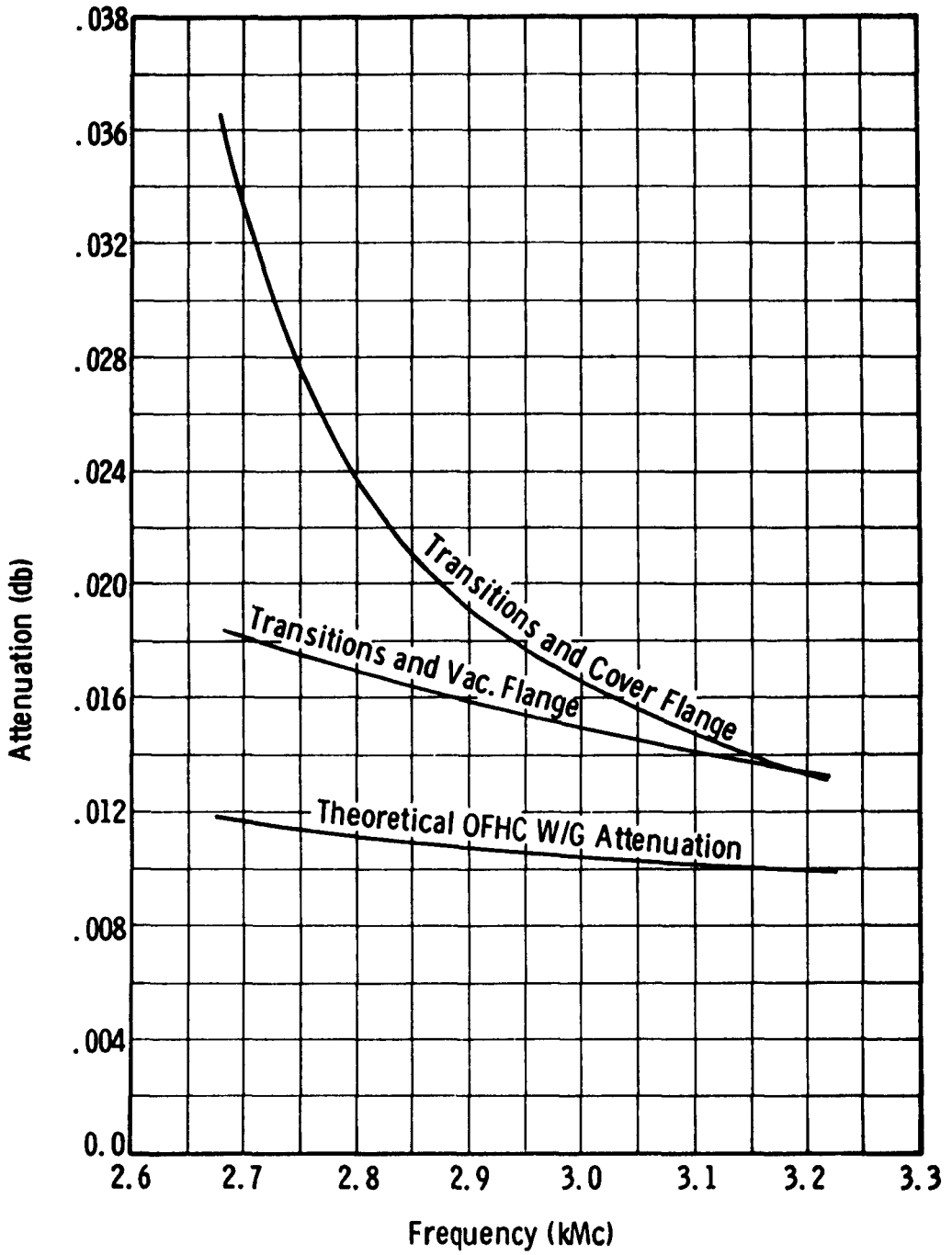

FIGURE 4
ATTENUATION IN TWO WR340 TO WR284 TRANSITIONS CONNECTED BACK TO BACK. ONE SET CONNECTED WITH WR340 VACUUM FLANGE. ONE SET CONNECTED WITH WR340 COVER FLANGES

by S. J. Miller[3] became apparent for either the low or high level gain measurements. Under certain loss conditions where coupling becomes critical, the longer pulses produce higher gains. The very high gains and extremely low losses which were shown by these experiments indicate that the estimated .1 db losses are at least 100 per cent too high. This fact, in addition to the highly overcoupled state of the resonant circuit, produces a ring pulse which for all practical purposes is an exact reproduction of the input pulse. This simplifies the peak power calculations using average power data. From top to bottom in Figure 5 can be seen the input pulse and the pulse shape within the ring.

B. High Power Transmission in Pressurized Guide

Calculating from the curves and equations provided by L. Gould,[4] the maximum pulsed power that WR 340 airfilled waveguide can handle, at atmospheric pressure, is 8.16 megawatts. The first high power experiment was made to test this calculation. By slowly increasing the power to breakdown it was found that arcing occurred throughout the ring at power levels between 8 and 10 megawatts. The variations in level of breakdown are believed due to differences in tuning of the circuit.

A series of experiments designed to evaluate waveguide power transmission when filled with Freon 12 was performed. To be sure that the waveguide contained Freon 12 only and no air, the system was evacuated first and then let down to Freon. Peak power versus gas pressure is shown plotted in Figure 6. As can be seen, even with waveguide filled with Freon at atmospheric pressure, the breakdown level is improved substantially. It should be noted that variations from the plotted breakdowns did occur and seemed to be a function of frequency of operation and mismatch in the ring.

C. High Power Transmission in an Evacuated Waveguide

Very little published data seems to exist concerning R.F. power breakdown and breakdown initiated X-rays in evacuated waveguide. It is true that at Varian among others, high power vacuum tube techniques are quite advanced but once the power has been generated and coupled to the waveguide through a window, evacuated systems are rarely used. Of course, most applications eventually require propagation of this energy into the outside world but between the generator and the antenna evacuated waveguide does offer at least one advantage as evidenced by experimental results. (See Table 1.) That is its extremely good transmission of very high peak and average power levels.

In Table 1 is listed a few of the more pertinent bits of experimental data accumulated with the WR 340 ring resonator to date.

- - - - - - -

3. S. J. Miller, "An Additional Consideration in the Design of Traveling Wave Resonators," Massachusetts Institute of Technology, October 26, 1960.

4. L. Gould, "Handbook on Breakdown of Air in Waveguide Systems," Microwave Associates, Inc., Burlington, Massachusetts.

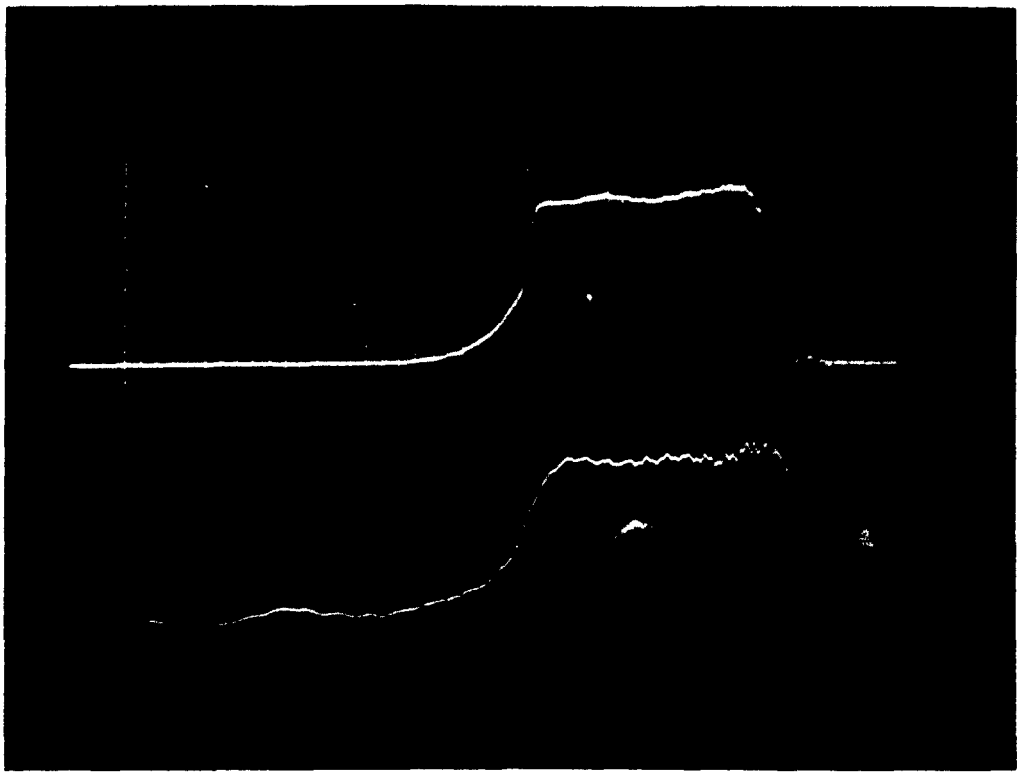

FIGURE 5
RING PULSE SHAPES

TABLE I

POWER LEVELS ATTAINED WITH WR 340 RESONANT RING

Test No.	Peak Power (Mw)	Average Power (kw)	Pulse Width (μsec)	Pulse Rep. Rate (c.p.s.)	Waveguide Pressure
1	225	50	2	111	10^{-5} to 10^{-7} Torr varying (breakdown at flange)
2	80	580	6	1200	2×10^{-7} Torr steady (no breakdown)
3	120	300	5	500	4×10^{-7} Torr steady (no breakdown)

In tests 2 and 3 the maximum powers were not attained simply because of insufficient drive to the ring. Breakdown was observed, with the aid of waveguide viewing ports in the vicinity of one of the waveguide junctions during test 1 producing very strong X-ray radiation as indicated on the radiation monitor. No radiation was apparent at any time except when visible breakdown was seen.

D. High Power Testing of Waveguide Windows

A rather extensive series of high power waveguide windows are now being evaluated using the "S" band, WR 340 ring circuit. Only preliminary results are available at this time but they are significant considering the power levels at which these windows broke. Half wavelength, ($\lambda g/2$) alumina oxide ceramic blocks metallized and sealed to copper waveguides comprise the basic window. Water cooling was used around the window edges where the waveguide thickness is reduced to approximately 30 thousandths of an inch. The bandwidth of this window exceeds 10 per cent and is mode free. Resonant modes are excluded from the operating band by the proper choice of reduced waveguide height and width.

Two AL 300 alumina oxide windows have been tested to destruction at power levels of 50 Mw peak, 200 kw average and 60 Mw peak 300 kw average respectively. Subsequent investigation has shown that neither of these windows was being cooled enough at the time of fracture because the flow rate was only 25 per cent of what it should have been.

Coolant water input and output temperatures were continuously monitored in order that heat dissipation could be calculated. Some localized hot spots in the ring circuit itself did develop and reached temperatures as high as 60°C (140°F). It is expected that in the near future windows built with beryllium oxide and lower loss aluminas will be tested with the goal of transmitting 1 Mw average power through them. Acquisition of a higher powered driver will be necessary.

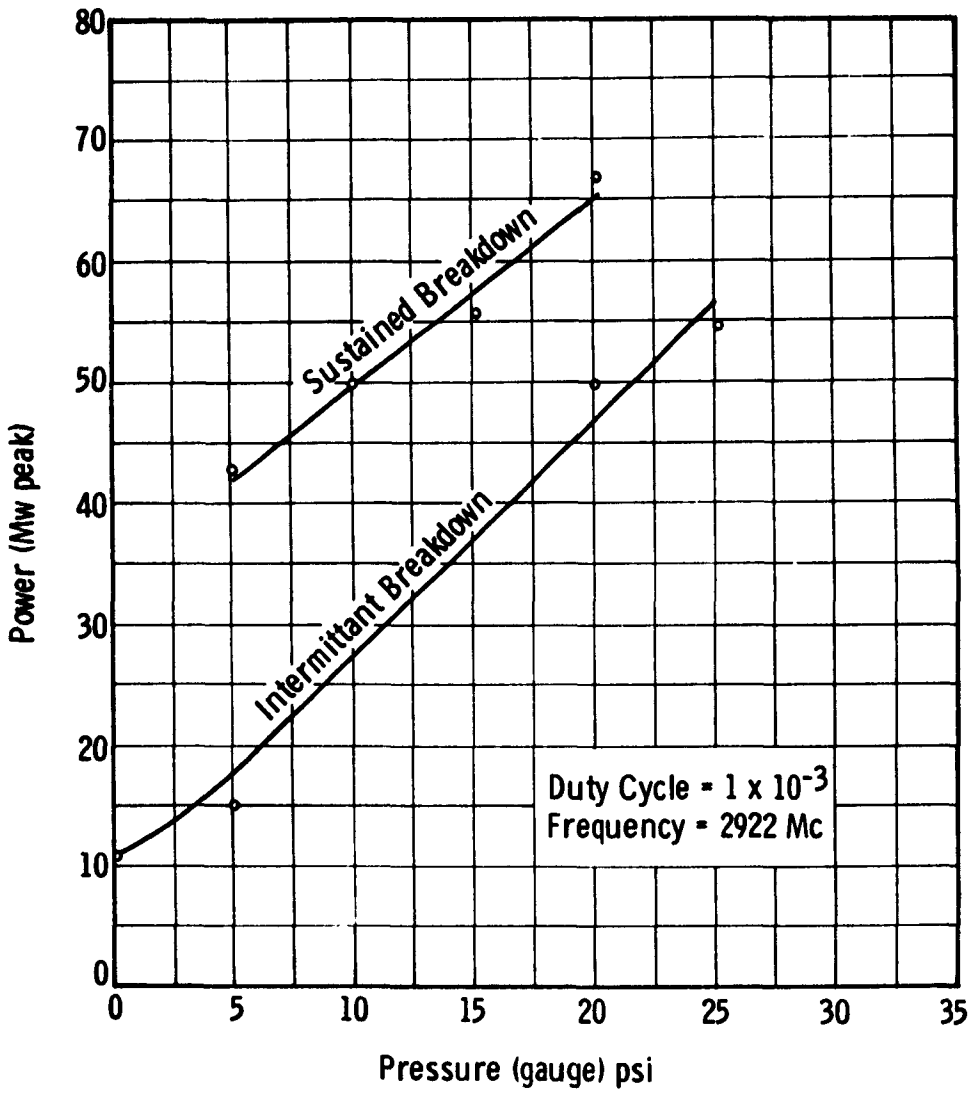

FIGURE 6
FREON-12 BREAKDOWN TESTS (WR340 RING RESONATOR)

IV. CONCLUSIONS

The principles of a resonant ring circuit are relatively simple and if the circuit itself can be kept simple it has been shown that extremely high powers can be circulated in waveguide. It should be reiterated that simplicity means that the ring is limited to waveguide and nothing else. The only modifications required to this rule is of course the power coupling holes of the sidewall coupler.

The circuits uses are manifold. Besides the tests described above it can be used to investigate other phenomena in high power R. F. fields such as the effect of strong magnetic fields on breakdown, multipactor, electron bombardment and others. However, it is not the intent of this paper to report on these subjects. It is merely pointing out that the ring circuit can and will be a very useful tool in broadening the state of the art in the high power microwave field.

THIS PAGE HAS BEEN LEFT BLANK INTENTIONALLY

HIGH AVERAGE POWER MICROWAVE WINDOW STUDY AT L-BAND

By

A.J.Prommer
A.J.Smith
J.J.Haruff

Litton Industries

Part I

ABSTRACT - This paper discusses approaches which have been used in the evaluation of different window designs for a 5 MW peak, 300 kW average power L-band klystron. Because of the comparatively low peak power the window problem in this case is due mainly to thermal stresses caused by excessive and non-uniform dissipation of RF energy. A short review of the basic design concepts for high average power windows and a summary of their theoretically predicted behavior will be presented first. Next an analog technique is discussed which has been used to solve the steady state temperature distribution for different window modes. This technique uses a resistance network analog to solve the heat flow equation which in this case has the form of a Poisson equation.

INTRODUCTION - One of the major problems in extending the art of high power klystrons to higher power levels is the limited power handling capacity of microwave windows. Due to the physical properties of dielectric materials there is a theoretical power limitation to even the best window design but in practical applications window problems are usually experienced considerably below this fundamental limit.

The problem is accentuated by difficulties in evaluating window performance without experimenting on full power tubes which is an extremely costly approach. Because the complexity of the problem excludes an analytical evaluation, techniques which allow the evaluation of a specific window design without the building of tubes are of great importance. This paper will discuss two experimental techniques which have been found very useful in analyzing and evaluating microwave windows.

The first method is an analog method which is used to solve the thermal gradient problem and the second method is the testing of windows under simulated high power conditions in a ring resonator. The paper will be given in two parts. In the first part we will present a short introduction into our specific window problem and describe the analog method. The second part will be given by C. Pappas[1] and it will discuss the work on the ring resonator.

The problem which stimulated this specific window program is the output window for a 5 MW peak-, 300 kW average-power, L-band klystron. The tube which is designated L-3401 is shown in Figure 1. The tube is tunable over

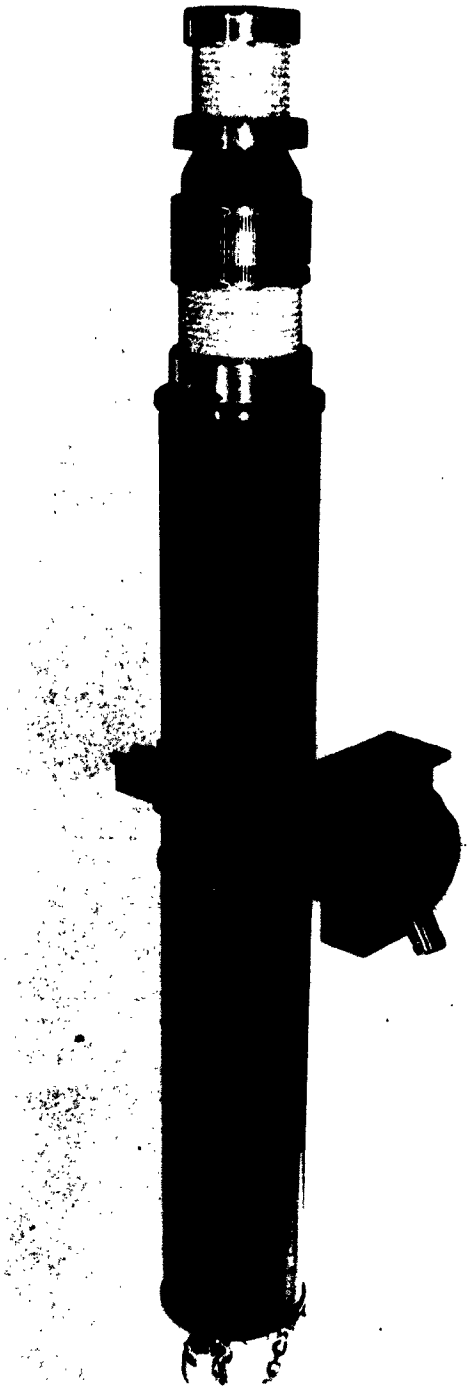

FIGURE 1 - L-3401 5MW/300 kw Klystron

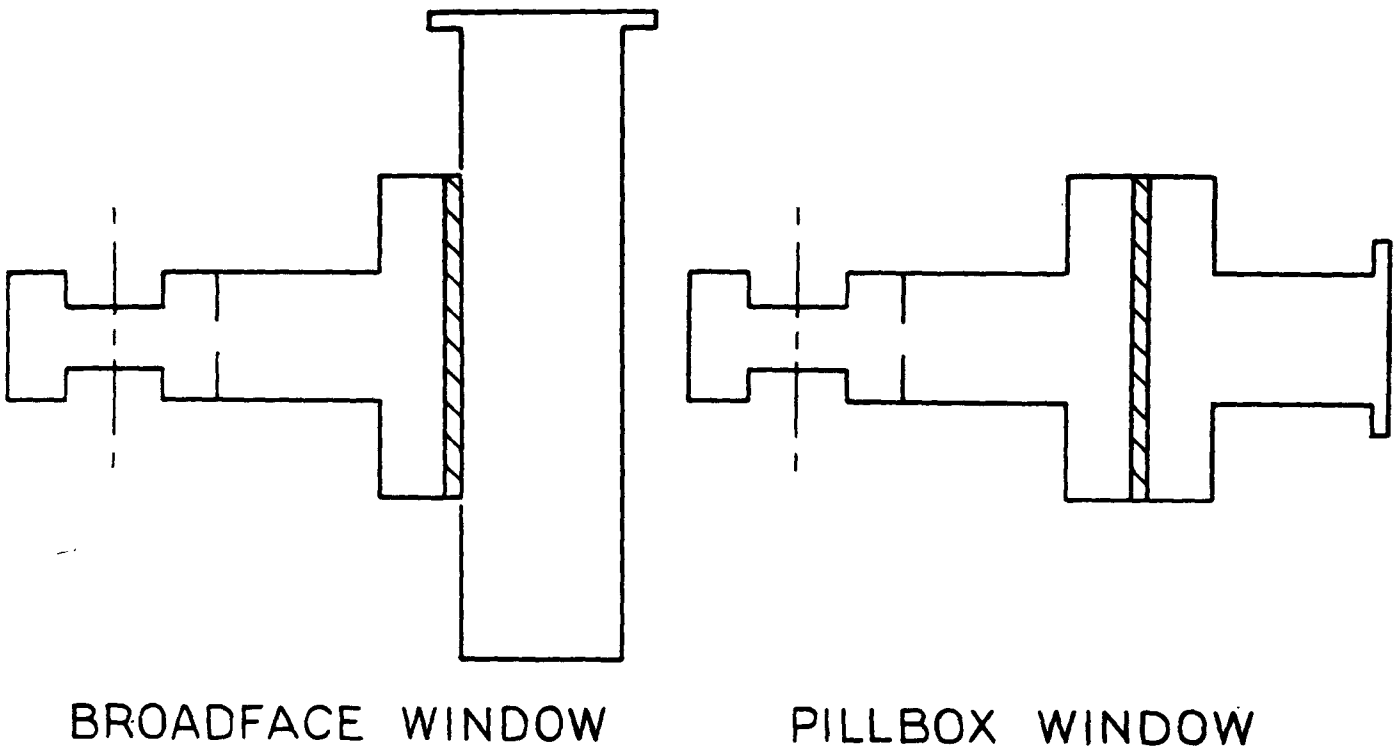

FIGURE 2 - Schematic Views of Window Confirgurations

± 5%, centered at 1320 Mc. This tube has been developed by Litton Industries under subcontract from RCA for the Tradex L-band transmitter. The work has been under the technical guidance of the Army Ordnance Missile Center and is sponsored by the Advanced Research Projects Agency.

The extremely high average power of this tube at a comparatively low peak power suggests that the window problem will be an average power problem. This means that its capability will be limited by thermal stresses. The susceptibility of ceramic materials to thermal stress and thermal shock failure is one of the main factors limiting their utility. The thermal shock problem can be controlled with proper transient schedules and is therefore not a fundamental problem. At these large duty cycles one can also ignore thermal shocks from impulse heating. Thermal stresses are however in general unavoidable but they have to be reduced to the smallest possible value. This can be done by proper choice of window materials, window configurations and cooling methods.

Heat is generated in microwave windows by two causes: dielectric losses and electron bombardment. The portion of the dielectric loss which is due to the RF fields which are necessary to transmit power through the window is unavoidable and can only be controlled by selection of the proper RF-mode. In most practical applications however, window performance is limited by parasitic or anamolous effects like heating due to unnecessary RF fields and electron bombardment.

The two window configurations which we have investigated so far are shown in Figure 2. On the left side is a schematic view of what we call the broadface window and on the right we show a pillbox type window. As window materials we use alumina and beryllia ceramics manufactured by Wesgo and Coors. Figure 3 shows a broadface window on an actual tube, Figure 4 a pillbox type window section ready for testing on the ring resonator.

So far the broadface window has shown the better performance on operating tubes. Full power operation of the L-3401 with 300 kW of average power through the window has been achieved with the broadface window. The development of the pillbox type window has been started as a backup program and so far excellent results have been achieved in the ring resonator but we have not been able to repeat this performance on operating tubes.

THERMAL STRESS ANALYSIS - Thermal stresses which are the limiting factor for high average power windows are caused by nonuniform temperature distributions. Nonuniform temperature distributions are due to nonuniform heating and to heat conduction. There are two problems to solve. First, one has to find for a given distribution of heat sources the corresponding temperature distribution and then one has to find from this temperature distribution the corresponding thermal stress distribution, specifically the point of maximum tensile stress. The maximum tensile strength is the fracture controlling quantity in ceramic materials.

The temperature distribution as a function of the heating is in the

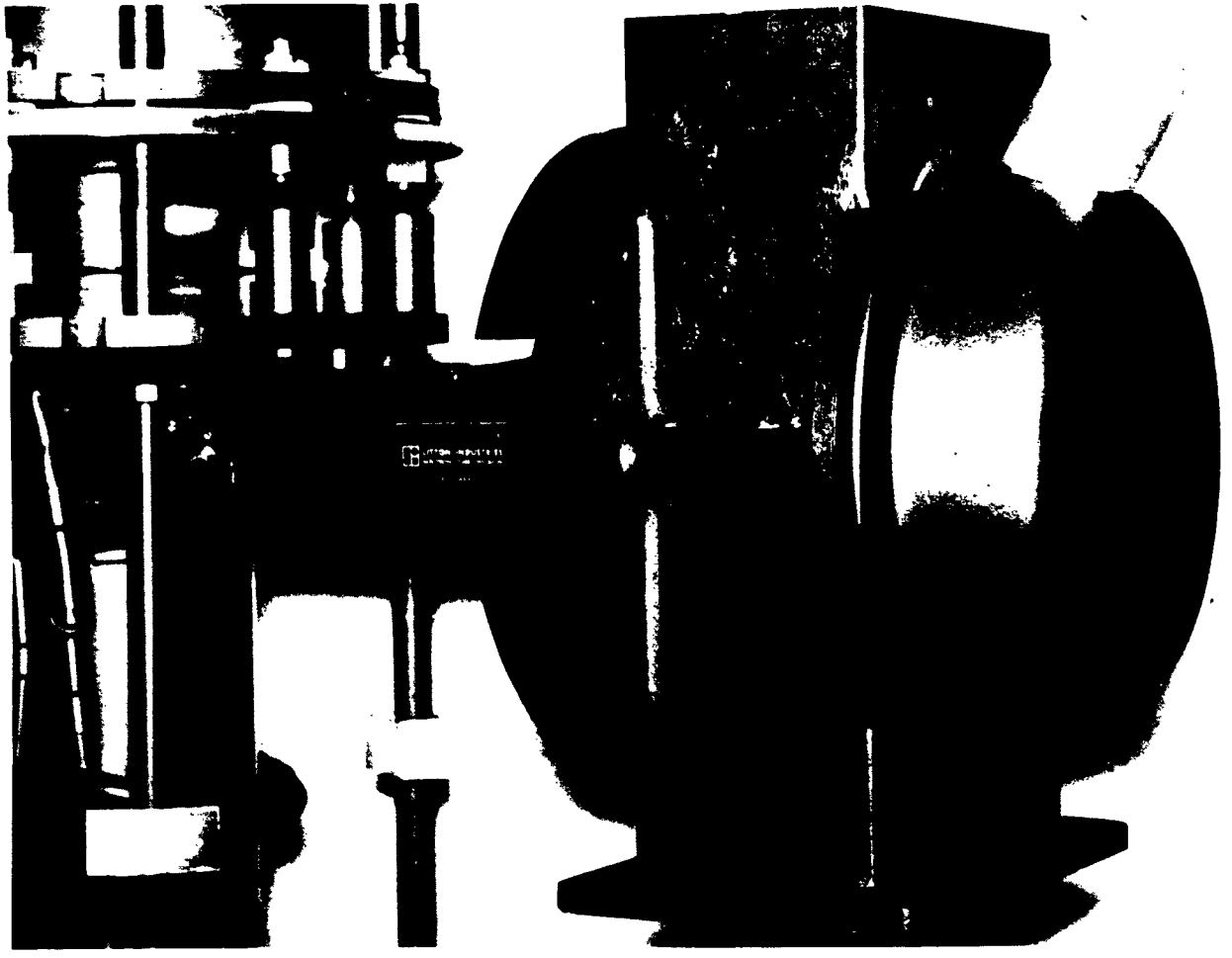

FIGURE 3 - Broadface Window

general case described by a differential equation which is of the form of a Poisson equation. The driving term of the equation is a function of the heat which is generated minus the power which is taken away by cooling. An analytical solution of this problem is difficult even for simple driving functions and it is virtually impossible to find an analytic solution for heating produced by the RF-mode patterns. We therefore, use an analog technique to solve the temperature distribution problem.

In the analog method a physical problem is solved by solving an analog problem which is described by the same mathematical formulism but for which the results can be easily measured. The solution of the problem appears therefore always as a physical magnitude. The accuracy of the method depends on the accuracy of the measurement and the tolerance of the analog. The analog technique which we use is a resistance network analog which, compared with other analog techniques, has the advantage of high accuracy and of expediency in setting up a problem.

As an example which demonstrates the method, we take the commonly encountered problem of the temperature distribution in a ceramic disc due to the dielectric loss of the TE_{11} mode. It is assumed that the disc is cooled at the edge only. Figure 5 shows the set-up of this problem on a resistance network analog. The problem is considered two dimensional and the set-up shows only a quarter of the disc because of the symmetry of the problem. The boundary of the disc is kept at a constant potential corresponding to a constant temperature and the lines which are connected to the inside of the disc feed in currents which are simulating the driving terms of the differential equation. In our case the driving term is given by the heat which is generated by the TE_{11} mode. Figure 6 shows a schematic picture of the power density distribution and it gives the formula which is used to compute it. Figure 7 shows the solution, namely the temperature distribution as a function of radius at two different planes. One is the plane of maximum electric field, the other is a plane rotated by 90^{o}.

This method can and has been applied to much more complicated driving functions. It is especially useful for evaluation of air cooling patterns. As an example it can be used to find a thermal stress free cooling arrangement.

After one has found the temperature distribution one has to find the corresponding stress and strain. The usual procedure is to compute the strain due to the thermal expansion and then use Hook's law to find the stress.

The thermal stress at any given point consists of [5]: (1) a uniform tension or compression in the plane of the disc which entirely suppresses thermal expansion; and, (2) a stress produced by body forces in radial direction together with normal edge forces.

For the example of the TE_{11} mode one can approximate the solution by assuming that the temperature distribution is axially symmetric. For this case

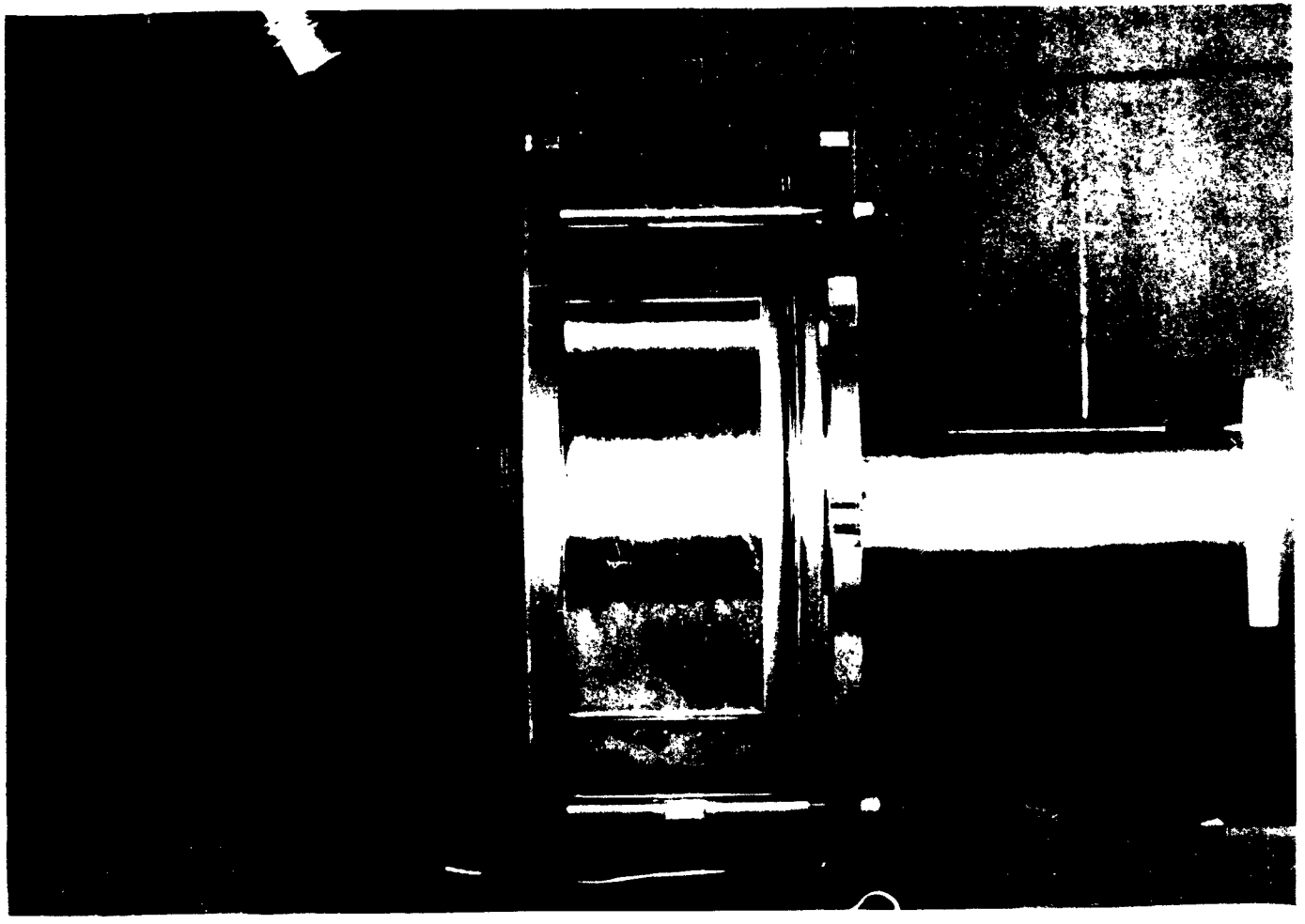

FIGURE 4 - Pillbox-Type Window

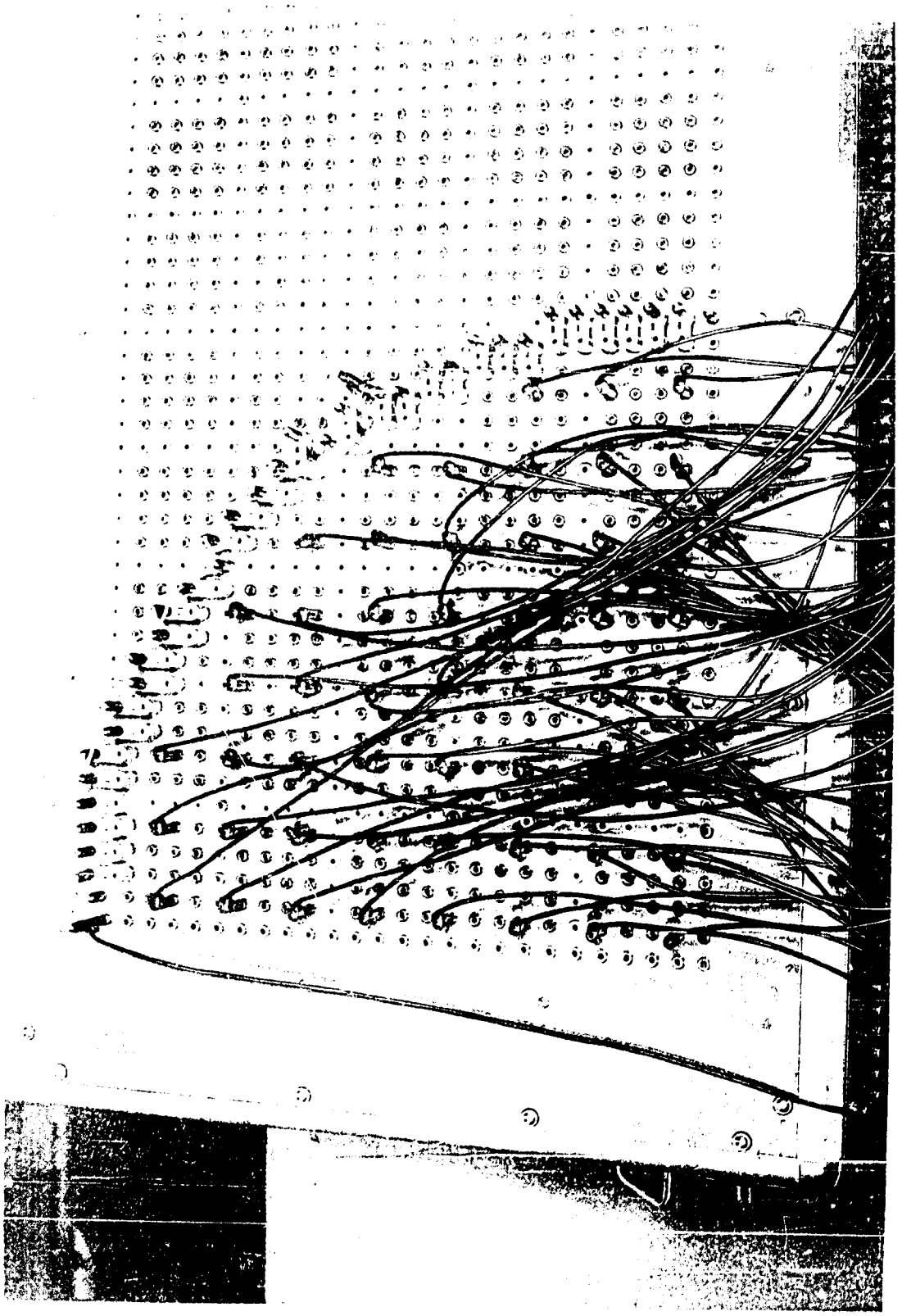

FIGURE 5 - Problem on Resistance Network Analog

the thermal stress is given by the following expression:

$$\sigma_r = \alpha E \left(\frac{1}{b^2} \int_o^b Trdr - \frac{1}{r^2} \int_o^r Trdr \right) \tag{1}$$

$$\sigma_\theta = \alpha E \left(- T + \frac{1}{b^2} \int_o^b Trdr + \frac{1}{r^2} \int_o^r Trdr \right) \tag{2}$$

where σ_r and σ_θ are stresses in the r and θ direction, α is the thermal expansion coefficient, E the modulus of elasticity, b is the outside radius of the disc and T the temperature. Using the results of Figure 7 and equations (1) and (2) we find that the maximum stress in this case is a tangential stress at the outer boundary of the disc in the plane of maximum electric field. Its numerical value is given approximately by:

$$\sigma_\theta \Big|_{r=b} \approx \frac{\alpha E T_M}{2} \tag{3}$$

T_M is the maximum temperature at the center of the disc which depends on the loss factor of the material, its thermal conductivity and the power flow through the window.

The technique which has been demonstrated here for the simple TE_{11} mode configuration can be applied to any desired mode combined with any desired cooling arrangement. The results which one gets for the maximum stress will however always involve the same material constants multiplied by different form factors. It appears therefore advantageous to lump all these constants together in a figure of merit. The figure of merit which is proposed is:

$$F_W = S \times F_T \times F_R$$

where:

S = Form factor

F_T = Thermal gradient factor = $\frac{K}{\tan \delta}$

F_R = Thermal stress resistance = $\frac{\sigma_{max\ R}}{\alpha E}$

S is a form factor which depends on the mode pattern and the cooling method. F_T, the thermal gradient factor, depends on the thermal conductivity K and the

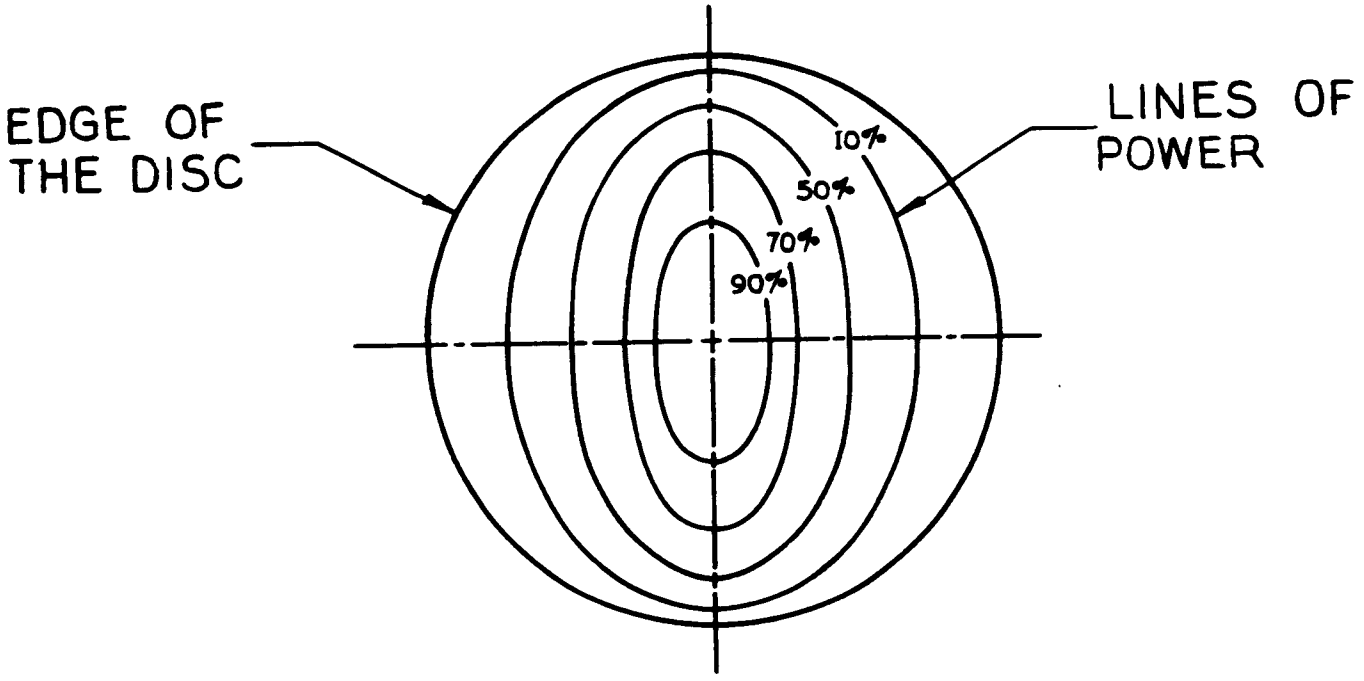

$$P_L = f(r,\phi)$$
$$= \frac{1}{8}\frac{\sigma}{\omega}\left(j\frac{nf}{f_c}\right)^2 E_o^2\left[J_o^2(k_c r) + J_2^2(k_c r) - 2J_o(k_c r)\,J_2(k_c r)\cos 2\phi\right]$$

FIGURE 6 - Power Dissipation of TE_{11} Mode

loss tangent. It is a measure for the amount of gradient which is developed for a certain heat generation. F_R is the thermal stress resistance it depends on the maximum tensile strength $_{max}$ the modulus of rupture R, the thermal expansion coefficient and the modulus of elasticity E. It is a measure for the temperature gradient which the material can stand before rupture. This figure of merit has the dimension cal/cm sec. It varies strongly with temperature due to the temperature dependence of the physical constants in its definition. Based on published data we compute the following figure of merits normalized by the form factor and the modulus of rupture.

Material	AL-300(Wesgo)	AL-995(Wesgo)	Bd-98(Coors)
$\frac{FW}{S \times R}$ (cal/cm sec)	18.3	171	93.2

Based on this data it appears that 99.5% pure Alumina is the best window material at room temperature for high average power windows mainly due to its low dielectric loss.

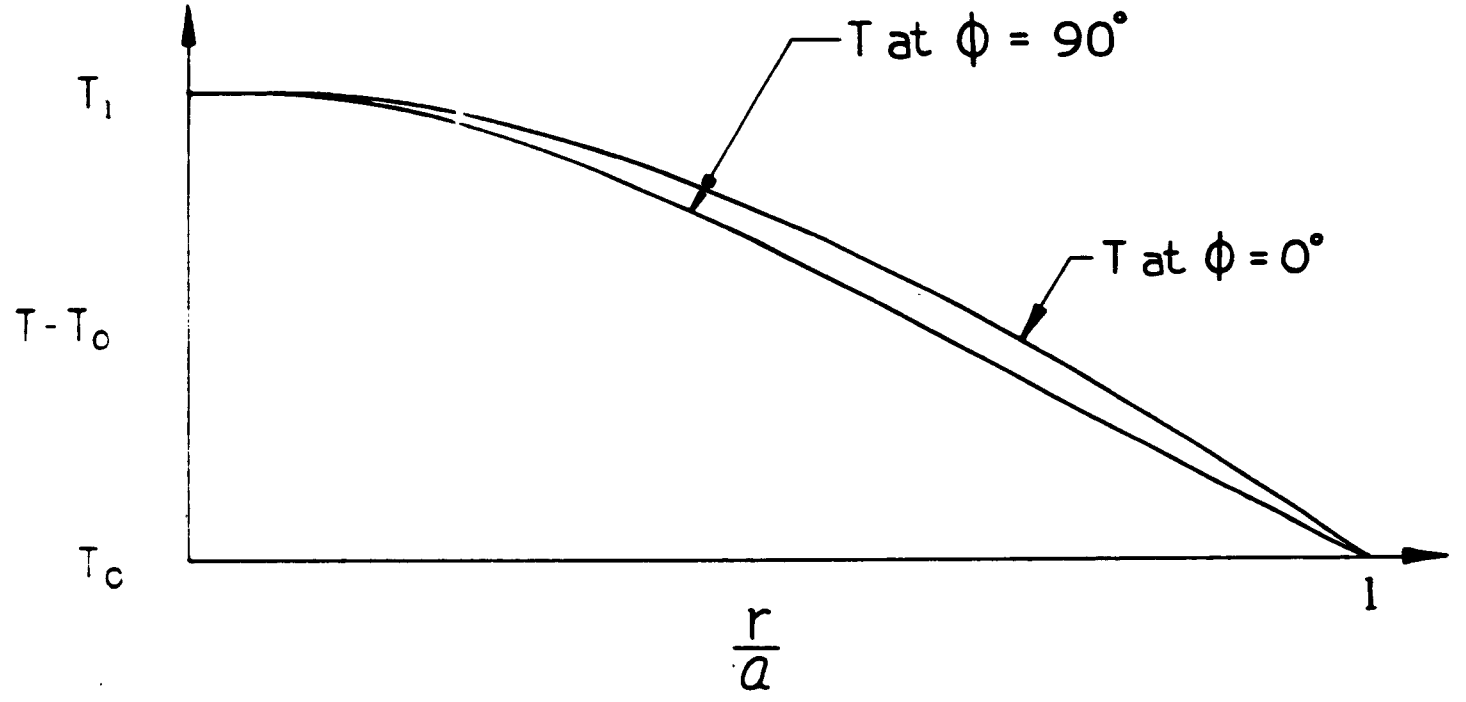

FIGURE 7 - Temperature Distribution in TE_{11} Mode Window With Edge Cooling

REFERENCES

1. C. Pappas : High Average Power Microwave Window Study at L-Band. Part II RCA September 1962 in this volume.

2. G. Liebmann: "Precise Solution of Partial Differential Equations by Resistance Networks"; Nature, vol. 164, pp 149-150; July 1949.

3. J.R.Hechtel: "Ein Widerstandsnetzwerk zur Loesung der Poissonschen Gleichung;" Die Telefunken-Roehre; pp 38-46; February 1955.

4. J.R.Hechtel: J.A.Seeger: "Accuracy and Limitations of the Resistor Network used for Solving Laplace's and Poisson's Equations"; Proc. IRE, pp 933-940; May 1961.

5. S.Timoshenko: "Theory of Elasticity"; McGraw-Hill Book Company 1934.

HIGH AVERAGE POWER MICROWAVE WINDOW STUDY AT L-BAND - PART II

By

C. Pappas

Radio Corporation of America

INTRODUCTION - Before discussing the material in this paper it is necessary to point out that this paper is Part II of an overall paper. Part I is being presented by the Electron Tube Division of Litton Industries and covers the theoretical requirements and experimental techniques[1] for the design of the windows discussed herein. Part II, which is this paper, covers the evaluation of the windows in an RCA resonant ring at Moorestown, New Jersey. For purposes of orientation and in order to preserve some continuity between Part I and Part II of this paper there is presented a brief review of Part I. Those who desire a more complete treatment of the theoretical requirements should refer to Part I. The end-product of this overall study program is the development of a microwave window for the L-3401 klystron[2] which is used in the TRADEX L-band transmitter developed under contract DA-36-034-ORD3063RD and sponsored by ARPA. Finally sufficient material is presented herein on the resonant ring and the related driving transmitter to permit some understanding of the test set-up and interpretation of the test results. Sufficient theory on the design and operation of resonant rings exists in technical literature and as such no material is presented on this item.

SUMMARY - The objective of the overall study program is the development of a microwave window for a 5 MW, 300 KW average power L-band (1320 ± 5% Mc) klystron[2] for TRADEX. The overall study program is divided into two parts. Part I discusses the theory, and Part II is the evaluation of the windows. As previously noted in the Introduction of this paper only the evaluation of the windows in a resonant ring[3] is presented in this part of the paper. Briefly summarized two windows have been evaluated to date. Window #1 is a pillbox design incorporating a 5/16 inch thick Wesgo AL-300 Alumina window with peripheral water cooling. This device was tested to 300 KW average power in an air-to-air environment and performed well. Analysis of this window after the test indicated that rounding of the flange corners may be helpful in eliminating arcing; and this device has the capability of handling large average power. The brazing techniques and the cylindrical configuration appear to be sound. Performance with respect to multipactor, thermal shock, etc. remain to be determined. Window #2 is a dual broadface design incorporating a vacuum section between the windows. One window is a 1/4 inch thick Wesgo AL-300 Alumina disc and the other is a 1/4 inch thick Coors BD-96 Beryllia disc. The alumina window in this device cracked at an average power of 204 KW, whereas the Beryllia window was sound after the test. Further tests on devices similar in configuration or parts thereof to the dual broadface assembly are necessary before meaningful results can be derived from this particular test.

REVIEW OF THEORETICAL REQUIREMENTS AND EXPERIMENTAL TECHNIQUES (PART I) - One of the major problems in extending the art of high power klystrons to higher power levels is the limited power handling capacity of microwave windows. Unfortunately, the theoretical understanding is not adequate for a comparative evaluation of different window designs and experimental techniques have to be employed. The large cost of evaluating window performance on full power tubes puts great emphasis on techniques which allow evaluation of window designs under simulated conditions. This paper discusses approaches which have been used in the evaluation of different window designs for a 5 MW peak, 300 KW average power L-band klystron. Because of the comparatively low peak power the window problem in this case is due mainly to thermal stresses caused by excessive and non-uniform dissipation of RF energy. A short review of the basic design concepts for high average power windows and a summary of their theoretically predicted behavior will be presented first. Next an analog technique is discussed which has been used to solve the steady state temperature distribution for different window modes. This technique uses a resistance network analog to solve the heat flow equation which in this case has the form of a Poisson equation.

Two devices, a dual broadface window and a pillbox window, have been designed and fabricated. The performance of these windows is evaluated in a high power resonant ring at RCA and the results discussed in Part II of this paper.

RESULTS OF WINDOW TESTS AT RCA - The results of the window tests at RCA together with related material now follows:

PILLBOX WINDOW TESTING - A cross section of the pillbox window design is shown in Figure 1. It consists basically of a large cylinder mounted to two large flat stainless steel flanges. The alumina window (Wesgo AL-300) is 5/16 inch thick and is brazed to the cylinder. The outside of the cylinder has a peripheral water cooling jacket made of copper. Figures 2 and 3 show this unit mounted in the resonant ring. Some test data taken on this window is given in Table 1.

TABLE I

Alumina Pillbox Window No. 1

F	PRF	PW		Ring RF AVG POWER	ΔT	Waveguide Pressure (g)	Q	Hotspot Temp.
MC	pps	usec	Du	KW	°C	#/in^2	GPM	°C
1276	1500	40	0.06	300	2.0	15	1.0	118
1350	1500	40	0.06	300	3.25	15	1.0	124

Test data as a function of time is plotted in Figures 4 and 5. From Figure 4 it can be seen that the window operated at 290 KW or above for about two hours at 1276 MC. From Figure 5 it is seen that this same window operated at 290 KW or above for about three hours at 1350 MC. Operation was in the resonant ring pressurized with air on both sides of the window. One interruption believed due to the transmitter occurred during this latter operation. Maximum observed hotspots were 106°C on the waveguide adaptor pieces and 124°C at the junction of the stainless steel flange and the square mounting flange. The overall operation of this device was good. The alumina window did not break after five hours of operation at 5 MW and 300 KW. However, one small burn mark (Figure 6) close to the window center and the size of a pin head

was observed, and appeared to be the start of a puncture. Some arcing occurred along the periphery and is shown in Figure 7. The other side of the window is clean and is shown in Figure 8. The RF was incident on this side of the window.

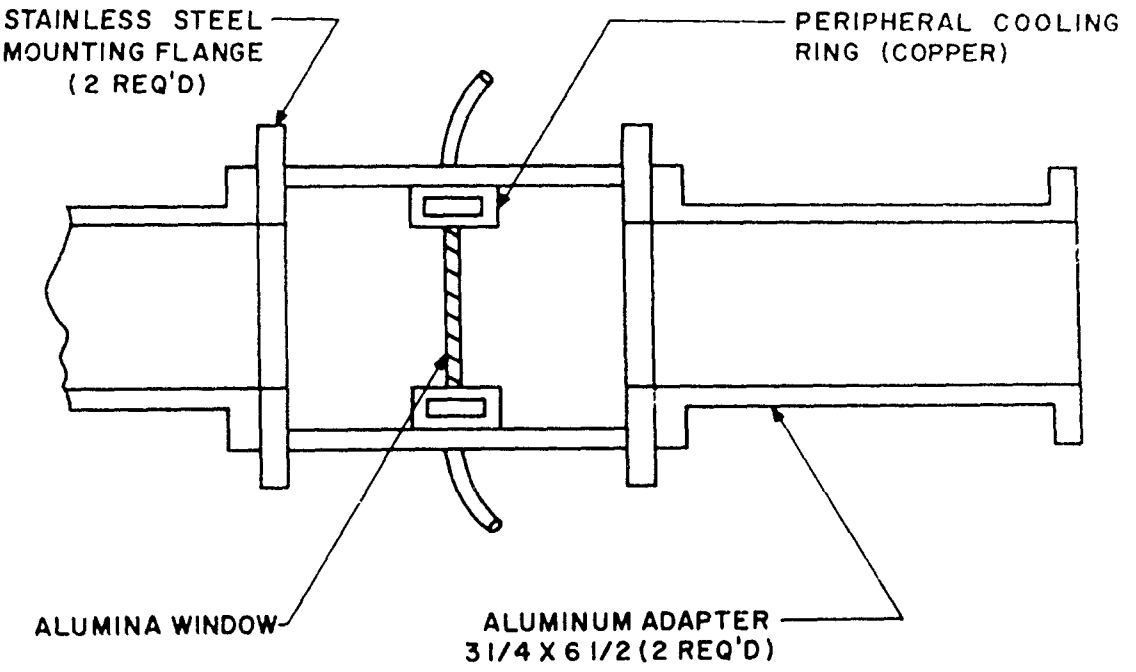

Figure 1 - Cross Section of Alumina Pillbox Window #1 Tested at RCA

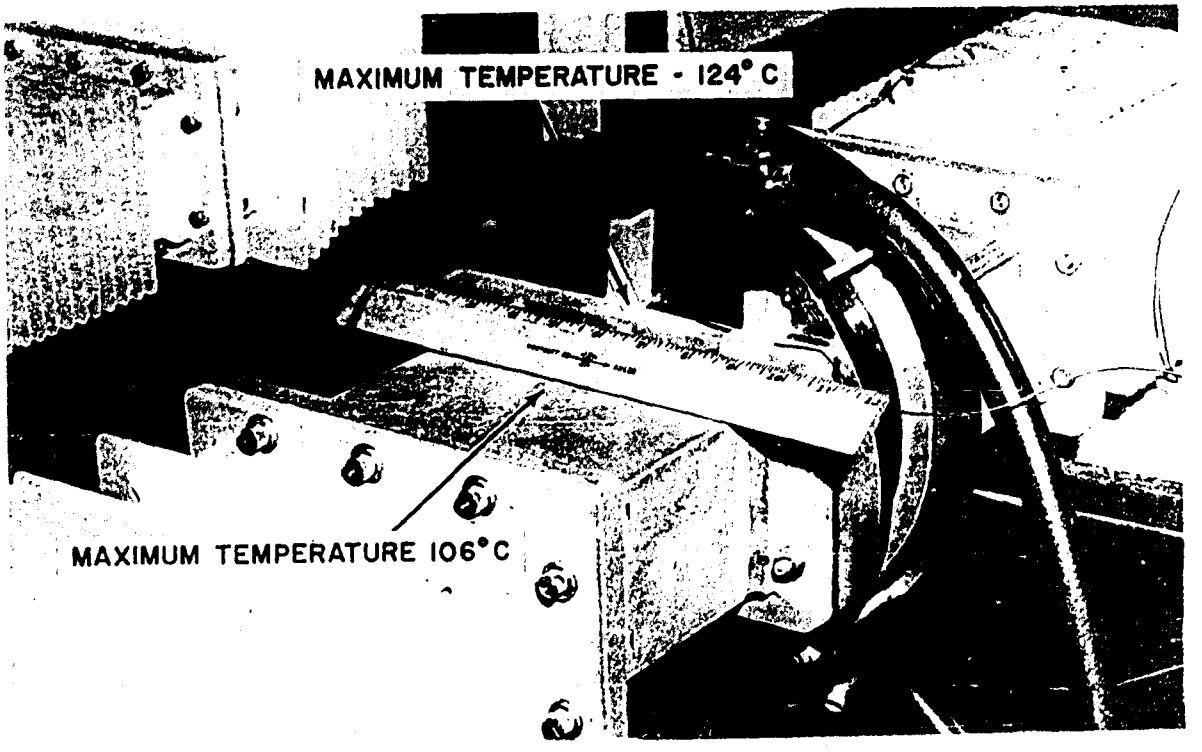

Figure 2 - Alumina Pillbox Window #1

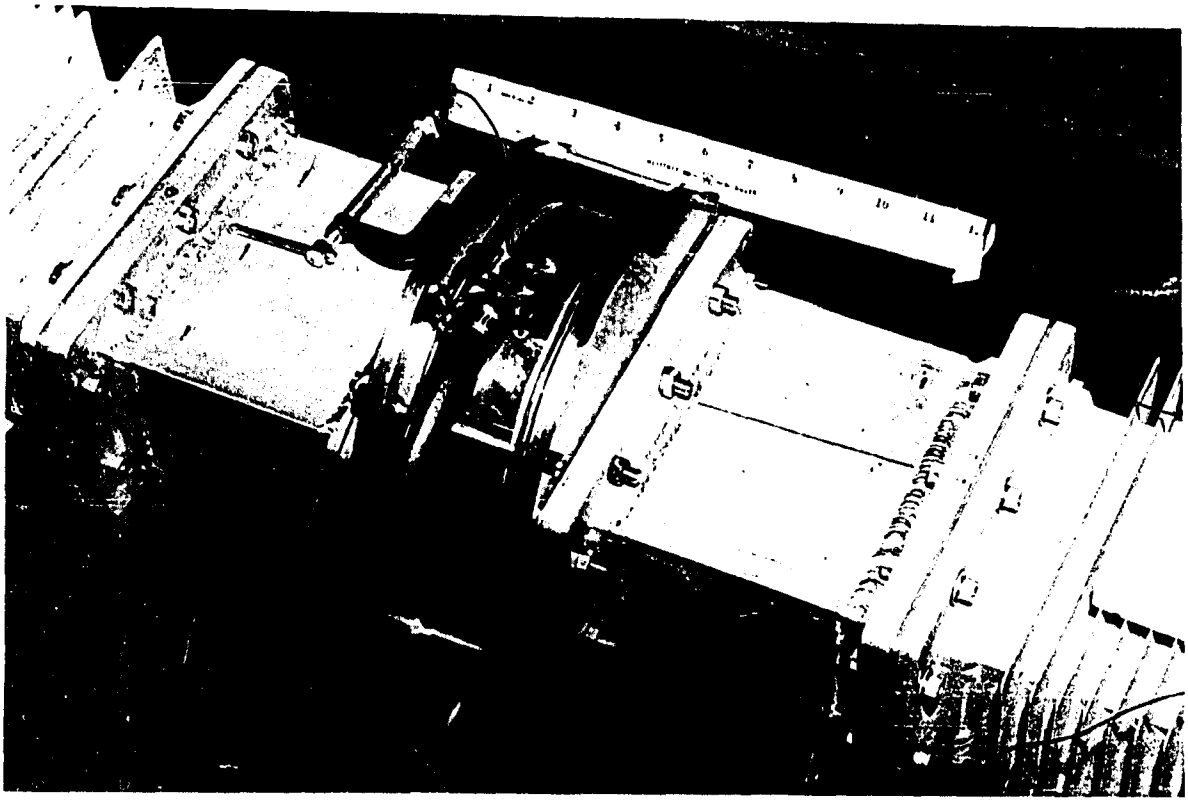

Figure 3 - Alumina Pillbox Window #1

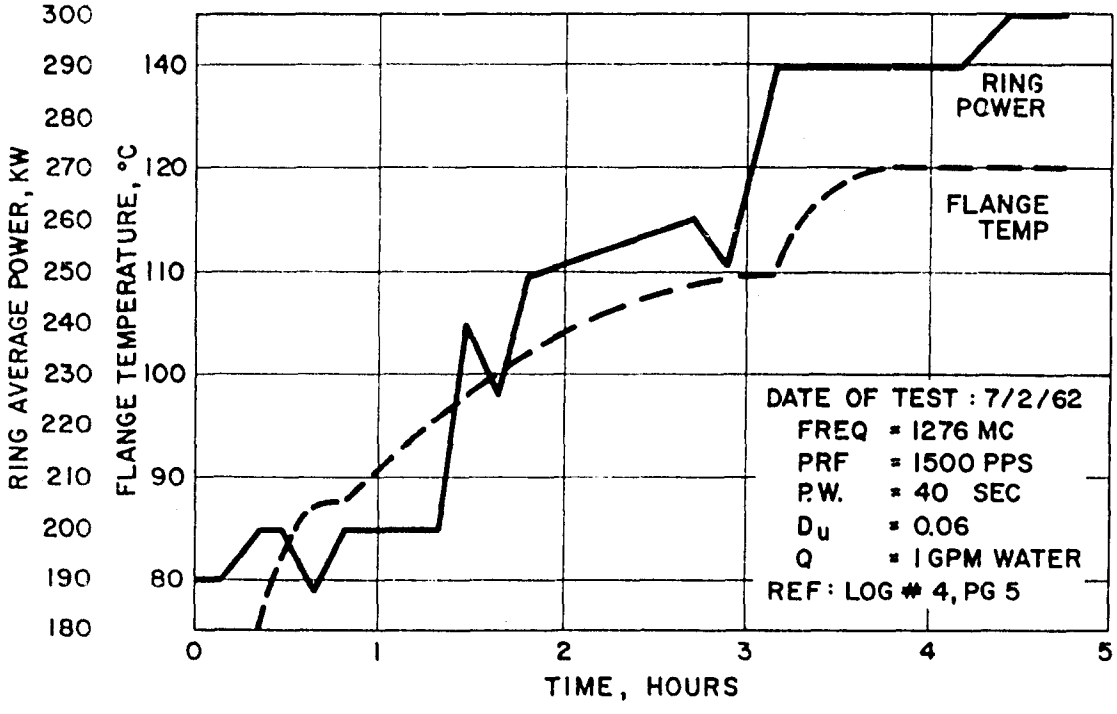

Figure 4 - Resonant Ring Testing of Litton L-3401 Klystron Window (Alumina Pillbox Window #1)

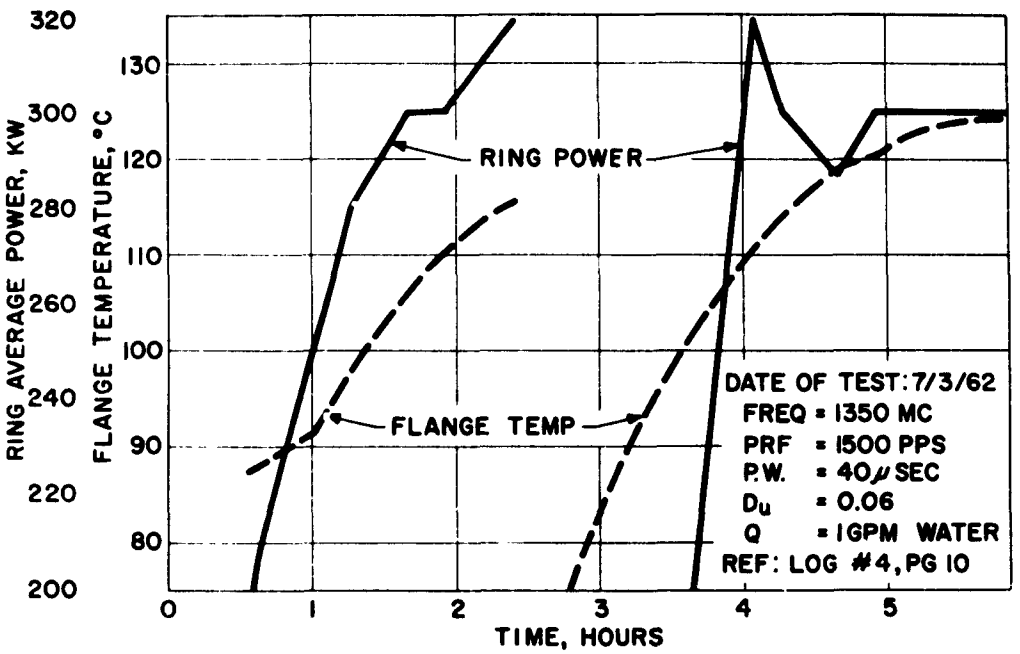

Figure 5 - Resonant Ring Testing of Litton L-3401 Klystron Window (Alumina Pillbox Window #1)

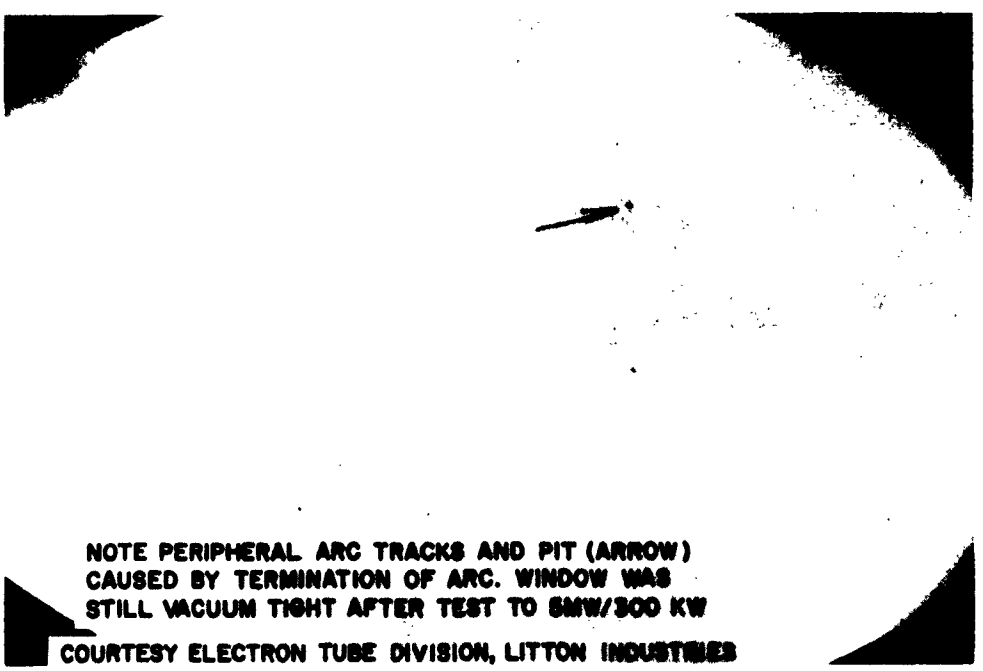

Figure 6 - Alumina Pillbox Window #1 Tested at RCA (5/16" WESGO AL-300)

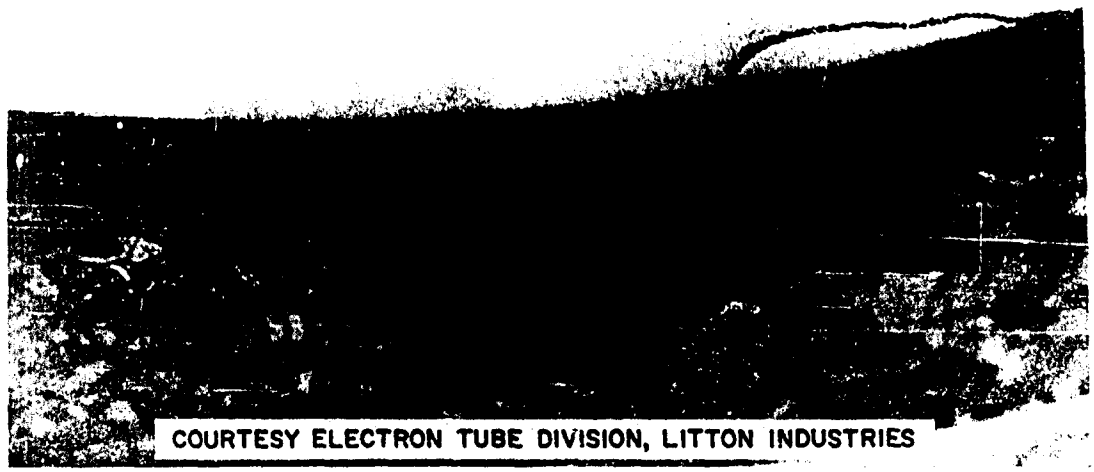

Figure 7 - Alumina Pillbox Window #1 Tested at RCA Showing Arc Pitting Along Periphery

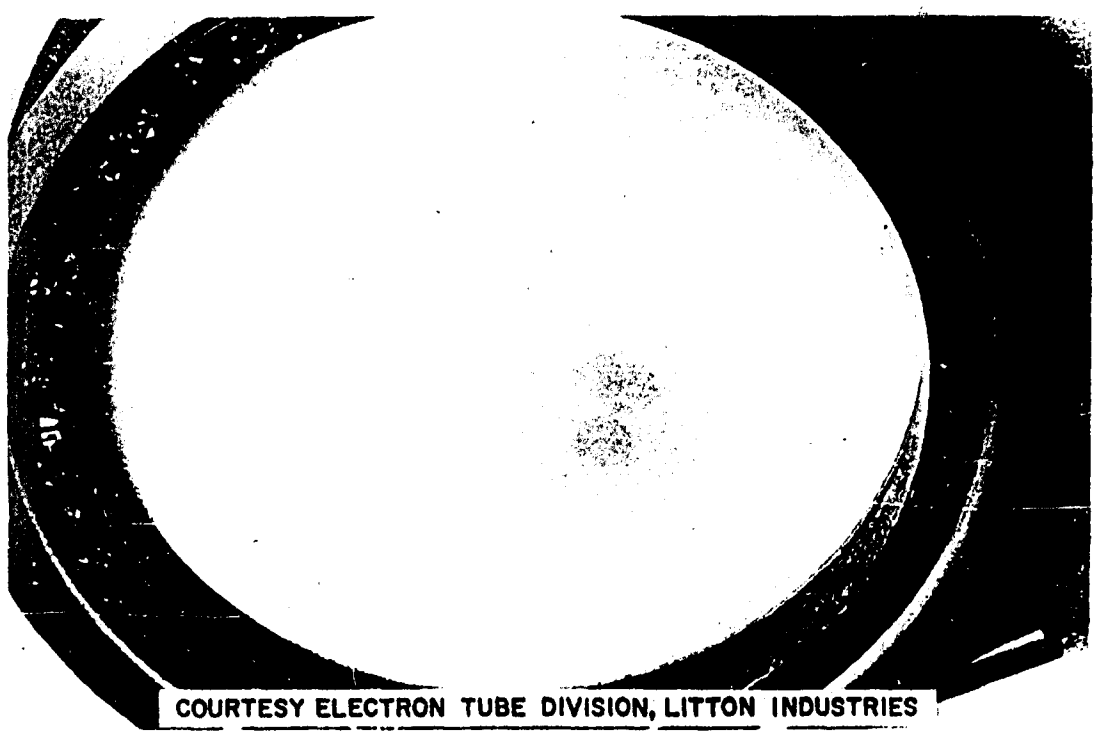

Figure 8 - Reverse Side of Alumina Pillbox Window #1. This side of Window is Clear (See Figures 6 and 7.)

BROADFACE WINDOW TESTING - The cross section of a dual broadface unit with a vacuum section is shown in Figure 9. It consists of an alumina window (Wesgo AL-300) and a beryllia window (Coors BD-96) connected by means of a vacuum section. A vac-ion connection is provided to monitor operation of the device. Both windows are 0.25 inch thick. Water cooling was provided for the window periphery only during the test of this unit. A photograph of the unit is shown in Figure 10. Test data taken on this window is given in Table II.

TABLE II

Dual Broadface Window Assembly Number 2

F	PRF	PW		Ring RF AVG POWER	ΔT	Waveguide Pressure (g)	Q	Hotspot Temp.
MC	pps	usec	Du	KW	°C	#/in^2	GPM	°C
1350	1500	40	0.06	150	1.0	20	3.0	116*

*Occurred at about 30° from vertical on weld flanges on both the Al and Be windows. The maximum recorded temperature was 143° on the Be window.

The broadface unit suffered a cracked alumina window at a power level of 204 KW average. Failure occurred as soon as this power level was reached. The Beryllia window suffered no visible damage. Total RF power operation of this tube prior to failure was about one hour at a power level of about 150 KW average. A plot of operation vs. time is given in Figure 11. A representation of the cracked window is given in Figure 12. Photographs 13, 14, and 15 show the failure in detail. Failure of the window was indicated by a sharp audible crack, inability to achieve high power in the ring thereafter and pegging of the vac-ion gauge.

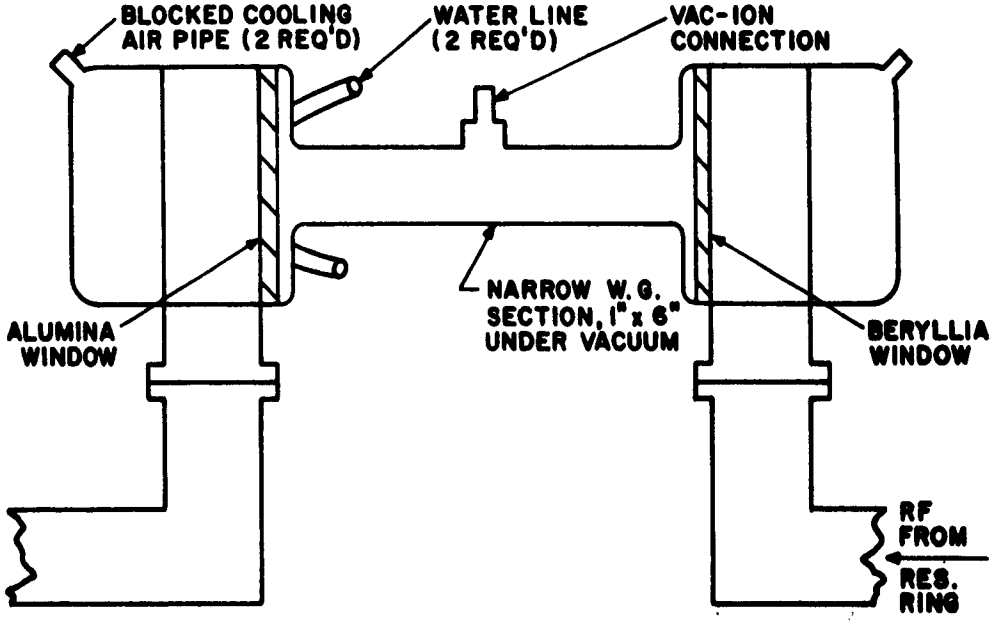

Figure 9 - Cross Section of Dual Broadface Window #2 Tested at RCA

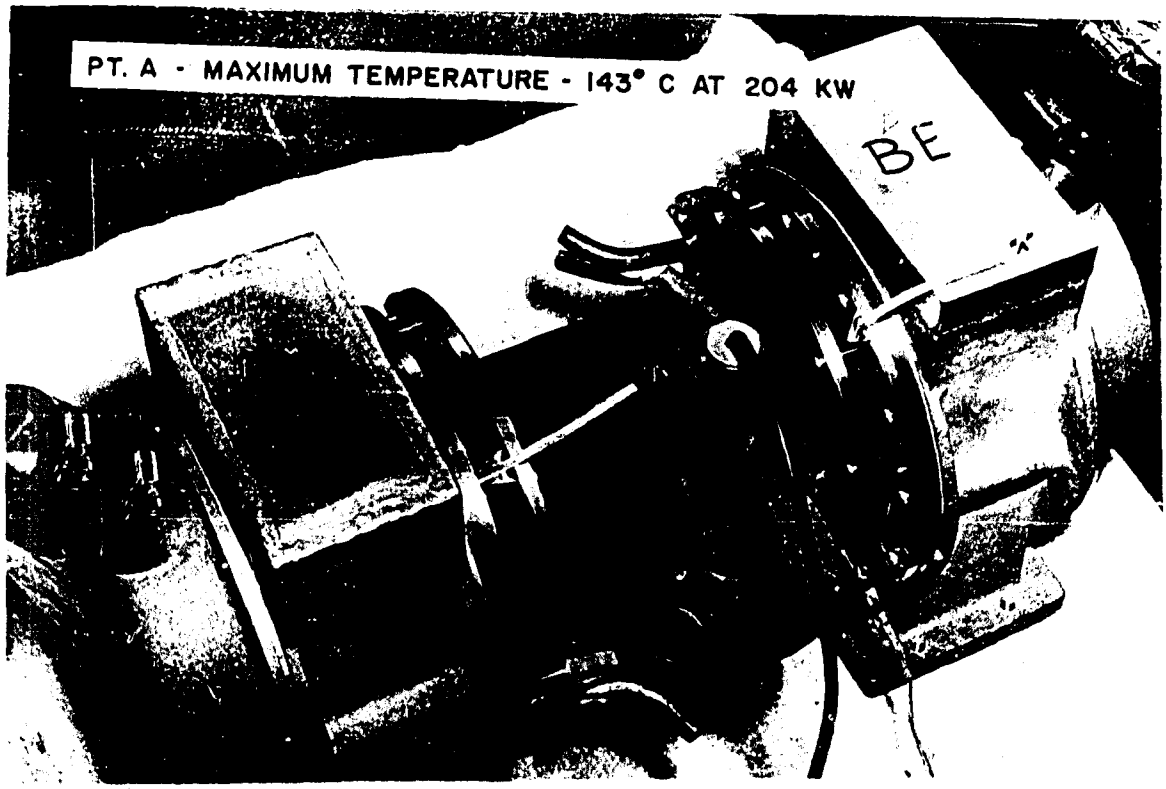

Figure 10 - Dual Broadface Window (Al and Be)

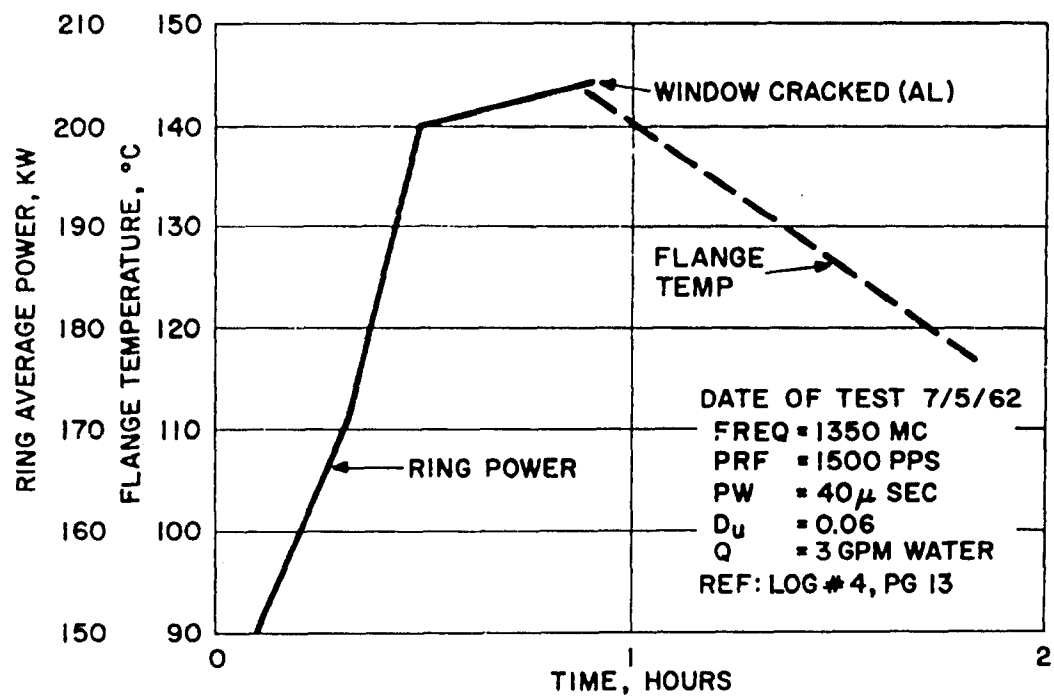

Figure 11 - Resonant Ring Testing Litton Dual Broadface Window (Al and Be) #2

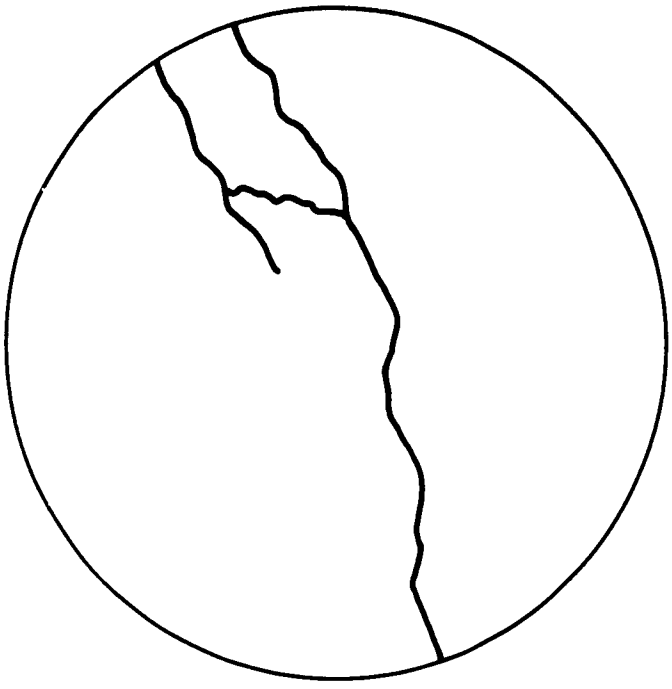

Figure 12 - Fracture Pattern of Broadface Window (Alumina, AL 300)

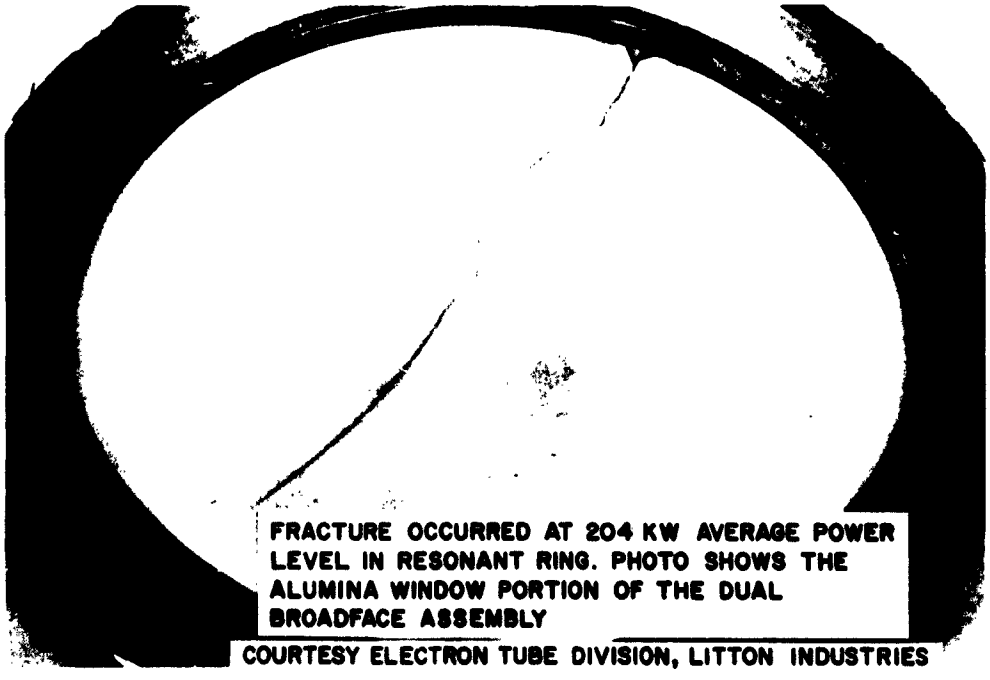

Figure 13 - Closeup View of the Alumina Broadface Window #2 Tested at RCA (1/4" WESGO AL-300)

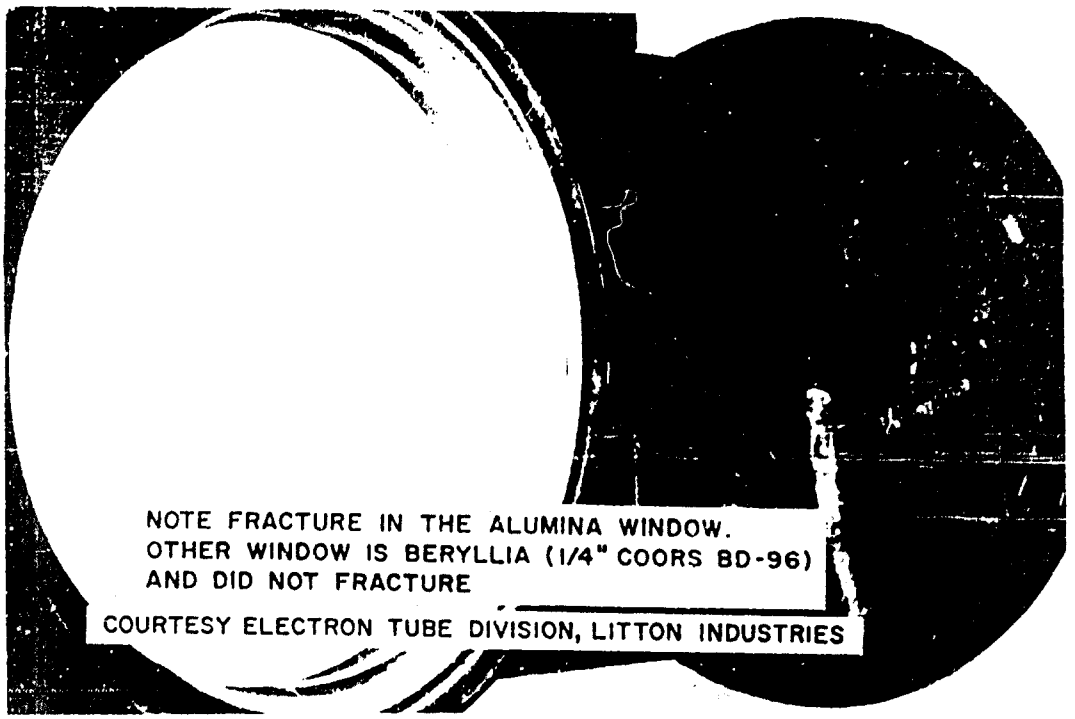

Figure 14 - View Showing Dual Broadface Window #2 Tested at RCA

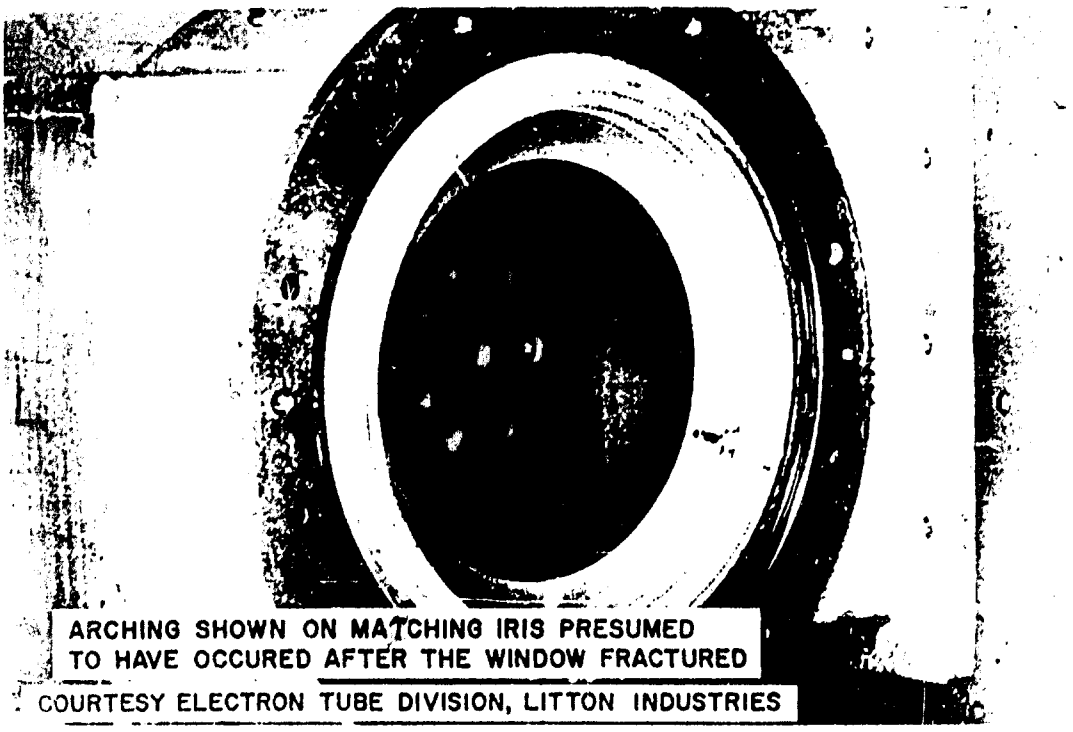

Figure 15 - Coupler Assembly for Mounting Alumina Broadface Window #2

L-BAND RESONANT RING DESCRIPTION - The resonant ring is designed to operate in the frequency band of 1320 ± 5% MC. Powerwise it is rated at 5 MW peak and 300 KW average at a 0.06 duty cycle. The nominal power gain is 20 with a rated input power of 0.25 MW peak and 15 KW average. A photograph of the unit is shown in Figure 16 and a block diagram is given in Figure 17.

The resonant ring is constructed primarily of a standard WR-650 aluminum waveguide. Epoxy resin bonded fins have been added to increase the pressure capability and to radiate the heat due to the normal waveguide attenuation. Predicted hotspot temperature is 82°, measured is 63°, for rigid waveguide at 320 KW average power. Parker seals are used at each flange to insure the pressure capability of the ring.

Using Figure 17, the operation of this ring is as follows. The transmitter output is through a ferrite isolator with a maximum insertion loss of 0.5 db. It is used to protect the transmitter klystron from long line effects and resonant ring tuning variations. The ring input is through a variable coupler A. This unit consists of three hybrid sections and variable waveguide bucket shorts. The output of the coupler section is to the resonant ring or to a matched high power dummy load (rated 17 KW average). The control of the variable coupler is remote and can vary the transmitter power from the dummy load into the ring section.

At each end of the ring are located variable tuners, B and C. These units are used as VSWR tuners to eliminate any reflections and insure a true power test on the system. The test area is adjustable and can accommodate units up to 15 feet in length with a minimum of assembly effort.

The control panel allows remote control of the VSWR tuners and the variable coupler network. It also provides meters for monitoring the transmitter forward and reverse power, the ring forward and reverse power, and the power coupled into the dummy load. Indicator dials provide a memory of the bucket short positions for ease of tuning.

With the use of calibrated coaxial pads, thermistor mount and power bridge, it is possible to measure the following:

Coupler #1 - Transmitter output forward or reverse power
Coupler #2 - Transmitter output from the isolator
Coupler #3 - Power into dummy load
Coupler #4 - Ring power forward or reverse
Coupler #5 - Ring power forward or reverse

Monitoring of the above powers completely defines the characteristics of the test facility. Figure 18 is a theoretical curve of ring power buildup as a function of coupling for a family of line losses.

A brief summary of typical units tested in the resonant ring at an RF pulse width of 40 microseconds and a PRF of 1500 pps follows:

a. Rotary joints at ring peak power of 2.8 MW, ring average power of 168 KW using air at 10 PSIG. The ring buildup was 16 - 22.

b. Waveguide (Finned)-(Rigid and Flexible) at ring peak power of 5.3 MW, and average power of 320 KW using air at 15 PSIG. The ring buildup was 24 - 26.

c. Ferrite Circulator at ring peak power of 2.5 MW, ring average power of 150 KW using air at 15 PSIG. The ring buildup was 10 - 12.

d. Klystron windows at ring peak power of 5.0 MW, ring average power of 300 KW using air at 15 PSIG. The ring buildup was 19 - 22.

TRANSMITTER - The transmitter for the L-band Resonant Ring uses a line-type modulator circuit with a GL-7890 hydrogen thyratron as a charging triode and a GL-7890 as the discharge tube. A block diagram is given in Figure 19. The final RF amplifier tube is an L-3486 klystron. The RF Exciter Unit uses an L-3465 magnetron. The transmitter has a nominal power output rating of 15 KW average and 250 KW peak at an RF duty cycle of 0.06. It is designed to operate at an RF pulse width of 40 microseconds and a PRF of 1500 pps. The transmitter operates in the frequency band of 1320 MC ± 5%. The transmitter feeds the L-band resonant ring via a ferrite isolator to protect the transmitter from high reflected power.

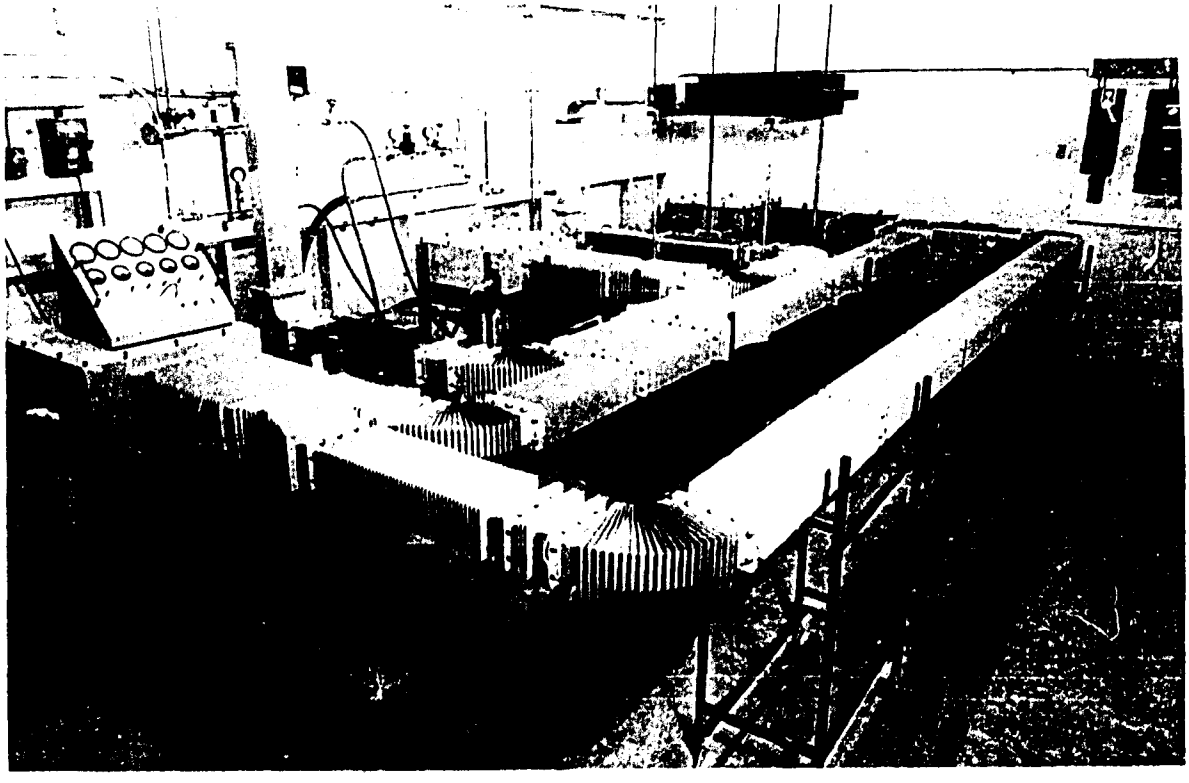

Figure 16 - RCA L-Band Resonant Ring

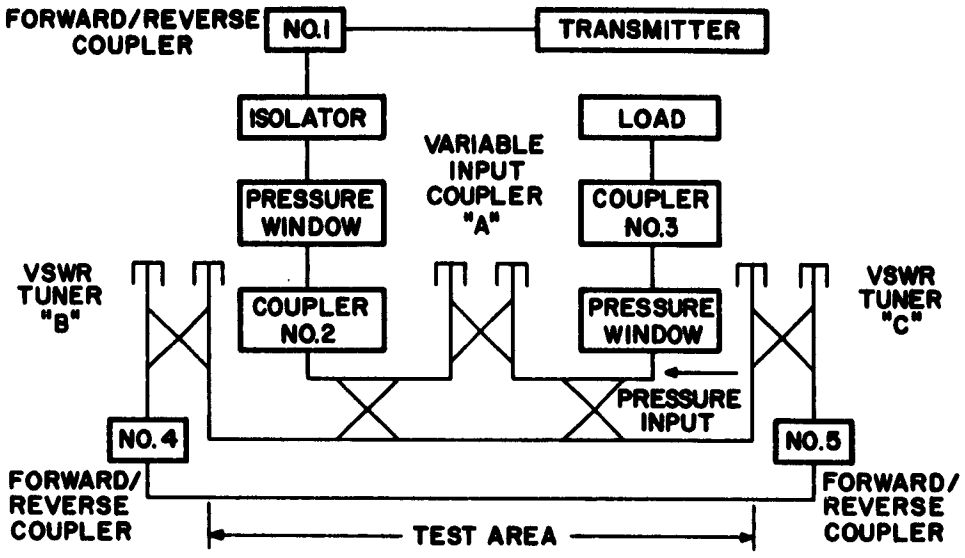

Figure 17 - Block Diagram of L-Band Resonant Ring

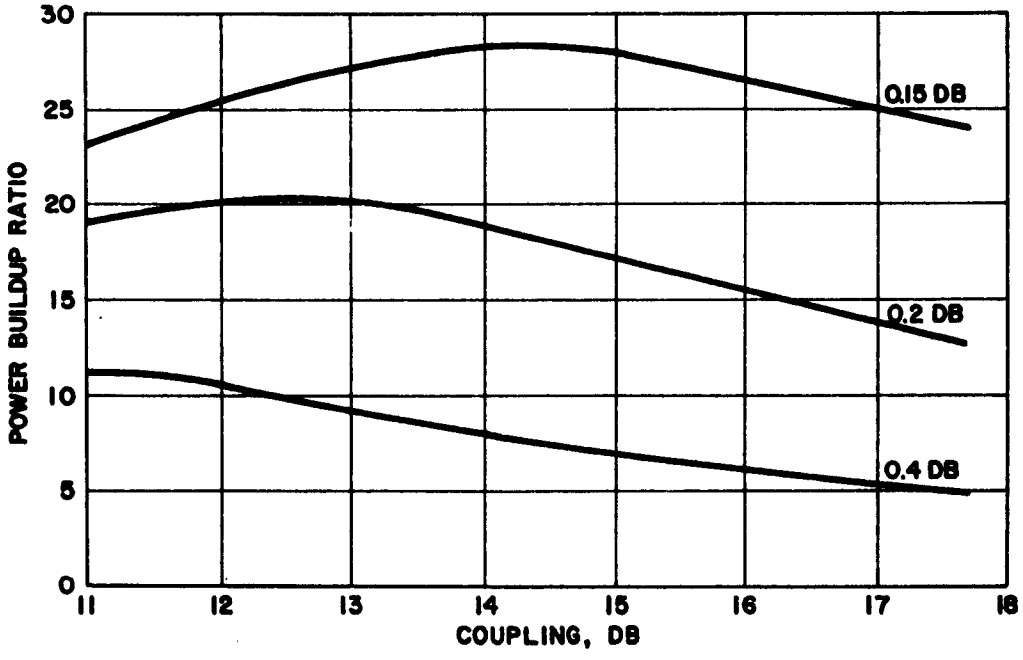

Figure 18 - Resonant Ring Power Buildup vs Coupling

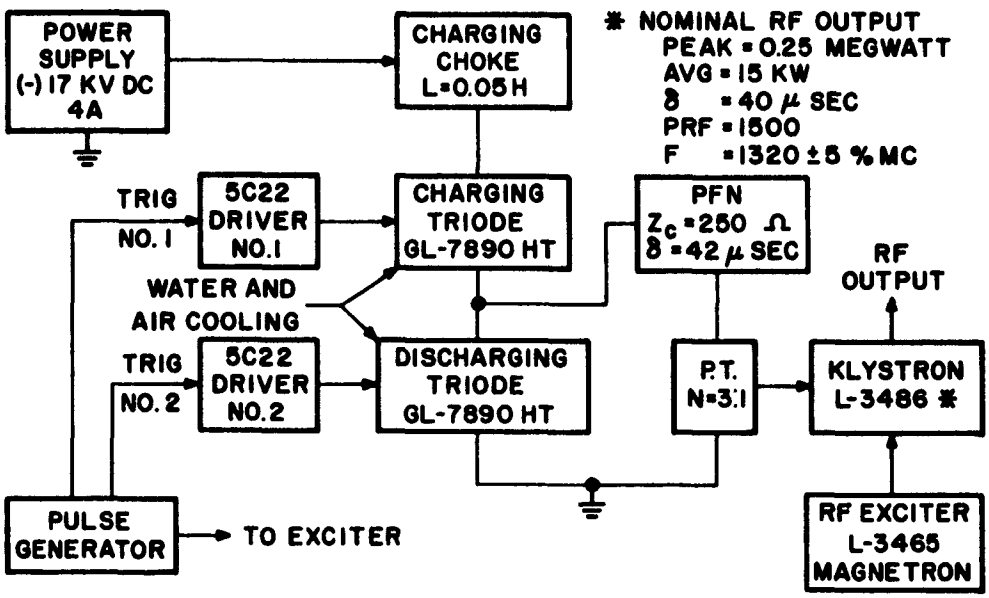

Figure 19 - Simplified Block Diagram of Transmitter for Resonant Ring

REFERENCES

1. A. J. Prommer, "High Average Power Microwave Window Study at L-band Part I", Electron Tube Division, Litton Industries, September, 1962.

2. The microwave windows described herein are a part of the TRADEX L-3401 Klystron R/D subcontract performed by Litton Industries. The TRADEX L-3401 Klystron was developed by Litton Industries for DEP, M&SR Division, Radio Corporation of America, under PO GX9-998030-0001-70-Q92 under the Department of the Army contract DA-36-034-ORD-3063RD under the technical guidance of the Army Ordnance Missile Center and sponsored by the Advanced Research Projects Agency.

3. The microwave window testing was performed under the Department of the Army Contract DS-36-034-ORD-3063RD, under the technical guidance of the Army Ordnance Missile Center and sponsored by the Advanced Research Projects Agency.

DUAL STAGE AMPLITRON FOR SUPER POWER

By

Curtis M. Hellenbrand

Raytheon Company

Introduction

About two years ago, RADC was interested in and sponsored a feasibility study program for the generation of one megawatt of average or CW rf power at X-band. Raytheon's technical approach toward this objective was the multi-stage Amplitron concept. Briefly stated, these were the considerations that led to the aforementioned recommendation.

The limiting factor on power output for X-band continuous-cathode, crossed-field devices is an anode consideration rather than a cathode consideration. Obtaining sufficient emission in continuous-cathode, crossed-field devices is rarely a limitation of these devices. The dissipation of the cathode back bombardment power is taken care of by the unique but proven cathode design of the proposed tube, permitting adequate cooling of the 2% thoriated tungsten cathode.

In generating large amounts of rf power in a device where anode dissipation from electron bombardment is the limiting factor, it is noted that the rf power which is generated inside the tube is a function of three factors: (1) area of that portion of the anode where electron bombardment occurs, (2) the dissipation density that can be applied to that area, and (3) the dc-to-rf energy conversion efficiency, η_e

These items are related in the formula:

$$\text{RF Power Generated} = \text{Anode Area} \times \text{Dissipation Density} \times \frac{\eta_e}{1 - \eta_e}$$

The rf power generated is not the same as the rf power output from the tube since there are circuit losses and cathode back bombardment losses which must be subtracted from the generated rf power. In general, these can be made low so that the output power presents most of the generated power.

Because the circuit efficiency, η_c and the back bombardment efficiency, η_b are so great, both being about 97% in this X-band design, it is immediately evident from the above equation that for a maximum obtainable electronic efficiency, η_e dissipation density and anode area are the only two factors left that make it possible to further increase the rf output power. Again, having obtained a maximum dissipation density, then the only factor left is the anode area. The anode area now becomes the most important factor in the consideration for the generation of super power at X-band. This paper, however, will discuss only the first generation of the multi-stage

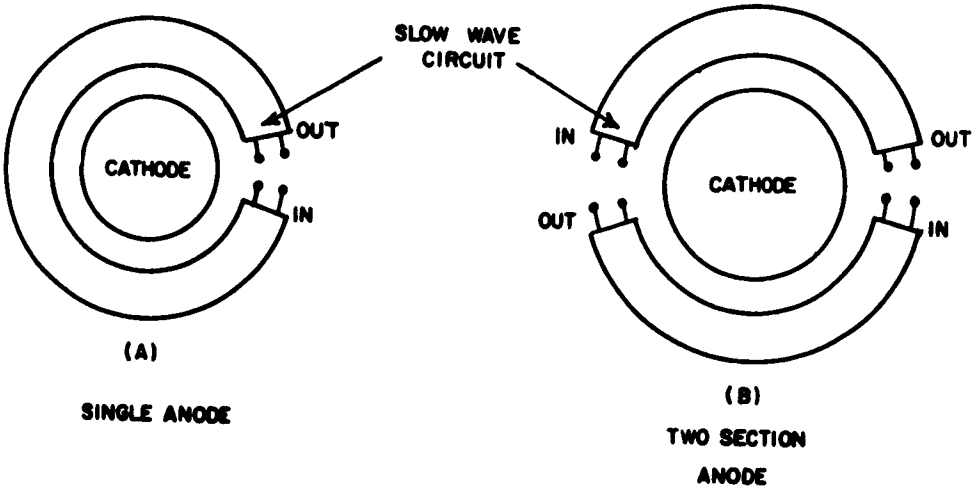

SIMPLE SCHEMATIC OF SINGLE
AND TWO SECTION AMPLITRON

FIGURE 1

concept, that is, the dual-stage Amplitron, which is presently company-funded at a moderate rate.

In the dual-stage Amplitron, the anode structure, consisting of two separate circuits, is placed concentrically around one common circular cathode of large dimensions so that the anode-cathode structure generally retains the simplicity of the conventional Amplitron structure. The connecting together of these circuits is done in such a way as to promote rf stability. This is accomplished by the use of a hybrid T junction in the Amplitron output arms and a hybrid T junction with differential phase shifters in the Amplitron input arms respectively.

Figure 1 represents schematically the structure of the conventional Amplitron. There is a cathode in the center surrounded by a two-terminal-pair network with the "in" and "out" terminals indicated. The properties of this device are such that there is rf gain in the "in" to "out" direction and neither gain nor significant loss in the "out" to "in" direction. Using the terminology of Figure 1, we may now portray the circuits of the dual-stage Amplitron by the schematic also shown in Figure 1. The interpretation of Figure 1 then is that we have two circuits which are identical in their characteristics, each having a gain in the "in" to "out" direction. They are of equal length and are arranged symmetrically around a large central cathode.

The construction of one of these circuits is shown in Figures 2 and 3. The structure is a strapped network of vanes similar to those used in the conventional Amplitron, and has a similar phase shift and impedance behavior as a function of frequency. The vanes are sufficiently long so that the ends may be covered over and the cavities, therefore, become short-circuited sections of waveguide. This arrangement makes it possible to connect the straps by means of a waveguide feed in which two of the vanes form the wall of the waveguides. A photograph of a two-section anode designed with this type of unit circuit is shown in Figure 4. This new structure has the advantage of much larger mechanical dimensions, and is amenable to very effective cooling. Its electrical characteristics result in a very clean passband, that is, a passband characteristic free from interfering resonances, end cavity modes, backwall modes, and interference common to other circuits. Because the location of the electromagnetic field is well defined, it is possible to obtain valid analytic expressions for the phase and characteristic impedance functions.

Figure 5 indicates schematically how the two sections of Figure 1 are coupled together to a common input and output. This schematic of Figure 5 is an example of what is known in network theory as a series connection of two-terminal-pair network.

It is, of course, important that the line connections shown between the waveguide connection and the network connections themselves be of equal length and preferably, but not necessarily, have the same characteristic impedance as the network sections.

Because the unit rf circuit and the interconnection of the circuit is such an important feature in this design, a great deal of effort has been devoted to the study of the circuits, both from the theoretical and experimental point of view. An analysis of the unit circuit is given later, also the result of an experimental cold test verification of the analysis and the results of the study of the interconnection of these circuits.

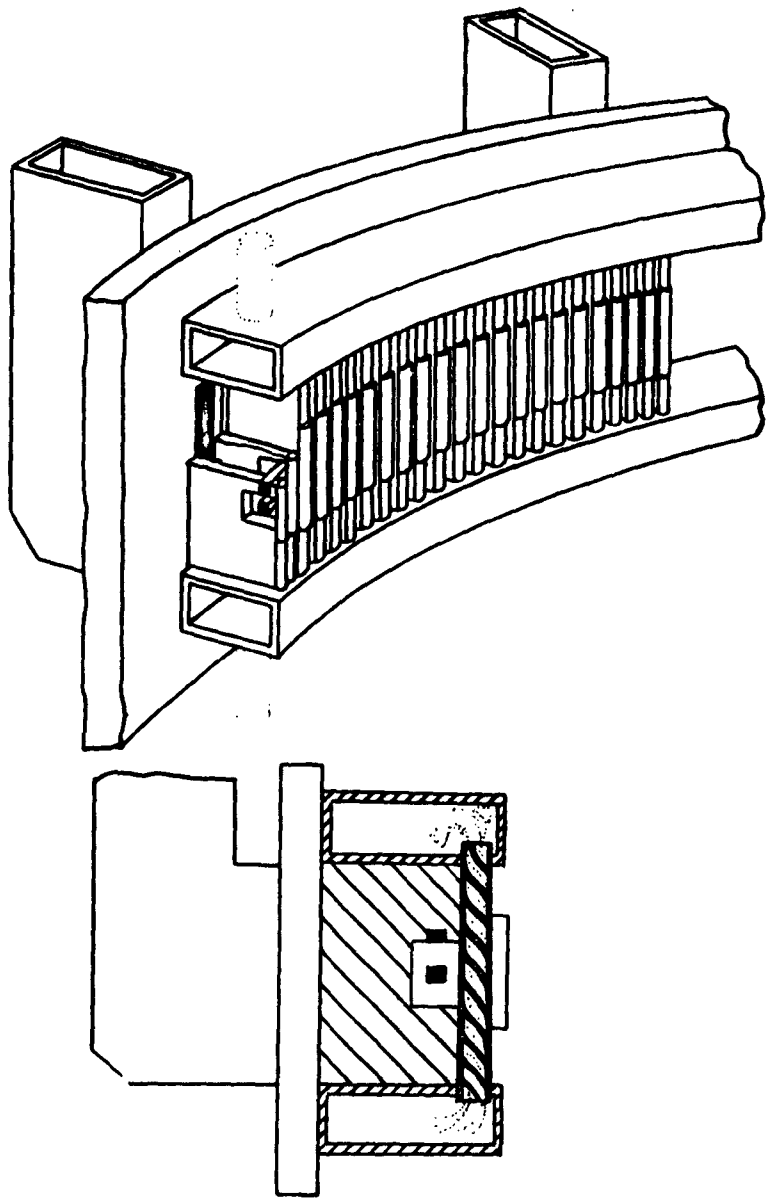

THREE-DIMENSIONAL DRAWING OF RF CIRCUIT UNIT

FIGURE 2

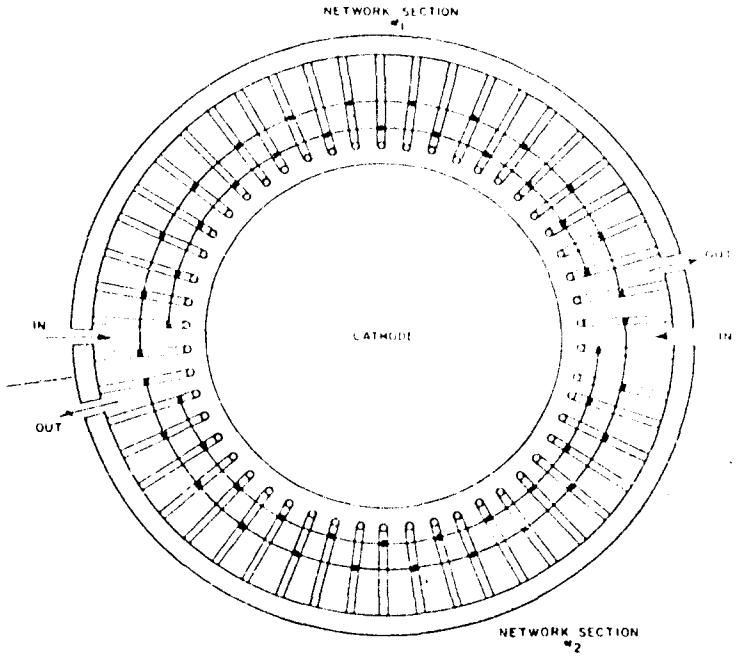

SCHEMATIC OF RF CIRCUIT UNIT

FIGURE 3

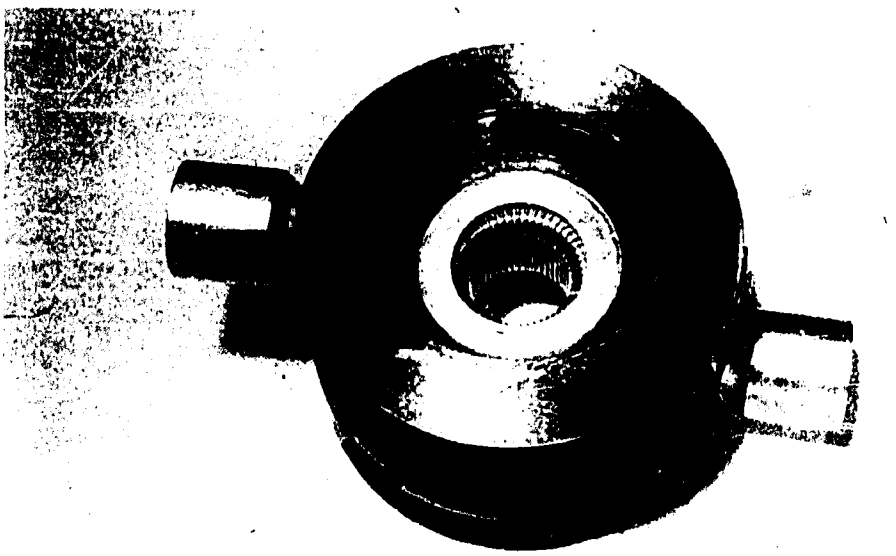

ANODE ASSEMBLY FOR THE TWO SECTION PROTOTYPE

FIGURE 4

These studies included consideration of operational stability, both from the theoretical point of view and from an experimental one, in the latter case by operating two Amplitrons in parallel. In this experiment, two QK622 Amplitrons were connected in parallel, having hybrid T sections both on their output and input terminals. Their combined outputs were measured in a common load on the output arm of the hybrid T section. To provide maximum power to the output load, it is essential that the power generated by the Amplitrons be balanced in phase and amplitude. Adequate phase balance was obtained readily across the full band simply by using waveguide sections of equal physical dimensions for the two branches of the circuit. The signal amplitude produced by each Amplitron is of importance, but less critical than phase balance for effective signal addition in the hybrid T. The test data indicated that more than 98% of the total rf output power of the parallel operated Amplitrons was measured in the common output load, whereas, the remaining rf power was measured as the out-of-phase power in the auxiliary arm of the output hybrid T. The experiments vividly demonstrate the capability of successfully operating two Amplitrons in parallel, and therefore lend credence to the application of this principle to the proposed dual-circuit Amplitron.

Figure 6 indicates schematically how connections are made between the slow-wave sections of the network structure and the output waveguide. Here we show the connections only on the output side of the tube. Similar connections are made on the input side of the tube, and in addition, a differential ferrite phase shifter is included in each of the two rf input feeds as shown in Figure 7. The differential phase shifter will effectively prevent any in phase reflected power feedback while still making it possible for the driving energy to be passed relatively unattenuated to the input of the Amplitron sections.

By dividing up a large number of vanes into two separate structures which are electrically isolated from each other within the tube itself, an anode area of sufficiently large size has been obtained for the intended application. Isolation is also maintained between the inputs of these sections by means of the hybrid section which permits driving energy to reach the slow-wave structures while the damping out of any feedback is accomplished by the use of the differential phase shift sections which guide reverse directed power into the auxiliary load of the input hybrid section. Isolating the section by this practice insures stable operation of the device. An anode structure of this size also makes it possible to provide a cathode of sufficient size to absorb the back bombardment power.

Figure 8 is a three-dimensional portrayal of the specific tube design under discussion. The output feeds are connected through a hybrid junction. The common output has a radome type vacuum seal. The auxiliary arm of the hybrid section and the two input feed arms have standard vacuum seals. The cathode support bushing may be seen on the bottom side of the anode. Figure 9 shows the internal construction of the tube, shown without the combining hybrid sections. The tube consists of two main subassemblies, the anode-waveguide subassembly and the cathode subassembly. The most important feature of the anode portion of the anode-waveguide subassembly is the slow-wave structure which consists of 50 vanes divided into two sections of 25 vanes each. Each section is isolated from the other rf-wise. Each of

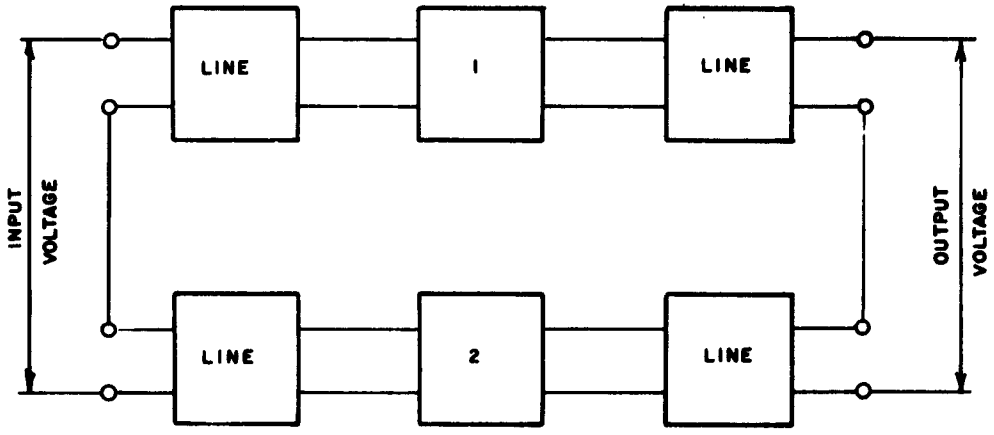

SCHEMATIC OF INTERCONNECTION OF DUAL CIRCUIT AMPLITRON

FIGURE 5

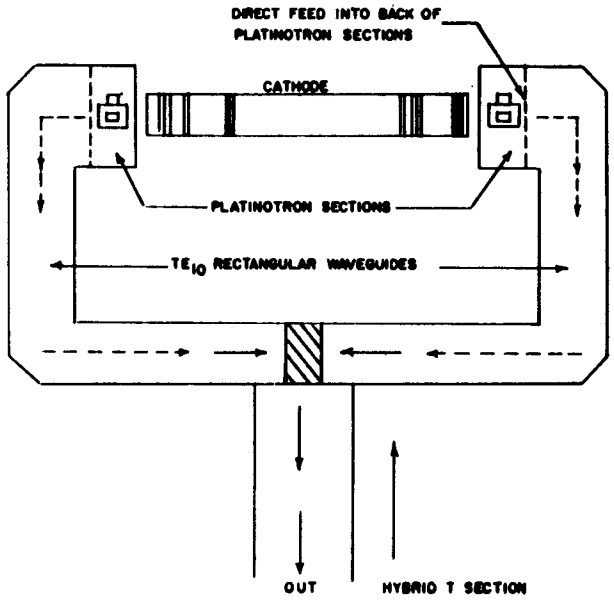

SCHEMATIC SHOWING HOW AMPLITRON RF CIRCUITS ARE CONNECTED THROUGH RECTANGULAR WAVEGUIDES TO A COMMON OUTPUT

FIGURE 6

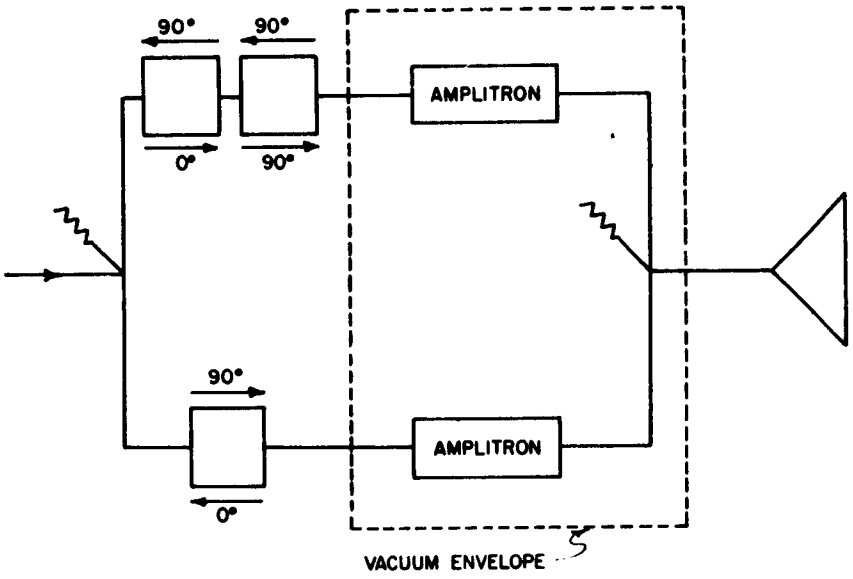

DUAL CIRCUITS WITH FERRITE PHASE SHIFTER

FIGURE 7

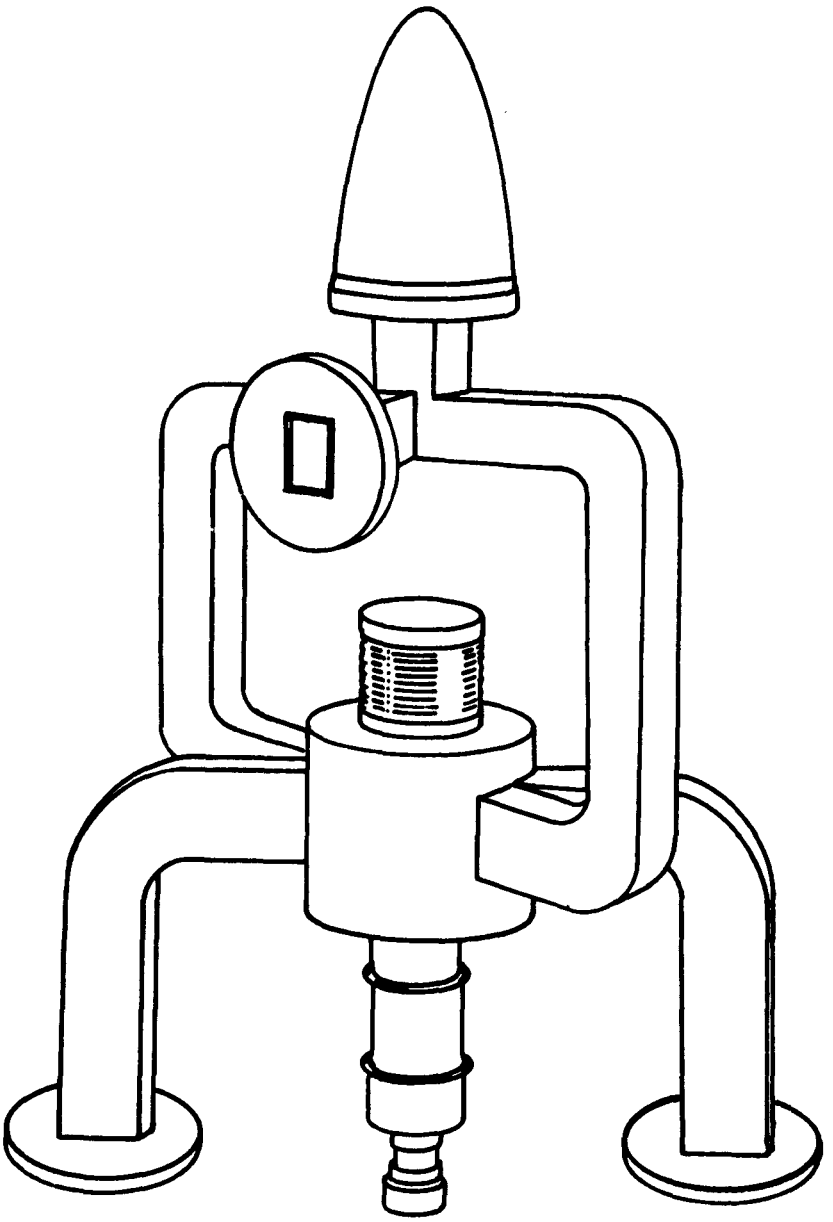

THREE DIMENSIONAL DRAWING OF DUAL CIRCUIT
X BAND AMPLITRON

FIGURE 8

the individual vanes has a single channel cooling system. The total anode dissipation capability will be about 150 kilowatts after allowing for dissipation distributed about the anode. The anode cooling area is thirty square centimeters and, therefore, a dissipation density of five kilowatts per square centimeter is the contemplated tube operation. This is indeed a conservative dissipation density requirement as compared to what has already been achieved in operating tubes in the super power S-band program.

Figure 10 shows a graph of the flow rate versus anode pressure drop of the anode as shown in Figure 4. A water flow of ten gallons per minute was measured through the anode, while the pressure drop across the anode was 365 pounds. With this much water flow, the anode should be fully capable of dissipating 150 kilowatts of power. 0.65 horsepower is required to circulate this much water flow. Taking into account pump inefficiencies, perhaps a two horsepower pump will be adequate. Pump pressure and water flow far in excess of these requirements are readily available here.

Again, referring to Figure 9, the most important feature in the cathode subassembly, is the cathode which consists of a solid piece of tungsten. The way in which this cathode is heated to emission temperature is made clear by referring to Figure 11. In this figure, it will be seen that the central portion of the cathode is heated by the passage of large amounts of current through it. The temperature drop from the central portion to the peripheral emitting surface of the cathode will be limited to a few hundred degrees so that enough thermionic emission will occur to permit the secondary emission operation to build up. Because the Amplitron operates on secondary emission principle, no heater power is required during full operation. The bulk of the heat resulting from back bombardment power flows back through the annular disc of tungsten and then divides and flows into equal parts to the water-cooled copper supports at either end of the tungsten cathode. The remaining amount of heat is directly radiated.

In the proposed tube under discussion, the cathode is almost identical in size with the cathode used in the QR849--the super power CW S-band Amplitron designed for operation in the range of 400 kilowatts. This cathode has shown excellent performance in this tube and no particular problems are anticipated with it in the X-band design. Figure 12 shows a picture of the directly-heated cathode assembly as will be used in the dual-stage Amplitron. Test data of a diode built with this cathode has shown a total cathode dissipation capability of more than 11 kilowatts can be obtained without adverse affect to the cathode. With a cathode back bombardment power of 3% of the generated rf power, the dissipation measurements indicate that this cathode should be fully capable of 400 kilowatts of CW power operation, which by far exceeds the contemplated output power of the dual-section Amplitron.

From the analysis of the circuit theory of the network, equations yielding phase shift and the characteristic network impedance as a function of frequency, for a given set of geometric configurations, can be obtained. Figure 13 shows in abbreviated form the network analysis with the resultant general network expressions. These general expressions can be further defined in terms of the specific network geometry. This is shown in Figure 14.

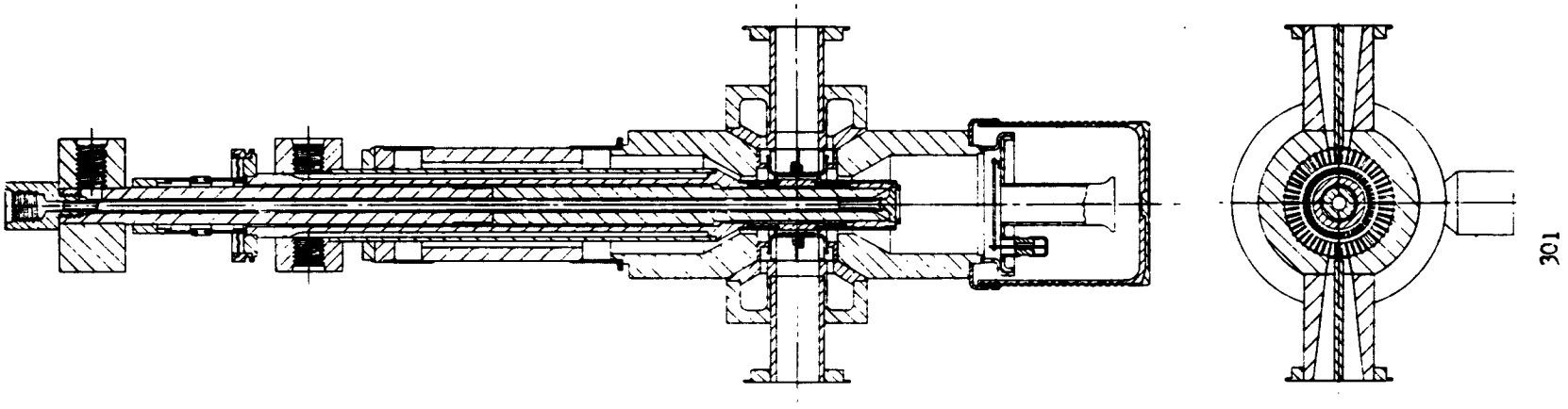

301

TWO SECTION AMPLITRON

FIGURE 9

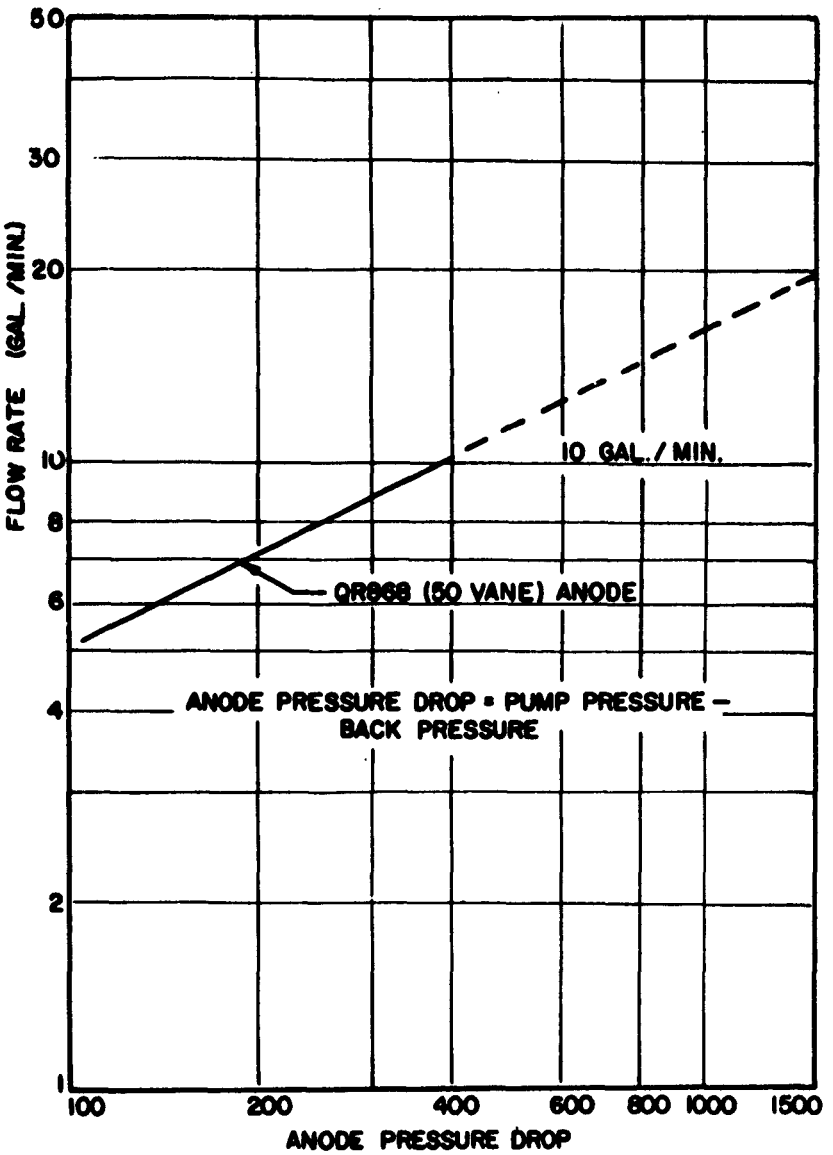

PRESSURE VS. FLOW RATE

FIGURE 10

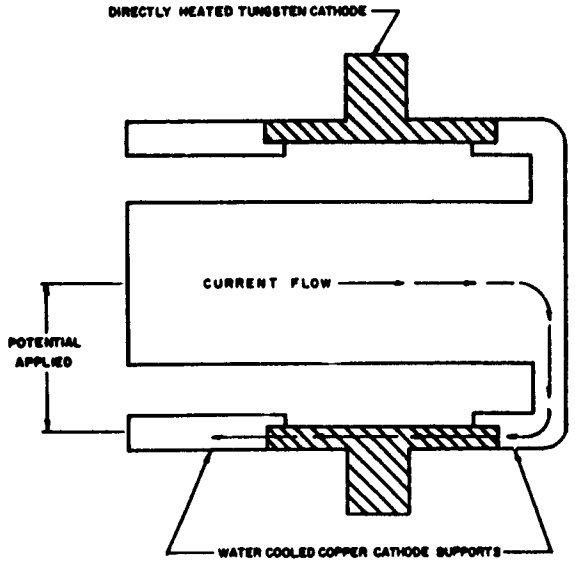

SCHEMATIC SHOWING PRINCIPLE OF COAXIAL DIRECTLY - HEATED TUNGSTEN CATHODE

FIGURE 11

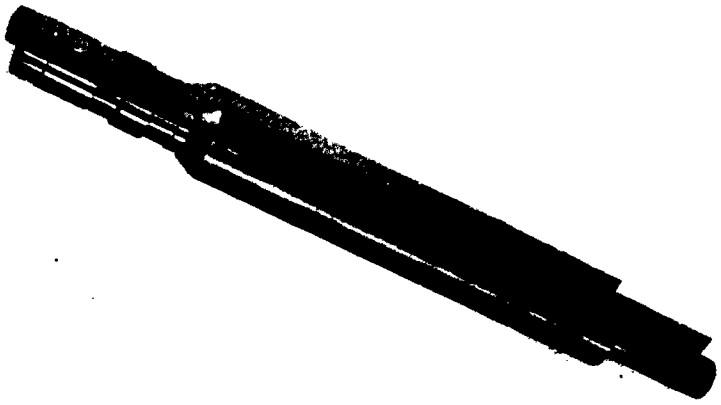

COAXIAL DIRECTLY-HEATED CATHODE ASSEMBLY
FOR THE "TWO-SECTION PROTOTYPE"

FIGURE 12

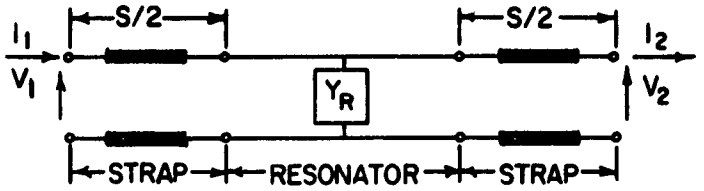

MATRIX EXPRESSION $T = T_S\, T_R\, T_S$

PHASE SHIFT PER SECTION $\cos\psi = \cos 2\theta + \frac{Y_R Z_S}{2} \sin 2\theta \cot\phi$

NETWORK IMPEDANCE $Z_P = {}_J Z_{12} \sqrt{1-\cos^2\psi}$

$$\frac{1}{Z_{12}} = {}_J Y_S \left[\sin 2\theta - \frac{Y_R Z_S}{2}(1+\cos 2\theta)\cot\phi\right]$$

ANALYSIS OF CIRCUIT THEORY

FIGURE 13

Definitions:

For Strap:

$2\theta = \frac{2\pi s}{\lambda}$ electrical length of strap

$Z_s = 120\pi \frac{b_s}{a_s}$ characteristic impedance of parallel plane transmission line

$k = \frac{Z_s}{2Z_0} = \frac{1}{4}\frac{(b_s/a_s)}{(b_r/a_r)}$ Strap factor

For Resonator:

$\phi = \frac{2\pi k}{\lambda_g} = \frac{2\pi k}{\lambda}\sqrt{1-\left(\frac{\lambda}{\lambda_c}\right)^2}$ electrical length of resonaton

$Z_r = \frac{Z_0}{\sqrt{1-\left(\frac{\lambda}{\lambda_c}\right)^2}} = \frac{120\pi\left(\frac{2k\pi}{a_r}\right)}{\sqrt{1-(\lambda/\lambda_c)^2}}$ characteristic impedance of resonator

$\lambda_c = 2a_r$ cut-off wavelength of resonator section

$$\cos\psi = \cos\frac{2\pi s}{\lambda} + k\sqrt{1-(\lambda/\lambda_c)^2}\sin\frac{2\pi s}{\lambda}\cot\frac{2\pi k}{\lambda}\sqrt{1-(\lambda/\lambda_c)^2}$$

$$1/Z_{12} = j\frac{1}{120\pi(b_s/a_s)}\left[\sin\frac{2\pi s}{\lambda} - k\sqrt{1-(\lambda/\lambda_c)^2}\,(1+\cos\frac{2\pi s}{\lambda})\cot\frac{2\pi k}{\lambda}\sqrt{1-(\lambda/\lambda_c)^2}\right]$$

FIGURE 14

The geometry of the network design was chosen so as to yield a lower cutoff frequency around 8000 megacycles per second. Figures 15 and 16 show the calculated phase shift and network impedance as a function of frequency. They also show how these functions vary as the strap factor k is reduced which is accomplished by more tightly coupling the straps to the network.

The cold test model was built and tested. Test data revealed that the lower cutoff frequency of the network was at 7200 megacycles per second, or about 10% lower than the calculated values. Figure 17 shows the test results. Despite the discrepancy between the theoretically predicted phase shift and the measured values, the agreement is sufficiently good to make the analysis a good working tool. When the resonator length a_r was reduced from 1.000 to 0.800", the desired phase shift was obtained. The cold test match in percent reflected voltage of this network as well as transmission characteristics is shown in Figure 18. A broadband match of better than 20% is obtained, well beyond the contemplated operating band of the tube, whereas transmission over this band is better than 90%.

Figure 19 shows plots of Hartree voltage as a function of magnetic flux density both from the 180° and 540° mode of operation. When operating with a magnetic field strength of 4500 gauss, operation in the 180° mode would require 22 kilovolts, whereas operation in the 540° mode would require 24 kilovolts of anode potential. Figure 20 is an ω-β plot. The slope of the straight lines coming from the origin and intercepting the ω-β diagram are proportional to the anode voltages necessary for operating in a given mode.

The V_0 and B_0 used in calculating the Hartree equations are 2.45 kV and 906 gauss respectively when the operating wavelength of the 180° phase shift mode is at 8300 megacycles per second.

Experimental Test Results

The cold test data, hydraulic measurements of the anode, dissipation measurements of the cathode, the parallel operation of two Amplitrons and other work were sufficiently encouraging to warrant the construction of an operating tube with this type of circuit, having an ultimate goal of 200 kilowatts of CW power at X-band. This two-section Amplitron is labeled QKS976 and is company-funded at a moderate rate. Figure 21 is a photograph of the constructed tube. The tube is built with four vacuum loads, since in the early testing stage the tube will be operated as a free-running oscillator.

The first hot tube was tested under pulsed conditions and showed tube operation at 8200 megacycles per second, or in the 180° mode. The magnetic field was 3500 gauss and anode voltage of 17.2 kilovolts with peak anode current of 40 amperes. Peak power output of 275 kilowatts was obtained. The tube was then operated under CW conditions. With an anode current of two amperes and 16 kilovolts of anode voltage, the output power was 10 kilowatts and rising when the tube failed. Subsequent analysis indicated a vane failure due to defective raw material. This was

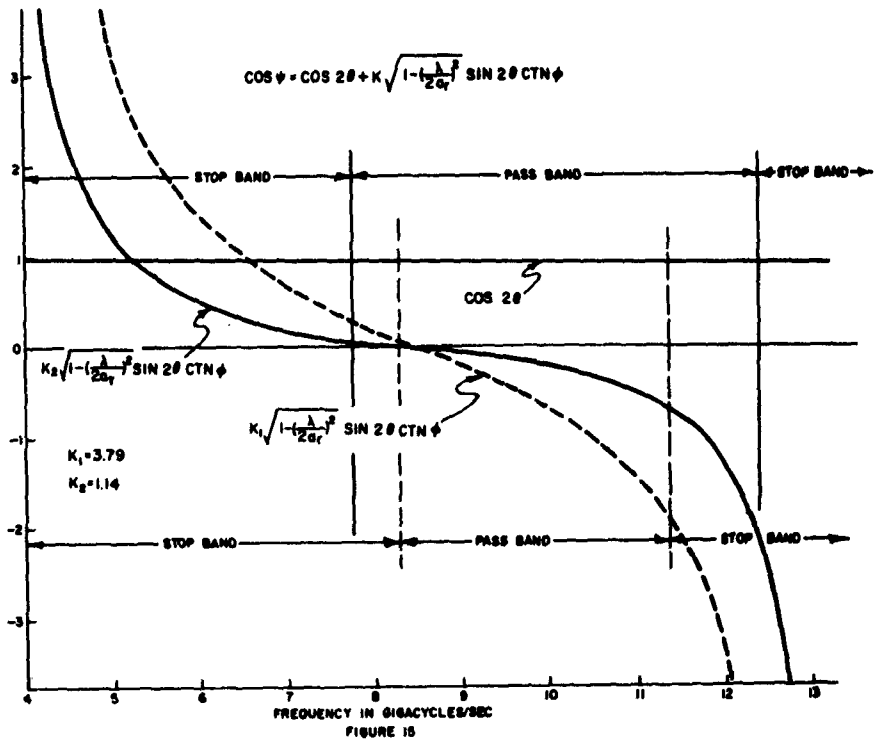

FIGURE 15

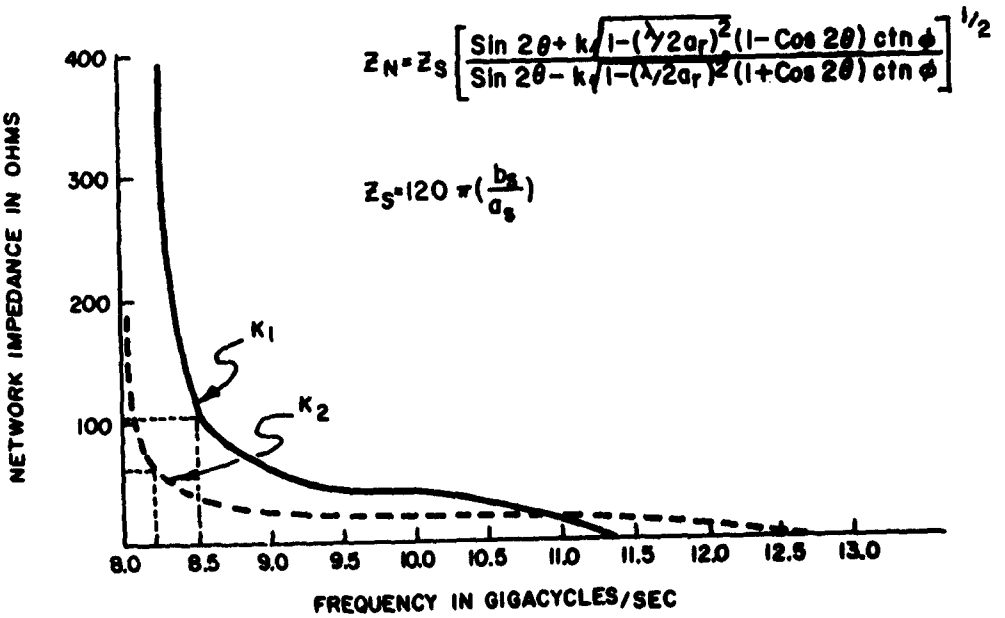

FIGURE 16

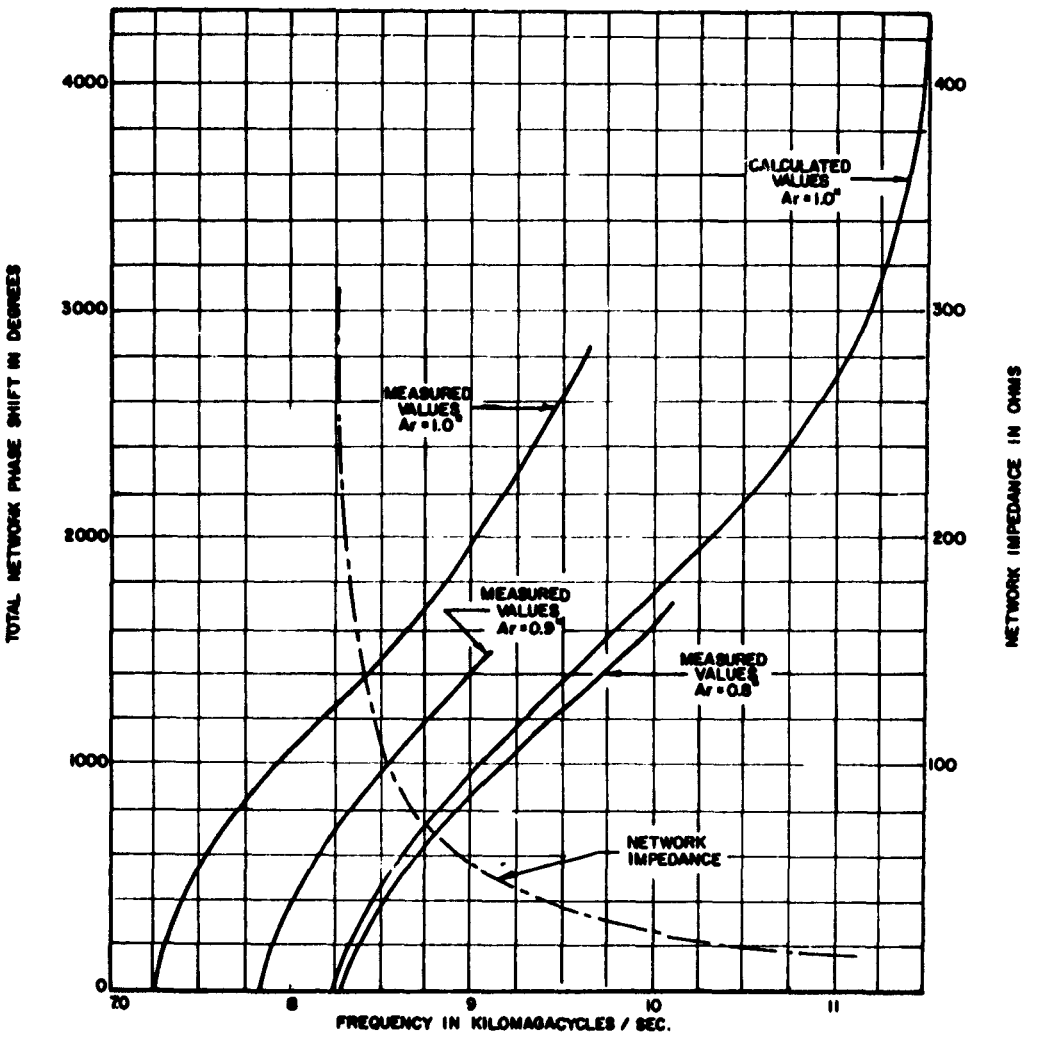

TOTAL PHASE SHIFT AND NETWORK IMPEDANCE VS. FREQUENCY (24 CAVITIES)

FIGURE 17

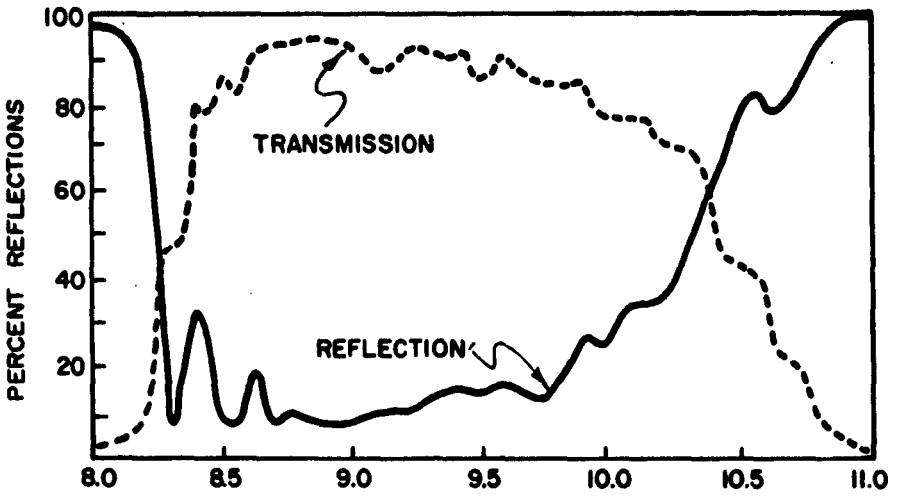

VOLTAGE REFLECTIONS AND
TRANSMISSION IN PERCENT

FIGURE 18

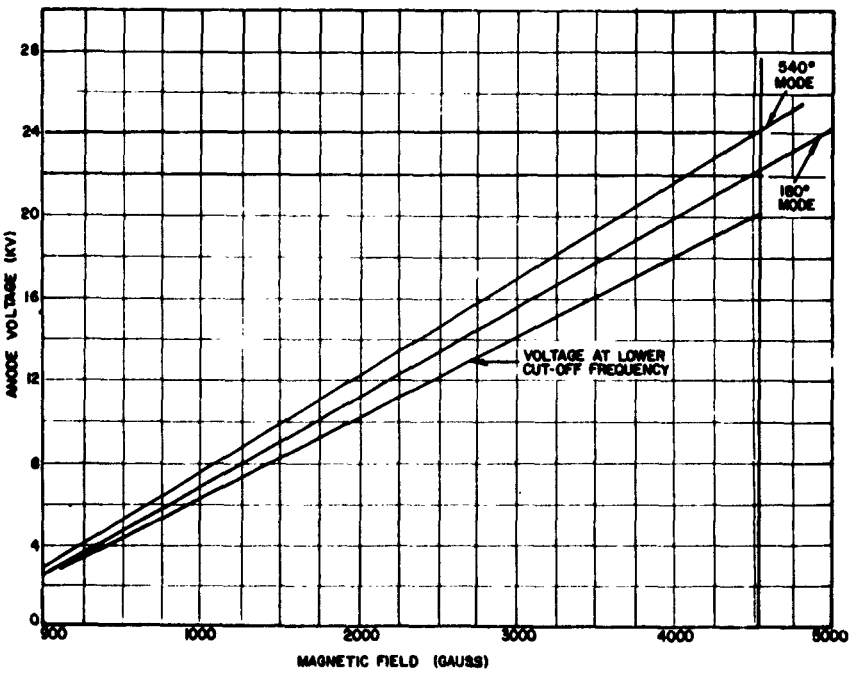

HARTREE VOLTAGE VS. APPLIED FIELD

FIGURE 19

due to a material control problem rather than a basic design problem. There was also an indication of possible multipactor discharge in the straps. The material control problem has been easily resolved by adequate inspection and specification. In order to assure that no limitations due to multipactor discharges across the straps will occur, changes in the strap spacing consistent with cold test data has been accomplished. A second tube with these changes is presently awaiting processing and testing.

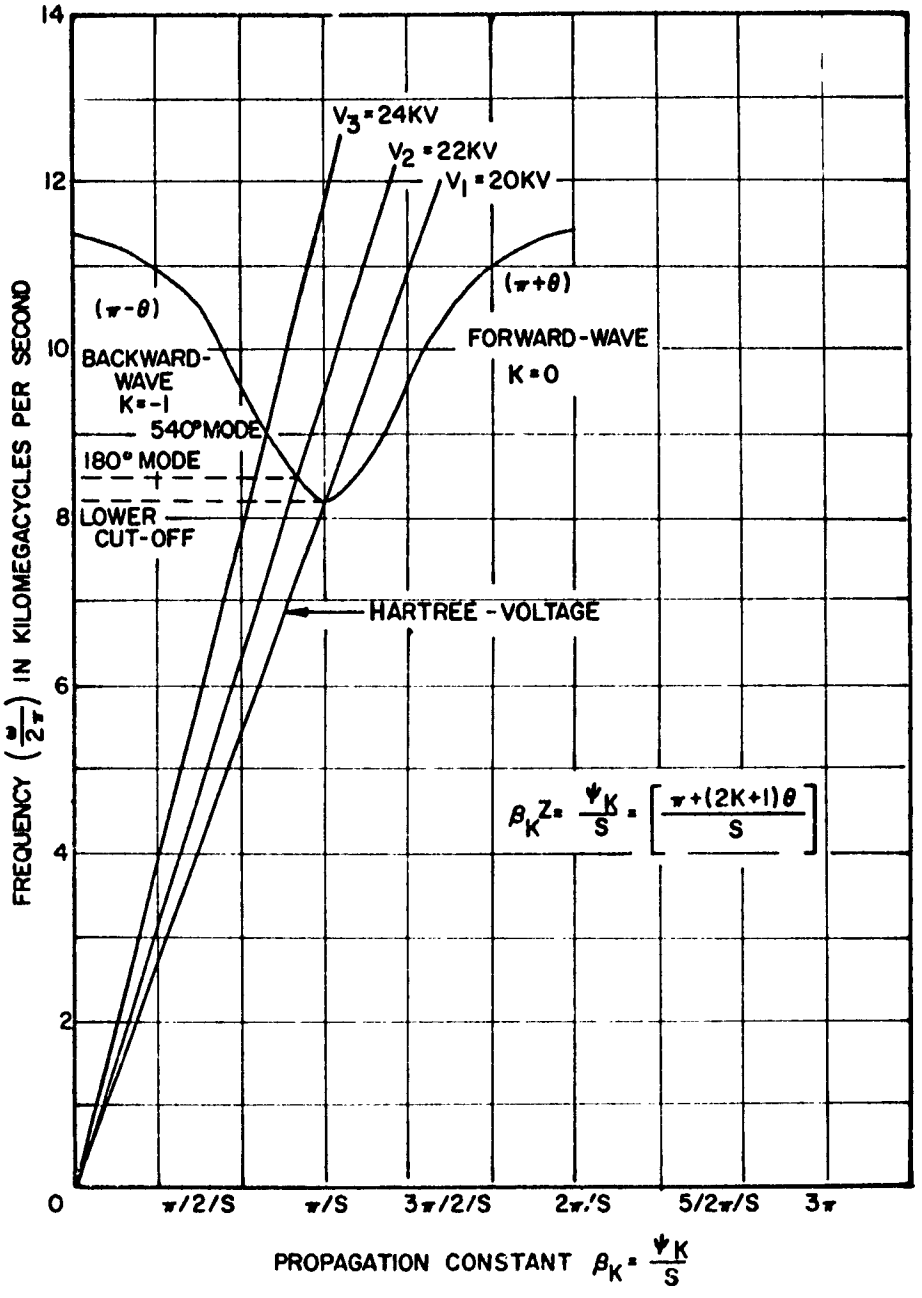

$W_1\beta$ DIAGRAM

FIGURE 20

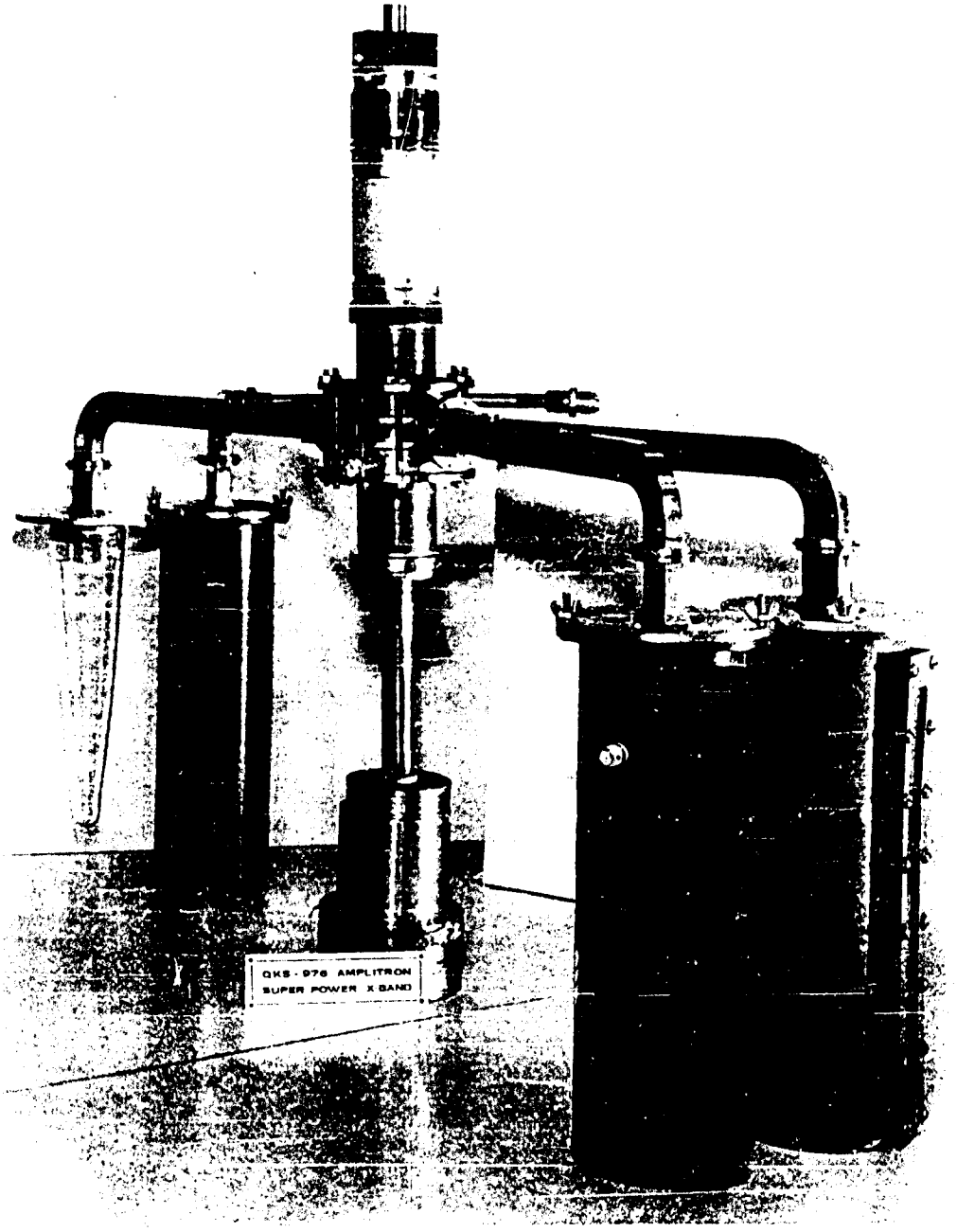

FIGURE 21

RECORD OF ATTENDEES

FOREIGN NATIONALS

British Navy Staff
P. O. Box 165
Benjamin Franklin Station
Washington, D. C.
J. Peters
J. C. Vokes

Compagnie Francaise de Thomson Huston
173 Blvd Haussmann
Paris 8, France
R. Metivier
J. Picquendar

Compagnie General de TSF
B. P. 10 Orsay (S&O)
France
B. Epsztein

Service Technique Des
Telecommunications De L'Air
129 Rue De La Convention
Paris 14eme - France
Michel Beignot-Devalmont

MILITARY ORGANIZATIONS

Advanced Research Projects Agency
Rm 2B263, Pentagon
Washington 25, D. C.
Lt. Col. W. B. Lindsay

Advisory Group on Electron Devices
346 Broadway, 8th Floor
New York 13, N. Y.
W. Kramer
B. Silverstein

Air Force Systems Command
111 East 16th Street
New York 3, New York
M. Pavane

Commander
ESD, L. G. Hanscom Field
Bedford, Mass.
Maj. J. W. VanHorn

Naval Air Development Center
Code EL83
Johnsville, Penn.
T. J. Massey
L. C. Metz

Naval Material Laboratory (Code 924)
N. Y. Naval Shipyard
Brooklyn 1, New York
J. Adelsberg
N. Cooper
H. Einstein

Office of the Secretary of Defense
Washington 25, D. C.
Lt. Col. C.G. Henline (Ret.)

Rome Air Development Center (RALTP)
Griffis Air Force Base
Rome, New York
H. Friedman (RAWED)
B. Werle
A. J. Wiejek

U. S. Army Electronics Materiel Agency
225 S. 18th Street
Philadelphia 3, Pa.
C. Mogavero
S. Sokalove

U. S. Army Electronics Materiel Agency
Fort Monmouth, N. J.
S. Zucker

U.S. ArmyElectronics Materiel Agency
C&M Branch, EDD Section
Coles Area, Fort Monmouth, N. J.
J. R. Drayer

Commander
ASD,Electron Tubes Branch
Wright-Patterson AFB, Ohio
E. R. Nichols

Military Organizations (Cont'd)

U. S. Army Ordnance Missile Command (AMSMI-MD)
Redstone Arsenal, Alabama
Lt. Col. E. J. Dotson
Maj. C. W. Goldey
C. L. Hunter

Bureau of Ships Code 681A1
Dept of the Navy
Washington 25, D. C.
W. J. Riegger

U. S. Army Electronics R&D Laboratory (USAELCTRDLAB Cont'd)
Fort Monmouth, N. J.
W. C. Brown
A. J. Buffa
J. Bruscella
X. L. Cotton
W. E. Cowan
W. F. Carbaugh
J. L. Carter
S. Del Vecchio
R. P. Dubois
S. Dixon, Jr.
E. DeCamp
Lt. A. S. Esbitt
E. V. Edwards
P. Fischer
G. Fincke, Jr.
A. Gottfried
L. N. Heynick
H. Hieslmair
H. J. Hersh
J. L. Hanley
A. Haisidozahl
C. P. Heinzman
E. Kaiser
L. L. Kaplan
H. M. Kaunzinger
W. F. Kennison
S. R. Leefe
S. Levy
A. Lisper
J. Luden
E. Nolan
V. Organic
I. Reingold
B. Reich
P. Richmond
D. Ricker
D. Salvano
H. Sanders
S. Schneider
M. Sedern
B. Smith
C. A. Stolckl
T. X. Szwajer
J. J. Tancredi
G. W. Taylor
R. M. True
G. C. Uchrin
F. Vorwerk
A. Wachtenheim
N. Wilson
N. Yeamans
H. A. Zahl
M. H. Zinn

COMMERCIAL ORGANIZATIONS

Amperex Electronics Corp.
230 Duffy Avenue
Hicksville, L. I., New York
S. Barbasso

Atlantic Research Corp.
Ithaca Research Labs
714 W. Clinton Street
Ithaca, N. Y.
A. R. Howland, Jr.

ARINC Research Corp.
1700 K. Street Northwest
Washington 6, D. C.
R. S. Strauss

Bell Telephone Laboratories
Whippany Road
Whippany, N. J.
R. C. Newhouse
H. A. Reise

Commercial Organizations (Cont'd)

Bell Telephone Laboratories
Murray Hill, New Jersey
R. J. Collier
G. D. Helm

Bendix Corp.
Bendix Radio Div
East Joppa Road
Towson 4, Maryland
B. C. Dodson, Jr.
R. J. Davis

Bendix Corp.
Route 35
Eatontown, New Jersey
G. Novick

Budd Electronics
43-22 Queens Street
Long Island City 1, N. Y.
M. Cohen
H. Lowenhar

Cornell Aeronautical Laboratory
4455 Genesee Street
Buffalo 21, N. Y.
L. H. Groth

Eitel McCullough, Inc.
San Carlos, Calif.
R. H. Giebeler
G. A. Huffman

FXR, Div. of Amphenol Borg
25-26 - 50th Street
Woodside 77, N. Y.
A. S. O'Keefe

General Electric Co.
60 Jackson Street
Holyoke, Mass.
R. S. Ringland
W. C. Stone

The Hallicrafters Co.
4401 W. Fifth Ave.
Chicago 2, Illinois
G. Rappaport

Bell Telephone Laboratories
Laureldale, Pennsylvania
W. H. Dufft
H. M. Olson
K. F. Sodomsky
L. H. Von Ohlsen

Bendix Corp.
Research Laboratories Div.
Southfield (Detroit), Michigan
A. G. Peifer

Bomac Laboratories
Salem Road
Beverly, Mass.
E. D. Benson
E. J. Cook
A. Westlund, Jr.

Continental Electronics Mfg Co.
P. O. Box 17040
Dallas 17, Texas
R. E. Ramsey

Cornell University
School of Electrical Engineering
Ithaca, N. Y.
L. F. Eastman
A. S. Gilmour, Jr.

Field Emission Corporation
P. O. Box 476
McMinnville, Oregon
F. M. Charbonnier

General Electric Co.
Box 1088
Schenectady, N. Y.
R. J. Bondley
G. M. Branch
R. A. Dehn
T. G. Mihran
W. J. Pohl
D. A. Wilbur

General Electric Co.
601 California Ave.
Palo Alto, Calif.
S. E. Webber

General Electric Co.
200 Main Ave., Clifton, N.J.
H. L. Tate

Commercial Organizations (Cont'd)

General Telephone & Electronics
208-20 Willets Point Blvd
Bayside 60, N. Y.
L. D. Cohen
H. Dressel

General Telephone & Electronics Lab.
730 - Third Ave.
New York 17, N. Y.
R. M. Bowie

Hughes Aircraft Co.
11105 La Cienega Ave.
Los Angeles 45, Calif.
B. A. Highstrete
A. L. Rousseau
L. M. Winslow

Hughes Research Laboratories
3011 Malibu Canyon Road
Malibu, Calif.
J. E. Nevins, Jr.

Hughes Microwave Tube Div.
30 Linden Place
Red Bank, N. J.
G. Berman

ITT Components Division
Electron Tube Laboratory
500 Washington Avenue
Nutley, 10, N. J.
H. J. Luettchau
R. W. Wilmarth

ITT Federal Laboratories
103 E. Front Street
Red Bank, N. J.
F. W. Enander

Jansky & Bailey
Div. of Atlantic Research Corp.
Shirley Highway & Edsall Rd
Alexandria, Virginia
A. W. Paul

Litton Industries
960 Industrial Road
San Carlos, Calif.
L. J. Fox
P. N. Hess
D. W. Reid
R. D. Harris
A. Prommer
A. J. Smith

Litton Industries
Eastern Regional Office
171 Main Street, P. O. Box 548
Manasquan, N. J.
F. M. Oakes

Massachusetts Institute of Technology
Lincoln Laboratory
Box 73
Lexington 73, Mass.
W. A. Both
R. Butman
C. Freed
J. Freedman
E. Gronroos
G. L. Guernsey
I. Hefni
J. R. Sandison
E. Silverman
G. E. Vibrans

Metcom Inc.
76 Lafayette Street
Salem, Mass.
L. W. Roberts
W. Dodds

Microwave Associates Inc.
Burlington, Mass.
C. S. Biechler

Microwave Electronics Corp.
4061 Transport Street
Palo Alto, Calif.
W. E. Waters

Commercial Organizations (Cont'd)

North American Aviation
4300 E. Fifth Avenue
Columbus, Ohio
J. W. Hull

Radio Corporation of America
Lancaster, Penn.
A. C. Grimm
W. N. Parker
E. E. Spitzer - F. G. Hammersand

Radio Corporation of America
Princeton, N. J.
B. Hershenov
M. Caulton
L. S. Nergaard
W. W. Siekanowicz
P. T. Smith
H. Sobol
F. E. Vaccaro

Raytheon Company
Spencer Laboratory
Burlington, Mass.
L. B. Anderson
W. Brown
H. F. Chapell
J. N. Lind
T. E. Ruden
H. D. Scharfman
J. F. Skowron
W.A. Smith
W. Zettler
C. M. Hellenbrand

Sperry Electronic Tube Div.
Gainesville, Florida
B. C. James
J. Fuhrer
K. R. Reichert
F. W. Warner
J. A. Westmeyer
G. Whittington

Stanford Research Institute
Menlo Park, Calif.
L. Feinstein
S. V. Yadavalli

Pollytechnic Institute of Brooklyn
Route 110
Farmingdale, N. Y.
M. Ettenberg
S. W. Rosenthal

Radio Corporation of America
Moorestown, N. J.
T. J. Boerner
T. Douma
C. Pappas

Radio Engineering Laboratories
29-01 Borden Avenue
Long Island City 1, N. Y.
D. F. Koijane

Radio Engineering Laboratories
Lakewood Road
Farmingdale, N. J.
M. B. Kraus, Sr.

S-F-D Laboratories
800 Rahway Avenue
Union, N. J.
J. Drexler
G. Farney
J. Feinstein
H. McDowell
J. Saloom

Sperry Gyroscope Co.
Great Neck, New York
D. B. Churchill
S. B. Dunn
L. W. Holmboe
A. Jorge
C. F. Lammert
V. R. Learned
J. McLinden
S. Porter
T. D. Sege
L. Swern
C . C. Wang
R. J. Timms

Stanford University
Stanford, Calif.
D. K. Winslow

Commercial Organizations (Cont'd)

Sylvania Electronic Products Inc.
500 Evelyn Avenue
Mountain View, Calif.
R. Eggers
J. S. Needle
T. Roumbanis

Sylvania Electric MDD
1891 E. Third Street
Williamsport, Pa.
D. W. Jewart
R. C. Sibley

Sylvania EDL
P. O. Box 205
Mountain View, Calif.
H. J. Bielefeld

University of Connecticut
Storrs, Connecticut
G. E. Dombrowski, U37

University of Michigan
3501 E. Engr Bldg
Ann Arbor, Michigan
G. T. Konrad
J. E. Rowe

Varian Associates
611 Hansen Way
Palo Alto, Calif.
S. E. Allen, Jr.
O. F. Johnson
L. L. Moore
R. Nelson
D. A. Oberndorf
J. A. Ruetz
A. Staprans
R. S. Symons
R. L. Walter
L. Zitelli

Watkins-Johnson Co.
3333 Hillview Avenue
Palo Alto, Calif.
J. W. Sedin

Westinghouse Electronic Tube Div.
Elmira, New York
D. F. Aldrich

Westinghouse Electric Corp.
P. O. Box 746
Baltimore 3, Md.
L. F. Cooper
G. Klein
J. M. Scott
D. E. Solomon
F. L. Washburn

Westinghouse Electric Corp.
Box 1897
Baltimore 3, Md.
W. R. Donsbach
W. E. Hosey
F. J. Rutter

Zenith Radio Corp.
6001 W. Dickens Avenue
Chicago 39, Illinois
W. M. Sackinger

AUTHOR INDEX

VOLUME 1

*Now at Mictron, Inc., Albany, N. Y.